Development and Mechanistic Modelling of Prussian Blue-based Multimodal Targeted Theranostic Nanocomposite for Cancer Treatment

Thesis submitted by

Panchanan Sahoo

Index No.- D-7/ISLM/104/19

Jadavpur University

Indian Statistical Institute

Doctor of Philosophy (Science)

School of Materials Science and Nanotechnology Faculty of Interdisciplinary studies, Law and Management

Jadavpur University

Kolkata-700032

India

2024

Development and Mechanistic Modelling of Prussian Blue-based Multimodal Targeted Theranostic Nanocomposite for Cancer Treatment

Thesis submitted by

Panchanan Sahoo

Index No.- D-7/ISLM/104/19

Jadavpur University

Indian Statistical Institute

Doctor of Philosophy (Science)

School of Materials Science and Nanotechnology Faculty of Interdisciplinary studies, Law and Management

Jadavpur University

Kolkata-700032

India

2024

INDEX No. - D-7/ISLM/104/19

1. Title of the thesis:

Development and Mechanistic Modelling of Prussian Blue-based Multimodal Targeted Theranostic Nanocomposite for Cancer Treatment

2. Name, Designation & Institution of the Supervisor:

(a) Dr. Chandan Kumar Ghosh
Assistant Professor
School of Materials Science & Nanotechnology
Jadavpur University
Kolkata – 700032
Email: chandu_ju@yahoo.co.in

(b) Dr. Abhishek Mukherjee
Associate Professor
Agricultural and Ecological Research Unit
Indian Statistical Institute (Giridih)
Jharkhand – 815301
Email: abhi.mukh@yahoo.com

3. List of Publications:

Thesis Work (Peer Reviewed International SCI journal)

(a) Fundamental understanding of the size and surface modification effects on r_1, the relaxivity of Prussian blue nanocube@m-SiO_2: a novel targeted chemo-photodynamic theranostic agent to treat colon cancer: **Sahoo P.**, Kundu, S., Roy, S., Sharma, K.S., Ghosh, J., Mishra, S., Mukherjee, A. and Ghosh, C. K, ***RSC Advances***, 2022 (IF **4.036**).

(b) Quercetin@Gd^{3+} doped Prussian blue nanocubes induce the pyroptotic death of MDA-MB-231 cells: combinational targeted multimodal therapy, dual modal MRI, intuitive modelling of r_1-r_2 relaxivities: **Sahoo, P.**, Jana, P., Kundu, S., Mishra, S., Chattopadhyay, K., Mukherjee, A., & Ghosh, C. K., **Journal of Materials Chemistry B**, 2023 (IF **7.571**).

(c) Lanthanide doped Prussian blue nanocube for dual responsive DOX delivery to treat MDA-MB-231 cells: combinational targeted multimodal therapy, dual modal MRI, intuitive modelling of r_1-r_2 relaxivities: **Sahoo P.**, Nandi, S. K., Das M., Ghosh, J., Mukherjee, A., & Ghosh, C. K. (**Under Review**)

(d) Recent advances of Prussian blue nanoparticles as biomedicine: **Sahoo, P.**, Kundu, T., Bhattacharya, S., Mukherjee, A., & Ghosh, C. K., **Coordination Chemistry Reviews** (Elsevier) (**Under review**)

Allied to Thesis Work (Peer Reviewed International SCI journal)

(e) Facile and green synthesis of novel fluorescent carbon quantum dots and its silver heterostructure: an *in-vitro* anticancer activity and imaging on colorectal carcinoma: Mishra, S., Das, K., Chatterjee, S., **Sahoo, P.**, Kundu, S., Pal, M., Bhaumik, A. and Ghosh, K. C., ***ACS Omega***, 2022 (IF **4.132**).

(f) Use of diformyl-triazolo Schiff base for Zn^{2+} sensing and intracellular live cell imaging: Maity, M. B., Bhunia, S., Patra, A., **Sahoo, P.**, Mishra, S., & Sinha, C., **Applied Organometallic Chemistry**, 2023 (IF **4.072**).

(g) Curcumin based nanoformulation leads pyroptotic death of MDA-MB-231 cells: understanding of size, composition dependent theranostic properties and potential factors: Kundu, S., Jana, P., **Sahoo, P.**, Nandi, S. K……, Chattopadhyay, K., & Ghosh, C. K., **ACS Applied Nano Materials,** 2024 (IF **6.14**).

(h) Response Surface Methodology Optimised Sorptive Removal of Fluoride using a Water-hyacinth based Biochar : A Waste to Wealth Quest: Nandi, R., Mondal, S., Bhattacharya, S., **Sahoo, P.**, Mandal, J & Bhattachrya, P., **ACS ES&T Water,** 2024 (IF **5.3**) (**Under Review**)

Book Chapter

(i) Nanoparticles in Biomedical Applications: MRI Contrast Agents. In Advanced Nanomaterials and Their Applications: Sahoo, P., Chowdhury, D., Kundu, S., Mukherjee, A., & Ghosh, C. K. CRC Press, 2023.

(j) Gold nanoparticles for photothermal and photodynamic therapy in cancer treatment: Sahoo, P., Mukherjee, A., & Ghosh, C. K. Elsevier (under review)

(k) Gold Nanoparticles in Point of Care Diagnostic Tools and Devices, Kundu S., Sahoo, P., Das, M., Nandi, S. & Ghosh, C. K. Elsevier (under review).

Conference Proceedings

(l) Best oral presentation award in International Conference on Nanomaterials in Biology (ICNB), 2021 organized by SMRS, Jaipur, India.

(m) Poster presentation in Young Scientists Colloquium, Materials Research Society of India (MRSI), Kolkata Chapter, 2022 organised by CGCRI, Kolkata.

(n) Best poster presentation in Young Scientists Colloquium, Materials Research Society of India (MRSI), Kolkata Chapter, 2023 organised by School of Materials Science and Nanotechnology, JU, Kolkata.

CERTIFICATE FROM SUPERVISOR

This is to certify that the thesis entitled **"Development and Mechanistic Modelling of Prussian Blue-based Multimodal Targeted Theranostic Nanocomposite for Cancer Treatment"** submitted by Mr. Panchanan Sahoo (**Reg. No. – D-7/ISLM/104/19**), who got his name registered on 01.11.2019 for the award of PhD (Science) degree of Jadavpur University is absolutely based upon his own work under the supervision of Dr. Chandan Kumar Ghosh, Jadavpur University and Dr. Abhishek Mukherjee, Indian Statistical Institute (Giridih).

14/05/2024

Abhishek Mukherjee, Ph.D.
Associate Professor
Agricultural and Ecological Research Unit
INDIAN STATISTICAL INSTITUTE
New Barganda, Giridih - 815 301
Jharkhand, India

Dr. Chandan Kumar Ghosh	Dr. Abhishek Mukherjee
Assistant Professor	Associate Professor
Jadavpur University	Indian Statistical Institute (Giridih)
(Signature of the supervisor, date with seal)	(Signature of the supervisor, date with seal)

Dr. Chandan Kumar Ghosh
Assistant Professor
School of Materials Science
& Nanotechnology,
Jadavpur University
Kolkata - 700 032

Statement of Originality

Panchanan Sahoo (**Reg. No. – D-7/ISLM/104/19**) registered on 01.11.2019 do hereby declare that this thesis entitled **"Development and Mechanistic Modelling of Prussian Blue-based Multimodal Targeted Theranostic Nanocomposite for Cancer Treatment"** contains literature survey and original research work done by the undersigned candidate as part of Doctoral studies.

All information in this thesis have been obtained and presented in accordance with existing academic rules and ethical conduct. I declare that, as required by these rules and conduct, I have fully cited and referred all materials and results that are not original to this work.

I also declare that I have checked this thesis as per the "Policy on Anti Plagiarism, Jadavpur University, 2019", and the level of similarity as checked by iThenticate software is ..10...%.

Signature of Candidate: Panchanan Sahoo

Date: 11.05.24

Certified by,

Supervisor(s):

.....11/05/2024.....

Dr. Chandan Kumar Ghosh

Assistant Professor

Jadavpur University,

(Signature of the supervisor, date with seal)

Dr. Chandan Kumar Ghosh
Assistant Professor
School of Materials Science
& Nanotechnology,
Jadavpur University
Kolkata - 700 032

.....

Dr. Abhishek Mukherjee

Associate Professor

Indian Statistical Institute (Giridih)

(Signature of the supervisor, date with seal)

Abhishek Mukherjee, Ph.D.
Associate Professor
Agricultural and Ecological Research Unit
INDIAN STATISTICAL INSTITUTE
New Barganda, Giridih - 815 301
Jharkhand, India

Declaration

I hereby declare that my research work embodied in this Ph.D. thesis entitled **"Development and Mechanistic Modelling of Prussian Blue-based Multimodal Targeted Theranostic Nanocomposite for Cancer Treatment"** have been carried out by me in the School of Materials Science and Nanotechnology, Jadavpur University and Agricultural and Ecological Research Unit (AERU), Indian Statistical Institute under the direct supervision of Dr. Chandan Kumar Ghosh and Dr. Abhishek Mukherjee.

I also confirm that this work is original and has not been submitted partially or in full for any other degree or diploma to this or other University or Institute.

Date: 11.05.24

Place: Kolkata

Signature

Panchanan Sahoo.

(Panchanan Sahoo)

Dedicated to

My Beloved Parents & My Wife

Acknowledgement

I feel fortunate to be surrounded by individuals who believe in me and offer their support, especially during moments when I may have lost faith in myself. This brief expression of gratitude cannot fully capture the significance of their impact on my life, but I will make an effort to acknowledge their contributions.

I want to express my sincere gratitude to my supervisors, Dr. Chandan Kumar Ghosh and Dr. Abhishek Mukherjee. Under their guidance, I've not only expanded my understanding of Physics but also fostered personal growth. I am so fortunate for having such wonderful supervisors whose everyday guidance, supervision and enormous discussion related my present problem as well as my stressful life help me to gain immense confidence and intellectual strength to enjoy the uncertainties of my research problems. Witnessing their qualities of kindness, care, respect, and most importantly, patience with all students has a profound impact on me. I continue to aspire to incorporate their work ethics and punctuality into my own journey.

I would also like to acknowledge my RAC members, Dr. Dipankar Chakraborti, Dr. Partha Roy, and Dr. Sourav Sarkar for their useful comments during my many presentations. I also thank my collaborators Dr. Jiten Ghosh, Krishnananda Chattopadhyay and Dr. Susmita Bhattacharya for being cooperative and helpful in our projects. Most importantly, their insightful questions help me to know many interesting facts.

My Jadavpur and ISI family is incomplete without my friends. First, I would like to thank my peers, Sudip, Pulak, Snehasis da, Shubham da, Sourav da and Mandira for giving me many fun-filled moments to cherish forever. A special thanks to my seniors Snehasis da and Sourav da for given me insightful thoughts to understand biological facts in the language of physics. My PhD journey would undoubtedly be much more challenging if I didn't have a healthy and supportive environment with caring seniors and juniors in my lab. Our daily ritual of coffee break was a real stress buster, making me into a coffee lover. My juniors Sudip, Riddhiman, Mandira and Shreeya have always been enthusiastic about everything from research discussions to gossip. Throughout my time in my PhD program, Pankaj da has consistently provided invaluable technical assistance whenever I needed it. I am thankful to Dr. Sumita Kundu and Dr. Yeshpal Kolangana Veettil of Eko X-Ray & Imaging Institute, Kolkata for their kind help for execution of the MRI experiment. I anticipate the continuation of our lab's

tradition of warmly welcoming new students, fostering a productive environment where everyone can work.

I would like to express my sincere gratitude to Dr. Souvik Chatterjee, Scientist, UGC-DAE Consortium for Scientific Research, Kolkata Centre, III/LB-8, Bidhannagar, Kolkata 700098, India for giving me opportunity to work on SQUID.

Finally, I would acknowledge the contribution of the two people that mattered the most, my parents. They have been the constant source of support from my childhood, encouraging me to pursue my dreams. Their unbounded love, patience, affection and blessings had helped me to carry out my research work without extreme adversity. Their sacrifice for my education and well-being is beyond words, and their teachings have made me who I am today. I will always be indebted to them, and I am happy that I am blessed with such loving and supportive parents. Now I want to express my immense gratitude to my beloved wife who constantly support me in my difficulties time and motivated me to pursue my dreams.

Last but not the least I would like to heartily acknowledge DST-INSPIRE Scheme (Grant No. DST/INSPIRE Fellowship/2018/IF180194) of Department of Science and Technology, Govt. of India for awarding me and proving financial support to carry out my thesis work and complete it successfully.

Abstract

Conventional chemotherapy, while a cornerstone in cancer treatment, is hampered by systemic toxicity, drug resistance and non-specific targeting. In addition, conventional cancer diagnostic techniques such as X-rays, CT scans, MRI, and ultrasound to tissue biopsies and blood-based biomarker analysis often suffer limitations such as low sensitivity, invasiveness, inherent long term toxicity, and inability to provide real-time monitoring of treatment response. Specifically, in MRI, patients with impaired kidney function may be at risk of developing Nephrogenic Systemic Fibrosis after exposure to certain gadolinium-based contrast agents, a condition characterized by skin and tissue thickening. Moreover, recent studies have also raised concerns about gadolinium retention in the body, particularly in the brain and bones, prompting questions about long-term health effects. Herein, my thesis presents a comprehensive exploration of a novel Prussian Blue-based multimodal targeted theranostic nanocomposite for both cancer therapy and diagnosis, addressing these limitations and highlighting the advantages of nanoparticle-based approaches.

The research initiates with the synthesis and characterization of the nanocomposite, where Prussian Blue based nanoparticles serve as the core material due to their exceptional multimodal theranostic property. Through surface modification, various functionalizing agents including targeting ligand are integrated onto the surface of nanoparticles, facilitating high surface area for loading of different drugs, specific recognition and binding to cancer cell and stimuli responsive drug release. Consequently, theranostic precision is enhanced by reducing off targeted drug delivery. In essence, a singular nanocomposite serves as a multimodal theranostic agent, encompassing modalities like photothermal therapy (PTT), photodynamic therapy (PDT), chemotherapy, magnetic resonance imaging (MRI), photoacoustic imaging (PAI) etc.

Moreover, my thesis delves into mechanistic modelling, investigating how the modulation of r_1 and r_2 relaxivity is influenced by changes in bare particle size, diverse doping, and various surface functionalization based on Solomon-Bloembergen-Morgan theory.

In vitro studies validate the effectiveness of the developed nanocomposites in tumor targeting, imaging contrast enhancement, stimuli responsive drug release and therapeutic outcomes, demonstrating its potential as a versatile platform for cancer diagnosis and treatment.

Overall, this thesis presents a comprehensive approach to address the limitations of conventional cancer diagnostics and treatments through the development of prussian blue based targeted multimodal theranostic nanocomposites and it's mechanistic modelling to explain the variation of r_1 and r_2 relaxivity due to various influencing parameter. By harnessing the unique advantages of nanoparticles and integrating multiple therapeutic and diagnostic modalities into a single platform, this research offers a promising avenue towards more effective and personalized cancer management.

Contents

Chapter 1

Introduction

Chapter 1. Introduction

1.1 Background of the problem: Prevalence of the cancer

Cancer represents one of the most significant health challenges of our time, affecting millions of individuals worldwide and posing a substantial burden on healthcare systems. It is characterized by uncontrolled cell growth, invasion into surrounding tissues, and potential metastasis to distant organs.[1] Its ability to disseminate to distant sites from its point of origin enhances its lethality, amplifying the severity of the disease. Overall, colon cancer is the third most common cancer worldwide a type of cancer that originates in the colon (large intestine) or rectum, poses a significant threat to human health and second leading cause of cancer-related deaths worldwide.[2] Meanwhile, breast cancer stands as the leading type of cancer among women and ranks as the second most common cancer globally. Additionally, breast cancer cells have the capability to spread to the lungs, heightening mortality rates among women and yielding a survival rate of just 20%.[3] The global burden of cancer has surged to a staggering 20 million new cases, accompanied by 9.7 million cancer mortality in 2022 alone. Early detection and rapid treatment pay pivotal roles in enhancing cancer survival rates. Any delays in diagnosing and commencing treatment generally lead to an elevated risk of death, as evidenced by numerous studies.

1.1.1 Historical perspective of cancer treatment and their limitations

Conventional cancer treatments typically include surgery, chemotherapy, radiation therapy, and most recently targeted immunotherapy, have been in practice for decades. Each of these treatments comes with its own set of potential side effects, which can vary depending on factors such as the type of cancer, the stage of the disease, the individual's overall health, and the specific treatment regimen.

Surgery

Throughout history, the earliest documentation of surgical tumor removal can be attributed to Maimonides in AD 1190.[4] However, significant strides in cancer surgery emerged in the nineteenth and early twentieth centuries, particularly with the advent of anesthesia in 1846. Notably, Halsted pioneered the radical mastectomy in the late nineteenth century. Presently, the standard approach for most breast cancer cases involves surgical removal of primary tumor

followed by adjuvant therapies such as radiation, chemotherapy, targeted therapy, or hormonal therapy. The progress made in cellular, molecular, and imaging technologies in the twentieth century played a pivotal role in refining surgical techniques. Diagnostic methods such as ultrasound (sonography), computed tomography (CT scans), magnetic resonance imaging (MRI scans), and positron emission tomography (PET scans) have supplanted exploratory surgeries previously used for cancer diagnosis. Additionally, advancements in surgical approaches include laparoscopic and thoracoscopic surgeries, endoscopy, as well as techniques utilizing lasers, cryoablation, and radiofrequency ablation.[5]

Cancer surgery carries risks such as bleeding, infection, and adverse reactions to anesthesia. Depending on the type and location of the surgery, patients may also experience pain, scarring, loss of function (in cases involving organ removal), and complications specific to the procedure performed. Besides this, the recognition and understanding of metastasis posed challenges to the efficacy of surgery in treating invasive cancer, leading to the introduction of alternative therapeutic interventions.

Radiotherapy

Following Wilhelm Rontgen's discovery of X-rays in 1895, the use of radiotherapy as a cancer treatment modality began to emerge. Presently, nearly half of all cancer patients undergo radiation therapy. Ionizing radiation induces DNA damage, leading to the demise of cancer cells. It also exerts detrimental effects on surrounding healthy tissues.[6] Within few years of its inception, radiation therapy was associated with the development of cancer itself (radiation carcinogenesis). Technological advancements in radiation physics and computer technology during the twentieth century facilitated the refinement of radiation therapy precision. Techniques such as conformal radiation therapy (CRT) utilize three-dimensional anatomical data of tumors and adjacent healthy tissues, enabling the implementation of three-dimensional conformal radiotherapy (3D-CRT). Radiation beams are directed at the tumor from multiple angles, enhancing treatment accuracy. Intensity-modulated radiation therapy (IMRT) further enhances precision by allowing for the adjustment of beam intensities, enabling the delivery of high doses to cancerous tissue while minimizing exposure to surrounding normal tissue.[7] Various technologies have been developed with the aim of safeguarding healthy tissue from the DNA-damaging effects of radiation, marking significant progress in the field of radiation oncology.

Radiation therapy causes several limitations like skin irritation or burns in the treated area, fatigue, hair loss in the treatment area, difficulty swallowing (if the throat or mouth is irradiated), nausea, diarrhea, and long-term effects such as fibrosis (scarring) of tissue. Most importantly, radiation carcinogenesis is still a big challenge to overcome.

Chemotherapy

The inception of chemotherapy was from the observations during World War II, where soldiers exposed to nitrogen mustard exhibited decreased white blood cell counts. Intravenous nitrogen mustard was subsequently found to impede the growth of lymphomas and leukemia in patients resistant to radiotherapy, leading to its approval for cancer treatment in 1949.[8] Following this, the first successful chemotherapy for childhood leukemia was achieved in 1948, and in 1950, the first nucleotide analogue chemotherapeutic agents were developed through rational design.[9] Aminopterin, discovered by Farber, served as the precursor to methotrexate, a widely used chemotherapy drug today. Since then, numerous chemotherapeutic agents have been developed, demonstrating efficacy in achieving long-term remission. Combination chemotherapy has proven superior to single agents, particularly in aggressive cancers like fast-growing leukemia and lymphoma. For instance, standard remission induction therapy for acute myeloid leukemia (AML) involves multiple cycles of intensive chemotherapy, often including drugs like cytarabine (Ara-C), etoposide, and anthracycline.[10] This regimen yields complete remission in 60-80% of patients under 60 years old. In pediatric AML, remission rates typically range from 85 to 95%, with event-free survival rates between 50 to 65%.[11]

Cytotoxic chemotherapy faces several limitations, including its nonspecific targeting ability, resulting in significant side effect towards normal cells that impact patient's quality of life. It commonly leads to nausea and vomiting, hair loss, fatigue, decreased appetite, diarrhea or constipation, mouth sores, increased risk of several infections due to decreased white blood cell count, easy bruising or bleeding due to decreased platelet count, nerve damage (neuropathy), and elevated risk of developing additional cancers in the future. Moreover, these drugs primarily target rapidly dividing cancer cells, often overlooking cancer stem cells, which contribute to treatment resistance. For instance, exposure to gemcitabine *in-vivo* over five days led to a notable enrichment of pancreatic cancer stem cells (47.2%) compared to primary cancer cell lines (1.47%).[12] One of the most prominent challenges in chemotherapy is the development of drug resistant. For instance, cytosine arabinoside (Ara-C) gets resistance and poses a significant challenge in managing AML.[13]

Targeted therapy

Progress in comprehending cancer biology and the human genome has revolutionized therapeutic approaches, particularly those targeting specific molecular pathways crucial for cancer cell growth, survival, progression, and metastasis. Targeted cancer therapies aim to disrupt specific components within the intricate network of altered signaling pathways, which ultimately lead to uncontrolled cell proliferation.[14] Molecular targeted treatments have demonstrated remarkable efficacy in combating various cancer types, such as leukemia, lung breast, colorectal, and ovarian cancers.[15] The pioneering targeted drug, tamoxifen received approval in 1977 for breast cancer treatment. By binding to the estrogen receptor (ER), tamoxifen modulates ER activity, offering an effective treatment for ER-positive breast cancer.[16] Various mechanisms contribute to the dysregulated activities of protein tyrosine kinases encoded by oncogenes, ultimately resulting in cellular transformation. Effective targeted therapeutic approaches, such as growth factor antagonists and receptor inhibitors, suppress cancer cell metastasis and progression while enhancing sensitivity to cytotoxic anticancer agents. Notable examples include Human epidermal growth receptor 2 (Her2) antibodies targeting the Her2 receptor in breast cancer and small molecule inhibitors targeting EGFR, IGF-1R, VEGFR, and PDGFR.[17]

A notable challenge encountered in targeted therapy is the development of drug resistance. This arises due to substantial cross-talk between receptor tyrosine kinase pathways, where multiple receptors typically activate the same pathway. Consequently, if the function of one protein at the upstream end of the signalling pathway is suppressed, it's probable that another protein will compensate for the disrupted function, resulting uncontrolled cell proliferation persists.[14] Importantly, triple negative breast cancer (TNBC) cells cannot be targeted using conventional hormonal targeted therapy, due to absence of all three ER, progestron receptor (PR) and Her2 receptors.

Targeted immunotherapy has demonstrated efficacy across various cancer types by leveraging the body's immune system to combat cancer cells. This approach encompasses a range of techniques, including monoclonal antibodies, CAR T cell therapy, immune checkpoint inhibitors, cancer vaccines, and immune system modulators. Challenges associated with cancer immunotherapy include cancer cell evasion from immune responses, resistance mechanisms, and logistical concerns regarding delivery techniques. Despite significant advancements in cancer research and treatment modalities over recent decades, the complexity and

heterogeneity of cancer continue to present tough obstacles to effective management. Hence, there is a growing imperative to devise alternative approaches to surmount the obstacles encountered by conventional treatments while concurrently diminishing the mortality rate associated with cancer. Utilizing nanocarriers as transport vehicles shows promise in addressing some of these challenges due to their expanded surface areas, controlled surface chemistry, targeted delivery capabilities, and enhanced permeation and retention properties.[17]

1.1.2 Conventional cancer diagnostic techniques and their limitations

Cancer diagnosis represents a critical cornerstone in the battle against this pervasive disease. Over the years, medical science has developed a myriad of diagnostic techniques to detect cancer in its various forms and stages. These techniques range from imaging modalities such as X-rays, CT scans, MRI, and ultrasound to tissue biopsies and blood-based biomarker analysis. While each method offers unique advantages, they are not without their limitations.[18]

Imaging modalities, such as X-rays, CT scans, MRI, and ultrasound, provide invaluable insights into the internal structures of the body, aiding in the detection and characterization of tumors. However, they may lack the sensitivity to detect smaller lesions or differentiate between benign and malignant growths accurately. Additionally, these techniques often come with high costs and may not be readily accessible in all healthcare settings. Specifically, MRI contrast agents, while invaluable in enhancing the clarity of MRI scans, do come with certain drawbacks and limitations. One significant concern is the potential for allergic reactions, albeit rare, particularly with contrast agents containing gadolinium. These reactions can range from mild skin irritation to severe allergic responses. Moreover, patients with impaired kidney function may be at risk of developing Nephrogenic Systemic Fibrosis (NSF) after exposure to certain gadolinium-based contrast agents, a condition characterized by skin and tissue thickening.[19] Recent studies have also raised concerns about gadolinium retention in the body, particularly in the brain and bones, prompting questions about long-term health effects. Furthermore, MRI contrast agents are generally not recommended for use in pregnant women or certain populations, and the associated cost can be prohibitive for some patients or healthcare systems. The process of administering contrast agents via intravenous injection may also cause discomfort, and additional screening for contraindications or allergies adds complexity to the imaging procedure. Despite their diagnostic benefits, these drawbacks underscore the importance of careful consideration and risk assessment before the use of MRI contrast agents in clinical practice.[20]

Tissue biopsy remains the gold standard for cancer diagnosis, offering detailed information about tissue morphology and molecular characteristics. However, biopsies are invasive procedures that carry inherent risks and may not always capture the full extent of tumor heterogeneity. Fine needle aspiration, while less invasive, can yield inadequate samples, leading to diagnostic uncertainty.[21]

Blood-based biomarkers, including tumor markers and liquid biopsies, provide a less invasive approach to cancer diagnosis, often through simple blood tests. While these biomarkers offer promise for early detection and monitoring of cancer, they suffer from limitations such as lack of specificity and sensitivity, resulting in false-positive or false-negative results. Moreover, the accessibility and cost of these diagnostic techniques pose significant challenges, particularly in resource-limited settings. Advanced imaging modalities and molecular diagnostic tests may not be universally available or affordable, leading to disparities in cancer care.[22]

In conclusion, while diagnostic techniques have significantly advanced our ability to detect and diagnose cancer, they are not without their limitations. Overcoming these challenges requires ongoing research and innovation aimed at improving the sensitivity, specificity, accessibility, and affordability of cancer diagnostic methods. Only through concerted efforts can we hope to achieve earlier detection, more accurate diagnosis, and improved outcomes for cancer patients worldwide.

1.2 Nanoparticle advantages in cancer theranostic

Nanotechnology has shown great promise in cancer therapy as it allows for the targeted delivery of drugs and other therapeutic agents to cancer cells, while minimizing damage to healthy cells. Nanoparticles (NPs) can be engineered to specifically target cancer cells, as they can be designed to recognize and bind to unique features of cancer cells such as overexpressed receptors or specific proteins. Once these nanoparticles have been delivered to cancer cells, either they can be used as a near infrared (NIR) induced phototherapeutic agent like photothermal therapy (PTT) and photodynamic therapy (PDT) or to deliver therapeutic agents such as chemotherapeutic drugs, radiation, or other agents that can induce cell death or inhibit cancer cell growth. Additionally, nanoparticles can be used for various imaging purposes like MRI, CT, PAI, PET, UCL enabling the early detection and diagnosis of cancer. NPs can also be engineered to have specific physical properties that enhance their effectiveness in cancer therapy, such as increased stability in the bloodstream or enhanced uptake by cancer cells.[23] Overall, the use of nanotechnology in cancer theranostic offers a promising approach to

improve treatment outcomes and reduce side effects associated with conventional cancer therapies. However, further research is needed to fully understand the safety and efficacy of these approaches, and to optimize the design of nanoparticles for specific cancer types and patient populations.

1.2.1 Recent Trends of nanoparticles in cancer theranostics

Because of their affordability, straightforward production, minimal toxicity, adjustable surface to volume ratio, biocompatibility and high encapsulation capacity, NPs are recently used in cancer theranostics application. This section of this chapter offers a thorough overview of cancer theranostics utilizing various NPs, such as organic NPs (liposomes, lipid, protein-based NPs, and metal-organic frameworks), Carbon-based NPs (carbon nanotubes (CNTs), carbon dots (CDs), graphene and fullerene) inorganic NPs (metal, metal oxide, quantum dots (QDs) and magnetic NPs) etc.[24] Nanocarriers exhibit enhanced and more efficient interactions with cancer cells, making them extensively studied for biomedical purposes. Bionanoparticles, owing to their unique physical and chemical attributes, have garnered significant attention lately. Among them, protein NPs, viral NPs, solid-lipid NPs, apoferritin, and aptamers emerge as highly promising candidates. Gold NPs (GNPs) conjugated with QDs can yield multifunctional nanohybride with superior anticancer and imaging capabilities. GNPs convert absorbed irradiated light energy into localized heat, effectively destroying tumor cells via PTT.[25] Nanocarriers, whether loaded with drugs or not, exhibited similar cytotoxic effects on cancer cell due to their inherent anticancerous property. Conversely, doping of Gd^{3+} ions with ZnS/CuInS QDs could enable MR and dual fluorescence imaging.[26] To prevent the fluorescence quenching of QDs, superparamagnetic Fe_3O_4 was encapsulated separately from fluorescent graphene−CdTe QDs within a SiO_2 shell.[27] This bifunctional, cytocompatible model could efficiently load with 5-fluorouracil, demonstrating efficacy against hepatoma cells. Overall, the incorporation of QDs with various inorganic NPs facilitates their application in multimodal imaging, encompassing fluorescence, MR and UCL imaging. Through the integration of magnetic hyperthermia, PTT, and PDT, synergistic cancer treatment could be realized.

Organic nanoparticles in cancer theranostics

Over the past decads, nanotechnology has seen significant growth in its application for disease detection and treatment, notably cancer. This technology enhances drug delivery, improving treatment effectiveness while minimizing side effects. Various types of nanomedicines, such

as liposomal, nonmetallic, viral, protein, and lipid nanoparticles, have been researched to address limitations in conventional therapies and improve tumor targeting.[28] Nanomedicines employ passive and active targeting, as well as triggered release mechanisms. Nanotechnology has revolutionized science and technology, especially in personalized medicine. Targeted drug delivery to tumor sites is essential to mitigate side effects. Theranostics, combining therapy, and diagnosis, is a promising approach. Doxil, the first FDA-approved nanomedicine, and polymeric micelle-based drugs in clinical trials demonstrate the potential of nanotechnology in cancer treatment.[29] Nanomaterials' biocompatibility, biodegradability, and multifunctionality expand their biomedical applications, including cancer theranostics. Below are details of an organic NPs based cancer theranostics platform.

Liposomes NPs in cancer theranostic

Liposomes, a type of biomimetic NPs, stand out as versatile lipid-based tools for cancer theranostics. Comprising concentric lipid bilayers around an aqueous core, they efficiently carry a variety of drugs, encapsulating hydrophilic ones within the core and hydrophobic ones within the bilayer.[30] Their benefits include biodegradability, biocompatibility, easy synthesis, low toxicity, sustained drug release, and the capacity to accommodate both hydrophobic and hydrophilic types of chemotherapeutic compounds. Moreover, their surfaces can be customized for targeted therapy. Liposomes can accumulate in cancerous tissues passively via enhanced permeability and retention (EPR) or angiogenic markers.[31] Combined with multimodal imaging, liposomal therapeutics allow for real-time monitoring of cancer progression and drug pharmacokinetics, aiding in predicting treatment efficacy. Many liposomal drugs are in clinical trials or have received approval due to their advantages. Liposomes have also been explored for delivering diagnostic agents such as isotopes (^{14}C, ^{64}Cu), quantum dots, and contrast agents.[32-35] Their potential as a theranostic tool for cancer patients is expected to be validated in upcoming clinical trials.

Lipid NPs in cancer theranostic

Lipid nanoparticles (LdNPs) continue to be a promising avenue for cancer theranostics due to their scalability and biocompatibility. They offer unique advantages that distinguish them from other nanoformulations. Recent research indicates that lipidic NPs based cancer theranostic hold great promise in enhancing cancer treatment efficacy.[36] LdNPs can effectively navigate through tumor blood vessels and deliver chemotherapy drugs to the tumor site. For instance, DiR (1,1′-dioctadecyl-3,3,3′,3′-tetramethylindotricarbocyanine iodide) dyes have

demonstrated enhanced tissue penetration, leading to superior antitumor effects.[37] The size of these nanoparticles varies depending on the target organ and imaging modality. Zhang et al. have developed fluorinated nanoemulsions for sensitive and specific tumor detection, leading to improved fluorescence imaging signals and effective PDT.[38] Other innovations include nanoemulsions with porphyrin shells for imaging and phototherapy, as well as LdNPs loaded with dye and siRNA for noninvasive monitoring of drug delivery.[39,40] Theranostic nanoplatforms like Fe_3O_4 conjugated with porphyrin-grafted LdNPs (Fe_3O_4@PGLNPs) have shown excellent photodynamic effects against cancer cells.[41] LdNPs are increasingly utilized in cancer theranostics due to their low toxicity, multifunctional potential, and adaptability, enabling them to overcome physiological barriers in treating various tumors.

Protein NPs in cancer theranostic

Researchers have extensively investigated protein nanoparticles (PnNPs) due to their natural abundance and compatibility with the body's physiology. Proteins, being biologically derived molecules with unique properties, offer great potential for applications in biomedicine and nanomaterials science. Their amphiphilic nature facilitates favorable interactions with solvents and drugs, making them ideal for NP formulation.[42] Additionally, their natural origin renders them biodegradable and easily modifiable for drug attachment and targeted ligand binding. Albumin, for instance, has gained recognition as a carrier for delivering imaging and anticancer drugs to tumor sites, exemplified by the success of Abraxane (paclitaxel bound to albumin) in clinical settings.[43] Other albumin-based formulations, such as albumin-bound rapamycin (ABI-009) for nonhematologic cancers, are also undergoing clinical trials.[44] Human serum albumin (HSA) caps present intriguing possibilities due to their abundance in the body. HSA has been explored as a carrier for various substances including superparamagnetic iron oxide and NIR activated photosynthesizer like indocyanine green (ICG) and IR825, which are gaining popularity for their deep tissue penetration and low autofluorescence interference.[45] Recent research has focused on encapsulating agents like gadolinium (Gd) and IR825 within HSA for dual imaging-guided PTT treatment to combat lymphatic metastases.[46] In an similar study pheophorbide-a and gemcitabine was loaded within HSA to develop a protein-based nanoparticles for multifunctional therapeutics targeting diseases like lymphatic pancreatic ductal adenocarcinoma (PDAC) metastases.[47]

Metal-organic frameworks (MOF) in cancer theranostic

MOFs represent a captivating category of porous hybrid coordination polymers, featuring metal ions or clusters as nodes and organic ligands as linkers. They have been synthesized and applied across various fields, including catalysis, sensing, gas storage, and biomedical applications such as cancer theranostics. MOFs address limitations in conventional cancer treatment by improving drug targeting to tumor sites while minimizing damage to healthy tissues. By varying metal types and organic linkers, thousands of structurally diverse MOFs can be synthesized with unique properties. Their notable features, including surface functionalization, structural diversity, high porosity, and biocompatibility, make MOFs ideal for cancer theranostics.[48] These materials enhance conventional therapies like radiation and chemotherapy and are compatible with emerging phototherapy methods. Moreover, MOFs serve as excellent carriers for various bioactive substances and can be tailored for imaging-guided cancer therapy.[49] For instance, Wang et al. developed Zn-based MOFs functionalized with 5,5′,5″-(1,3,5-triazine-2,4,6-triyl)- tris(azanediyl)triisophthalate ligands which have been utilized as nanocarriers for anticancer drugs like 5-fluorouracil (5-FU).[50] Additionally, multifunctional MOF nanocomposites have been developed for targeted drug delivery, combining features like fluorescence imaging, MRI, and controlled release. These advancements include surface modifications with targeting agents like folic acid and antibodies for selective cancer cell absorption.[51] *In-vivo* study demonstrated that UiO-66-NH2- FA-5-FAM/5-FU accumulated within tumors and exhibited enhanced effectiveness against tumors due to prolonged drug release.[52] In a separate investigation, Cherkasov and colleagues developed an MOF using antibodies to selectively target HER2/neu positive cancer cells.[53] Another biomimetic MOF, Hf-DBP-Fe, was created to improve cancer treatment by combining radiation therapy with immune checkpoint blockade in a synergistic manner.[54] Such innovative approaches demonstrate the potential of MOFs in enhancing cancer therapy outcomes and reducing postoperative recurrence.

Carbon based nanoparticles in cancer theranostics

In recent times, carbon-based NPs have made significant strides in enhancing the theranostic efficiency of cancer and neurodegenerative ailments. Various scientific teams have focused their efforts on advancing carbon-based NPs like carbon nanotubes (CNTs), carbon dots (CDs) graphene, fullerene, and their derivatives for medical purposes, including cancer theranostics. These NPs possess remarkable attributes such as tunable pore size, large surface area, and facile surface modification, rendering them well-suited for biomedical applications, especially cancer diagnosis. This, in turn, presents new opportunities for enhancing therapeutic approaches.

Furthermore, these NPs boast exceptional biodegradability, biocompatibility, and versatile functionality in biosensing, diagnostics, bioimaging, and therapies, thereby enhancing their potential in the realm of biomedicine.[55]

Carbon nanotubes (CNTs) in cancer theranostic

One investigation highlighted the potential of CNTs as drug carrier, specifically targeting triple-negative breast cancer (TNBC) with ginsenoside Rg3-loaded CNTs, forming Rg3-CNT. This study demonstrated Rg3-CNT's effectiveness as a therapeutic approach for TNBC immunotherapy.[56] Another study explored M13 phage-functionalized CNTs (M13-CNTs) for fluorescence imaging of target specific tumors, achieving successful detection even at low concentrations.[57] Ghosh et al. utilized a targeted M13 virus-stabilized CNT probe to detect human ovarian tumors with high signal-to-noise ratio, outperforming visible and NIR dyes in detecting submillimeter tumors.[58] Ceppi et al. developed a fluorescence imaging system for ovarian cancer using single-walled carbon nanotubes (SWCNTs) conjugated to M13 bacteriophage carrying a peptide-specific protein, facilitating real-time intraoperative tumor debulking.[59] *In-vivo* CNT fluorescence imaging surgery exhibited improved survival rates compared to conventional surgery. Lee et al. designed CNTs conjugated with a platelet-derived aptamer, demonstrating significant NIR fluorescence changes due to conformal aptamer alterations.[60] Zhang et al. developed CNTs and CDs based nanocomposite for dual-modal cancer cell imaging.[61] Peptides with aromatic content exhibited strong binding affinity to CNTs through π−π interactions. Functionalized SWCNTs proved effective as DOX carriers for treating MCF-7 cells, with SWCNT-PEG-PEI showing the most significant antitumor impact and drug delivery capacity among variants.[62] CNTs are particularly suitable for pH-responsive drug release due to their susceptibility to acidic environments, holding promise for drug therapy. Lu et al. synthesized CNTs nanocomposite functionalized with poly(acrylic acid) for folate receptor (FA)-targeted DOX drug loading, achieving higher efficiency compared to free DOX, likely due to π−π stacking and hydrogen bonding. This platform serves as an efficient tool for cancer theranostics.[63]

Carbon dots (CDs) in cancer theranostic

Due to their diminutive dimensions, CDs hold significant promise, particularly in targeting cancerous tumors through EPR effects. CDs can be efficiently eliminated via the urinary system, minimizing *in-vivo* toxicity. Moreover, CDs serve as a versatile platform for delivering various therapeutic agents, finding applications in chemotherapy, PDT, PTT, radiation therapy

and gene therapy. Studies examining the cellular uptake of bare CDs and ligand-conjugated CDs on cancerous (A-549 and MDA-MB) and healthy (MDCK) cells have shown preferential treatment of cancerous cells over healthy ones. Ligand-conjugated CDs internalized by cancer cells demonstrate target-selective receptor mediated endocytosis. Furthermore, the EPR effect significantly influences the tumor's uptake of nanosized CDs.[64] The photosensitizing behaviours of CDs are extensively explored for near-infrared (NIR) light-triggered PDT, either alone or in conjunction with photosensitizing agents, inducing reactive oxygen species (ROS) production for cancer cell treatment.[65] Various carbon-based nanomaterials, including carbonized polydopamine, exhibit fluorescence emissions and NIR-responsive photothermal conversion, contributing to cancer cell destruction. Hybrid CD-based systems are investigated for PTT, PDT, and stimuli (pH- or NIR) responsive drug release simultaneously, enabling synergistic cancer therapy. For example, CD nanogels integrated with PEG−chitosan demonstrate PTT against tumor cells and dual NIR-light and pH-responsive drug release.[66] Additionally, NIR-responsive core−shell nanostructure, such as HA-g-PLA/HCDs, are developed for the selective recognition of cancer cells overexpressing CD44 receptors, facilitating NIR-triggered chemo-phototherapy of solid tumors.[67] Combining NIR-triggered PTT with anticancerous drug may harness the potential benefits of CDs, potentially overcoming resistance to apoptosis through alternative routes like necroptosis. Furthermore, CDs functionalized with biotin and irinotecan exhibit controlled release and imaging of cancer cells, demonstrating potential as safe and effective theranostic agents in breast cancer treatment.[68] Doped CDs with oxygen and nitrogen show excellent therapeutic efficacy and bioimaging ability, achieving tumor destruction without damaging healthy cells.[69] Moreover, CDs are explored for tracking and bioimaging of stem cells via endocytosis, owing to their nanosize, surface charge, and physicochemical properties, they can easily uptake by the stem cell without affecting cell differentiation or expression of specific markers.[70] The strategic design of CDs is expected to complement the fluorescence probes, currently used in biomedical applications.

Graphene in cancer theranostic

Graphene and its derivatives have garnered attention for their application in biomedicine, attributed to their facile functionalization, high surface areas, and biocompatibility. These properties enable high drug loading capacity and position them as potential candidates for imaging and drug delivery. For instance, Chen et al. developed an rGO/PEG/ICG nanosystem by functionalizing reduced graphene oxide (rGO) with Indocyanine Green (ICG) and

polyethylene glycol (PEG), serving as a dual-modal contrast agent.[71] This nanoplatform exhibited prolonged *in-vivo* presence and demonstrated tumor-targeting capabilities. Mirrahimi et al. utilized graphene oxide (GO) to anchor SPIOs and gold nanoparticles (GNPs) adapted with phase-change material (PCM) for stimulus-responsive drug release.[72] The synergistic effects of MRI contrasting efficiency from SPIOs, NIR absorbance from GO, X-ray attenuation from GNPs, and thermosensitive features from PCM make this nanoplatform suitable for controlled thermo-chemotherapy. Graphene's potential applications extend to PET imaging and dual-modal fluorescence/MR imaging. A novel nanoplatform employing PEGylated GO and oxidized sodium alginate was employed to load the drug paclitaxel, yielding a synergistic chemotherapy/PTT/PDT effect.[73] In their study, Yang et al. anchored a molecular beacon (MB) onto GO, leading to an amplified fluorescence quenching effect on cy5 compared to inherent self-quenching.[74] Upon binding to miRNA-21, the nanoplatform prompted the fluorescence reactivation of cy5. This approach not only heightened fluorescence intensity but also mitigated the background fluorescence in imaging.

Inorganic nanoparticles in cancer theranostics

Because of their distinctive physicochemical properties, inorganic like gold, platinum (Pt), silica (Si), silver (Ag), palladium (Pd), zinc oxide (ZnO), iron oxides, and rare earth oxides have found extensive utilization in various biomedical fields, encompassing cancer theranostics, drug delivery, nucleic acid delivery, biosensing and bioimaging.

NPs derived from natural sources, such as GNPs and AgNPs, hold promise for delivering anticancer drugs both in *in-vitro* and *in-vivo*. Mukherjee and colleagues showcased the efficacy of GNPs produced from Peltophorum pterocarpum leaf extract in delivering doxorubicin (DOX) to melanoma tumors in mice.[75] These natural GNPs outperformed chemically synthesized ones in terms of biological compatibility, resulting in better tumor inhibition. Similarly, Ganeshkumar et al. targeted breast cancer cells using 5- fluorouracil loaded folic acid-linked GNPs derived from Punica granatum fruit peel extract, leveraging bioactive compounds (anticancerous phytochemicals like flavonoids, isoflavone, taxol, polyphenols etc.)) adhering to the nanoparticle surface.[76] Mukherjee et al. further demonstrated the multifunctionality of biosynthesized AgNPs, including anticancer properties, antibacterial activity and cell imaging.[77] Additionally, Lantana montevidensis leaf extract-derived GNPs exhibited antitumor effects due to specific phytochemicals.[78] Fazal et al. highlighted the photothermal ablation potential of anisotropic GNPs synthesized from cacao seed extract

against epidermoid carcinoma cells.[79] Wang et al. illustrated the utility of fluorescence-based bioimaging using in situ GNPs for cancer cell identification.[80] Furthermore, greener GNPs synthesized from Zinnia elegans plants were shown to be biocompatible and suitable for diagnostic imaging.[81] AgNPs, known for their antibacterial properties since ancient times, have garnered attention in cancer theranostics due to their unique properties. Austin et al. employed AgNPs for imaging cancer cells via light-scattering microscopy, while Gurunathan et al. reported the apoptosis of lung carcinomas without harming normal lung cells using AgNPs synthesized from Artemisia princeps leaf extract.[82,83] Padinjarathil et al. employed a surfactant-free method to synthesize environmentally friendly AgNPs, offering a potential platform for both anticancer therapy and immunomodulation.[84] Oves et al. synthesized AgNPs using Phoenix dactylifera root extract which exhibited anticancer and antimicrobial properties, inducing cell cycle arrest in sub-G1 and S phases.[85] Biogenic AgNPs (2−50 nm) were produced from Calotropis gigantean latex extract, demonstrating toxicity against various cancer cell lines without harming mice or human lymphocytes, suggesting their potential as chemotherapeutic agents.[86] The mechanism of action involves ROS production that triggered apoptosis followed by DNA damage and suppression of vascular endothelial growth factor activity that is crucial for angiogenesis. Dinparvar et al. utilized Cuminum cyminum seed extract to develop AgNPs, which showed reduced cytotoxicity compared to chemically synthesized counterparts, yet exhibited potent inhibitory effects against human breast cancer cells.[87] Kumar et al. developed AgNPs from Andean mora leaf and found them effective against Hep-G2 human liver cancer cells, highlighting their potential for anticancer therapy and drug delivery applications.[88] These studies underscore the potential of natural nanoparticle-based approaches in cancer diagnosis and treatment.

Copper-based NPs (CuO, Cu_2O, CuS, Cu_2S, CuSe, Cu_2Se, etc.) have garnered attention for their biocompatibility and distinctive physicochemical traits. Zhao et al. synthesized $Ag_{2-x}Cu_xS$ QDs, demonstrating their potential as all-in-one theranostic nanomedicine for PTT with high conversion efficiency under a 635 nm laser without prolonged toxicity.[89] CuSNPs were integrated onto gelatin NPs, forming transformable CuS@GeNPs for thermal ablation of MDA-MB-231 tumors.[90] The spatiotemporal behavior of CuS@GeNPs within tumor tissue was visualized *in-vivo* via photoacoustic imaging, indicating enhanced PTT. Wang et al. developed iron−copper codoped polyaniline (Fe−Cu@PANI) NPs for simultaneous imaging and PTT, exploiting glutathione (GSH) for tumor microenvironment activated therapy.[91] Copper-doped carbon dots (Cu-CDs) were prepared for PDT, exhibiting effective tumor

suppression on HeLa cells and SH-SY5Y 3D multicellular spheroids (MCs) through ROS generation upon LED light exposure. Deng et al. synthesized CuNPs with tunable acid dissociation constants (pKa) for H_2O_2 self-supplying chemodynamic therapy (CDT), with lower pKa NPs demonstrating better retention and lysosome-mediated cell death induction in tumor cells via Fenton reaction-derived hydroxide free radicals.[92]

In recent years, researchers have devoted considerable attention to developing advanced multimodal drug delivery systems. Quantum dots (QDs) have emerged as versatile tools in theranostic applications, owing to their unique physicochemical characteristics. These semiconductor crystals, typically sized between 2 to 10 nm, exhibit emission spanning from visible to NIR wavelengths, coupled with remarkable light stability.[93] QDs with robust photoluminescence and high molar extinction coefficient values are particularly favored for cancer biomarker detection and cell labelling. Despite their advantages, concerns regarding QDs' toxicity, especially those containing Cd, have arisen due to Cd ion release and damage healthy cells.[94] To address this, strategies have been devised to enhance QDs' biocompatibility and tumor targeting efficacy, including their hybridization with lipids, proteins, polysaccharides, and polymers aiming to minimize toxicity and prevent systemic circulation escape.

Stabilized protein-bound QD (protein-QD) nanocomplex in biological environments is crucial for effective bioimaging. QDs can bind to proteins through physical entrapment or chemical interactions.[95] For example, gemcitabine-loaded HSA NPs were successfully decorated with hyaluronic acid functionalized graphene QDs by Nigam et al. for targeted drug delivery to pancreatic cancer.[96] In another study, spray-dried single BSA nanospheres encapsulated various-sized CdTe/CdS QDs to create multifluorescent nanoplatform. These nanoplatform, when having a high QD:BSA ratio, demonstrated stable fluorescence emission, highlighting their potential for long-term biomedical fluorescence observation.[97] Song et al. synthesized a nanoplatform of phosphorus QDs with bismuthene and Bi@RP-PEG-DOX, showcasing an effective platform for PTT and PDT effects alongside controlled drug release under NIR-II exposure.[98] Zein−ZnS QD nanocomposite have been proposed for 5-fluorouracil delivery, with biocompatibility confirmed by Girija Aswathy et al. through viability tests on cancer cells.[99] Furthermore, the fluorescence of zein−ZnS QD nanocomposite indicated successful cellular uptake. Biodegradable titanium nitride quantum dots (Ti_2N QDs) synthesized by Shao et al. exhibited excellent photothermal conversion efficiency under NIR, coupled with enhanced efficiency in PTT and PAI.[100] Multi-stage QD nanocomposite, such as Si-coated QDs attached

to gelatin NPs, demonstrated enhanced tumor penetration by exploiting tumor microenvironmental factors.[101] Overall, protein-mediated hybridization of QDs offers a promising avenue to extend circulation time, enhance stability, target tumors, and reduce toxicity. The conjugation of hyaluronic acid QDs has emerged as a promising approach to enhance intracellular delivery into liver cells, facilitated by CD44 receptor interaction, enabling real-time *in-vivo* monitoring.[102] In a separate study, CdTe QD theranostic nanoplatform, coated with chondroitin sulfate and loaded with celecoxib and rapamycin for cancer treatment, were developed.[103] To prevent inadvertent absorption of chondroitin sulfate nanocapsules by healthy cells, a cationic gelatin-coupled QD exterior coating was applied. Gelatin degradation by matrix metalloproteinases at tumor sites facilitated the release of drugs and QDs into cancer cells for imaging.[104] Similarly, lactoferrin, an iron-binding cationic protein, was employed instead of gelatin to induce an on-off effect, wherein QD fluorescence was initially quenched and later restored upon intracellular bond cleavage, demonstrating nanoplatform localization both *in-vitro* and *in-vivo* within breast cancers. These findings highlight the potential of polysaccharide-QD combinations to enhance tumor targeting through receptor interactions, exploiting cancer cell overexpression, thereby increasing QD accumulation at the tumor site.

Magnetic NPs find widespread application in MRI and drug delivery, often comprising metal or metal oxides. These NPs are typically coated with organic compounds such as polymers and fatty acids to improve biocompatibility and stability.[105] Superparamagnetic iron oxide (SPIO) NPs conjugated with LHRH demonstrate effectiveness in targeting and imaging breast cancer.[106] Additionally, magnetic NPs are utilized in magnetic hyperthermia to induce thermal ablation of cancer cells. Notable magnetic nanoparticles available in the market or undergoing clinical trials include Resovist® and Feridex®, primarily for liver metastasis and colon cancer treatment.

1.2.2 Significant challenges in clinical translation of nanoparticles

As nanotechnology has advanced, there has been a significant increase in the research and understanding of nanoparticles. However, only a select few progress to clinical trials, with many remaining at the *in-vivo* and *in-vitro* stages. Each nanoformulation encounters specific challenges in transitioning to clinical use, with common obstacles falling into categories such as biological, and study-design related challenges.

Biological hurdles encompass various factors such as limited administration routes, challenges in regulating biodistribution, navigating biological barriers, degradation, and potential toxicity

of NPs.[107] Typically, NPs are administered via intravenous injections directly into the bloodstream, leading to rapid dispersal away from the intended target site. This necessitates the use of higher drug concentrations, which may not always yield the desired therapeutic outcomes.[108] However, magnetic NPs offer a promising solution to this issue, with several *in-vitro* and *in-vivo* studies demonstrating the ability to manipulate NP movement against blood flow using 3D magnetic fields. Nonetheless, further research is required to understand the effects of magnetic fields on the human body, potential interference between magnetic fields, and the impact of a large number of NPs in circulation. Managing the biological behavior of NPs poses significant challenges and requires careful attention. Despite efforts to formulate NPs with biocompatible materials and optimize their properties to extend retention time and half-life, there remains a risk of lung, liver, and kidney toxicity. Factors influencing toxicity include surface area, particle shape and size, solubility, and tendency to agglomerate.[109] NPs have been found to preferentially deposit in the lungs, leading to inflammatory, oxidative, and cytotoxic effects. Research indicates that healthy cells may also be impacted by free radicals produced by NPs.[110] Another challenging obstacle involves evading the mononuclear phagocytic system (MPS). In biological fluids, NPs bind proteins to form a protein corona (PC), which facilitates MPS uptake of NPs. Efforts to circumvent this issue have included coating NPs with materials to inhibit protein corona formation, yet these approaches have yielded limited success. One potential strategy to overcome this problem is to design NPs that specifically target macrophages, thereby serving as novel drug carriers.[111] One of the significant hurdles in the realm of nanotheranostics lies in the development of single nanoplatform, encompasses numerous functionalities for multimodal theranostic purpose.

Challenges in study design, such as determining study size, objectives, and timing of NP therapies during treatment, significantly impact clinical studies. Many studies rely on *in-vitro* and *in-vivo* models, which may not reliably translate to human trials, making it difficult to accurately mimic natural reactions in the human body. Additionally, research into the cancer metastasis is crucial, given the importance of metastasis in cancer progression. Furthermore, personalized medicine may necessitate clinical studies, considering various factors like genetics, environment, and medical history.[112,113] Another significant challenge is that NPs are seldom used as first-line therapies. Despite the approval of nanoformulations, they are typically reserved for subsequent treatment if disease progression occurs during clinical trials. This tendency for patients to have progressed on multiple therapies or developed drug resistance can

skew clinical trial results and diminish the likelihood of NP treatment benefiting those who may still be responsive to treatment.

For instance, QDs have garnered considerable attention across several biological domains owing to their numerous advantages over traditional dyes in bioimaging. Nevertheless, these applications encounter multiple challenges, such as cellular toxicity stemming from the generation of ROS and cadmium leakage, posing potential risks to patients post-treatment. Moreover, graphene QDs have shown promise in being safe and non-toxic to normal cells.[114] However, thorough *in-vivo* toxicity assessments are imperative before considering their application in cancer theranostics. Despite the efficacy of QDs in cancer theranostics, a major concern revolves around the possibility of nonspecific reticuloendothelial absorption, diminishing the probability and efficacy of these theranostic agents binding to the intended cancer site.[115] An exhaustive tabulation delineating the merits and demerits of NPs across various cell lines (Table 1).

However, it is imperative to establish a cost-effective synthesis approach and streamline purification methods to facilitate the large-scale production of nanomaterials. Additionally, attention must be given to efficiently delivering genetic material to cancer cells for enhanced cancer theranostics. Currently, the comprehensive utilization of nanomaterials in cancer treatment remains underexplored due to challenges such as nanotoxicity and the bioaccumulation of nanoparticles, which limit their wider application. Given these challenges, there is an urgent requirement for an alternative versatile nanoplatform to address these issues. Importantly, prussian blue based NPs are one of the options. Notably, one potential solution lies in utilizing of prussian blue based nanoparticles. In the next chapter we have broadly discussed about the various synthesis and surface functionalization method and their cancer theranostic applications.

Table 1: Various nanoparticles employed in cancer treatment with their formula, advantages, disadvantages, mechanisms of action, and targeted cell types.

Sl no.	Name of NP	Cell lines	Advantages	Disadvantages	Mode of action	Ref.
1	Au, Ag-Nps	Human peripheral blood mononuclear cells	Wide surface area enhance the sustainability hydophilicity of cancer mediated drugs	Target is not limited, eyes and skin irritations	Activated the compliment ad produce cytokines	116

2	Au-Nps toxins	MCF-7	Ease to synthesis, amendable in shape and size.	Difficult to treat precised tumors	Down-expression of CDK-4 and MAPK	117
3	Fe_3O_4@AuNC@erlotinib	PANC-1	Biocompatibility nontoxicity and high stability	Caused skin and eye irritation in drugsensitive patients	Selective targeting of overexpressed EGFR	118
4	Fe_3O_4	HepG2	Used in hyperthermia, magnetic storage, and Biosensors	Cause ulcer, inflammation, and retorted the growth rate, decline the alterations in neurobehavioral cell lines	ATP-citrate lyase-dependent RAS signaling	119
5	V_2O_5/O_5V_2	B16F10, A549, and PANC1	Used to treat the melanoma, Maintain blood glucose level with type 2 diabetes	Toxic and cause irritation of skin eyes, and, upper respiratory tract	ROS-induced apoptosis	120
6	Fe@Fe_3O_4@heparin	4T1 breast tumor cell line, HUVEC cell	H2O2 generated by La in the tumor and used as a 4T1 xenograft model to enhance nanozymemediated tumor therapy	lethal effect on normal cells	Reactive oxygen species production	121
7	Rh-PEG NDs	CT-26 colon tumor	For colon cancers treatment	Limited efficacy	Down expression of TNF-α and IL-6	122
8	TiO_2 NPs	LL2 mouse lung cancer cell line	Cancer cells can be effectively destroyed by the use of X-ray irradiated nano-sized TiO2	Limited efficacy in drug delivery, also damage some normal cell	Production of ROS and cytokine induction	123
9	Pt NPs	A549	Antioxidant activity which reduce the growth of tumor	Difficult to control size, and shape Endotoxin Production and time-consuming purification processes	Production of apoptosis and cell life cycle arrest	124
10	Pt NPs	Human foreskin fibroblast cell	Reduce tumor growth	Production of Endotoxin	DNA destruction and limitation of DNA replication	125
11	ZnO NPs	MCF-7	Destruction of selective tumor cells	mitochondrial dysfunction	Over expression of caspase-8 and p53	126

12	TiO_2 NPs	HepG2, A549, MCF-7 and IMR-90	Destroy cancer cells by the use of X-ray irradiated TiO2	Lethal for normal cells	ROS production	127
13	CeO_2 NPs	Mouse fibrosarcoma cell line	Cytotoxic towards prostate cancer cell lines	Cause chronic inflammation in lungs	Reactive oxygen species production in apoptosis	128
14	CeO_2 NPs	A549	To treat prostate cancer cell	Lungs inflammation	ROS-triggered apoptosis	129
15	DNA-modified magnetic NPs	MCF-7	Regeneration of tissue, inhibition of inflammation, antitumor drug delivery	Difficult to construct these particles	Limitation of RNA marker	130
16	PEGylated ZnO NPs	PANC1	Effect in pancreatic cancer cells	skin irritation	Reactive oxygen species apoptosis	131
17	RBC membrane-coated PLGA NPs	Pancreatic ductal adenocarcinoma	Stop the metastases growth of lungs	Sometime cause haemolysis	Tumor microenvironment modulation	132

Reference

1. Gutschner, T., & Diederichs, S. (2012). The hallmarks of cancer: a long non-coding RNA point of view. *RNA biology*, *9*(6), 703-719.
2. Benson, A. B., Arnoletti, J. P., Bekaii-Saab, T., Chan, E., Chen, Y. J., Choti, M. A., ... & Willett, C. (2011). Colon cancer. *Journal of the National Comprehensive Cancer Network*, *9*(11), 1238-1290.
3. Sharma, G. N., Dave, R., Sanadya, J., Sharma, P., & Sharma, K. (2010). Various types and management of breast cancer: an overview. *Journal of advanced pharmaceutical technology & research*, *1*(2), 109-126.
4. Morton, J. (1997). Reviews. Thesis Eleven, 51(1), 131–132.
5. Ghossain, A., & Ghossain, M. A. (2009). History of mastectomy before and after Halsted. *Le Journal medical libanais. The Lebanese medical journal*, *57*(2), 65-71.
6. Wang, K., & Tepper, J. E. (2021). Radiation therapy-associated toxicity: Etiology, management, and prevention. *CA: a cancer journal for clinicians*, *71*(5), 437-454.
7. Cho, B. (2018). Intensity-modulated radiation therapy: a review with a physics perspective. *Radiation oncology journal*, *36*(1), 1.
8. Goodman, L. S., Wintrobe, M. M., Dameshek, W., Goodman, M. J., Gilman, A., & McLennan, M. T. (1946). Nitrogen mustard therapy: Use of methyl-bis (beta-chloroethyl) amine hydrochloride and tris (beta-chloroethyl) amine hydrochloride for hodgkin's disease, lymphosarcoma, leukemia and certain allied and miscellaneous disorders. *Journal of the American Medical Association*, *132*(3), 126-132.
9. Farber, S., Diamond, L. K., Mercer, R. D., Sylvester Jr, R. F., & Wolff, J. A. (1948). Temporary remissions in acute leukemia in children produced by folic acid antagonist, 4-aminopteroyl-glutamic acid (aminopterin). *New England Journal of Medicine*, *238*(23), 787-793.
10. De Rooij, J. D., Zwaan, C. M., & van den Heuvel-Eibrink, M. (2015). Pediatric AML: from biology to clinical management. *Journal of clinical medicine*, *4*(1), 127-149
11. Kim, H. (2020). Treatments for children and adolescents with AML. *Blood research*, *55*(Suppl), S5.

12. Hermann, P. C., Huber, S. L., Herrler, T., Aicher, A., Ellwart, J. W., Guba, M., ... & Heeschen, C. (2007). Distinct populations of cancer stem cells determine tumor growth and metastatic activity in human pancreatic cancer. *Cell stem cell*, *1*(3), 313-323.
13. Bista, R., Lee, D. W., Pepper, O. B., Azorsa, D. O., Arceci, R. J., & Aleem, E. (2017). Disulfiram overcomes bortezomib and cytarabine resistance in Down-syndrome-associated acute myeloid leukemia cells. *Journal of Experimental & Clinical Cancer Research*, *36*, 1-14.
14. Aleem, E., & Arceci, R. J. (2015). Targeting cell cycle regulators in hematologic malignancies. *Frontiers in cell and developmental biology*, *3*, 16.
15. Lee, Y. T., Tan, Y. J., & Oon, C. E. (2018). Molecular targeted therapy: Treating cancer with specificity. *European journal of pharmacology*, *834*, 188-196.
16. Yan, L., Rosen, N., & Arteaga, C. (2011). Targeted cancer therapies. *Chinese journal of cancer*, *30*(1), 1.
17. Mansour, M. A., Caputo, V. S., & Aleem, E. (2021). Highlights on selected growth factors and their receptors as promising anticancer drug targets. *The International Journal of Biochemistry & Cell Biology*, *140*, 106087.
18. Fass, L. (2008). Imaging and cancer: a review. *Molecular oncology*, *2*(2), 115-152.
19. Liu, D., He, C., Poon, C., & Lin, W. (2014). Theranostic nanoscale coordination polymers for magnetic resonance imaging and bisphosphonate delivery. *Journal of Materials Chemistry B*, *2*(46), 8249-8255.
20. Strijkers, G. J., M Mulder, W. J., F van Tilborg, G. A., & Nicolay, K. (2007). MRI contrast agents: current status and future perspectives. *Anti-Cancer Agents in Medicinal Chemistry (Formerly Current Medicinal Chemistry-Anti-Cancer Agents)*, *7*(3), 291-305.
21. Dagogo-Jack, I., & Shaw, A. T. (2018). Tumour heterogeneity and resistance to cancer therapies. *Nature reviews Clinical oncology*, *15*(2), 81-94.
22. Loke, S. Y., & Lee, A. S. G. (2018). The future of blood-based biomarkers for the early detection of breast cancer. *European journal of cancer*, *92*, 54-68.
23. Ahmed, N., Fessi, H., & Elaissari, A. (2012). Theranostic applications of nanoparticles in cancer. *Drug discovery today*, *17*(17-18), 928-934.
24. Wang, J., Mi, P., Lin, G., Wáng, Y. X. J., Liu, G., & Chen, X. (2016). Imaging-guided delivery of RNAi for anticancer treatment. *Advanced drug delivery reviews*, *104*, 44-60.
25. Chen, L., & Liang, J. (2020). An overview of functional nanoparticles as novel emerging antiviral therapeutic agents. *Materials Science and Engineering: C*, *112*, 110924.
26. Caiyan, Y. U., Tongtong, X. U. A. N., Sunqi, L. O. U., Xiaoxiao, L. I. U., Guohai, L. I. A. N., & Huili, L. I. (2017). Gd3+ doped CuInS2/ZnS nanocrystals with high quantum yield for bimodal fluorescence/magnetic resonance imaging. *Journal of Rare Earths*, *35*(4), 382-388.
27. Yang, W., Guo, W., Gong, X., Zhang, B., Wang, S., Chen, N., ... & Chang, J. (2015). Facile synthesis of Gd–Cu–In–S/ZnS bimodal quantum dots with optimized properties for tumor targeted fluorescence/MR in vivo imaging. *ACS applied materials & interfaces*, *7*(33), 18759-18768.
28. Chan, M. H., Chang, Z. X., Huang, C. Y. F., Lee, L. J., Liu, R. S., & Hsiao, M. (2022). Integrated therapy platform of exosomal system: hybrid inorganic/organic nanoparticles with exosomes for cancer treatment. *Nanoscale Horizons*, *7*(4), 352-367.
29. Operti, M. C., Bernhardt, A., Grimm, S., Engel, A., Figdor, C. G., & Tagit, O. (2021). PLGA-based nanomedicines manufacturing: Technologies overview and challenges in industrial scale-up. *International Journal of Pharmaceutics*, *605*, 120807.
30. Xing, H., Hwang, K., & Lu, Y. (2016). Recent developments of liposomes as nanocarriers for theranostic applications. *Theranostics*, *6*(9), 1336.
31. Onzi, G., Guterres, S. S., Pohlmann, A. R., & Frank, L. A. (2021). Passive targeting and the enhanced permeability and retention (EPR) effect. *The ADME Encyclopedia: A Comprehensive Guide on Biopharmacy and Pharmacokinetics*, 1-13.
32. Al-Jamal, W. T., Al-Jamal, K. T., Tian, B., Cakebread, A., Halket, J. M., & Kostarelos, K. (2009). Tumor targeting of functionalized quantum dot− liposome hybrids by intravenous administration. *Molecular pharmaceutics*, *6*(2), 520-530.

33. Biankin, A. V., Waddell, N., Kassahn, K. S., Gingras, M. C., Muthuswamy, L. B., Johns, A. L., ... & University of California, San Francisco Tempero Margaret A. 56. (2012). Pancreatic cancer genomes reveal aberrations in axon guidance pathway genes. *Nature*, *491*(7424), 399-405.
34. Wang, Y., & Tang, M. (2018). Review of in vitro toxicological research of quantum dot and potentially involved mechanisms. *Science of the Total Environment*, *625*, 940-962.
35. Lamichhane, N., Udayakumar, T. S., D'Souza, W. D., Simone, C. B., Raghavan, S. R., Polf, J., & Mahmood, J. (2018). Liposomes: clinical applications and potential for image-guided drug delivery. *Molecules*, *23*(2), 288.
36. Feng, L., Cheng, L., Dong, Z., Tao, D., Barnhart, T. E., Cai, W., ... & Liu, Z. (2017). Theranostic liposomes with hypoxia-activated prodrug to effectively destruct hypoxic tumors post-photodynamic therapy. *ACS nano*, *11*(1), 927-937.
37. Pansare, V. J., Hejazi, S., Faenza, W. J., & Prud'homme, R. K. (2012). Review of long-wavelength optical and NIR imaging materials: contrast agents, fluorophores, and multifunctional nano carriers. *Chemistry of materials*, *24*(5), 812-827.
38. Zhang, H., Yu, Q., Li, Y., Yang, Z., Zhou, X., Chen, S., & Jiang, Z. X. (2020). Fluorinated cryptophane-A and porphyrin-based theranostics for multimodal imaging-guided photodynamic therapy. *Chemical communications*, *56*(25), 3617-3620.
39. Patel, N. R., Piroyan, A., Ganta, S., Morse, A. B., Candiloro, K. M., Solon, A. L., ... & Coleman, T. P. (2018). In Vitro and In Vivo evaluation of a novel folate-targeted theranostic nanoemulsion of docetaxel for imaging and improved anticancer activity against ovarian cancers. *Cancer biology & therapy*, *19*(7), 554-564.
40. Lin, Q., Jin, C. S., Huang, H., Ding, L., Zhang, Z., Chen, J., & Zheng, G. (2014). Nanoparticle-enabled, image-guided treatment planning of target specific RNAi therapeutics in an orthotopic prostate cancer model. *Small*, *10*(15), 3072-3082.
41. Liang, X., Chen, M., Bhattarai, P., Hameed, S., Tang, Y., & Dai, Z. (2021). Complementing cancer photodynamic therapy with ferroptosis through iron oxide loaded porphyrin-grafted lipid nanoparticles. *ACS nano*, *15*(12), 20164-20180.
42. Jahanshahi, M. (2004). Re-design of downstream processing techniques for nanoparticulate bioproducts. *Iranian Journal of Biotechnology*, *2*(1), 1-12.
43. Zhao, M., Lei, C., Yang, Y., Bu, X., Ma, H., Gong, H., ... & Fang, Q. (2015). Abraxane, the nanoparticle formulation of paclitaxel can induce drug resistance by up-regulation of P-gp. *PloS one*, *10*(7), e0131429.
44. Gonzalez-Angulo, A. M., Meric-Bernstam, F., Chawla, S., Falchook, G., Hong, D., Akcakanat, A., ... & Kurzrock, R. (2013). Weekly nab-Rapamycin in patients with advanced nonhematologic malignancies: final results of a phase I trial. *Clinical Cancer Research*, *19*(19), 5474-5484.
45. Gou, Y., Miao, D., Zhou, M., Wang, L., Zhou, H., & Su, G. (2018). Bio-inspired protein-based nanoformulations for cancer theranostics. *Frontiers in pharmacology*, *9*, 421.
46. Chen, Q., Liang, C., Wang, X., He, J., Li, Y., & Liu, Z. (2014). An albumin-based theranostic nano-agent for dual-modal imaging guided photothermal therapy to inhibit lymphatic metastasis of cancer post surgery. *Biomaterials*, *35*(34), 9355-9362.
47. Yu, X., Zhu, W., Di, Y., Gu, J., Guo, Z., Li, H., ... & Jin, C. (2017). Triple-functional albumin-based nanoparticles for combined chemotherapy and photodynamic therapy of pancreatic cancer with lymphatic metastases. *International journal of nanomedicine*, 6771-6785.
48. Safaei, M., Foroughi, M. M., Ebrahimpoor, N., Jahani, S., Omidi, A., & Khatami, M. (2019). A review on metal-organic frameworks: Synthesis and applications. *TrAC Trends in Analytical Chemistry*, *118*, 401-425.
49. Giliopoulos, D., Zamboulis, A., Giannakoudakis, D., Bikiaris, D., & Triantafyllidis, K. (2020). Polymer/metal organic framework (MOF) nanocomposites for biomedical applications. *Molecules*, *25*(1), 185.
50. Sun, C. Y., Qin, C., Wang, C. G., Su, Z. M., Wang, S., Wang, X. L., ... & Wang, E. B. (2011). Chiral nanoporous metal-organic frameworks with high porosity as materials for drug delivery. *Advanced Materials (Deerfield Beach, Fla.)*, *23*(47), 5629-5632.

51. Gao, X., Zhai, M., Guan, W., Liu, J., Liu, Z., & Damirin, A. (2017). Controllable synthesis of a smart multifunctional nanoscale metal–organic framework for magnetic resonance/optical imaging and targeted drug delivery. *ACS applied materials & interfaces*, *9*(4), 3455-3462.
52. Gao, X., Cui, R., Ji, G., & Liu, Z. (2018). Size and surface controllable metal–organic frameworks (MOFs) for fluorescence imaging and cancer therapy. *Nanoscale*, *10*(13), 6205-6211.
53. Cherkasov, V. R., Mochalova, E. N., Babenyshev, A. V., Rozenberg, J. M., Sokolov, I. L., & Nikitin, M. P. (2020). Antibody-directed metal-organic framework nanoparticles for targeted drug delivery. *Acta Biomaterialia*, *103*, 223-236.
54. Ni, K., Lan, G., Song, Y., Hao, Z., & Lin, W. (2020). Biomimetic nanoscale metal–organic framework harnesses hypoxia for effective cancer radiotherapy and immunotherapy. *Chemical Science*, *11*(29), 7641-7653.
55. Priyam, J., & Saxena, U. (2023). Therapeutic applications of carbon nanomaterials in renal cancer. *Biotechnology Letters*, *45*(11), 1395-1416.
56. Luo, X., Wang, H., & Ji, D. (2021). Carbon nanotubes (CNT)-loaded ginsenosides Rb3 suppresses the PD-1/PD-L1 pathway in triple-negative breast cancer. *Aging (Albany NY)*, *13*(13), 17177.
57. Yi, H., Ghosh, D., Ham, M. H., Qi, J., Barone, P. W., Strano, M. S., & Belcher, A. M. (2012). M13 phage-functionalized single-walled carbon nanotubes as nanoprobes for second near-infrared window fluorescence imaging of targeted tumors. *Nano letters*, *12*(3), 1176-1183.
58. Ghosh, D., Bagley, A. F., Na, Y. J., Birrer, M. J., Bhatia, S. N., & Belcher, A. M. (2014). Deep, noninvasive imaging and surgical guidance of submillimeter tumors using targeted M13-stabilized single-walled carbon nanotubes. *Proceedings of the National Academy of Sciences*, *111*(38), 13948-13953.
59. Ceppi, L., Bardhan, N. M., Na, Y., Siegel, A., Rajan, N., Fruscio, R., ... & Birrer, M. J. (2019). Real-time single-walled carbon nanotube-based fluorescence imaging improves survival after debulking surgery in an ovarian cancer model. *ACS nano*, *13*(5), 5356-5365.
60. Lee, J. H., Yigit, M. V., Mazumdar, D., & Lu, Y. (2010). Molecular diagnostic and drug delivery agents based on aptamer-nanomaterial conjugates. *Advanced drug delivery reviews*, *62*(6), 592-605.
61. Zhang, M., Wang, W., Wu, F., Yuan, P., Chi, C., & Zhou, N. (2017). Magnetic and fluorescent carbon nanotubes for dual modal imaging and photothermal and chemo-therapy of cancer cells in living mice. *Carbon*, *123*, 70-83.
62. Yang, S., Wang, Z., Ping, Y., Miao, Y., Xiao, Y., Qu, L., ... & Wang, J. (2020). PEG/PEI-functionalized single-walled carbon nanotubes as delivery carriers for doxorubicin: synthesis, characterization, and in vitro evaluation. *Beilstein Journal of Nanotechnology*, *11*(1), 1728-1741.
63. Lu, Y. J., Wei, K. C., Ma, C. C. M., Yang, S. Y., & Chen, J. P. (2012). Dual targeted delivery of doxorubicin to cancer cells using folate-conjugated magnetic multi-walled carbon nanotubes. *Colloids and Surfaces B: Biointerfaces*, *89*, 1-9.
64. Lin, C., Sun, K., Zhang, C., Tan, T., Xu, M., Liu, Y., ... & Whittaker, A. (2020). Carbon dots embedded metal organic framework@ chitosan core-shell nanoparticles for vitro dual mode imaging and pH-responsive drug delivery. *Microporous and Mesoporous Materials*, *293*, 109775.
65. Li, H., Shao, F. Q., Huang, H., Feng, J. J., & Wang, A. J. (2016). Eco-friendly and rapid microwave synthesis of green fluorescent graphitic carbon nitride quantum dots for vitro bioimaging. *Sensors and Actuators B: Chemical*, *226*, 506-511.
66. Jia, Q., Zhao, Z., Liang, K., Nan, F., Li, Y., Wang, J., ... & Wang, P. (2020). Recent advances and prospects of carbon dots in cancer nanotheranostics. *Materials Chemistry Frontiers*, *4*(2), 449-471.
67. Mauro, N., Utzeri, M. A., Drago, S. E., Nicosia, A., Costa, S., Cavallaro, G., & Giammona, G. (2021). Hyaluronic acid dressing of hydrophobic carbon nanodots: A self-assembling strategy of hybrid nanocomposites with theranostic potential. *Carbohydrate Polymers*, *267*, 118213.
68. Nicosia, A., Cavallaro, G., Costa, S., Utzeri, M. A., Cuttitta, A., Giammona, G., & Mauro, N. (2020). Carbon nanodots for on demand chemophotothermal therapy combination to elicit necroptosis: Overcoming apoptosis resistance in breast cancer cell lines. *Cancers*, *12*(11), 3114.
69. Geng, B., Yang, D., Pan, D., Wang, L., Zheng, F., Shen, W., ... & Li, X. (2018). NIR-responsive carbon dots for efficient photothermal cancer therapy at low power densities. *Carbon*, *134*, 153-162.

70. Tasnim, K. N., Adrita, S. H., Hossain, S., Akash, S. Z., & Sharker, S. (2020). The prospect of stem cells for HIV and cancer treatment: a review. *Pharmaceutical and Biomedical Research*.
71. Chen, J., Liu, C., Zeng, G., You, Y., Wang, H., Gong, X., ... & Song, L. (2016). Indocyanine green loaded reduced graphene oxide for in vivo photoacoustic/fluorescence dual-modality tumor imaging. *Nanoscale research letters*, *11*, 1-11.
72. Mirrahimi, M., Alamzadeh, Z., Beik, J., Sarikhani, A., Mousavi, M., Irajirad, R., ... & Shakeri-Zadeh, A. (2022). A 2D nanotheranostic platform based on graphene oxide and phase-change materials for bimodal CT/MR imaging, NIR-activated drug release, and synergistic thermo-chemotherapy. *Nanotheranostics*, *6*(4), 350.
73. Guo, W., Chen, Z., Feng, X., Shen, G., Huang, H., Liang, Y., ... & Hu, Y. (2021). Graphene oxide (GO)-based nanosheets with combined chemo/photothermal/photodynamic therapy to overcome gastric cancer (GC) paclitaxel resistance by reducing mitochondria-derived adenosine-triphosphate (ATP). *Journal of nanobiotechnology*, *19*(1), 146.
74. Yang, L., Liu, B., Wang, M., Li, J., Pan, W., Gao, X., ... & Tang, B. (2018). A highly sensitive strategy for fluorescence imaging of microRNA in living cells and in vivo based on graphene oxide-enhanced signal molecules quenching of molecular beacon. *ACS applied materials & interfaces*, *10*(8), 6982-6990.
75. Mukherjee, S., Sau, S., Madhuri, D., Bollu, V. S., Madhusudana, K., Sreedhar, B., ... & Patra, C. R. (2016). Green synthesis and characterization of monodispersed gold nanoparticles: toxicity study, delivery of doxorubicin and its bio-distribution in mouse model. *Journal of Biomedical Nanotechnology*, *12*(1), 165-181.
76. Ganeshkumar, M., Sathishkumar, M., Ponrasu, T., Dinesh, M. G., & Suguna, L. (2013). Spontaneous ultra fast synthesis of gold nanoparticles using Punica granatum for cancer targeted drug delivery. *Colloids and Surfaces B: Biointerfaces*, *106*, 208-216.
77. Mukherjee, S., Chowdhury, D., Kotcherlakota, R., Patra, S., Vinothkumar, B., Bhadra, M. P., ... & Patra, C. R. (2014). Potential theranostics application of bio-synthesized silver nanoparticles (4-in-1 system). *Theranostics*, *4*(3), 316.
78. Mukherjee, S., Dasari, M., Priyamvada, S., Kotcherlakota, R., Bollu, V. S., & Patra, C. R. (2015). A green chemistry approach for the synthesis of gold nanoconjugates that induce the inhibition of cancer cell proliferation through induction of oxidative stress and their in vivo toxicity study. *Journal of materials chemistry B*, *3*(18), 3820-3830.
79. Fazal, S., Jayasree, A., Sasidharan, S., Koyakutty, M., Nair, S. V., & Menon, D. (2014). Green synthesis of anisotropic gold nanoparticles for photothermal therapy of cancer. *ACS applied materials & interfaces*, *6*(11), 8080-8089.
80. Wang, J., Zhang, G., Li, Q., Jiang, H., Liu, C., Amatore, C., & Wang, X. (2013). In vivo self-bio-imaging of tumors through in situ biosynthesized fluorescent gold nanoclusters. *Scientific reports*, *3*(1), 1157.
81. Kotcherlakota, R., Nimushakavi, S., Roy, A., Yadavalli, H. C., Mukherjee, S., Haque, S., & Patra, C. R. (2019). Biosynthesized gold nanoparticles: In vivo study of near-infrared fluorescence (NIR)-based bio-imaging and cell labeling applications. *ACS Biomaterials Science & Engineering*, *5*(10), 5439-5452.
82. Austin, L. A., Kang, B., Yen, C. W., & El-Sayed, M. A. (2011). Plasmonic imaging of human oral cancer cell communities during programmed cell death by nuclear-targeting silver nanoparticles. *Journal of the American Chemical Society*, *133*(44), 17594-17597.
83. Gurunathan, S., Jeong, J. K., Han, J. W., Zhang, X. F., Park, J. H., & Kim, J. H. (2015). Multidimensional effects of biologically synthesized silver nanoparticles in Helicobacter pylori, Helicobacter felis, and human lung (L132) and lung carcinoma A549 cells. *Nanoscale research letters*, *10*, 1-17.
84. Padinjarathil, H., Joseph, M. M., Unnikrishnan, B. S., Preethi, G. U., Shiji, R., Archana, M. G., ... & Sreelekha, T. T. (2018). Galactomannan endowed biogenic silver nanoparticles exposed enhanced cancer cytotoxicity with excellent biocompatibility. *International journal of biological macromolecules*, *118*, 1174-1182.
85. Oves, M., Aslam, M., Rauf, M. A., Qayyum, S., Qari, H. A., Khan, M. S., ... & Ismail, I. M. (2018). Antimicrobial and anticancer activities of silver nanoparticles synthesized from the root hair extract of Phoenix dactylifera. *Materials Science and Engineering: C*, *89*, 429-443.

86. Maity, P., Bepari, M., Pradhan, A., Baral, R., Roy, S., & Choudhury, S. M. (2018). Synthesis and characterization of biogenic metal nanoparticles and its cytotoxicity and anti-neoplasticity through the induction of oxidative stress, mitochondrial dysfunction and apoptosis. *Colloids and Surfaces B: Biointerfaces*, *161*, 111-120.
87. Dinparvar, S., Bagirova, M., Allahverdiyev, A. M., Abamor, E. S., Safarov, T., Aydogdu, M., & Aktas, D. (2020). A nanotechnology-based new approach in the treatment of breast cancer: Biosynthesized silver nanoparticles using Cuminum cyminum L. seed extract. *Journal of Photochemistry and Photobiology B: Biology*, *208*, 111902.
88. Kumar, B., Smita, K., Seqqat, R., Benalcazar, K., Grijalva, M., & Cumbal, L. (2016). In vitro evaluation of silver nanoparticles cytotoxicity on Hepatic cancer (Hep-G2) cell line and their antioxidant activity: Green approach for fabrication and application. *Journal of Photochemistry and Photobiology B: Biology*, *159*, 8-13.
89. Liu, K., Liu, K., Liu, J., Ren, Q., Zhao, Z., Wu, X., ... & Li, B. (2020). Copper chalcogenide materials as photothermal agents for cancer treatment. *Nanoscale*, *12*(5), 2902-2913.
90. Li, X., Xiang, C., Yuan, Y., Chen, J., Qing, G., Ma, J., ... & Guo, W. (2021). Structure transformable nanoparticles for photoacoustic imaging-guided photothermal ablation of tumors via enzyme-induced multistage delivery. *Chemical Engineering Journal*, *421*, 127747.
91. Wang, S., Zhang, L., Zhao, J., He, M., Huang, Y., & Zhao, S. (2021). A tumor microenvironment–induced absorption red-shifted polymer nanoparticle for simultaneously activated photoacoustic imaging and photothermal therapy. *Science Advances*, *7*(12), eabe3588.
92. Deng, H., Yang, Z., Pang, X., Zhao, C., Tian, J., Wang, Z., & Chen, X. (2022). Self-sufficient copper peroxide loaded pKa-tunable nanoparticles for lysosome-mediated chemodynamic therapy. *Nano Today*, *42*, 101337.
93. Liu, R., An, Y., Jia, W., Wang, Y., Wu, Y., Zhen, Y., ... & Gao, H. (2020). Macrophage-mimic shape changeable nanomedicine retained in tumor for multimodal therapy of breast cancer. *Journal of controlled release*, *321*, 589-601.
94. Filali, S., Pirot, F., & Miossec, P. (2020). Biological applications and toxicity minimization of semiconductor quantum dots. *Trends in biotechnology*, *38*(2), 163-177.
95. Nezhad-Mokhtari, P., Arsalani, N., Ghorbani, M., & Hamishehkar, H. (2018). Development of biocompatible fluorescent gelatin nanocarriers for cell imaging and anticancer drug targeting. *Journal of materials science*, *53*(15), 10679-10691.
96. Nigam, P., Waghmode, S., Louis, M., Wangnoo, S., Chavan, P., & Sarkar, D. (2014). Graphene quantum dots conjugated albumin nanoparticles for targeted drug delivery and imaging of pancreatic cancer. *Journal of Materials Chemistry B*, *2*(21), 3190-3195.
97. Chu, M., Wu, F., Zhang, Q., Liu, T., Yu, Y., Ji, A., ... & Zhu, J. (2010). A novel method for preparing quantum dot nanospheres with narrow size distribution. *Nanoscale*, *2*(4), 542-547.
98. Song, H., Wang, J., Xiong, B., Hu, J., Zeng, P., Liu, X., & Liang, H. (2022). Biologically safe, versatile, and smart bismuthene functionalized with a drug delivery system based on red phosphorus quantum dots for cancer theranostics. *Angewandte Chemie*, *134*(22), e202117679.
99. Girija Aswathy, R., Sivakumar, B., Brahatheeswaran, D., Fukuda, T., Yoshida, Y., Maekawa, T., & Sakthi Kumar, D. (2012). Biocompatible fluorescent zein nanoparticles for simultaneous bioimaging and drug delivery application. *Advances in Natural Sciences: Nanoscience and Nanotechnology*, *3*(2), 025006.
100. Shao, J., Zhang, J., Jiang, C., Lin, J., & Huang, P. (2020). Biodegradable titanium nitride MXene quantum dots for cancer phototheranostics in NIR-I/II biowindows. *Chemical Engineering Journal*, *400*, 126009.
101. Wong, C., Stylianopoulos, T., Cui, J., Martin, J., Chauhan, V. P., Jiang, W., ... & Fukumura, D. (2011). Multistage nanoparticle delivery system for deep penetration into tumor tissue. *Proce.*
102. Kim, K. S., Kim, S., Beack, S., Yang, J. A., Yun, S. H., & Hahn, S. K. (2012). In vivo real-time confocal microscopy for target-specific delivery of hyaluronic acid-quantum dot conjugates. *Nanomedicine: Nanotechnology, Biology and Medicine*, *8*(7), 1070-1073.

103. AbdElhamid, A. S., Helmy, M. W., Ebrahim, S. M., Bahey-El-Din, M., Zayed, D. G., Zein El Dein, E. A., ... & Elzoghby, A. O. (2018). Layer-by-layer gelatin/chondroitin quantum dots-based nanotheranostics: combined rapamycin/celecoxib delivery and cancer imaging. *Nanomedicine*, *13*(14), 1707-1730.
104. AbdElhamid, A. S., Zayed, D. G., Helmy, M. W., Ebrahim, S. M., Bahey-El-Din, M., Zein-El-Dein, E. A., ... & Elzoghby, A. O. (2018). Lactoferrin-tagged quantum dots-based theranostic nanocapsules for combined COX-2 inhibitor/herbal therapy of breast cancer. *Nanomedicine*, *13*(20), 2637-2656.
105. Castaneda, R. T., Khurana, A., Khan, R., & Daldrup-Link, H. E. (2011). Labeling stem cells with ferumoxytol, an FDA-approved iron oxide nanoparticle. *JoVE (Journal of Visualized Experiments)*, (57), e3482.
106. Basoglu, H., Goncu, B., & Akbas, F. (2018). Magnetic nanoparticle-mediated gene therapy to induce Fas apoptosis pathway in breast cancer. *Cancer gene therapy*, *25*(5), 141-147.
107. Lv, Y., Zou, Y., & Yang, L. (2012). Uncertainty and sensitivity analysis of properties of phase change micro/nanoparticles for thermal protection during cryosurgery. *Forschung im Ingenieurwesen*, *76*, 41-50.
108. Ryman-Rasmussen, J. P., Riviere, J. E., & Monteiro-Riviere, N. A. (2006). Penetration of intact skin by quantum dots with diverse physicochemical properties. *Toxicological sciences*, *91*(1), 159-165.
109. Jia G, Han Y, An Y, Ding Y, He C, Wang X, Tang Q (2018) NRP-1 targeted and cargo-loaded exosomes facilitate simultaneous imaging and therapy of glioma in vitro and in vivo. Biomaterials 178:302–316.
110. Awasthi, R., Pant, I., T Kulkarni, G., Satiko Kikuchi, I., de Jesus Andreoli Pinto, T., Dua, K., & Ramana Malipeddi, V. (2016). Opportunities and challenges in nano-structure mediated drug delivery: where do we stand?. *Current Nanomedicine (Formerly: Recent Patents on Nanomedicine)*, *6*(2), 78-104.
111. Xia, T., Kovochich, M., Brant, J., Hotze, M., Sempf, J., Oberley, T., ... & Nel, A. E. (2006). Comparison of the abilities of ambient and manufactured nanoparticles to induce cellular toxicity according to an oxidative stress paradigm. *Nano letters*, *6*(8), 1794-1807.
112. Love, K. T., Mahon, K. P., Levins, C. G., Whitehead, K. A., Querbes, W., Dorkin, J. R., ... & Anderson, D. G. (2010). Lipid-like materials for low-dose, in vivo gene silencing. *Proceedings of the National Academy of Sciences*, *107*(5), 1864-1869.
113. Schork, N. J. (2015). Personalized medicine: time for one-person trials. *Nature*, *520*(7549), 609-611.
114. Chong, Y., Ma, Y., Shen, H., Tu, X., Zhou, X., Xu, J., ... & Zhang, Z. (2014). The in vitro and in vivo toxicity of graphene quantum dots. *Biomaterials*, *35*(19), 5041-5048.
115. Zhang, H., Yee, D., & Wang, C. (2008). Quantum dots for cancer diagnosis and therapy: biological and clinical perspectives.
116. González-Ballesteros, N., Diego-González, L., Lastra-Valdor, M., Rodríguez-Argüelles, M. C., Grimaldi, M., Cavazza, A., ... & Simón-Vázquez, R. (2019). Immunostimulant and biocompatible gold and silver nanoparticles synthesized using the Ulva intestinalis L. aqueous extract. Journal of materials chemistry B, 7(30), 4677-4691.
117. Bhowmik, T., & Gomes, A. (2017). Down–regulation of cyclin–dependent kinase-4 and MAPK through estrogen receptor mediated cell cycle arrest in human breast cancer induced by gold nanoparticle tagged toxin protein NKCT1. *Chemico-biological interactions*, *268*, 119-128.
118. Nebu, J., Devi, J. A., Aparna, R. S., Abha, K., & Sony, G. (2018). Erlotinib conjugated gold nanocluster enveloped magnetic iron oxide nanoparticles–A targeted probe for imaging pancreatic cancer cells. *Sensors and Actuators B: Chemical*, *257*, 1035-1043.
119. Wang, P., Liu, S., Hu, M., Zhang, H., Duan, D., He, J., ... & Liang, M. (2020). Peroxidase-like nanozymes induce a novel form of cell death and inhibit tumor growth in vivo. *Advanced Functional Materials*, *30*(21), 2000647.
120. Das, S., Roy, A., Barui, A. K., Alabbasi, M. M. A., Kuncha, M., Sistla, R., ... & Patra, C. R. (2020). Anti-angiogenic vanadium pentoxide nanoparticles for the treatment of melanoma and their in vivo toxicity study. *Nanoscale*, *12*(14), 7604-7621.
121. Chen, M., Deng, G., He, Y., Li, X., Liu, W., Wang, W., ... & Yang, S. (2019). Ultrasound-enhanced generation of reactive oxygen species for MRI-guided tumor therapy by the Fe@ Fe_3O_4-based peroxidase-mimicking nanozyme. *ACS Applied Bio Materials*, *3*(1), 639-647.

122. Miao, Z., Jiang, S., Ding, M., Sun, S., Ma, Y., Younis, M. R., ... & Zha, Z. (2020). Ultrasmall rhodium nanozyme with RONS scavenging and photothermal activities for anti-inflammation and antitumor theranostics of colon diseases. *Nano Letters*, *20*(5), 3079-3089.
123. Fujiwara, R., Luo, Y., Sasaki, T., Fujii, K., Ohmori, H., & Kuniyasu, H. (2015). Cancer therapeutic effects of titanium dioxide nanoparticles are associated with oxidative stress and cytokine induction. *Pathobiology*, *82*(6), 243-251.
124. Dobrucka, R., Romaniuk-Drapała, A., & Kaczmarek, M. (2019). Evaluation of biological synthesized platinum nanoparticles using Ononidis radix extract on the cell lung carcinoma A549. *Biomedical microdevices*, *21*, 1-10.
125. Nejdl, L., Kudr, J., Moulick, A., Hegerova, D., Ruttkay-Nedecky, B., Gumulec, J., ... & Adam, V. (2017). Platinum nanoparticles induce damage to DNA and inhibit DNA replication. *PLoS One*, *12*(7), e0180798.
126. Kadhem, H. A., Ibraheem, S. A., Jabir, M. S., & Kadhim, A. A. (2019). Zainab Jihad taqi, and mihailescu dan florin, zinc oxide nanoparticles induce apoptosis in human breast cancer cells via caspase-8 and P53 pathway. *Nano Biomed. Eng*, *11*(1), 35-43.
127. Ahamed, M., Khan, M. M., Akhtar, M. J., Alhadlaq, H. A., & Alshamsan, A. (2017). Ag-doping regulates the cytotoxicity of TiO_2 nanoparticles via oxidative stress in human cancer cells. *Scientific reports*, *7*(1), 17662.
128. Nourmohammadi, E., Khoshdel-Sarkarizi, H., Nedaeinia, R., Sadeghnia, H. R., Hasanzadeh, L., Darroudi, M., & Kazemi oskuee, R. (2019). Evaluation of anticancer effects of cerium oxide nanoparticles on mouse fibrosarcoma cell line. *Journal of cellular physiology*, *234*(4), 4987-4996.
129. Parvathya, S., & Venkatramanb, B. R. (2017). In vitro antibacterial and anticancer potential of CeO_2 nanoparticles prepared by co-precipitation and green synthesis method. *J. Nanosci. Curr. Res*, *2*(02), 1-9.
130. Bakshi, S., Zakharchenko, A., Minko, S., Kolpashchikov, D. M., & Katz, E. (2019). Towards nanomaterials for cancer theranostics: a system of DNA-modified magnetic nanoparticles for detection and suppression of RNA marker in cancer cells. *Magnetochemistry*, *5*(2), 24.
131. Du, Y., Zhang, J., Yan, S., Tao, Z., Wang, C., Huang, M., & Zhang, X. (2019). PEGylated zinc oxide nanoparticles induce apoptosis in pancreatic cancer cells through reactive oxygen species. *IET Nanobiotechnology*, *13*(5), 536-540.
132. Jiang, T., Zhang, B., Zhang, L., Wu, X., Li, H., Shen, S., ... & Jiang, X. (2018). Biomimetic nanoparticles delivered hedgehog pathway inhibitor to modify tumour microenvironment and improved chemotherapy for pancreatic carcinoma. *Artificial Cells, Nanomedicine, and Biotechnology*, *46*(sup1), 1088-1101.

Chapter 2

Literature Survey:

Outlook of Prussian Blue Based Nanoparticles: Synthesis, Surface Modification and Multimodal Theranostic Applications

Chapter 2. Literature Survey

Outlook of Prussian Blue Based Nanoparticles: Synthesis, Surface Modification and Multimodal Theranostic Applications

2.1 Introduction

Prussian blue (PB) was initially discovered as a pigment in the early of 18th century by an artist from Berlin, Diesbach.[1] Later, in 1936, Keggin and Miles revealed its coordinated cubic structure through x-ray diffraction which was further validated by Herren using diffraction pattern of single crystal in the year 1980.[2,3]. PB, a prospective metal organic framework (MOF) with optimal formula of $Fe_4^{III}[Fe^{II}(CN)_6]_3.nH_2O$, is composed of a dual-valance hexacyanoferrate encompassing Fe^{2+} and Fe^{3+} ions. Within this framework, low spin Fe^{2+} is linked with C atom, while high spin Fe^{3+} is bonded with N atom. This $Fe^{2+} - CN - Fe^{3+}$ unit possesses five unpaired electrons each, alongside redundant Fe^{3+} sites enabling versatile modifications. It's unit cell includes interstitial vacancies offering scope for insertion of counter cation and small molecules. Moreover, it possesses benefit inherent to cyano-bridged coordination, including a recognized and adaptable molecular structure, adaptable chemical and physical properties, porosity, minimal density, the capacity to merge diverse characteristics within a singular multifunctional NP and straightforward synthesis approach. Based on molecular structures, PB can be categorized into two forms: insoluble PB (IPB) with chemical formula $Fe_4^{III}[Fe^{II}(CN)_6]_3.nH_2O$, where n = 12-14, while soluble PB (SPB) having chemical formula $AFe^{III}[Fe^{II}(CN)_6].xH_2O$, where x = 1-5 and A is monovalent cation like Na^+, K^+ or NH_4^+ (shown in Figure 1).[4] SPB features embedded K^+ inclusions within an aqueous environment yielding net negative ionization effect along crystal surface which facilitates to form a stable dispersion for smaller crystal size. Conversely, with IPB, vacancies within the flawed lattice structure are occupied by two types of H_2O molecules to maintain charge equilibrium. They are either directly coordinated with Fe^{3+}, referred as coordinated H_2O molecules, or hydrogen bonded with coordinated H_2O molecules, termed as zeolitic-like H_2O molecules. In the realm of SPB, alkali metal ions replace H_2O molecules within the cavities to maintain charge balance. Leveraging its porous nature, PBNP demonstrates an aptitude for adsorbing small molecules. This remarkable trait has led PBNP as a 'chemical sponge', giving extensive utility in diverse applications including environmental remediation, gas storage, drug

delivery and many more.[5] PB has got attention for energy storage devices, catalytic processes and sensor development, owing to its remarkable electrochemical and optical characteristics. Additionally, PBNPs exhibit excellent enzymatic activities which facilitate catalytic reduction of H_2O_2 at diminished dosage enabling PBNPs as a potential candidate for biosensors.[6] Despite the abundance of research concerning PBNPs, the majority of research predominantly centered around its applications as energy storage device and biosensors, rather than its potential role in disease theranostics. With the ongoing progression of nanotechnology, the development of nanocomposites has ignited significant research interest, driven by the distinct advantages of NPs, including their size similarity to biological molecules, substantial surface-to-volume ratio (S/V), simplified surface modification and functionalization, impressive solubility and stability, sustained drug release capabilities, and targeted theranostic effects. Herein, PBNPs having these remarkable features including its capabilities in adsorption, ion exchange and mechanical entrapment have led to the endorsement by U.S. Food and Drug Administration (FDA) in 2003 as an antidote for addressing internal radioactive contamination involving cesium and thallium.[7] Moreover, tuneable absorption in between 600 and 900 nm due to Fe^{2+} - Fe^{3+} transition, high biocompatibility, excellent cellular uptake has led PBNPs in the biomedical field, particularly as a novel next-generation reactive oxygen species (ROS) and reactive nitrogen species (RNS) mediated phototherapeutic agent. In this context, it may be also stated that PBNPs exhibits higher molar extinction coefficient ($1.09 \times 109\ M^{-1}cm^{-1}$) than other few phototherapeutic agents such as $Cu_{2-x}Se$ ($7.7 \times 107\ M^{-1}cm^{-1}$; 980 nm), carbon nanotubes ($7.9 \times 106\ M^{-1}cm^{-1}$;808 nm) etc.[8,9] Additionally, PBNPs are noted to decompose H_2O_2 into O_2, thus counteracting solid tumor hypoxia through nanoenzymatic activities including peroxidase (POD), catalase (CAT), and superoxide dismutase (SOD). PBNPs also find extensive utility as contrast agents (CAs) in photoacoustic (PA) and T_1-T_2 weighted magnetic resonance imaging (MRI) due to their potent magnetic properties and distinct structure. Leveraging, their porous and surface-modifiable characteristics, PBNPs possess the capability to transport active molecules, thereby addressing the limitations of traditional drugs such as poor solubility, inadequate target specificity and systemic adverse effect. Recently, a multifaceted therapeutic approach has emerged for complete cancer eradication. In this context, the integration of multimodal diagnostic techniques and chemo-phototherapy utilizing PBNPs, in conjugation with diverse metal ions, biological agents and chemotherapeutic drugs hold great potential to emerge as a highly encouraging therapeutic approach for cancer treatment in the upcoming times.

In this chapter, we initially focus on the advancement of synthetic techniques for PBNPs, aiming to achieve precise control over their dimension, morphology and uniformity. Furthermore, a range of techniques are employed to modify the PBNP surfaces, enhancing their biocompatibility, bolstering physiological stability, ensuring optimal blood circulation time, and enabling precise targeting. We also emphasize their diverse activities in biomedical realms, encompassing *in-vitro* and *in-vivo* applications such as varied tumor therapies, combatting bacterial infections, addressing inflammatory ailments and facilitating biomedical imaging. Concisely, we provide an overview of the potential toxicological impacts of PBNPs. Finally, we discuss some novel designing approaches and future research trajectory of PBNPs.

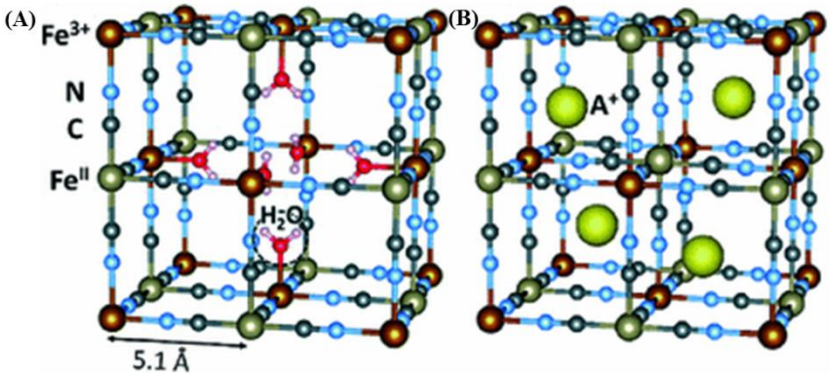

Figure 1: Unit cell structure of (A) insoluble and (B) soluble prussian blue nanoparticle

2.2 Pioneering strategies in developing PBNPs for biomedical advancements

Generally, preparative strategies are important as they tune structural, micro-structural properties of PBNPs, like any other nanomaterials, those in consequence have significant effects on opto-electronic applications of PBNPs, particularly in the realm of diagnosis and therapeutic activity. Various synthetic protocols including co-precipitation, hydrothermal, template-assisted fabrication, and microwave-assisted techniques etc. have been extensively explored to unlock boundless potentiality of PBNPs and they, classified into double-precursor synthesis and single-precursor synthesis (schematic representation shown in Figure 2(A)), are briefly discussed in the subsequent section.

Among diverse techniques to produce SPB or IPB, co-precipitation, one of the most traditional processes, relies on dual precursors (e.g. iron salt and hexacyanoferrate salt) or oxidation/reduction of a single precursor (hexacyanoferrate salt). In dual precursor approach, either iron(III) salt (e.g. $FeCl_3$) and ferrocyanide salt (e.g. $K_4[Fe(CN)_6]$), or iron(II) salt (e.g. $FeCl_2$) and ferricyanide salt (e.g. $K_3[Fe(CN)_6]$) are taken as precursors. In addition, few reports

also available wherein iron(II) salt reacts with ferrocyanide salt ($K_4[Fe(CN)_6]$) to generate PBNPs. Primarily, precipitate, known as 'Berlin White,' gets formed having features of ferrous ferrocyanide ($Fe_2[Fe(CN)_6]$) and subsequently, it is oxidized in the presence of oxidising agents like H_2O_2 which yields SPB or IPB depending on concentration of iron salt.[10,11] It is important to note that iron(II) salt and ferricyanide salt ($K_3[Fe(CN)_6]$) react to result a blue precipitate, referred as 'Turnbulls Blue' having features similar to PB as confirmed by Mössbauer spectroscopy, x-ray diffraction etc. This double-precursor approach has the advantage of less reaction time and works without any reducing agent. In contrast, single-precursor method, pioneered first by Deng and his colleagues in 1998, typically employs either $K_3[Fe(CN)_6]$ or $K_4[Fe(CN)_6]$ as initial precursor. It has been studied that Fe^{2+} / Fe^{3+} are released from precursor and subsequently get oxidized or reduced into Fe^{3+} or Fe^{2+} in an acidic environment.[12] Released, oxidized Fe^{2+} or Fe^{3+} promptly reacts with un-decomposed ions and leads formation of PBNPs. The notable advantage of this technique is the ability to achieve desirable uniformity of PBNPs through straightforward procedures, owing to the gradual kinetics of the reaction processes.

Hydrothermal technique is an alternative method to prepare nano- and micro-scale PBNPs wherein aqueous solutions of the precursors are introduced into an autoclave reactor which is subjected to an elevated temperature (≥ 100 °C) and high pressure. Main advantage is that various morphologies can be easily generated by varying solvents, organic additives and reaction temperatures. However, rapid crystallization, followed by fast internal growth in the presence of high temperature and pressure has rendered this approach incompatible to obtain nano-scale PBNPs. In some cases, minimization of surface energy during hydrothermal reaction generates aggregated pattern which in consequence leads formation of mesocrystals of moderate size (~ 100 nm). These aggregations undergo into a compact structure by eliminating pores and consequently lead formation of larger sized PBNPs (~ 200 nm) (schematic representation shown in Figure 2(B)). Various capping agents like polyethyleneimine (PEI), poly vinylpyrrolidone (PVP), polyethylene glycol (PEG) and polyaniline (PANI) etc. are utilized to restrict growth of the nanostructure through stabilization PBNP's surface in the aqueous solution.[13,14] As an example, PVP decreases size of PBNPs. Excess amount of PEG in hydrothermal reaction truncates cubic shape of PBNPs which comprise of eight truncated and six square faces, while less PEG generates cubic shape, implying promotion of meso-crystallization of PEG functionalized PBNPs.[15] Length chain of PEG also effects on the synthesis of PBNPs. As an example, Wu and colleagues have obtained

meso-crystalline pseudo-truncated cubic PBNPs (~ 5 – 6 nm) from a hydrothermal reaction (120°C for 20 hr) using $K_3[Fe(CN)_6]$ and PEG 4000 under acidic environment, while PEG 2000 yields meso-crystalline truncated cubes of smooth as well as curved surface.[16] Qian *et al.* has achieved nanoscale PBNPs from hydrothermal reaction (180 °C for 6 hr) by employing a mixture of ferric ions, hexacyanoferrate(III) ions, sodium acetate, ethylene glycol, PEG 2000, sodium dodecyl sulfonate (SDS) and HCl.[17] Zhang and co-workers also has slightly modified the reaction condition (140 °C for 24 hr) to obtain polyaniline coated PBNPs.[14]

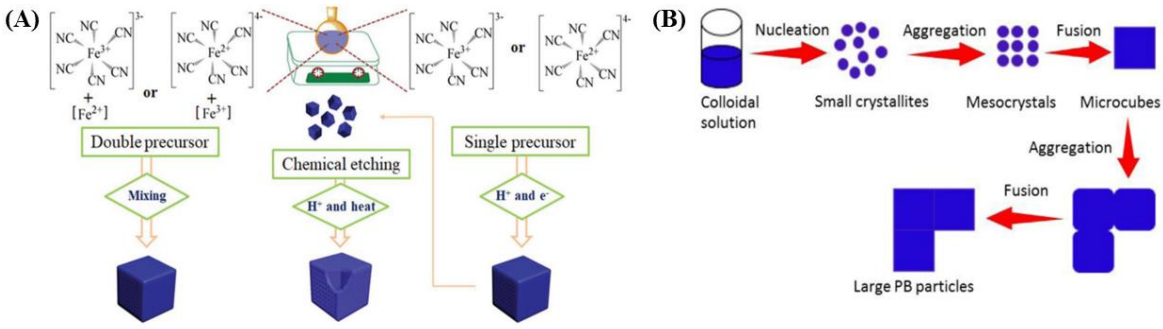

Figure 2: (A) Demonstration of the synthetic pathways of PBNPs. (B) Schematic representation of hydrothermal based growth mechanism for producing sizable PB particles.

In this context, it may be stated that biomedical applications of PBNPs greatly rely on their physicochemical properties wherein considerable efforts have been dedicated to explore innovative synthetic techniques to tune physicochemical properties of PBNPs of desirable characteristics. As an example, magneto-resonance imaging primarily depends on magnetic property of PBNPs which is closely associated with crystallinity. With this in mind, Qin *et al.* has employed a magnetic internal heating method with the help of an alternating current magnetic field to improve crystallinity of PBNPs which consequently benefited longitudinal relaxivity in magneto resonance imaging.[18] In the realm of use of PBNPs as nano-catalytic medicine, enzyme-like activity has got significant importance. In this regard, Komkova et al. has successfully prepared PBNPs by coprecipitation which exhibits much higher peroxidase (POD) property through catalytic activation of H_2O_2.[19]

Chemical etching and template synthesis are also two popular methods for the synthesis of PBNCs. In former technique, hollow PBNCs are obtained from solid PBNCs by selective etching at elevated temperature and acidic condition. In this typical synthesis procedure, Lee and Huh have shown that concentrated HNO_3 plays a pivotal to produce various shapes including truncated cubes, octahedra, and star-like hexapods (shown in Figure 3(A)).[20] The

same research group has performed preferential etching of {111} planes. In this context, Hu and colleagues have developed meso-crystalline PBNC having hollow interior cavity without disintegrating native structure through precise chemical etching by concentrated HCl solution at 140 °C for 4 h wherein polyvinylpyrrolidone (PVP) acts as a capping agent and protects other surfaces from etching. Mostly, H^+ diffuses within meso-crystalline PB through defect-mediated permeation, creates high acidic environment in the inner region, etches faster etching at the center in comparison with exterior region / surface of PBNPs leading formation of hollow cavity.[21] The same group has further developed shell-in-shell hollow PBNPs by manipulating rate of crystal growth under different acidic environment (shown in Figure 3(B)).[22]

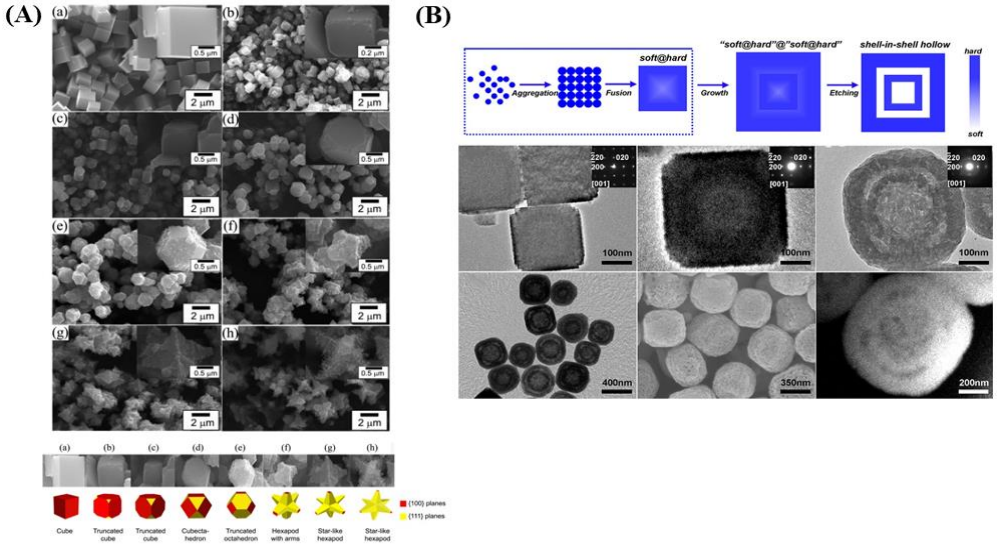

Figure 3: (A) SEM images of PBNPs and their morphological transformation from cubic to star-like hexapods with increasing concentrations of HNO_3 during synthesis. (Copyright 2012. Reproduced with permission from *Bulletin of the Korean Chemical Society*).[20] (B) Schematic representation of development of shell-in-shell FeFe hollow NPs and corresponding TEM images of FeFe NPs, 'soft@hard'@'soft@hard' FeFe NPs and shell-in-shell hollow FeFe NPs. Additionally, Low-magnified TEM image, SEM image and HAADF-STEM image of shell-in-shell hollow FeFe NPs. (Copyright 2013. Reproduced with permission from *American Chemical Society*).[22]

Various sacrificial template strategies have also been employed to generate different hollow nanostructures of PBNPs encompassing nanospheres, nanotubes, nanorods, and nanocubes. For instance, Shen *et al.* has synthesized hollow PBNPs utilizing silver nanostructures as sacrificial templates, wherein reaction facilitates PBNP's shape as per template shape. In general, template is consumed to generate hollow interiors, while blue toning technique is employed for black/white film colorization (shown in Figure 4(A)).[23] Cai *et al.* has employed

bovine serum albumin (BSA) as self-sacrificial templates to fabricate hollow white capsules of PB (shown in Figure 4(B)) which exhibits remarkable intrinsic properties for attenuating Tau-related neurodegeneration.[24] Zhang and colleagues also have synthesized Bi^{3+} assisted hollow PB nanozymes (HPBZs), where Bi^{3+} ions initially lead metastable hollow $BiFe(CN)_6$ intermediate through bonding with $Fe(CN)_6^{3-}$, which subsequently serves as a template for HPB growth (shown in Figure 4(C)).[25] Hu and colleagues have used PVP as a reducing agent to synthesis and control size (~ 20 nm, 100 nm, and 200) of PBNPs using single precursor approach (e.g. $K_3[Fe(CN)_6]$) in acidic environment (HCl), wherein a non-classical crystallization mechanism has been observed.[26] In literature, there are few reports where PB microstructures have been generated through incorporation of ascorbic acid as electron donor into the reaction mixture. Furthermore, graphene oxide, polysaccharides and polyaniline have also been employed as electron donors in the single-precursor based synthesis of PBNPs.[27,28,14] Notable, Cornelissen *et al.* has used non-RNA cowpea green spot virus (CCMV) as templates to prepare mono-dispersed PBNPs of size ~ 18 nm, wherein CCMV capsids are assembled or disassembled depending on pH to encapsulate $[Fe(C_2O_4)_3]_3$ and $[Fe(CN)_6]_3$, thereby generating uniform PBNPs.[29] In this context, it may be stated that hard templates like anodized alumina, mesoporous silica, polystyrene nanospheres, liposomes, apoferritin and carbon nanotubes have also been employed for PBNP synthesis. As their removal typically requires strong acid that shortens lifespan PBNPs in biomedical applications, thus soft templates are preferred due to ease removal under milder conditions.[30] In addition to acid concentration and templates, temperature and reductant are also crucial to generate PBNPs of various size and morphology. In a study, Shen *et al.* has found that hydrothermal reaction temperature < 130°C yields combination of nanocubes and nanospheres, while temperature > 140°C leads only nanospheres.[31] Although both soft and hard template methods yield PBNPs with diverse morphologies but complete template removal possesses challenges, highlighting importance of selecting templates with suitable original morphology and size. Among various approaches, the self-sacrificial template method offers broader applicability, as it reduces damage to the PBNP shell during template removal. Doping in some cases is found to reduce / enhance size of PBNPs. As an example, Shou *et al.* has decreased the size of PBNPs by Zn^{2+} doping, wherein growth kinetics has been found to be changed significantly by doping. They have examined that 10% Zn doping has decreased the size from 38.5 nm to 3.8 nm.[32]

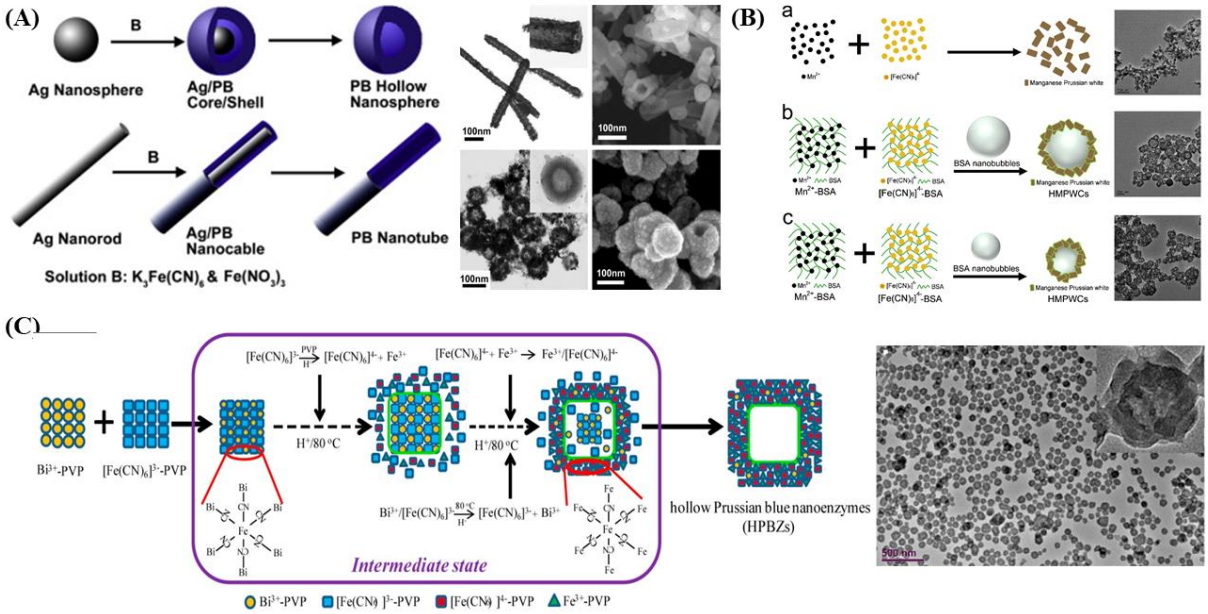

Figure 4: (A) Schematic representation of fabrication process of PB hollow structures from Ag nanostructures using the sacrificial template method. (Copyright 2014. Reproduced with permission from *Journal of Electroanalytical Chemistry, Elsevier*).[23] (B) The influence of BSA on the synthesis of HMPWCs: (a) Without BSA addition, compared to (b-c) where HMPWCs are achieved following BSA addition. (Copyright 2020. Reproduced with permission from *Biomaterials, Elsevier*).[24] (C) Schematic representation of HPBZ development and it's TEM image. (Copyright 2019. Reproduced with permission from *Nano letters, American Chemical Society*).[25]

Another potential method to generate various shapes of PBNPs is the outfield-assisted technique, where nucleation rate, formation and crystallization of PBNPs are controlled throughout the synthesis process through external stimulation. For instance, Hu and colleagues have obtained uniform PBNC by dissociating $K_4[Fe(CN)_6]$ in an acidic environment and ultrasonic condition. In this work, they have regulated size and distribution of the nanocubes by varying concentration of the precursors and reaction temperature.[33] Gu and colleagues have presented a novel method employing an alternating magnetic field to facilitate synthesis of PBNPs through magnetocaloric effect (shown in Figure 5(A)).[34] This innovative synthesis technique has the potency to ensure consistent and homogeneous heating of the reaction mixture, surpassing the conventional external heating and results top-notch PBNPs. Micro-emulsion, regarded as an innovative approach, has enhanced dispersion in comparison to other method involving nucleation, followed by crystal growth. Wang et al. has introduced micro-emulsion peripolymerization (MEPP) technique to prepare nano-shell of PB with controlled

size where metal-organic surfactants are employed to form micro-emulsion droplets followed by coordination polymerization and resulting uniformity in size of PBNPs (shown in Figure 5(B)).[35] In contrast, Vaucher and colleagues have introduced bis(2-ethylhexyl) sulfosuccinate (AOT) as an anion surfactant based reverse micro-emulsion technique wherein $[Fe(C_2O_4)_3]^{3-}$ and $[Fe(CN)_6]_3$ are encapsulated simultaneously for the development of uniform PBNPs.[36] They have noted that $[Fe(C_2O_4)_3]^{3-}$ undergoes a gradual reduction in the presence of daylight and leads formation of Fe^{2+} ions. Subsequently, they react with $[Fe(CN)_6]^{3-}$ in water droplets, giving rise to the generation of numerous nuclei and clusters.

Various methods employed for the synthesis of PBNPs with diverse size and shape are consolidated in Table 1.

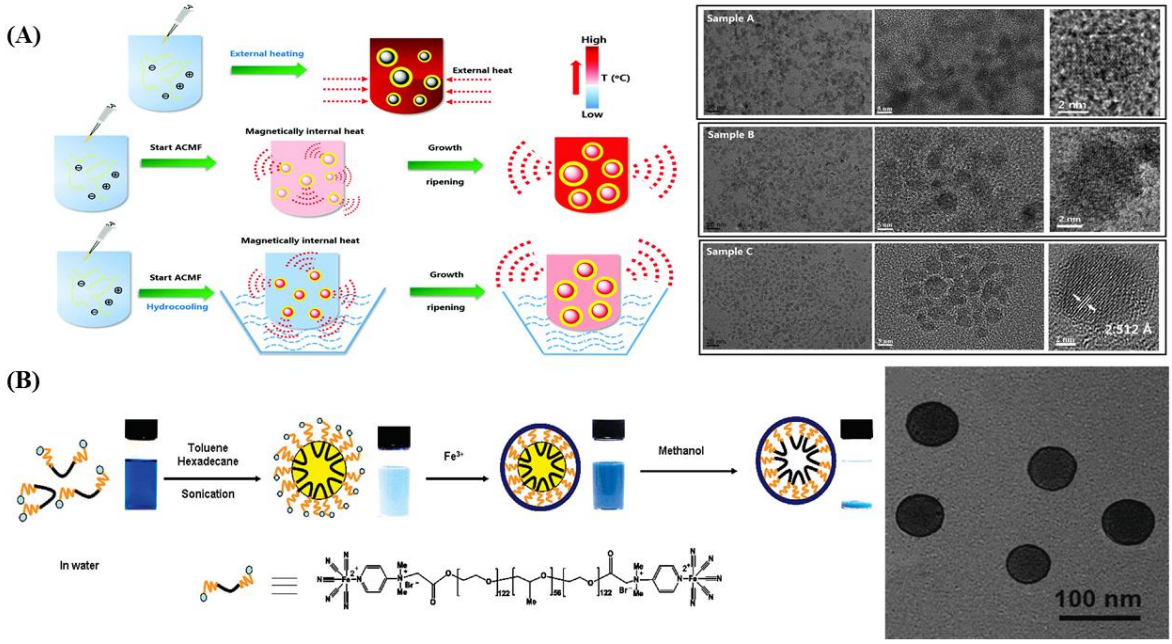

Figure 5: (A) Schematic representation of synthesis of PBNPs in the presence and absence of internal magnetic field and heat. Corresponding SEM and HRTEM images (Copyright 2018. Reproduced with permission from *Nanoscale, RSC*).[34] (B) Schematic illustration of synthesis of PB nanoshells via MEPP technique, alongside corresponding TEM images. (Copyright 2009. Reproduced with permission from *American Chemical Society*).[35]

Table 1: Various synthesis method to develop PBNPs with diverse size and shape

Method	Temperature (°C)	Reaction time	Particle size	Morphology	Ref.
Co-precipitation (Citric acid reduction system)	Room temp.	0.1 hr	20-30 nm	Cubic	37
Co-precipitation (citric acid used as chelator)	60	20 min	8-16 nm	Cubic	38
Co-precipitation (PVP and $K_3[Fe(CN)_6]$)	80	1 day	65 nm	cubic	39
Hydrothermal ($K_3[Fe(CN)_6]$ and glucose)	140	8 hr	60 nm	Nanosheet	40
Hydrothermal (PVP as stabilizers)	60	0.5 hr	70 nm	cubic	41
Hydrothermal (Cd-based PBA)	140	4 hr	80 nm	cubic	42
Hydrothermal method (PEG-4000 assisted)	120	20 hr	5-6 µm	Truncated cubes with smooth faces and curved surfaces	16
Hydrothermal method (Hydrochloric acid was used)	120	24 hr	6-7 µm	octahedron	43
Hydrothermal method (Glucose was used)	120	24 hr	10-20 nm	Microcubes	44
Template Assisted method ($AgNO_3$ as templates)	Room Temp.	30 min	100 nm	nanorods	23
Template assisted method (P4VP stabilized PS templates)	Room temp	-	25 nm	spherical	45
Template assisted method (Sodium dodecyl sulfate-templates)	Calcination:500	3 hr	20 nm	Spherical	46

Template assistated method (Polystyrene-template)	-	10 deposition cycle	400-450 nm	3D macroporous structure	47
Template assisted method (Ni foam as templates)	40	10 hr	150 nm	cubic	48
Reverse micro emulsion	Room temp.	2 days (Photored uction)	16 nm	Smooth, well defined faces cube.	36
Microemulsion (Triton X-100, hexanol, cyclohexane were used)	Room temp	0.5 hr	34 nm	cubic	49
Microemulsion (EPE-Fe, EPE-DMA were used)	Room temp	48 hr	280 nm	cubic	50
Microemulsion (Distilled water and EPE-Py-Fe)	Room temp	72 hr	100-200 nm	Nanoshells	51

2.3 Surface modifications

The major concerns of using bare PBNPs are biocompatibility, physiological stability and adequate blood circulation. The instability can be primarily manifested in the following two aspects: inability for sustain dispersion due to aggregation of small sized PBNPs that causes opsonization effects and eliminates PBNPs from physiological system. Numerous techniques have been employed to stabilize PBNCs under physiological condition which in consequence enhances efficacy in biomedical applications and they are described below.

Polymers: Biocompatible polymers such as chitosan (CS), polyvinyl alcohol (PVA), PEG, PVP, and hyaluronic acid (HA) are well accepted to increase interfacial biocompatibility, target specificity of PBNPs to ensure premature drug release. Various in-situ and post synthesis physiochemical interactions such as hydrophobic, covalent, electrostatic, and Van der Waal's etc. are utilized for these functionalizations. For instance, Schauer *et al.* has prepared monodisperse chitosan@PBNPs (average size ~ 5 – 20 nm) wherein CS plays a crucial role in impeding crystal expansion and subsequent nucleation.[52] In a separate study, Chen and co-workers demonstrated oleylamine and DSPE-PEG (1,2-distearoyl-sn-glycero-3-phosphoethanolamine-N-[carboxy(polyethylene glycol)) based simple strategy for surface modification of insoluble PBNPs having specific potency in cancer treatment.[53] Similarly, Xue

et al. has confirmed significant improvement in biocompatibility of Fe_3O_4@PB nanostructures due to DSPE-PEG functionalization (shown in Figure 6(A)). Their study reveals that hydrophobic portion of PEG facilitates encapsulation of hydrophobic drugs due to hydrophobic interaction.[54] Moreover, Dai and co-workers has prepared HA functionalized PB@quantum dot that helps in targeted PTT guided NIR fluorescence and bimodal MRI. In another work, Fe_3O_4@PB NPs have been synthesized by growing PB shells on Fe_3O_4 cores, followed by polyethyleneimine (PEI) coating. Subsequently, bovine serum albumin (BSA) coated $CuInS_2$-ZnS (ZCIS) quantum dots (BQDs) and HA have been used to more functionalize Fe_3O_4@PB@PEI through coupling reaction between amino group of PEI and carboxyl groups of both BQDs and HA, yielding enhanced stability, biocompatibility, and functionality in Fe_3O_4@PB@PEI@BQDs-HA NPs.[55] In an independent investigation, Zhou and colleagues engineered PBNCs with HA modifications to enable precise NIR mediated photodynamic and photothermal therapy. Their findings showcased that HA not only elevates biocompatibility, stability of colloidal PBNCs, but also increases effective tumor targeting via CD44 receptors (Shown in Figure 6(B)).[56]

Biomolecules: Apart from aforementioned polymers, wide variety of biomolecules, including protein, antibodies, avidin, red blood cells (RBC), albumins have also been attached to the surface of PBNPs to enhance their physiological stability, biocompatibility, targeting. The advent of biomolecules functionalized PBNPs circumvents multi-drug resistant and defeats various biological obstacles such as the reticuloendothelial system, elevated tumor interstitial pressure and intracellular transport mechanisms.[57] For instance, Chen *et al.* developed a novel nanocarrier system (HMPB@RBC) to enhance cancer combination therapy, employing hollow mesoporous PBNPs (HMPB), tagged with RBC membranes. This innovative approach facilitates tremendous potential for revolutionizing cancer treatment, as it exhibits remarkable advancement in stability, immune evasion, and blood retention compared to unmodified HMPB NPs.[58] In a comparable study, researchers successfully engineered RBC membrane coated doxorubicin coated nanocarriers comprising of PB/manganese dioxide nanocomposite (PBMn@DOX@RBC) to extent blood circulation time and achieve efficient photothermal conversion efficiency (η) in the tumor region (shown in Figure 6(C)). Notably, PBMn@DOX@RBC demonstrates a higher temperature (59.6^{o}C) than those treated with PBMn (49.3^{o}C) upon NIR exposure (808 nm; 1.5 W/cm^{-2}; 5 minutes). RBC membrane coating significantly enhanced nanocarrier accumulation at the tumor site, leading to improved synergy of chemo-photothermal effect. Moreover, remarkable biodegradability of RBCs and their

ability to avoid toxic byproduct formation render them highly desirable for enhancing anticancer activity. Their semipermeable cell membranes prevent rapid clearance of encapsulated cargoes, ensuring sustained drug release for prolonged therapeutic effectiveness.[59] Moreover, utilizing antibody-based treatment approaches enables precise recognition of antigens present on tumor cell surfaces.[60,61]. This makes targeted drug therapy in conjugation with multifunctional biologics, a highly promising strategy to overcome systemic and tumor related obstacles in anticancer treatment. Gene therapy has emerged as a revolutionary treatment approach for life-threatening conditions, including cancer. To address this, a versatile PBNP based nanostructure with enhanced magnetic properties was designed, capable of serving both gene therapy and photothermal therapy purposes. The surface modification of PB@Fe_3O_4 nanostructure with chitosan (CS) and plasmid DNA (pDNA) led to remarkable colloidal stability and efficient magnetic targeting capabilities.[62] In a pioneering study, He *et al.* has introduced innovative and sensitive immunosensors for detecting hepatitis B surface antigens. They achieved this by electrodepositing gold NPs onto PBNPs modified glassy carbon electrode. This cost effective and straightforward detection method holds significant value for clinical immunoassays, offering great potential for improving hepatitis B diagnostics.[63] In a similar investigation, researchers employed PBNPs / Au nanoparticles (GNPs), coated with organic polymers, to create an amperometric immunosensor having high sensitivity and selectivity to detect carcinoma antigen 125 (CA125). Primarily, PBNPs are synthesized using CS and poly(diallyldimethylammonium chloride) (PDDA) as protective matrices and then they are directly applied onto the glass carbon electrode surface. In the next step, GNPs are assembled onto the electrode *via* robust binding interactions between amino groups of CS and electrostatic attraction with oppositely charged PDDA. Finally, CA125 antibody (anti-CA125) has been introduced onto the surface of GNPs (Shown in Figure 6(D)). In this context, it may be stated that the incorporation of antibody opens a promising avenue for advanced application in the field of biosensors and biocatalysts.[64]

Core-shell structure: The embedded PBNPs within the protective layers of either organic or inorganic materials have led the scope to obtain stable, biologically compatible core-shell nanocomposites, wherein core of PBNP holds a permeable lattice arrangement, endowing it with the capability to absorb and retain metal ions in order to preserve electrostatic equilibrium. Moreover, PBNPs, coated with one or more functional shells, provide the opportunity of additional functionalization. Notably, PBNPs serve not only as hosts with enhanced stability, but it also offers to deliver other supplementary *via* these core-shell architectures. In a prior

investigation, scientists have formulated Mn^{2+} doped PB analogous (MnPBA) coated with hollow mesoporous PB (HMPB) onto both inner and outer surface to form a core-shell hollow structure (HMPB-Mn). Notably, HMPB-Mn appears to be highly responsiveness to pH, leads release of Mn^{2+} at the specific tumor site and serves as an intelligent T_1-weighted MRI CA. Furthermore, distinctive hollow structure and substantial surface area provide high DOX loading capacity. It has been identified that Mn^{2+} ions and DOX can be simultaneously released from the synthesized HMPB-Mn under acidic pH.[65] In a separate investigation, Chang and colleagues effectively have constructed PB@Fe_3O_4 core-shell nanostructure utilizing a straightforward single-step synthesis approach. The nanostructure not only retained it's magnetic properties but also displayed excellent water dispersibility and remarkable efficiency in removing Cs^+ ions. These core-shell nanostructures hold promise for utilization in the realms of biomedical exploration and diagnostics.[66] Moreover, Avidin-modified biofunctionalized PB core-shell structure not only retained their physical stability but also exhibited MR and Mn^{2+} fluorescence-based imaging properties.[67]

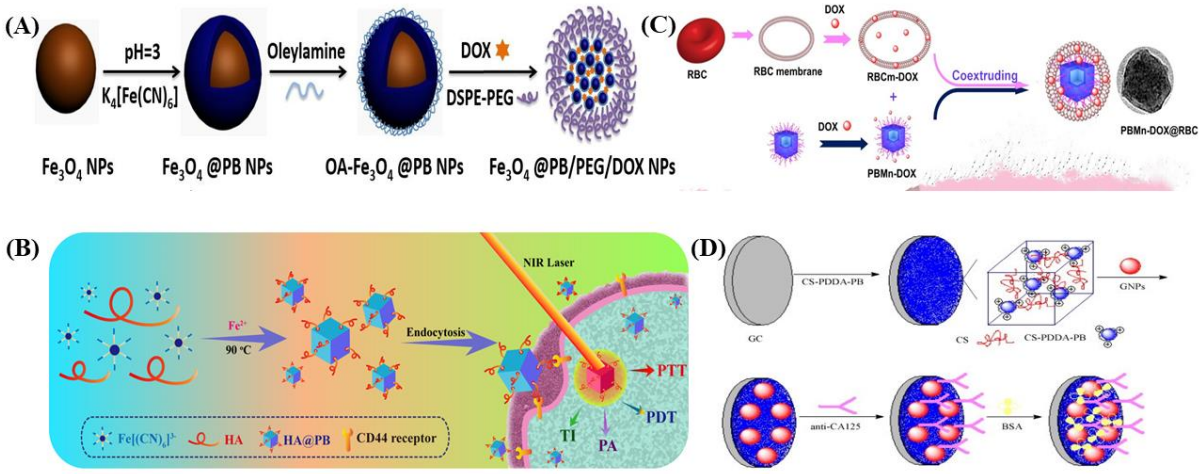

Figure 6: Schematic representation of (A) development of Fe_3O_4@PB@PEG@DOX nanocomposite (Copyright 2018. Reproduced with permission from *Journal of colloid and interface science, Elsevier*).[54] (B) Fabrication of HA@PB and their targeted multimodal theranostic application (Copyright 2018. Reproduced with permission from *ACS applied materials & interfaces*).[56] (C) Creation of a PBMn–DOX@RBC Nanocarrier (Copyright 2017. Reproduced with permission from *ACS applied materials & interfaces*).[59] (D) the preparation of PDDA and chitosan based immunosensor (Copyright 2008. Reproduced with permission from *Sensors and Actuators B: Chemical*).[64]

Inorganic Materials: Inorganic materials exhibit various properties including magnetic moment (manganese, iron oxide or cobalt oxide NPs), high electron density and strong light absorption coefficient (silver and gold NPs), hence surface modification of PBNPs with these inorganic materials allows to alter charges and functional groups, thereby stability, compatibility, and biological efficacy of PB get improved. As example, hydrophilic coating with carbon nanomaterials enhances water dispersibility, stability and shields magnetic core from oxidation.[68] Recently, PB@RGO nanocomposite has emerged as non-enzymatic H_2O_2 sensor. Glassy carbon electrode (GCE) underwent covalent interaction with GO and serves as a platform for in-situ production of electroactive PB.[69] Similarly, Fe_3O_4 NPs exhibit biocompatibility, cost-effectiveness and scalability, hence they are promising for applications in both biomedical and chemical domains. However, their susceptibility to oxidation leads to instability, altering magnetic properties and catalytic performance. Various studies have employed a shell-growing technique to immobilize PBNPs onto Fe_3O_4 nanocores, introducing ferrous ions to enhance catalytic reactions and bio-detection capabilities.[70] In addition, owing to the intriguing characteristics of Au NPs including surface enhanced Raman scattering and LSPR, they emerge as prime candidates for incorporation in biomedical and electrochemical devices such as the nanoelectrode, pressure sensors and DNA detector. In this context, Au capped PB@Au core-satellite structure has been innovated to facilitate multimodal diagnostic and therapy.[71] In a recent study, a novel electrochemical immunosensors has been developed for the detection of alfa-fetoprotein using Au NPs based nanocomposite which contains polydopamine and PB-carbon nanotube. This immunosensors exhibits remarkable detection capabilities within a concentration span of 0.005 to 80 ng/mL.[72] In summary, surface modifications with various innovative inorganic materials emerge as a strategy to mitigate drug resistance, amplify biocompatibility, and optimize the biodistribution and drug delivery efficiency of NPs.

2.4 Biomedical applications:

2.4.1 Cancer therapeutic applications

Regrettably, due to the diverse and varied nature of cancer, there are no completely comprehensive approaches available for its treatment. The existing treatments are primarily restricted to surgery, radiation therapy, chemotherapy, targeted therapy and immunotherapy. While these therapies can be effective, they also have certain limitations. Surgery can be curative for some cancers but is not always possible, especially if the cancer has spread to other

parts of the body. Radiation therapy can damage healthy tissue and may cause long-term side effects while chemotherapy causes hair loss, nausea and fatigue, and may not be effective for some types of cancer.[73,74] NPs can be engineered to specifically target cancer cells, as they can be designed to recognize and bind to unique features of cancer cells such as overexpressed receptors or specific proteins. Once these NPs have been delivered to cancer cells, either they can be used as a monotherapeutic agent like PTT and PDT or to deliver other therapeutic agents such as chemotherapeutic drugs or other molecules that can induce cell death or inhibit cancer cell growth via heat generation or free radicals. Herein, PBNPs have superior properties compared to other NPs, such as strong accumulation rates and NIR absorption properties, greater biocompatibility, and simple surface chemistry. The size and shape of PBNPs have a profound effect on their NIR (700-1000 nm) absorption property. When exposed to NIR light, the absorbed energy can be transformed into heat energy that can harm cancer cells through localized hyperthermia, known as PTT, or accelerated to discharge the enclosed drug. Moreover, PBNPs with different shapes can be tailored to achieve different optical and physicochemical properties, which can be optimized for specific PDT applications via ROS generation. This versatility and tunability make PBNPs with different shapes promising candidates for third generation photosensitizers in PDT. Combining PTT with PDT/chemotherapy can increase targeted drug accumulation and overcome resistance to hyperthermia. However, PBNPs have the potential to improve cancer therapy by enhancing drug efficacy, reducing systemic toxicity, and allowing for targeted delivery, PDT and localized hyperthermia.

2.4.1.1Photothermal Therapy

PTT is a definite form of hyperthermia, a noninvasive approach of heat abscission where incident light energy converted into localized heat within the biological tissue, used to destroy pathologic cells. PTT is specifically used in targeted cancer treatment with the assistant of near infrared (NIR) active, biocompatible nanoagent at a high tissue penetration depth and with very minimal impairment to nearby non-labelled normal cells. Selective thermal ablation of cancer offers an exceptional strategy to the patients who suffers from the complication of traditionally used therapies like chemo and radio therapy due to lack of specificity.

Generally, PTT occurs in three elementary modes such as: (a) with only light, (b) light in the presence of endogenous molecules that converts light to heat energy and (c) light in the presence exogenous metal nanoagent for selective PTT with enhanced performance.[75] These

nanoagents are designed in such a way that they can absorb the incident photons (NIR range) and transfer the energy to the electron on the surface. This causes the electrons to oscillate and convert the incident energy into heat with high conversion efficiency and confine hyperthermia in abnormal cells. Thus the third approach is most effective than others in terms of selective cancer treatment by heat generation in the presence of photosensitizing agent.

Mechanism of PTT:

- **Laser tissue interaction and heat generation:**

Heat can be generated through the interaction between incident laser light (photon particle) and tissue that can be explained in a macroscopic or microscopic level. In microscopic level, a molecule within the tissue is excited after absorbing the incident photon energy and subsequently decayed to the equilibrium state after transferring the energy to other molecule /atom /electron through inelastic collision. The total energy of the second molecule represents it's enhanced thermal vibration and as a consequence microscopic temperature enhancement has been observed.

In macroscopic level, laser propagation in the tissue plays a vital role for laser-tissue interaction and heat generation. In general, the incident laser beam is subjected to reflection and penetration in the tissue. A part of the penetrated light is absorbed and other part is scattered which are characterized by absorption (μ_a) and scattering (μ_s) coefficient. These two coefficients are tissue specific and highly depend on the laser properties like wavelength, power density. So, herein total heat loss can be expressed as-

$$Q(r,z) = (\mu_a + \mu_s)I(z) \qquad (1)$$

Where, $I(z)$ is the laser beam intensity at a propagation length z.

- **PTT with the assistant of nanoagent:**

The mechanistic behaviour of heat generation through nonradiative transition for organic nanoagent is different from traditionally used inorganic nanoagents like different metals and semiconductor type nanoparticles which are associated with surface plasmon resonance. In general, nanomaterials are first stimulated to an excited state under laser exposure and then decayed via three processes i.e. (i) fluorescence, (ii) intersystem crossing and (iii) nonradiative relaxation.[76] In nonradiative transition nanomaterials decay to the ground state via transmitting energy through vibrational state while first two pathways related to photon emission (shown in

Figure 7). First two relaxation pathways must be efficiently reduced in a designed nanoparticle in order to improve photothermal conversion efficiency. In this context, ozturk and co-worker designed a molecular sensitizer stacked conjugated polymer which shows improved heat generation via nonradiative relaxation pathway followed by it's fluorescence quenching property.[77] The NP induced temperature enhancement at the tumor site specifically depends on power density of laser, photothermal conversion efficiency and concentration of accumulated NPs. Herein, NIR active NPs are more acceptable as it penetrates more deeply into biological tissue than visible light.

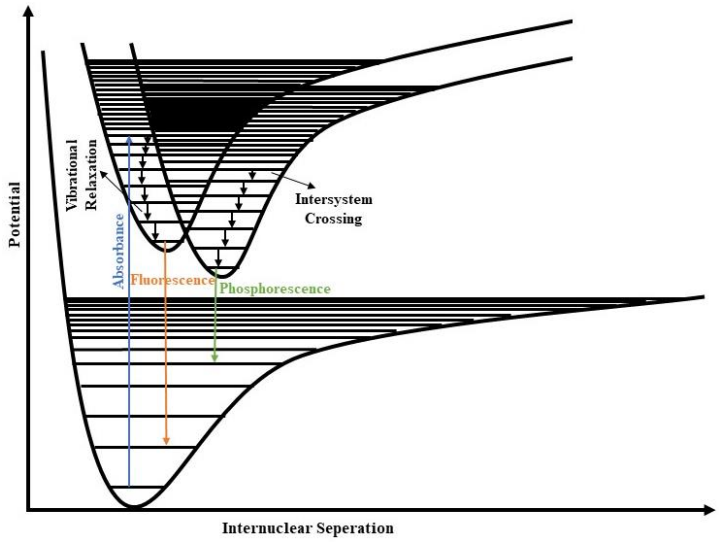

Figure 7: Energy release mechanism through vibrational state.

PBNPs as a PTT agent:

Owing to ability to absorb light in the NIR range through charge transfer between Fe^{3+} to Fe^{2+} via cyanide bridge, PBNPs have been explored as innovative agent for laser-guided tumor ablation during PTT (Table 2). This technique holds great promise in targeted tumor treatment, as the laser can be accurately regulated. In PTT, the employed laser wavelength is carefully chosen within the "tissue optical window" (600-1300 nm) to absorb by healthy tissue which prevents any unwarranted temperature rise in healthy cells. In this context, PBNPs revealed considerably greater molar extinction coefficient (1.09×10^9 M^{-1} cm^{-1}; 808 nm) compared to conventional photothermal (PT) agent like $Cu_{2-x}Se$ (7.7×10^7 M^{-1} cm^{-1}; 808 nm) and carbon nanotubes (7.9×10^6 M^{-1} cm^{-1};808 nm) which endows PBNPs with a remarkable light-to-heat conversion efficiency. Furthermore, PBNPs exhibit exceptional photostability and excellent dispersibility in both aqueous and biological mimic environments. As a result, PBNPs have gained widespread recognition as a potent agent for photothermal ablation in disease treatment.

For instance, Fu and colleagues pioneered the utilization of PBNPs in cancer therapy, employing an 808 nm laser for the first time.[78] The study demonstrated that the temperature could be raised in the treated cancer cells to a critical threshold of 43 °C under irradiation of laser for a duration of 3 minutes even at a low concentration of 500 ppm. Similarly, Hoffman and team used PBNPs as a PT agent against *in-vitro* cancer treatment with η value of approximately 20.5% under 808 nm laser irradiation.[79] In an another study, Cheng et al. successfully developed PEG-functionalized PBNPs, measuring an average size of 60 nm (Shown in Figure 8(A)). The utilization of PEG coating on the surface of PBNPs not only enhanced their physiological stability but also facilitated their preferential accumulation within tumor tissues, leading to a notable improvement in the photothermal effect. The remarkable efficacy observed during *in-vivo* therapy demonstrated that the injection of PBNPs followed by laser irradiation resulted in complete tumor ablation (temp rise ~ 60 °C), considerably prolonging the survival rate.[80] These exceptional findings firmly establish PBNPs as an outstanding candidate for photothermal nanomaterial, showcasing their immense potential for advancing tumor photothermal therapy.

The effectiveness of PTT is contingent upon various factors, including the concentration, morphology, size, surface modification and chemical composition of NPs. Additionally, external factors such as laser power and irradiation time can also exert a significant influence on the overall treatment efficiency.[81] Indeed, Li and colleagues devised a straightforward approach to confer PB nanocubes with tunable localized surface plasmon resonance (LSPR) and heightened PTT efficiency through the in-situ doping of platinum (Pt) NPs onto PB nanocubes. Their findings demonstrated that the coordination of Pt with cyanide in Pt doped PB nanocubes not only reduced the occurrence of $[Fe(CN)_6]$ vacancy but also expanded the routes for electron transitions, resulting in the red shift of absorption peak and an overall improvement in PTT efficiency (shown in Figure 8(B)).[82] Moreover, functional substances like genes, peptides, antibodies and other functional molecules can be attached with PBNPs to enhance their PTT efficiency. In an enlightening study, Li and colleagues developed glypican-3 antibody functionalized PBNPs (antiGPC3-PBNPs) which exhibited selective delivery to the tumor tissue and enhanced *in-vitro* PTT efficiency.[83] Hollow PBNPs exhibit a remarkable effectiveness in PTT, boasting an exceptional η value of 41.4%. Additionally, they possess a significant molar extinction coefficient of 1.2×10^{11} M^{-1} cm^{-1} when exposed to an 808 nm laser (shown in Figure 8(C)).[84] In order to further enhance the η value, Yu et al. devised a novel strategy involving the development of a core-shell nanostructure containing $NaNdF_4$@PBNP

where an enhanced PTT performance was observed through cross relaxation pathway.[85] They also observed that the nanocomposites achieved an impressive tumor inhibition rate of 76.7% under 808 nm laser irradiation in comparison with the individual efficacy of PBNP (18.8%) and $NaNdF_4$ (14%).

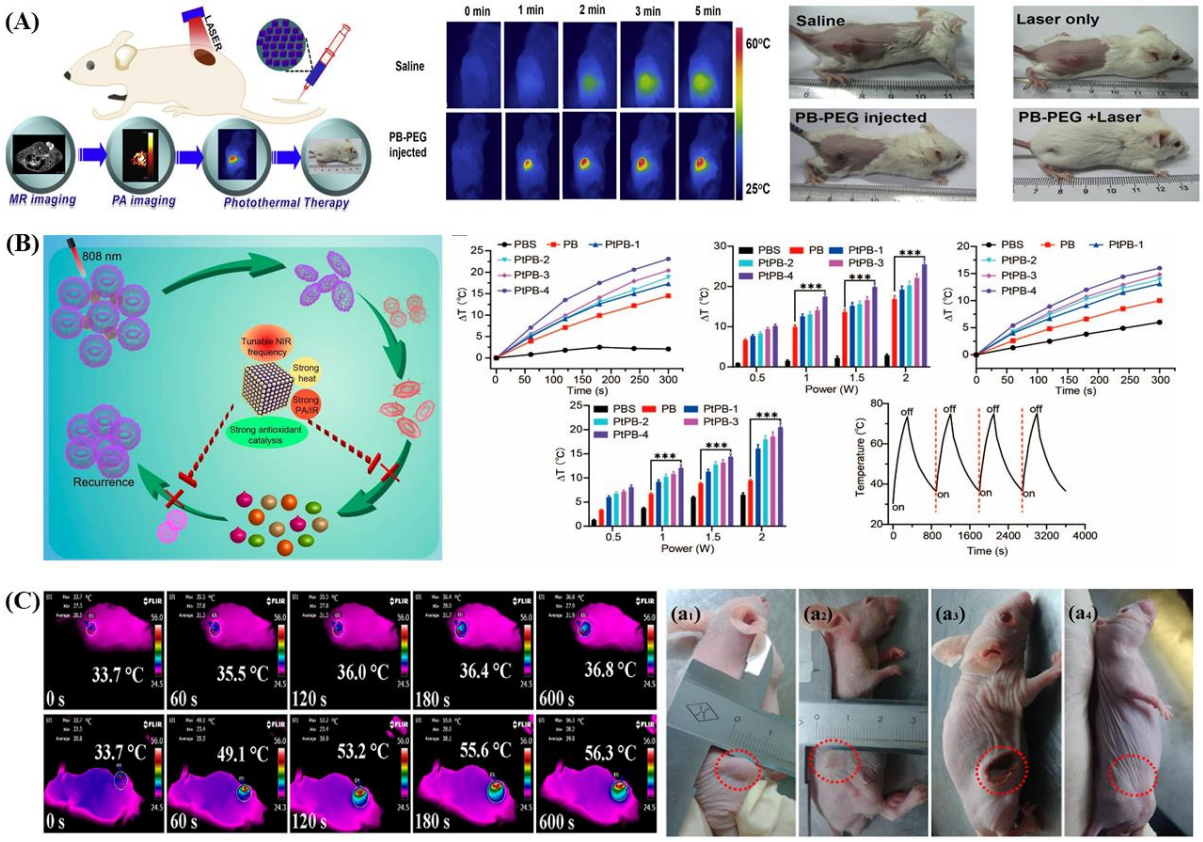

Figure 8: (A) Schematic illustration of PBNPs used for PTT and bimodal imaging; it's efficiency in *in-vivo* PTT. (Copyright 2014. Reproduced with permission from *Biomaterials, Elsevier*).[80] (B) Schematic representation of PtPB nanoenzyme-mediated imaging-guided PTT with relief of inflammation and it's *in-vitro* PTT efficiency (Copyright 2014. Reproduced with permission from *ACS nano*).[82] (C) Thermal infrared camera images of control group and the treatment group at various time points post-irradiation. Additionally, digital photographs of nude mouse tumor (marked with a red dotted circle) throughout the entire therapeutic process: (a1) before therapy, (a2) after laser irradiation, (a3) on the second day after laser irradiation, and (a4) one month after laser irradiation. (Copyright 2015. Reproduced with permission from *ACS applied materials & interfaces*).[84]

Table 2: Photothermal therapeutic efficiency of PB based nanocomposite under laser exposure

Photothermal agent	Incident laser (808 nm) (W/cm^2)	Conversion Efficiency (η) (%)	Max. Temp. (°C)	Ref.
PB @PMO	1	20.4	80.2 (5 min)	86
PEGylated PB	0.8	36.7	64.1 (5 min)	80
CpG coated PB	1.5	20.5	60 (5 min)	87
PLGA–PB–PTX–PEG–FA	0.647	36.1	60-70 (10 min)	88
HA@RBC@PB@CS-6 NPs	1	23.1	56 (5 min)	89
PB@PDA@PEG-FA	2	45.8	53.5 (10 min)	90
$NaNdF_4$@PB	0.6	60.8	40 (10 min)	85
$NaDyF_4$: 50% Lu@PB	1.33	50.7	58.5 (10 min)	91
Fe_3O_4@GdPB	1.875	16.1	~70 (10 min)	92
HA@PB	1	35	30 (10 min)	93
PB:Mn(15%)-PEG	0.8	20	55 (5 min)	94
Zn (10%) doped PB	1.2	47.3	42 (5 min)	95
Fe_3O_4@PB@PDA/AlPc/BSA	1.32	22.3	40 (10 min)	96
Au@PB	0.8	44	57 (5 min)	97

2.4.1.2Photodynamic therapy (PDT)

PDT is a medical treatment that uses photosensitizing agents and light to destroy cancer cells and treat various medical conditions, such as skin disorders, macular degeneration, and precancerous lesions. PDT involves administering a photosensitizing agent to the patient, which is then activated by a specific wavelength of light to produce a toxic form of oxygen that destroys the targeted cells. The photosensitizing agent is typically a drug that is administered either orally or intravenously. The agent is absorbed by cells throughout the body, but it is retained for a longer period of time by cancer cells and other abnormal cells. Once the agent has been given time to distribute throughout the body, a specific wavelength of light is applied

to the affected area, activating the agent and causing the release of reactive oxygen species (ROS), which can damage or destroy cells. It has great potential in targeted cancer therapy with good therapeutic efficiency, minor injury, remote controllability, as well as low systemic toxicity. It has been shown to be effective in treating a range of conditions, including skin cancer, esophageal cancer, and lung cancer. However, PDT may cause side effects, such as redness, swelling, and blistering, depending on the location and severity of the treated area.[98]

Mechanism of PDT

PDT is another kind of photo assisted therapeutic approach involving laser irradiation and photosensitizing agent, used to generate reactive oxygen and nitrogen oxygen spices like hydroxyl radicals ($^{\cdot}OH$), superoxide ($O_2^{\cdot-}$), singlet Oxygen ($^1O_2$), nitric oxide ($^{\cdot}NO$), nitrogen dioxide ($^{\cdot}NO_2$) etc. to elicit cancer cell death. Among them $^1O_2$ has strong oxidizing properties and it can persist for $10^{-6} – 10^{-3}$ s in solution and about an hour in gaseous state.[99] PDT involves NP as a photosensitizer (PS) which transfer the absorbed optical energy (particularly NIR light) to the molecular oxygen, generating cytotoxic ROS and RNS to kill the cancer cell. A comprehensive analysis of the photochemical mechanisms involved in PDT is presented in Figure 9(a). Upon absorbing a photon of the appropriate wavelength, PS becomes activated from its ground state (S_0) to either the first singlet excited state (S_1) or the second singlet excited state (S_2). S_2 (life span ~ fs) rapidly undergoes internal conversion (IC) to decay to S_1, which can either produce heat or cease releasing light (i.e. fluorescence) during IC due to its unstable nature and short lifespan at the nanosecond level. S_1 may undergo intersystem crossing (ISC), resulting in the formation of a more stable excited triplet state (T_1) (extended life span ~ μs), which is capable of undergoing multiple photochemical processes. For instance, T_1 can transfer energy to O_2 to create $^1O_2$, which is considered as the type-II PDT process. Additionally, T_1 can produce various radicals by reacting with intracellular substrates like proteins, nucleic acids and lipids through an electron transfer process. These radicals can then interact with O_2 or H_2O to generate more ROS such as $O_2^{\cdot-}$ and $^{\cdot}OH$, which is referred to as type-I PDT process. Moreover, semiconductor nanomaterials can generate electron-hole pairs under illumination, and the resulting separated electrons and holes can react with O_2 or H_2O to create ROS such as $O_2^{\cdot-}$ and $^{\cdot}OH$. A recent discovery has identified a new process for ROS production through heat-induced thermionic emission of electrons which interact with the surroundings to create ROS. The various processes for generation of ROS and RONS is explained below (shown in Figure 9(b))-

$$MO + h\nu \longrightarrow e^-_{CB} + h^+_{VB}$$

Photoinduced electrons mediated process

$(O_2)_{ads} + e^-_{CB} \longrightarrow O_2^{\cdot -}$

Dismutation Of $O_2^{\cdot -}$ produces H_2O_2

$2H^+ + 2O_2^{\cdot -} \longrightarrow H_2O_2 + O_2$

$H_2O_2 + e^- \longrightarrow OH^- + \cdot OH$

Photoinduced holes mediated process

$h^+ + (H_2O)_{ads} \longrightarrow h^+ + (H^+ + OH^-)_{ads} \downarrow \cdot OH + H^+$

$h^+ + O_2^{\cdot -} \longrightarrow {}^1O_2$

$O_2^{\cdot -}$ Induce secondary generation of $\cdot OH$

$O_2^{\cdot -} + H_2O \longrightarrow \cdot HO_2 + OH^-$

$\cdot HO_2 + \cdot HO_2 \longrightarrow H_2O_2 + O_2$

$H_2O_2 + O_2^{\cdot -} \longrightarrow O_2 + \cdot OH + OH^-$

Fenton equation:

$Fe^{2+} + H_2O_2 \longrightarrow Fe^{3+} + \cdot OH + OH^-$

$Fe^{3+} + H_2O_2 \longrightarrow Fe^{2+} + \cdot OOH + H^+$

Furthermore, research has demonstrated that specific organic compounds possessing extensive π-conjugated structures can retain $^1O_2$ by producing endoperoxide at low temperatures. In contrast, when exposed to high temperatures, the accumulated $^1O_2$ can be released to eradicate cancerous cells.[100] In this context, it can be stated that the main disadvantage of PSs used for treatment, such as those derived from phthalocyanine and porphyrin, is their absorption band in the UV-visible region where tissues receive minimal light and contain high photo-bleaching effect. To address this, researchers have focused on developing new types of PSs, activated by NIR light, which can penetrate deeper into tissues with lower photobleaching and phototoxicity effect. However, most organic PSs with significant absorbance in NIR range display hydrophobic nature, resulting to agglomeration and reduced $^1O_2$ generation in aqueous medium [108]. To overcome this issue, researchers have developed a two-photon excitation (TPE) technique that uses a NIR-pulsed laser as an excitation source. To achieve instantaneous absorption, the energy source for TPE should be a fast laser pulse (approximately 100 fs) with high intensity. By absorbing two photons, this method can excite electron of a PS from its ground state to an excited electronic state, which leads to the abolish of cancer cells followed by type-I or type-II procedures. TPE PDT offers superior spatial resolution in fluorescence imaging and more accurate phototherapy compared to conventional single-photon excitation

(SPE) PDT. Moreover, it can treat deeper tumors as NIR lasers can penetrate materials more deeply than visible or UV light. Additionally, upconversion nanoparticles (UCNPs) can absorb numerous photons, producing high-energy anti-Stokes fluorescence due to the extended lifespan and energy levels of lanthanide ions.[101]

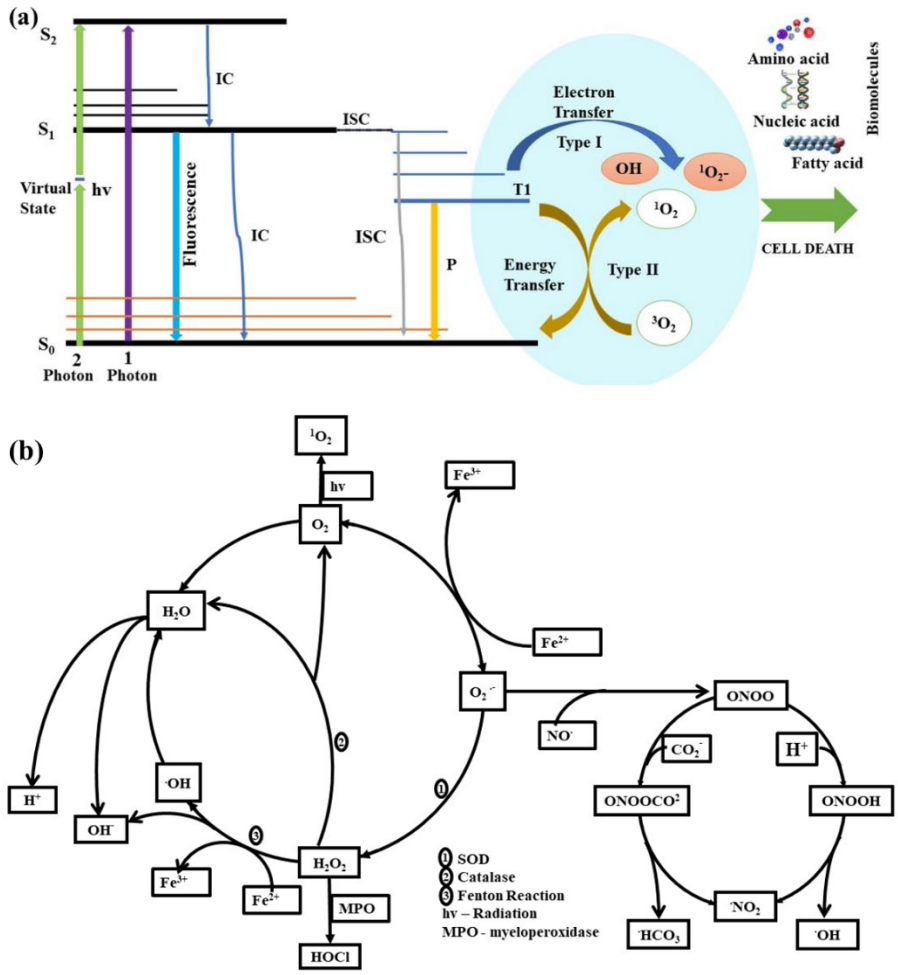

Figure 9: (a) Jablonski enegy level diagram for ROS generation. (b) The various processes for generation of ROS and RONS.

PBNPs as a PDT agent:

PDT is another kind of photo assisted therapeutic approach involving laser irradiation and photosensitizing agent, used to generate ROS and RNOS like hydroxyl radicals ($\cdot OH$), superoxide ($O_2^{\cdot -}$), singlet Oxygen ($^1O_2$), nitric oxide ($\cdot NO$), nitrogen dioxide ($\cdot NO_2$) etc. to elicit cancer cell death. Among them $^1O_2$ has strong oxidizing properties and it can persist for 10^{-6} – 10^{-3} s in solution and about an hour in gaseous state. In contrast to conventional approaches like chemotherapy and surgery, PDT offers distinct benefits including diminished invasiveness and minimized side effects. It boasts exceptional selectivity, impressive curative effects and holds substantial potential for clinical applications. For instance, Zhou and colleagues have

recently published a study showcasing their findings on the remarkable capabilities of HA modified prussian blue nanocubes (HA@PBNC) on cancer theranostic applications. According to them, these nanoplatform exhibited exceptional proficiency in generating $^1O_2$ and demonstrated remarkable photothermal conversion efficiency when exposed to NIR irradiation. Their investigations by both *in-vitro* and *in-vivo* studies confirmed that this multifunctional nanoplatform not only possessed the ability to destroy CD44 overexpressed cancer cells but also effectively impedes tumor growth which was primarily attributed to the synergistic effect of PTT and PDT, bolstered by target specificity (shown in Figure 10(A)).[56] However, the effectiveness of this therapeutic approach is constrained by solid tumor hypoxia, resulting from tumor rapid growth and abnormal tumor blood vessels which accelerate the therapeutic resistance and facilitate tumor progression.[102] Hence, mitigating hypoxia emerges as a crucial focus in tumor treatment. Recent studies indicate that PBNPs can mimic catalase like behaviour, effectively catalyzing H_2O_2 in tumor microenvironment (~50-100 μM) and accelerating O_2 production. This remarkable capability of PBNPs serve to significantly enhance the efficiency of PDT.[103] In their study, Wang and colleagues engineered PEG functionalized mesoporous silica coated PBNPs equipped with zinc phthalocyanine (PSP@ZnPc) for improved PDT followed by endogenous O_2 generation. Initially, PBNPs catalyzed H_2O_2 in the tumor microenvironment to produce O_2. Subsequently, ZnPc converted O_2 into $^1O_2$ when exposed to 671 nm light. Ultimately, they substantiated that the ROS generation through a solitary laser application could effectively mitigate tumor hypoxia, leading to a substantial improvement in the therapeutic efficacy of PDT.[104] To mitigate the DNA damage caused by oxidative stress, cancerous cells respond to ROS assaults by initiating DNA repair mechanisms. One such mechanism involves the activation of mutt homologue 1 (MTH1), a nucleotide pool sanitizing enzyme. Unfortunately, this adaptive response significantly curtails the therapeutic effectiveness of PDT. Importantly, TH287 has the ability to hinder the activity of MTH1 and accelerate the DNA damage caused by oxidative stress. In their study, Hu et al. developed mesoporous organosilica-coated PBNPs, loaded with a photosensitizer tetraphenylporphyrin zinc (Zn-Por) along with TH287. Within these nanocomposite PBNPs facilitated the O_2 supply while Zn-Por produced $^1O_2$ from O_2 under 660 nm laser irradiation, intensifying the oxidative damage inflicted on tumor cells. Simultaneously, TH287 inhibited the repair of MTH1-mediated damage, thereby augmenting the oxidative damage leading to enhanced cell death during PDT (shown in Figure 10(B)).

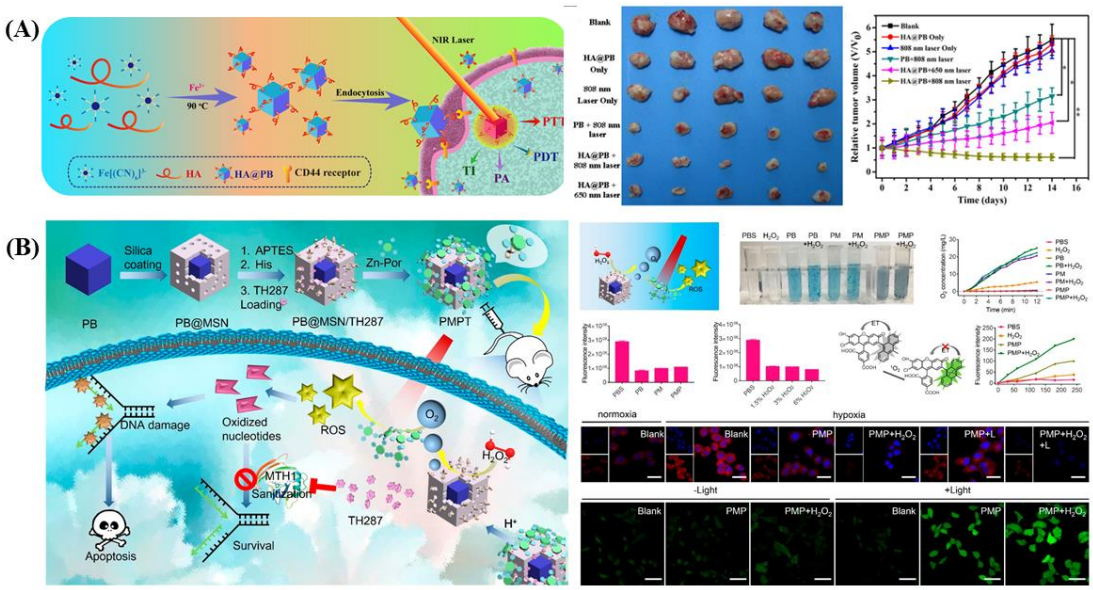

Figure 10: (A) Schematic Illustration of development of HA@PB and it's targeted phototherapy and dual-modal imaging. Corresponding *in-vivo* phototherapeutic study; Photographs of tumor tissues and growth rates of tumor after being treated by various methods. (Copyright 2018. Reproduced with permission from *ACS applied materials & interfaces*).[56] (B) Schematic illustration of enhancement of oxidative damage with improved PDT processes and MTH 1 inhibition for tumor therapy; it's *in-vitro* therapeutic efficiency (Copyright 2019. Reproduced with permission from *Nano Letters, ACS*).[105]

2.4.1.3 PBNPs as a drug delivery agent

PBNPs presents an innovative and promising avenue in drug delivery, owing to its inherent features that ensure stability in the bloodstream, compatibility with living organisms, minimal cytotoxicity to cells, biodegradability, affordability, easy preparation, tunable size and shape. These distinctive features make them well-suited for fulfilling diverse drug delivery requirements including high drug loading efficiency and precise targeting. Over the past few decades, PBNPs based drug delivery system have witnessed significant advancement in cancer and infection disease.[106] They have also demonstrated their ability to enhance the therapeutic effectiveness, diminish systemic toxicity and facilitate target specificity after surface modification.

Regarding the drug delivery, there exist two approaches to meet the demands for loading drug onto PBNPs (shown in Figure 11(A)). One strategy involves creating hollow mesoporous PBNPs (HMPBNPs) to enhance the surface area, resulting enhancement of drug loading capacity. For instance, Chen et al. developed a NIR responsive co-delivery system

(PCM@HMPBNs) using 1-tetradecanol as a phase change molecule (PCM) and HMPBNPs. The development of this arrangement simply entailed filling the hollow mesoporous shell with PCM which functioned as both thermosensitive gatekeeper and a carrier for encapsulation of both hydrophilic doxorubicin and hydrophobic camptothecin drugs. The HMPBNPs exhibited PTT effect under NIR exposure, causing the PCM to melt and escaped from the pore, consequently releasing the enclosed drugs into surrounding medium. The synthesized PCM@drugs@HMPBNs arrangement exhibited minimal release of both drugs while enabled precise drug delivery activation or deactivation through different NIR light treatments to effectively induce cellular apoptosis against HeLa cancer cells.[107] However, the shallow extent of tissue penetration poses a constraint on the effectiveness of anti-cancer drugs. The application of losartan enables the degradation of extracellular matrices and facilitates the permeation of PBNPs. In an innovative approach, Zhang and colleagues encapsulated both losartan and DOX within HMPBNPs to enhance the penetration of tumor tissues. By applying this concurrent encapsulation technique, they achieved a profound tissue penetration, thereby greatly improved DOX efficiency (Shown in Figure 11(B)).[108]

Regrettably, as mentioned previously, unmodified HMPBNPs have a tendency to be eliminated by the immune system and release the drug prematurely, resulting in diminished therapeutic effectiveness and heightened toxic side effects. Recent findings indicate that grafting HA onto PEG-coated HMPBNPs loading with 10-hydroxycamptothecin enhances their colloidal stability, prolongs circulation time in the bloodstream and improves their target specificity.[109] Nonetheless, while PEGylation offers some protection against nonspecific protein adsorption, it falls short in completely preventing it, especially when longer-chain PEGs exhibit heightened hydrophobic properties.[110] In addition, PEGs can trigger an immune response by generating anti-immunoglobulin M antibodies.[111] To enhance immune evasion, researchers developed RBC membrane-coated HMPBNPs encapsulating with DOX, achieving a drug loading capacity of 130%. Both *in-vitro* and *in-vivo* experiments demonstrated that this system exhibited minimal toxicity and showcased excellent synergistic photothermal-chemotherapy for cancer treatment.[58]

An alternative strategy for enhancing drug carrying potential of PBNPs involves surface modification using organic or inorganic substances, as well as alternative cell membrane and metal-organic frameworks (MOFs). Peng et al. developed gelatin stabilized PBNPs conjugated with DOX for synergistic PTT and chemotherapy.[112] Moreover, MOFs hold great potential as promising candidate for integrated cancer treatment involving simultaneous diagnosis and

therapy, owing to their substantial porosity, tunable functionality and large surface area. In a recent investigation, Wang et al. engineered a core-shell nanostructure composed of ZIF-8 coated PBNPs, encapsulating with DOX that demonstrated multifunctional capabilities as both imaging agent for MRI and FOI, as well as a therapeutic agent for photothermal and chemotherapy treatments. The researchers unveiled the nanostructure's capability to respond to dual stimuli (pH and NIR), resulting in controlled drug release. Notably *in-vivo* study showcased that the nanocomposite exhibited a remarkable enhancement in anti-tumor efficacy under NIR irradiation, with a 7.16 and 5.07-fold increase compared to solo chemotherapy and thermal therapy respectively.[113] To enhance drug loading capacity and extend blood circulation time, Liu et al. formulated HA@RBC@PB@CS-6 (HRPC) nanocomposite for targeted delivery of CS-6 at the tumor site. The incorporation of RBC membrane into PBNPs extended blood circulation time significantly to 10 hr, resulting a notable improvement by 60% in immune evasion capabilities.[114]

Both of these loading approaches possess their own advantages. The procedure for fabricating drug encapsulated HPBNPs is simple and adaptable, yet lacks industrial viability. On the other hand, PBNPs with surface modifications offer numerous benefits, including substantial drug loading capacity, improved stability, favourable biocompatibility, the ability to integrate multiple functions. However, the level of reproducibility and control does not meet the desired standard.

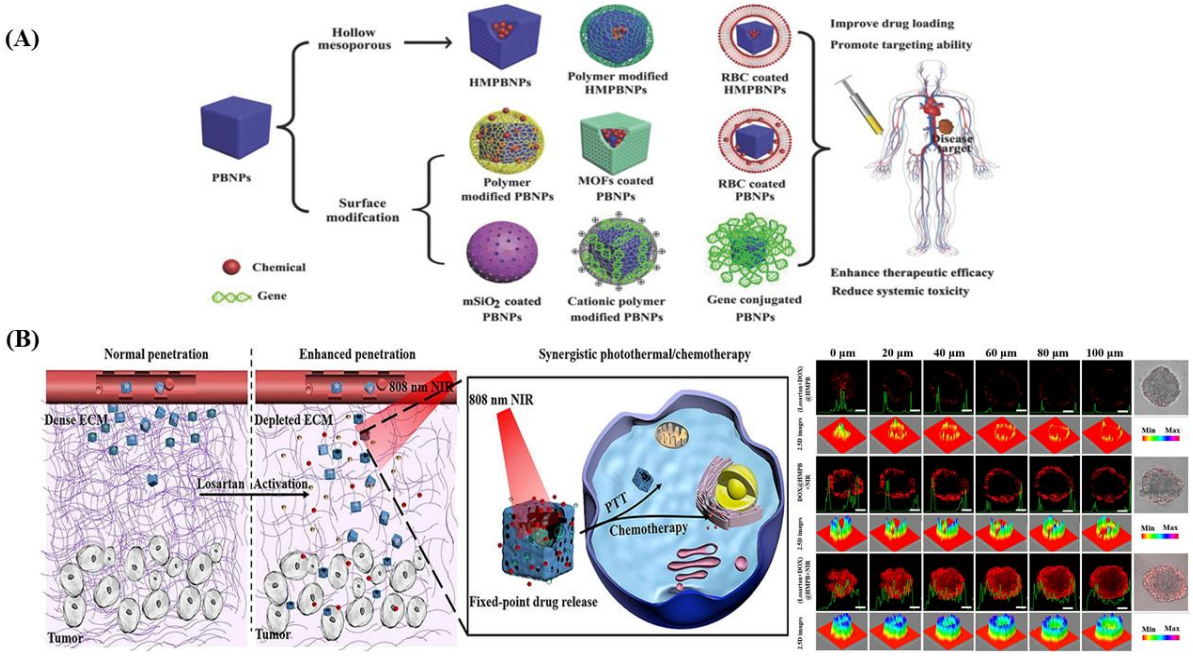

Figure 11: (A) Various drug delivery nanoplatforms utilizing PBNPs range from hollow mesoporous structures (HMPBNPs), including polymer-modified and RBC-coated versions, to

surface-modified PBNPs such as polymer-modified, MOF-coated, RBC-coated, $mSiO_2$-coated, cationic polymer-modified, and gene-conjugated varieties. (B) schematic representation and confirmation of DOX penetration into 4T1 MCSs CLSM and 2.5D images. (Copyright 2019. Reproduced with permission from *Acta Biomaterialia, ACS*).[108]

2.4.1.4PBNPs against inflammatory diseases

Inflammation is an innate reaction of the immune system in response to any damage or infection. Extensive research suggests that an excessive inflammatory response is detrimental and contribute to various pathological disorders.[115] It has been found that the abnormal production of ROS plays a crucial role in the development of inflammation.[116] Consequently, a viable strategy to counter inflammation involves scavenging the excessive ROS and controlling the subsequent aberrant inflammatory reaction.[32]

Inflammatory-related diseases primarily occur due to some major ROS such as H_2O_2, ·OH and $O_2^{\cdot-}$ radicals. Within normal physiological environment, antioxidants enzymes like catalase (CAT), peroxidase (POD) and superoxide dismutage (SOD) have the crucial function in both scavenging of H_2O_2 and $O_2^{\cdot-}$ radicals and generating of molecular O_2 effectively, thereby ensuring a balanced oxidative state. Nanozymes represent an innovative artificial enzyme that harness nanomaterials to mimic the catalytic properties of natural enzymes. The mixed valance state of PBNPs endows the remarkable ability to exhibit multifunctional enzymatic activities. PBNPs possess CAT-mimicking properties that have the ability to facilitate the decomposition of H_2O_2 into O_2, even in a neutral environment. The resulting O_2 can alleviate the condition of tumor hypoxia, exerting a crucial influence on the growth and metasis of tumors. Yang et al. first introduced the concept of PBNPs mediated CAT-like activity, effectively employing it to facilitate the generation of molecular oxygen from H_2O_2 at the site of liver inflammation in mice.[117] Zhang et al. made a significant discovery that PBNPs possess effective ROS scavenging abilities through their activity resembling POD, CAT and SOD. Unlike the Fenton reaction that generate ·OH, PBNPs were identified as POD mimetics capable of inhibiting ·OH production. The researchers proposed for the first time that the diverse forms of PBNPs contribute to their remarkable multienzyme-like activities, facilitated by their abundant redox potentials, thus functioning as efficient electron carriers (shown in Figure 12). To investigate the ROS scavenging capabilities of PBNPs, the researchers established a range of *in-vitro* models to induce ROS using chemicals, oxidized low-density lipoprotein, UV radiation, reperfusion, high glucose levels and oxygen glucose deprivation. Additionally, an *in-vivo*

inflammation model employing lipoprotein was developed to demonstrate the ROS scavenging potential of PBNPs. Finally, they concluded that PBNPs hold tremendous promise in inhibiting ROS induced damage in various pathological processes.[41]

Inflammatory bowel disease (IBD) and colitis are commonly occurred inflammation based diseases. In their study, Zhao and colleagues employed PVP modified PBNPs to address colitis. The NPs demonstrated remarkable efficacy in scavenging excessive ROS and inhibiting the generation of proinflammatory cytokines. Consequently, they mitigated colitis in mice without any detrimental side effects.[118] Additionally, Zhao and team developed manganese doped PB nanozyme (MPBZs) to alleviate IBD. The MPBZs mitigated oxidative stress and suppressed inflammation. Notable, the oral administration of MPBZs demonstrated promising anti-inflammatory effects in IBD mice, as confirmed by pathological findings.[119]

PBNPs have also exhibited their potential in mitigating neuroinflammation associated with nervous system injury and neurodegenerative disorders. In this context, Alzheimer's desease is a multifaceted neurodegenerative disorder characterized by neuroinflammation and the Tau-related abnormalities. In an effort to alleviate the symptoms of Alzheimer's, Cai and colleagues developed HMPWCs based therapeutic approach. HMPWCs demonstrated the ability to effectively scavenge ROS and conquer the triggering of astrocytes and microglia, thereby inhibiting neuroinflammation. Furthermore, HMPWCs exhibited inhibitory effects on Tau-related pathology through the AKT/GSK-3β pathway. The synergistic effect highlighted the potential of HMPWCs for the treatment of Alzheimer's disease.[24]

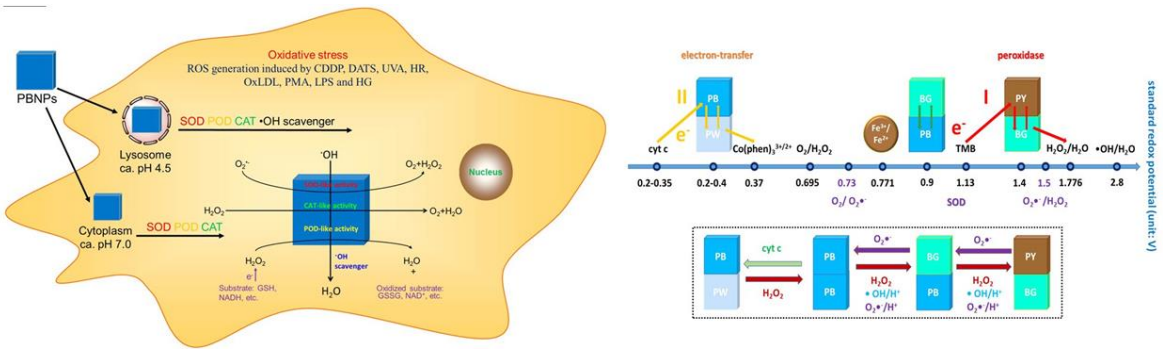

Figure 12: Illustration depicting the intracellular dynamics of PBNPs *in-vitro* and the mechanistic explanation of their multienzyme-like activity based on the standard redox potentials of various compounds in the reaction systems. (Copyright 2016. Reproduced with permission from *Journal of the American Chemical Society, ACS*).[41]

2.4.1.5PBNPs against bacterial infection

Bacterial infections pose a global healthcare hazard, endangering public health worldwide. The persistent misuse of antibiotics has led to the development and proliferation of drug resistant bacteria, posing a significant threat. A prime example of this is the treatment of Staphylococcus aureus (S. aureus) infections, where the prevalence of methicillin-resistant S. aureus (MRSA) stains has escalated, presenting a considerable tough challenge to the existing healthcare infrastructure. Hence, there is an urgent need to advance in the field of antibacterial treatment and devise innovative therapeutic strategies. Herein, it is important to note that PBNPs can be used as a bactericide agent due to it's improved photothermal and photodynamic action. For instance, Maaouri and colleagues employed PVP coated PBNPs (PVP/PBNPs) to eliminate harmful microorganisms, specifically aggressive strains of E. coli and drug-resistant S. aureus. The treated bacteria underwent exposure to NIR (either 810 or 980 nm; $1Wcm^{-2}$) for a duration of 10 minutes. Through a comprehensive analysis of the photothermal impact on bacteria in relation to the viability of HeLa cells, the researchers concluded that utilizing laser irradiation (980 nm) and maintaining NP concentration below 50 µg/mL can effectively target bacteria while preserving the viability of mammalians cells. Scanning electron microscopy (SEM) analysis revealed the aggregation of PVP/PBNPs in close proximity to the bacteria, both before and after irradiation. As the nanocomposite did not penetrate into the bacteria, the observed mechanism of action likely involved the heating of the bacterial environment (shown in Figure 13(A)).[120] Recently, Jiang et al. introduced a novel, cost-effective, scalable and highly efficient approach for water sterilization by employing Fe_3O_4@PB nanocomposite. These nanocomposites demonstrated a remarkable photothermal efficacy in deactivating bacteria under solar-light irradiation, achieving near complete inactivation of bacterial cells within a mere 15 minutes. Notably, even when faced with mixed bacteria present in real water samples, the nanocomposites exhibited outstanding performance in eradicating them. Additionally, the highly magnetized iron core of the nanocomposite facilitated magnetic separation and recycling. Extensive cycling tests revealed that the nanocomposites possessed excellent stability and reusability.[121]

The combination of two elements has the potential to trigger a synergistic impact or enhance the performance of the individual, thereby opening up a novel opportunity in the field of antibacterial treatment. From this perspective, Liu and colleagues have also recently proposed an intriguing approach in their published scientific reports.[122,123] They adorned PBNP and Au@PBNP core-shell nanostructures encapsulated with vancomycin, a WHO approved widely

recognized antibiotic. The vancomycin encapsulated onto PBNPs not only enhanced the antibacterial and wound-healing effects compared to unadorned PBNPs, but also served as a targeting unit for bacteria detection.

The incorporation of MOF to create a core-shell structure with PBNPs offers a promising strategy for boosting antibacterial therapy. In their study, Luo et al. successfully synthesized a PB@MOF core-shell nanocomposite against bacterial-infected wounds and environmental disinfection. The porphyrin ligands present in the MOF shell stimulated the generation of photocatalytic $^1O_2$ by inhibiting electron-hole recombination, under 660 nm laser illumination. Moreover, the nanocomposite demonstrated an impressive photothermal conversion efficiency (η) of 29.9% under 808 nm laser irradiation. Remarkable, under the simultaneous exposure of 808 nm NIR and 660 nm red light for a duration of 10 minutes, the nanocomposites exhibited exceptional antibacterial efficiency of 99.31% and 98.6% against S. aureus and E. coli respectively. Additionally, the presence of minute quantity of Fe and Zr ions stimulated the immune system, promoting would healing.[124]

Generally, biofilm formation is a common defence mechanism used by bacteria to shield themselves from antibiotics and host immune responses, often accompanied by the production of mucus. Self-assembled monolayers formed using PBNPs have been employed as a strategy to impede biofilm formation and reduce mucus secretion. For instance, Cai et al. devised a novel approach utilizing PBNPs modified with acetylcysteine (AC-PBNP) for efficient NIR radiated photothermal sterilization and localized infection treatment. AC-PBNP demonstrated multifunctional capabilities, with PBNP acting as a potent photothermal agent and AC preventing bacterial cluster formation in biofilms and reducing bacterial adhesion to tissue, thereby reducing mucus secretion and enhancing efficiency. Concentration-dependent photothermal sterilization was observed with AC-PBNP under 980 nm NIR laser irradiation, with 50 μg/mL eradicating up to 74% of Gram-positive S. aureus and up to 75% of Gram-negative E. coli, while exhibiting minimal cytotoxicity to mammalian cells (shown in Figure 13(B)).[125]

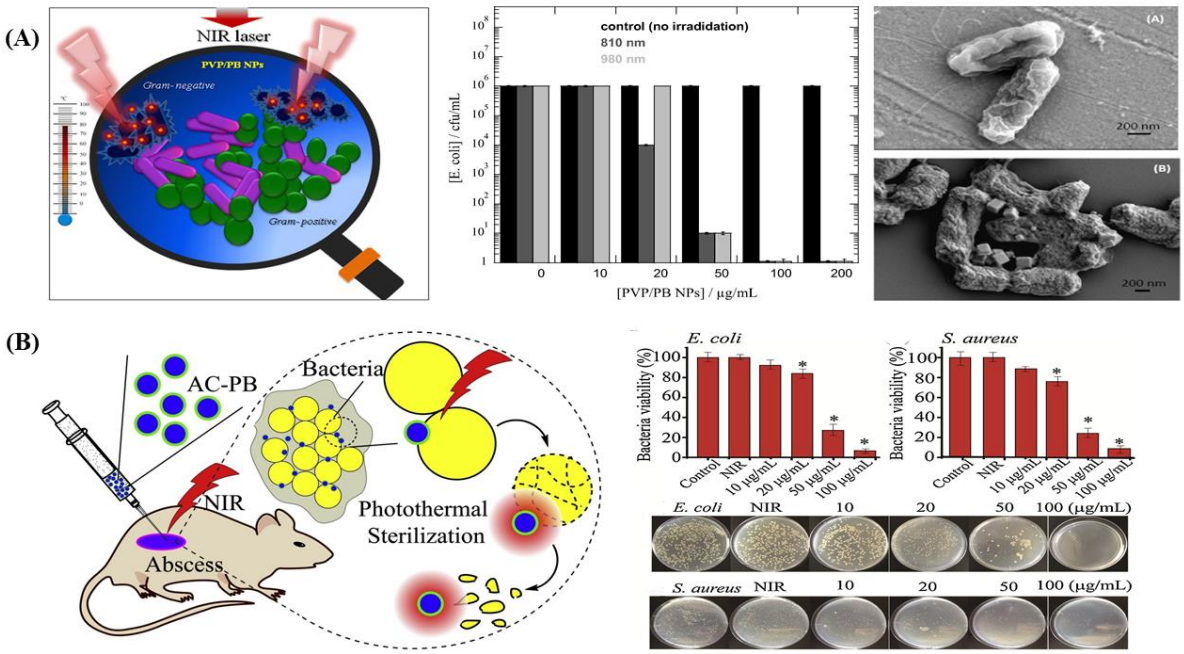

Figure 13: (A) Graphical abstract. Treating E. coli UTI89 (at a concentration of 10^6 CFU mL^{-1}) with varying concentrations of PVP/PB nanocomposite employing two distinct laser. Corresponding SEM images of E. coli UTI89 before and after laser (980 nm; 1Wcm^{-2}) exposure in the presence of PVP/PB NPs. (Copyright 2016. Reproduced with permission from *Journal of colloid and interface science, Elsevier*).[120] (B) The antibacterial impact of AC-PBNP on E. coli and S. aureus following treatment with varying concentrations of AC-PBNP under NIR irradiation (980 nm, 2.0 W/cm²) for 10 minutes. (Copyright 2019. Reproduced with permission from *Colloids and Surfaces B: Biointerfaces*).[125]

2.4.1.6PBNPs as a combinational therapetic agent

Despite the widespread utilization of PBNPs in monotherapy, encompassing PTT and PDT, numerous preclinical and clinical investigations have demonstrated that monotherapy falls short of expected effectiveness. The limited success of monotherapy can be a attributed to tumor metastasis and the emegence of drug resistance resulting from prolonged application of a single treatment approach. In contrast, the concept of combined tumor therapy involves the concurrent delivery of multiple therapeutic agents in a single nanoplatform or integration of diverse treatment modalities which has attracted more clinical interest due to its inherent advantages over monotherapy.[126] A key advantage of combinational therapy lies in its potential to generate synergistic effects, wherein the overall therapeutic outcomes of combined agents surpass the cumulative impact of their sole anti-cancer effects. Herein, as previously discussed, PBNPs exhibit notable PTT effect surpassing PDT effect due to their unique physiochemical

properties. While PTT has shown promising therapeutic results, complete ablation of malignant tumors through sole PTT still remains challenging. Recently, the utilization of PTT based combinational therapy using PBNPs has emerged as a promising strategy, yielding satisfactory therapeutic outcomes.

PTT-CDT based combinational therapy

Chemodynamic therapy (CDT) represents an innovative approach for therapeutics that generates highly reactive ·OH in the presence of endogeneous H_2O_2, utilizing Fenton or Fenton like reactions. These radicals effectively target and distrupt the DNA of cancer cells, inactivate proteins and trigger peroxidation in phospholipid membranes, ultimately leading to tumor cell death. However, the effectiveness of ·OH is limited as it can be efficiently neutralized by intracellular antioxidants. To overcome this, PTT may be a promising avenue that elevates the tumor's temperature, thereby accelerating the rate of Fenton reaction and boosting ·OH production. Herein, it is important to note that PBNPs can be degraded within low pH tumor microenvironment (TME), yielding Fe^{3+}/Fe^{2+} ions that serve as catalysts for the Fenton reaction. Consequently, the combinational therapy of PBNPs mediated PTT-CDT exhibits a remarkable synergistic effect, offering a highly promising and potent therapeutic approach.

Lie and their team achieved a remarkable feat by successfully fabricating a NIR responsive core-shell nanocomposite (PBFS), consisting of PBNP (~ 60 nm) at core and a fibrous mesoporous silica (~ 110 nm) at shell. The PBFS nanocomposites were effectively modified with a GSH responsive cationic polymer (PSS) for targeted delivery of nano-fenton reactor (DiFe) and SOD. Remarkable, the loading capacities of SOD and DiFe were determined to be 1077 and 126 mg/g respectively. The presence of PBNP core imparted outstanding photothermal conversion performance. *In-vitro* experiments demonstrated that the PBFS-PSS-DiFe-SOD nanocomposites exhibit excellent biocompatibility and can competently release the 7-amino-4-methylcoumarin probe, DiFe and SOD simultaneously at an elevated GSH environment. Moreover, the nanocomposite showed an outstanding dual CDT-PTT effect on tumor cell, making them highly promising for potential applications in cancer treatment.[127]

Tian et al. also created a NIR-triggered theranostic nanoplatform (GA-PB-MONs-LA) containing PBNPs within mesoporous organosilica nanoparticles (MONs), followed by the encapsulation of gambogic acid (GA), an HSP90 inhibitor and enveloping with thermo-responsive lauric acid (LA) which combined mild PTT and PTT-induced Fenton nanocatalytic therapy, providing imaging-guided treatment for hypoxic tumors. Under NIR irradiation, the

GA-PB-MONs-LA nanoplatform generated moderate hyperthermia (44 °C), effectively inducing apoptosis in tumor cells. Simultaneously, it triggered the controlled release of GA molecules which inhibited the expression of HSP90, thereby suppressing tumor thermoresistance. The thermal effect significantly enhanced the catalytic activities of the nanoplatform, leading to the generation of abundant O_2 and highly toxic ·OH species in the acidic TME. Both *in-vitro* and *in-vivo* experiments demonstrated a superior anti-tumor efficacy of GA-PB-MONs-LA nanoplatform due to synergistic effect of PTT and CDT.[128]

PTT-RT based combinational therapy

Radio therapy (RT) is a widely used clinical approach that includes ionizing radiation to eliminate tumor cells through inducing oxidative stress and damaging their RNA/DNA.[128] However, the the lack of O_2 in the TME reduces tumor sensitivity towards X-rays or gamma rays, rendering RT ineffective against hypoxic solid tumor.[129] To overcome this challenges, RT can be synergistically combined with PTT where the elevated temperature improves O_2 level at the tumor site through enhanced blood flow and significantly boosting therapeutic efficiency compared to RT alone. Although, PBNPs do not have a radiosensitization effect, they can be used to enhance RT of tumors when combined with other NPs that have strong X-ray attenuation ability and poses a promising potential in achieving a synergistic PTT-RT based combinational therapy to treat cancer.

For instance, Ren et al. developed a novel theranostic agent (HMPB@ Bi_2S_3) comprising ultra-small bismuth sulfide quantum dots (Bi_2S_3 QDs) embedded within hollow mesoporous prussian blue nanocubes (HMPB) that aimed promising potential for amplified tumor oxidative stress to enhance photo-radiotherapy. The unique redox property of $Fe^{2+/3+}$ within the HMPB@ Bi_2S_3 allowed for the disruption of redox homeostasis by consuming GSH and generating ·OH. This amplified oxidative stress was expected to induce significant damage to DNA, improve cell membrane permeability and heighten hyperthermia sensitivity, all contributing to enhance photo-/radiotherapy outcomes. Both *in-vitro* and *in-vivo* investigations demonstrated that this theranostic agent displayed antiproliferation efficacy that significantly inhibited tumor growth.[130]

Dou and team also fabricated PEG modified PB and Au based core-satellite NPs (CSNPs) to enable PTT-RT based therapy and MR-CT based multimodal imaging. The CSNPs demonstrated multimodal imaging-guided synergistic PTT-RT therapy under both NIR and X-ray exposure. This was achieved due to the high photothermal conversion efficiency of PBNP

cores and excellent radio sensitization from AuNP satellites, resulting in significantly superior therapeutic effects compared to individual ones. Remarkably, the intravenous injection of CSNPs led to complete tumor eradication without regrowth over the 14-day of therapeutic period (shown in Figure 14).[71]

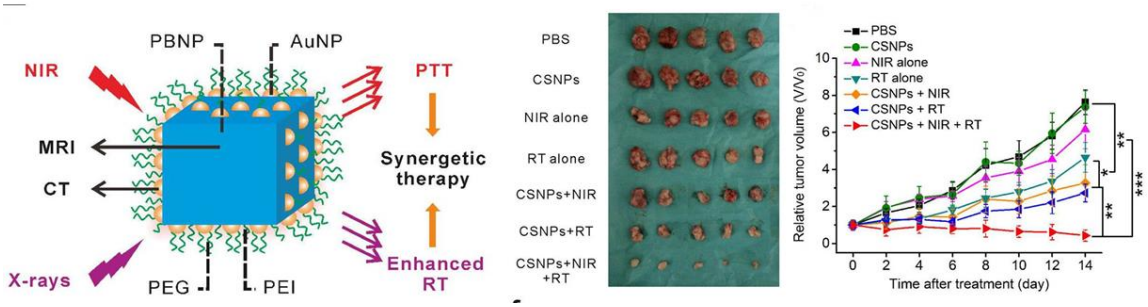

Figure 14: Design of PB@Au based coresatellite nanostructure. Illustrative images showing tumors collected from mice on day 14 post various treatments (n = 5). Additionally, tumor growth inhibition curves are depicted. (Copyright 2017. Reproduced with permission from *ACS Applied Materials & Interfaces*).[71]

PTT-ST based combinational therapy

Cancer cells have high demand for substantial energy supplies during their proliferation, growth and metastasis. Notable, cancer cells diverge from normal cells by predominantly obtaining sufficiently energy and metabolic componants via aerobic glycolysis (Warburg effect). Starvation therapy (ST) represents a promising and emerging approach for tumor treatment, employing glucose oxidase (GOx) to convert tumor glucose into H_2O_2 and gluconic acid. This process significantly curtails the nutritional supply, thereby impeding the rapid tumors growth. Additionally, PTT can trigger the upregulation of ATP-dependant heat shock proteins (HSPs) in tumors, rendering the cells more resistant to heat. Nevertheless, the combination of PTT with ST yeilds a remarkable outcome by suppressing the expression of tumor ATP-depedent pathways, thereby impeding the transcription and translation and stress-related proteins.

In their investigation, Zhou et al. successfully developed a tumor-targeted multifunctional nanocomposite, integrating tumor starvation and low-temperature PTT. The nanocomposite was ingeniously constructed using NIR activated hollow porous PBNPs (PHPBNPs), encapsulated with GOx and then functionalized with hyaluronic acid (HA) moieties linked by disulfide bonds. Incorporating the HA units resulted in improved accumulation and uptake of the nanocomposite by tumors overexpressing CD44 receptors. Subsequently, the encapsulated

GOx could be released in response to the elevated levels of intracellular glutathione (GSH). The released GOx effectively depleted glucose in the tumor site by consuming O_2 while PHPBNPs efficiently decompose intracellular H_2O_2 into O_2, further amplifying the tumor starvation effect, especially in hypoxic tumor regions. The GOx induced tumor starvation not only directly suppressed tumor growth but also effectively blocked HSPs expression. The nanocomposite demonstrated remarkable suppression of tumor growth (reduction of 32.5% in tumor volume). Furthermore, the median survival time of the treated mice extended to 59 days (shown in Figure 15(A)).[131]

Liang and colleagues also devised a approach to create a nanoplatform by functionlizing Cu^{2+} doped mesoporous prussian blue (CMPB) with HA, encapsulated with GOx, further modified with a nitric acid donor (HN). These innovative GOx@CMPB@HN nanoplatform synergistically integrate multiple therapeutic strategies including PTT, CDT and ST. Notable, doping of Cu^{2+} ions played a crucial role in accelarating these therapeutic approaches. Furthermore, the HN coating confered active targeting of CD44 receptors on cancer cells and improved vascular permeability. Both *in-vitro* and *in-vivo* experiments substantiated that the GOx@CMPB@HN nanoplatform effectively suppressed tumor growth by leveraging the unique properties of TME (shown in figure 15(B)).[132]

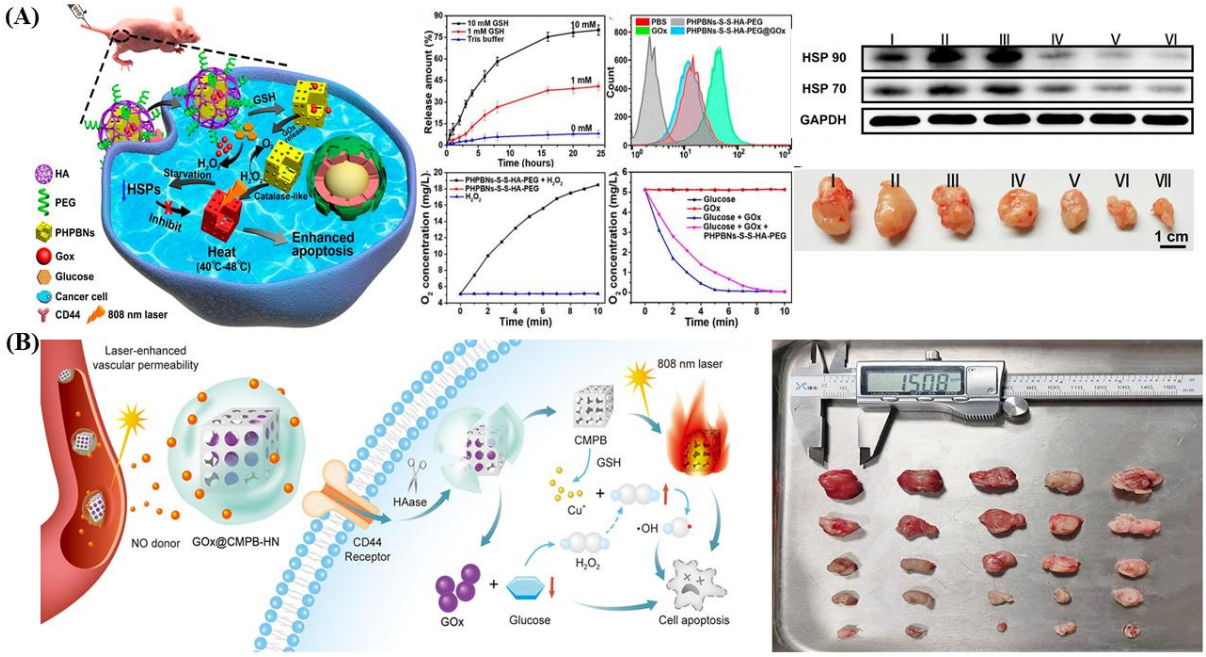

Figure 15: (A) Demonstration of GOx-induced starvation to augment mild temperature starvation to augment mild temperature PTT within a hypoxic tumor microenvironment. Hypoxia induced photothermal resistance was overcome by PHPBN-mediated tumor

reoxigeneration. *In-vitro* therapeutic efficiency measured by GOx releasing, iROS generation and O_2 concentration under various treatments. Characteristic Western blotting of HSP 90 and HSP 70 expression under different conditions. Typical photographs of HepG2 tumor tissues acquired after various treatment. (Copyright 2018. Reproduced with permission from *ACS nano).*[131] (B) Illustration depicting GOx@CMPB-HN NPs for in situ improved PTT/CDT/starvation therapy. Representative visuals of dissected tumor tissue. (Copyright 2023. Reproduced with permission from *ACS Applied Materials & Interfaces*).[132]

PTT-IT based combinational therapy

Immunotherapy (IT) is a groundbreaking approach that stimulates the body's immune system to recognize and attack cancer cells. Immune checkpoint inhibitors, adoptive T cell therapy, and cancer vaccines are some examples of clinically used immunotherapeutic strategies. Its potential for long-lasting responses and memory, reduced systemic side effects compared to traditional treatments like chemotherapy and its applicability across a range of cancer types. Several recent studies have demonstrated that the integration of PBNP-based PTT with IT capitalizes on their complementarymechanisms. The localized hyperthermia induced by PBNps not only directly damages tumor cells but also promotes the release of tumor antigens and danger-associated molecular patterns (DAMPs). This, in turm, activates the immune system and enhances antigen presentation by antigen-presenting cells. Owing to the recent favorable results in terms of survival and recurrence rate, immunotherapy has emerged as a highly auspicious approach to cancer treatment. The combinational approach involving anticytotoic T lymphocyte-associated protein 4 (anti-CTLA-4) and PBNP based PTT was first documented for addressing neuroblastoma. *In-vivo* experiments revealed that this combinational therapy led to complete regression of tumors and prolonged survival in 55.5% of tumor-bearing mice. In contrast, only 12.5% survived when treated solely with anti-CTLA-4 antibody, while those treated with PBNPs alone, PTT alone, or no treatment exhibited 0% survival. This enhanced long-term survival was ascribed to the dual action of PTT stimulating an immune response and anti-CTLA-4 countering T cell exhaustion and immunosuppression. Further, their research involving CD4+ and CD8+ cell depletion affirmed the crucial role of these T cell subsets in driving improved therapeutic outcomes (shown in Figure 16).[133] An alternative widely employed strategy involves conveying immunostimulant oligonucleotides to the tumor site using nanocarriers. This approach enhances immune stimulation when exposed to NIR laser, leading to a harmonized therapeutic effect by merging PTT with IT. For instance, Fernandes and colleagues, effectively fabricated CpG oligonucleotide-coated PBNPs

(CpG@PBNPs) through a modest layer-by-layer coating process which held a promise as a PTT-IT based nano-combined therapy for neuroblastoma. The CpG@PBNPs heightened the antigenicity and adjuvanticity of treated tumors, fostering a potent antitumor immune response through a multi-faceted mechanism. The inherent strong NIR absorption capability of PBNPs within the CpG@PBNPs formulation allowed for PTT, initiating both tumor cell death and the liberation of tumor antigens to enhance antigenicity. Concurrently, the CpG coating functioned as an external molecular adjuvant to supplement internal adjuvants (like calreticulin, ATP, and HMGB1), released by PTT. More importantly, the integration of CpG-PBNPs with PTT yielded a notably improved rate (70% at 60 days) of total tumor regression within the mouse neuroblastoma model (Neuro2a cells) in comparison to the control group. Moreover, the cured mice that survived long-term after CpG@PBNP-PTT treatment reject subsequent challenges with Neuro2a cells, indicating the therapy's capacity to generate immunological memory. The study underscored the significance of concurrent antigenicity, adjuvanticity and cytotoxicity for the generation of robust and enduring antitumor imune responses against neuroblastoma.[134]

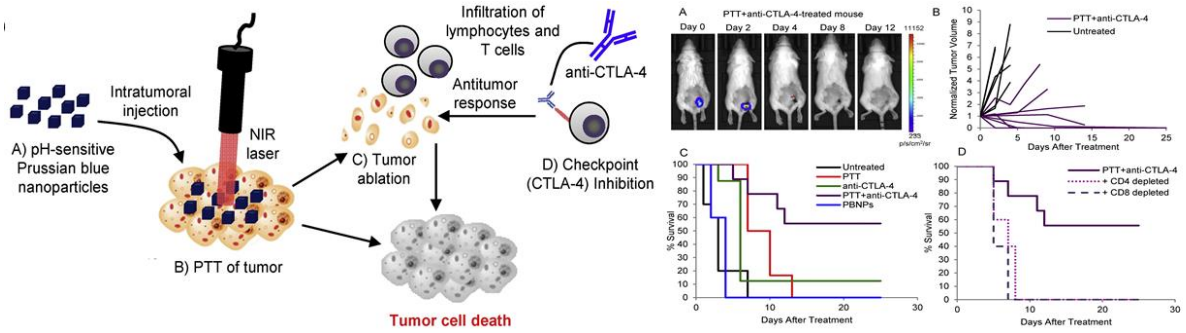

Figure 16: Schematically representation of PTT using PBNPs coupled with checkpoint inhibition for the photothermal treatment and immunotherapy of neuroblastoma. Impact of PTT-IT (PTT + anti-CTLA-4 therapy) on tumor regression and long-term survival in the neuroblastoma mouse model. (Copyright 2017. Reproduced with permission from *Nanomedicine: Nanotechnology, Biology and Medicine*).[133]

2.4.2 Cancer Diagnostic applications

Biomedical imaging, encompassig MRI, ultrasound (US) imaging, optical imaging, computed tomography (CT) imaging and PAI stands as a cornerstone in comprehensive cancer care. The array of benefits it offers includes real-time monitoring, non-destructive accessibility to tissue, minimal invasiveness and its applicability across a wide spectrum of biological and pathological processes.[135] PBNPs have emerged as exceptional external CA for MRI and PAI.

They serve as valuable tools for monitoring therapeutic effects and guiding treatment procedures due to their unique properties. Additionally, PB-based nanocomposites have been engineered for multimodal imaging of tumors, effectively incorporating functional elements like manganese, gadolinium and luminescent materials. The pivotal factor that fosters growing interest in PBNPs lies in their remarkable biocompatibility and safety within the realm of biomedical imaging.

2.4.2.1PBNPs as a MRI contrast agent

MRI represents a highly valuable and noninvaisve diagnostic tool in radiology, utilized to visualize the internal structure, anatomy and physiological processes within the body. Its superiority over other imaging modalities is evident, boasting outstanding spatial resolution, utilization of nonionizing radiation, deep tissue penetration, excellent soft tissue contrast and multiplaner imaging capabilities.[136] This technique relies on the fundamental principle of Nuclear Magnetic Resonance (NMR) with the presence of magnetic field gradients that encode signals in all three directions. The NMR signal is influenced by the water density and the transverse (r_2) and longitudinal (r_1) proton relaxivities of the tissue's protons. Consequently, two types of CA can be utilized to locally alter relaxation rates and control image contrast effectively. In principle PBNPs possess the potential to serve as CA for both T_1 and T_2-weighted MRI. However in practical applications, PBNPs are primarily utilized as T_1-weighted agents. The PB crystal contains two distinct iron centers: nitrogen bonded Fe^{3+} with high spin; S=5/2 and carbon bonded Fe^{2+} with low spin; S=0. A deficiency of $[Fe(CN)_6]^{4-}$ in the unit cell structure of PBNPs creates a structural vacancy to make electrically neutral that permits the entry of both coordinated and zeolitic water molecules. As a result, the longitudinal relaxivity of PBNPs is attributed to the interaction between inner sphere coordinated water protons and the Fe^{3+} atoms, along with outer sphere zeolitic water protons.

In 2010, shokouhimehr et al. achieved a groundbreaking advancement in the field of medical imaging by pioneering PBNPs with an exceptional crystal arrangement which served as a remarkable T_1-weighted CA. Their research showcased that the r_1 and r_2 values of these PBNPs measured 0.079 and 0.488 $mM^{-1}s^{-1}$ at 1.5 T respectively.[137] In comparison to commercially available MR CA like Gd^{3+} based paramagnetic complexes (T_1W CA) or superparamagnetic iron oxide NPs (T_2W CA), the relaxivities values achieved with PBNPs are relatively lower.[138] Nevertheless, PBNPs continued to garner significant interest in the field of biomedical imaging due to their remarkable stability, exhibiting minimal cyanide and iron ion

release in physiological conditions. Additionally, they demonstrated low toxicity, excellent biocompatibility and versatile functionalities.[139] Various approaches have been extensively investigated to enhance the longitudinal and transverse relaxation rate of PBNPs. The first approaches is the doping with high spin transition metal ions into PB crystal structure. For instance, Zhu et al. successfully developed Mn^{2+} doped PBNPs and demonstrated a increasing treand of r_1 value with measured value of 5.73, 5.85, 7.08, 7.64 $mM^{-1}s^{-1}$ at 3T for PBNP, PB:Mn(5%), PB:Mn(15%) and PB:Mn(25%) respectively. Additionally, a noticeable brightening effect was also observed at the tumor site following the intravenous administration of PB:Mn(15%) into 4T1 tumor bearing mice at 24 hr (shown in Figure 17(A)).[94] In a separate study, Dumont and colleauuges showcased a remarkable ninefold enhancement in MRI signal intensity by incorporating Gd^{3+} (S = 7/2) in the lattice site of PBNP, surpassing the signal intensity of conventionally used MR contrast agent. Notable, their *in-vitro* investigations demonstrated that the nanocomposite could accurately visualize eosinophilic cells through MRI imaging.[140] The next approach involves creating PBNPs based nanocomposite, effectively combining the magnetic materials with PBNPs to greatly enhance their imaging capabilities. For example, Wang and colleagues skillfully fabricated PBNP@MIL-100 (Fe), dual MOF based nanocomposite and utilized them as a T_1W-T_2W dual modal MRI CA for image guided cancer treatment. The r_1 and r_2 values of the nanocomposite were meticulously determined to be 1.313 and 22.258 $mM^{-1}s^{-1}$ respectively. More notably, after intravenous administration of these nanostructures into mice, a discernible enrichment was observed in MR imaging, providing further evidence of the remarkable T_1W-T_2W MR imaging efficacy of PBNP@MIL-100 (Fe) nanocomposits (shown in Figure 17(B)).[106] In an another work, Kale et al. developed a core-shell nanocomposite consisting magnetite at core and Gd^{3+} doped PBNPs at the shell as a dual modal MRI CA. The relaxivities were measured to be r_1~5.5 and r_2~126 $mM^{-1}s^{-1}$ at 3 T magnetic field.[92]

2.4.2.2PBNPs as a PAI contrast agent

Photoacoustic imaging (PAI) emerges as a novel and burgeoning molecular imaging approach that has recently captured substantial attention from researchers. Its potential for clinical translation and numerous advantages compared to other imaging techniques make it particularly promising. As a highly promising non-ionizing, non-invasive, and remarkably sensitive molecular imaging method, PAI effectively leverages the fusion of optical and acoustic imaging, surmounting the depth limitations encountered in traditional optical imaging techniques. In essence, PAI operates by absorbing optical energy, converting it partially into

heat, which gives rise to transient thermoelastic expansion and consequent ultrasonic emission.[141] These ultrasonic signals are then captured by ultrasonic transducers, forming detailed images. Additionally, PAI delivers real-time functional and molecular insights into tumors with exceptional imaging contrasts and ultrasonic spatial resolution. Notably, near-infrared (NIR) photothermal agents used in PAI exhibit minimal light absorption in the surrounding background tissue, making them highly efficient PA CA. This efficiency enhancement significantly contributes to an improved signal-to-noise ratio, further enhancing the imaging process.[142]

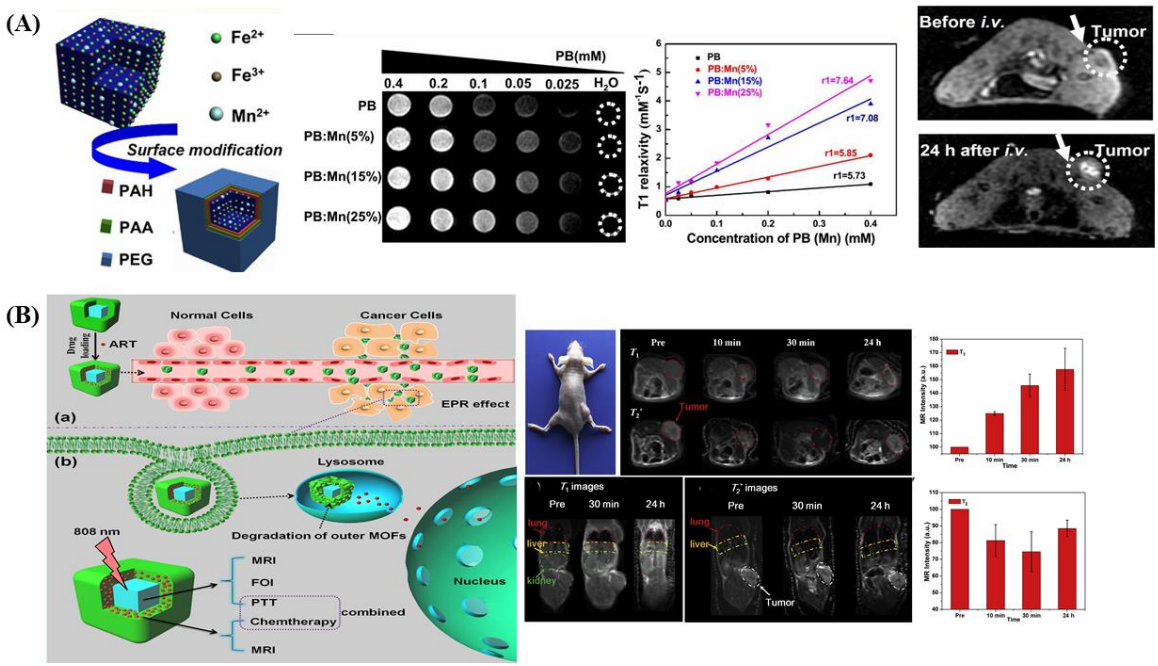

Figure 17: (A) Schematic representation of functionalized Mn^{2+} doped PBNPs and their T_1-T_2W MRI efficiency in both *in-vitro* and *in-vivo* model. (Copyright 2015. Reproduced with permission from *ACS Applied Materials & Interfaces*).[94] (B) Schematic representation of d-MOFs based MRI guided targeted cancer therapy. *In-vivo* T_1-T_2W MRI images after various time interval. (Copyright 2016. Reproduced with permission from *Biomaterials, Elsevier*).[106]

In their pioneering work, Liang and colleagues unveiled the remarkable potential of PBNPs as a highly efficient CA for enhancing photoacoustic imaging due to their strong molar extinction coefficient in the NIR region. The photoacoustic efficiency of PBNPs significantly surpassed that of hemoglobin in blood, owing to their strong absorption of NIR laser pulses at a specific wavelength of 765 nm. This unique feature also allowed them to enhance the PA signal even through 4.3 cm thickness of chicken breast muscle *in-vitro* at a relatively low concentration of 60 µg/mL. Encouragingly, *in-vivo* experiments demonstrated that upon intravenous

administration of PBNPs, a clear brain vasculature image persisted from 15 to 60 minutes, indicating prolonged blood circulation time. Moreover, histological sections revealed no apparent acute toxicity to vital organs within a 30-day observation period. This study unveiled a promising avenue for PBNPs in the realm of contrast agents, heralding new possibilities for advanced photoacoustic imaging applications with enhanced biocompatibility and outstanding imaging capabilities.[143] In a separate study, Kim et al. conducted a study wherein they elucidated the efficacy of a highly responsive photoacoustic contrast agent to visualize stem cells. They effectively engineered poly-L-lysin coated prussian blue (PB-PLL) to serve as a biocompatible and effective PAI contrast agent, specifically tailored for labelling and tracking human mensenchymal stem cell (hMSCs). Notably, the process of PBNP labeling exerted no adverse effects on cell viability or stem cell differentiations. Upon implantation, the labeled hMSCs displayed robust photoacoustic contrast, exhibiting a linear response with a *in-vivo* detection limit of 200 cells/μL. The photoacoustic contrast obtained from these labeled nanocomposite was both sensitive and enduring that enabled noninvasive and prolonged monitoring of engrafted hMSCs in living organism for up to 14 days (shown in Figure 18). Remarkably, this technique allowed real-time, image-guided cellular injections, even through an intact skull for brain intraparenchymal injection. Consequently, it opens up exciting possibilities for advanced cellular imaging and tracking, fostering a deeper understanding of stem cell behavior *in-vivo*.[144]

Moorthy and colleagues exhibited impressive photothermal efficacy of prussian blue nanoflack based amine-enriched mesoporous organosilica hybrid nanocomposite (PB@MSH@EDA), showcasing their potential as exceptional CA for photoacoustic imaging to investigate the accumulation dynamics of PB@MSH@EDA nanocomposites. Prior to the administration of PB@MSH@EDA nanocomposite, the photoacoustic signal of the tumor showed minimal activity. However, upon intratumor administration of PB@MSH-EDA nanocomposite, the PA signal in tumor-bearing mice exhibited a substantial and noteworthy enhancement.[145]

In order to enhance the efficiency of photoacoustic imaging while using reduced dosage and laser intensity, Cai et al. introduced Gd^{3+} ions into the lattice site of PBNP (GPB), resulting in the fine tuning of the NIR absorption peak from 710 nm to 910 nm, leading to the deeper tissue penetration. The emergence of this tunable LSPR effect can be attributed to the alterations in electronic transitions, electron density, and orbital energies occurred due to the incorporation of Gd^{3+} ions. These advancements hold promise for the development of high-performing

chemical probes in various optical applications.[146] Similarly, Zhu and colleagues also devloped Mn^{2+} doped PBNPs to get photoacoustic CA with improved efficiency.[94]

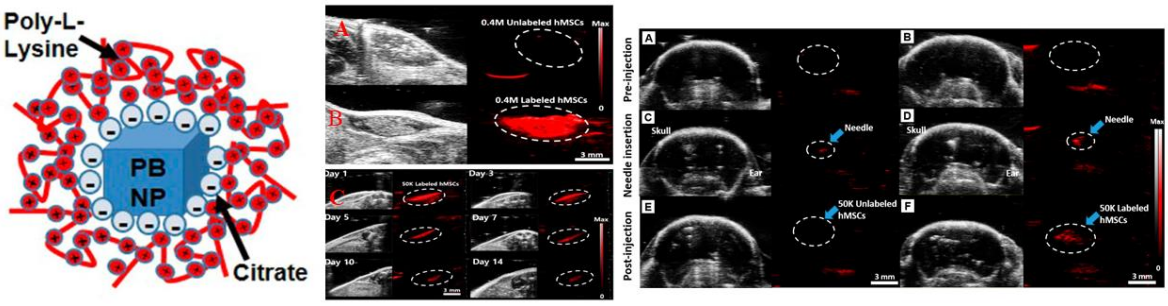

Figure 18: Schematic illustration of PB–PLL nanocomplexes. *In-vivo* visualization. (A) B-mode ultrasound (gray scale) and photoacoustic (red) images of unlabeled hMSCs (top) and labeled hMSCs (bottom) injected subcutaneously into nude mice. (C) Longitudinal photoacoustic imaging of transplanted cells *in-vivo* after 1, 3, 5, 7, 10, and 14 days. Strong photoacoustic contrast was still detectable 14 days post-injection. Additionally, deep tissue visualization. B-mode ultrasound (gray scale) and PA (red) images of unlabeled hMSCs (A, C, E) and labeled hMSCs (B, D, F) injected into the murine brain. Images captured pre-injection (A, B), after needle insertion (C, D), and post-injection of the cells (E, F). (Copyright 2017. Reproduced with permission from *ACS nano*).[144]

2.4.2.3PBNPs as a multimodal imaging-guided therapeutic contrast agent:

Despite the widespread utilization of single-modal imaging in disease diagnosis, it remains plagued by inherent limitations. However, the combination of multiple imaging modalities holds promise for overcoming these shortcoming and achieving enhanced and precise imaging of pathological tissues.[147] The current trend in clinical devlopment points towards the integration of diagnostic and therapeutic functions into a single nanoplatform. Such nanomedicines, endowed with multimodal theranostic (therapy+diagnosis) capabilities offer distinct advantages, including visible biodistribution and real time feedback that making them highly promising for personalized tumor therapy.[148] Extensive research has been conducted on PBNPs that boast multiple theranostic modes and excellent drug loading capacity. They have shown great promise in the realm of multimodal imaging-guided therapy and have been proven to exhibit outstanding performance in various experiments.[80] For instance, Tian et al. introduced an innovative imaging-guided photothermal-chemotherapy approach for TNBC utilizing a periodic mesoporous organosilica coated Prussian blue (PB@PMO) nanoplatform. The PB@PMOs exhibited remarkable features, including organic-inorganic frameworks, high

surface area (866 m^2 g^{-1}), uniform diameter (125 nm), large pore size (3.2 nm), high drug loading capacity (µg/mg), excellent photothermal conversion capability as well as proficiency in MR and PA imaging. These imaging properties facilitated tumor imaging and exhibited the nanoplatform's accumulation in the tumor region. *In-vivo* tumor-bearing mouse model of MDA-MB-231-Luc, the combined photothermal-chemotherapy strategy proved more effective in inhibiting TNBC compared to monotherapy, as evident from reduced bioluminescence intensity and tumor volume. Moreover, histopathological analysis demonstrates that the combination therapy induces extensive apoptosis and necrosis in the tumor without causing apparent side effects in major organs.[86] In a separate study, Zhang and colleagues synthesized a nanotheranostic agent (HMPBs-DOX/PFH) utilizing hollow mesoporous PBNPs to encapsulate doxorubicin and perfluorohexane. Both *in-vitro* and *in-vivo* investigations confirmed HMPBs-DOX/PFH as an amplifiable dual-mode imaging contrast agent, capable of enhancing USI and PAI for precise guidance and monitoring of tumor therapy. When exposed to HIFU, this versatile agent augmented the cavitation effect, allowing lower HIFU intensity to achieve coagulative necrosis. Additionally, it expedited DOX release, leading to enhanced chemotherapeutic efficacy while minimizing systemic side effects. This innovative theranostic nanoplatform, integrating dual-mode guided imaging with improved therapeutic outcomes and reduced side effects, holds great promise for noninvasive synergistic tumor therapy.[149]

PBNPs also have the capability to merge with other NP/CA, giving rise to multimodal theranostic core-shell nanoplatform with enhanced theranostic efficiency. Du et al. devloped multifunctional nanoplarforms (MFNPs) composed of PEG and HA fubctionalized $NaYF_4$@Fe_3O_4-PBNPs throuugh layer-by-layer assembly technique which served as trimodal imaging-guided PTT based contrast agent, combining T_2W-MR, UCL, PAT modalities to evaluate the cancer therapeutic efficacy. Significantly, the dual-targeting MFNPs demonstrated superior cancer ablation capabilities and exhibited enhanced PTT effects under NIR laser exposure. Remarkably, even with a high accumulation of NPs in the reticuloendothelial system (RES), no evident toxicity was observed in animals treated with MFNPs.[150] In an another study, a multifunctional therapeutic nanocomposite (MPB@AuNPs@MnO_2) was formulated, encompassing ultra-small gold nanoparticles (AuNPs) and manganese dioxide (MnO_2) on PBNP surface, serving as a platform for MRI-guided PTT and enhanced CDT. Here, the AuNPs acted as catalysts, facilitating the generation of H_2O_2, thereby enhancing the effectiveness of CDT. Simultaneously, MnO_2, in response to glutathione (GSH), released Mn^{2+} ions, which effectively augmented the .OH generation efficiency (80.0% to 90.84%) and enhanced

longitudinal relaxation (9.96 $mM^{-1}s^{-1}$) rate of the nanocomposite. Demonstrating exceptional photothermal performance, the nanocomposite achieved an impressive η of 42.62%. The *in-vivo* study utilizing MDA-MB-435 tumor-bearing nude mice further validated the therapeutic potential of this synergistic PTT/CDT approach. Substantial inhibition of tumor growth was observed, leading to complete tumor ablation within 15 days (shown in Figure 19). These results underscore the promising and multifaceted capabilities of the nanocomposite for effective image-guided cancer therapy.[151] Similarly, wang and colleagues devloped lanthanide based core-shell-shell theranostic agent (PEG-CSS@PB), consisted of PB coated $NaErF_4$@$NaYF_4$@$NaNdF_4$ nanocrystals encapsulated in a phospholipid PEG micelle. These theranostic agents demostrated both imaging and hyperthermia abilities when activated by NIR light. The inner core ($NaErF_4$) enriched with Er^{3+} emitted tissue-penetrating luminescence (1525 nm) which enabled high-resolution optical imaging of blood vessels and tumors under 980 nm excitation. Meanwhile, the high concentration of Nd^{3+} in the outer $NaNdF_4$ shell efficiently converted absorbed NIR light (808 nm) into heat, making them suitable for PTT. *In-vitro* study on HeLa cells, the PEG-CSS@PB theranostic agent demonstrated low toxicity and caused ~80% of cell death at a dose of 600 µg/mL under NIR laser (808 nm; 1 W/cm^2; 10 minutes). Moreover, in *in-vivo* tumor-bearing mice, a single PTT treatment reduced the tumor size by ~12 fold compared to untreated tumors under same light dose.[152] In a study, Wang constructed (PBNP-DOX)@Fe_3O_4@PEG-PLGA microcapsules using the premixed membrane emulsification method for combined trimodal (US/MRI/PAI) imaging-guided PTT and chemotherapy. The PBNPs exhibited efficient photothermal conversion efficiency, enabling magnetic targeting-guided PTT through the Fe_3O_4 NPs. Moreover, the microcapsules were capable of encapsulating DOX for chemotherapy. *In-vivo* experiments revealed substantial enrichment of the microcapsuls at the lesion site, with notable T_2-weighted MRI signals were observed.[153] The aforementioned examples have thoroughly demonstrated the extensive potential applications of PB NPs or nanocomposites in imaging-based diagnostics, offering valuable insights and directions for cancer therapy.

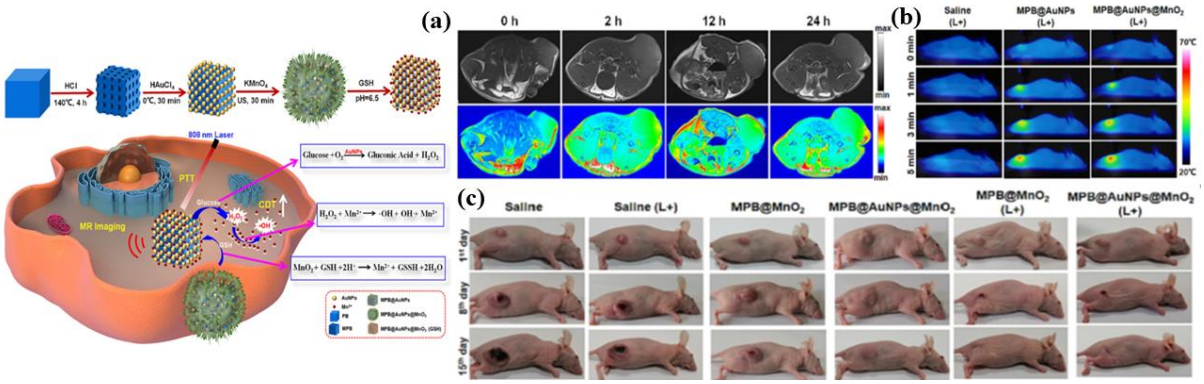

Figure 19: Schematically illustration of the devlopment of MPB@AuNPs@MnO_2 Nanoplatform for MRI responsive to tumor microenvironment and augmented cancer treatment. *In-vivo* efficiency in MR imaging and PTT/CDT based therapy (a) MR imaging, (b) IR thermal imaging of targeted tumor site. (c) real images of treated mice under various conditions. (Copyright 2023. Reproduced with permission from *Chemical Engineering Journal*).[151]

2.5 Toxicological impact of PBNPs

The clinical utility of NPs is mainly constrained by the potential toxicity stemming from their non-specefic accumulation in the healthy tissues and organs following systemic administration. Hence, when devloping NPs, it is imperious to take into account the safety and toxicological aspects. While PBNPs offer diverse possibilities in both diagnostics and therapeutics, the potential for adverse impacts on healthy tissues, systemic responses and prolonged toxicity still remains uncertain. Consequently, it is imperative to investigate the clinical safety profile of PBNPs. Prior to embarking on human clinical trials, a comprehensive assessment of PBNPs should be carried out in animal models, encompassing their effectiveness, biocompatibility, biodistribution, metabolic and excretion pathways, inflammatory responses, pharmacokinetic attributes, and the potential for long-term adverse effects. As previously mentioned, PBNPs have received approval from the FDA for safe human usage, except in the case of children under the age of two. They are primarily employed in the treatment of poisoning caused by radioactive and nonradioactive elements such as Ce (cerium) and Tl (thallium). In these therapeutic regimens, the recommended daily dosage is 6 gm of PBNPs. According to guidelines from the International Atomic Energy Agency (IAEA), adult males can safely consume a minimum of 10 gm of PBNPs per day without encountering significant harm. The most frequently reported side effects include constipation and gastrointestinal discomfort. However, it's worth noting that due to their ability to capture potassium ions, the administration

of PBNPs may potentially lead to hypokalemia or other nutritional imbalances in individuals not exposed to contamination. One possible reason for the lack of toxicity and favorable biosafety profile of PBNPs is attributed to the robust affinity of their cyano (-CN) groups to bind with iron ions, thereby inhibiting the generation of harmful effects on healthy cells. For instance, Liang and colleagues revealed that PBNPs exhibited negligible acute harm to vital organs (at a dosage of 20 mg/kg, i.v injection), underscoring their suitability for use in cancer theranostic without safe concern.[143] Moreover, Chen and colleagues also conducted a comprehensive investigation into the immune reaction, biodistribution, long-term toxicity and metabolic processes of PBNPs following a short-term *in-vivo* exposure at a dose of 8 mg/kg via i.v. injection. The histological findings revealed that PBNPs primarily accumulated within the liver and spleen. In the spleen, there was an initial decline in T cell frequency observed one day post-injection, followed by a gradual return to normal levels over the course of 60 days. Simultaneously, in the bloodstream, T cell frequency initially decreased after PBNPs injection, but subsequently rebounded, reaching normal levels after 7 days. Moreover, liver function serum markers, including alanine transaminase, aspartate transaminase, total bilirubin, and alkaline phosphatase, exhibited a swift and notable increase within just one hour of injection, indicative of acute liver damage. However, these markers gradually declined and normalized after 60 days of injection. Hence, the findings from their experiments demonstrated that PBNPs did not excert any noteworthy impact on the survival rate, immediate toxicity or long-term toxicity in mice following short-term exposure, highlighting the exceptional safety profile of PBNPs.[154] In a similar study, Fu and colleagues determined the cytotoxicity of PBNPs to HeLa cells and reveled that PBNPs did not exhibit any significant variation in cell viability without NIR exposure even at a concentration of 16 mg/mL, indicating that PBNPs had little impact on cell survival even at higher concentrations.[78] Furthermore, as previously discussed, suitable surface modification and functionalization techniques can enhance the stability and localization of NPs, leading to improved physiological stability and tumor specefic targeting, notable biocompatibility, prolonged blood circulation time, thus mitigating or even eradicating these unwanted repercussions and side effects. As examples, hylauronic acid functionalized PBNPs exhibited no harmful effects on normal cells owing to improved stability as well as receptor based targeting ability.[56] Moreover, citrate coated PBNPs were also found to be non-toxic to the healthy cells.[38] A recent investigation into PBNPs has unveiled that the PEGylation has notable mitigated the toxic impacts of NPs on the vital organs of Balb/c nude mice, even when administered at a dosage of 20 mg/kg.[80] Similarly, PEGylation was found to extend the blood circulation time due to biocompatibility and non-toxic nature of the functionalized NPs. Of

greater significance is the fact that the toxicity on vital organs is heavily influenced by the composition of NPs. Yet, additional physicochemical characteristics such as particle shape, size, surface alterations, and the gradient of protein absorption in physiological environment also hold significant sway in dictating the NP toxicity.[155] A comprehensive research of the implications of adorning NPs with PBNPs is imperative, encompassing factors like biodistribution, pharmacokinetics, metabolic and excretion pathways, inflammatory responses, and long-term toxicity. Consequently, numerous challenges still persist on the path to realizing the clinical utility of PBNPs.

2.6 Research gap

Certainly, despite the promising potential of Prussian blue-based nanoparticles in cancer theranostics, several research gaps still exist that warrant further investigation.

Understanding the *in-vitro* and *in-vivo* stability and biodegrability of prussian blue based NPs is crucial for their long-term safety and efficecy. Research is needed to assess their behaviour in biological environments, including their degradation kinetics and potential accumulation in organ over time.

Investigating the immunogenicity and biodistribution of prussian blue based NPs for assessing their systemic effects and potential immune responses. Further research is needed to understand how these nanoparticles interact with the immune system and how their biodistribution impacts overall therapeutic efficacy.

While prussian blue-based NPs can be functionalized for targeted delivery to cancer cells, the mechanisms underlying targeting specificity need to be elucidated further. Research is needed to explore the interactions between NP surface ligands and cancer cell receptors to enhance targeting efficiency and reduce off-target effects and to develop a novel functionalization approach.

Research is needed to optimize the loading and release kinetics of therapeuti payloads within prussian blue-based NPs. This includes investigating various drug encapsulation strategies, as well as assessing the release profiles and bioavailability of loaded drugs in cancer cells.

Integrating multimodal theranostic modalities into functionalized prussian blue-based nanocomposite for cancer treatment, requires further research. This includes developing novel imaging agents or conjugation strategies to enable simultaneous imaging and therapy

monitoring *in-vivo*. In this context, it is also crucial to take some strategy to modify core prussian blue NPs itself for improving their inherent theranostic efficiency.

Bridging the gap between preclinical studies and clinical translation is essential for the practical application of prussian blue-based nanoparticles in cancer theranostics. Research is needed to address regulatory hurdles, optimize manufacturing processes, and conduct rigorous clinical trials to evaluate safety and efficacy in human patients.

Furthermore, there exists a scarcity of comprehensive studies regarding the impact of particle size, shape, various functionalizations, doping variations, etc., on the modulation of r_1 and r_2 relaxivity. There is a pressing need for research aimed at delving into this fundamental understanding and developing a dual-modal MRI contrast agent capable of both T_1 and T_2-weighted imaging.

Addressing these research gaps will contribute to the continued advancement of prussian blue-based nanocomposite as versatile agent for cancer diagnosis, imaging, and therapy.

2.7 Objectives of the present work

Following a comprehensive literature survey, the specefic objectives of my thesis are outlined as follows:

- Optimization of synthesis protocol to achieve optimal size and shape of PBNPs.
- Devlopment of novel functionalization approach to enhance biocompatibility, enable receptor based targeting and mitigate off target effects.
- Devlopment of prussian blue based NPs with enhanced theranostic capability including PTT, PDT, and improved performance in both T_1-T_2W MR imaging.
- Utilization of hydrophobic natural flabonoid in targeted cancer theranostic applications involving prussian blue based NPs as drug carrier.
- Understanding of the relation between T_1-T_2W MRI relaxivities and influencing parameters like NPs size variation, several modifications and various doping.

Reference

1. Kong, B., Tang, J., Selomulya, C., Li, W., Wei, J., Fang, Y., ... & Zhao, D. (2014). Oriented mesoporous nanopyramids as versatile plasmon-enhanced interfaces. *Journal of the American Chemical Society*, *136*(19), 6822-6825.
2. Keggin, J. F., & Miles, F. D. (1936). Structures and formulae of the Prussian blues and related compounds. *Nature*, *137*(3466), 577-578.

3. Herren, F., Fischer, P., Ludi, A., & Hälg, W. (1980). Neutron diffraction study of Prussian Blue, Fe4 [Fe (CN) 6] 3. xH2O. Location of water molecules and long-range magnetic order. *Inorganic Chemistry*, *19*(4), 956-959.
4. Zakaria, M. B., & Chikyow, T. (2017). Recent advances in Prussian blue and Prussian blue analogues: synthesis and thermal treatments. *Coordination Chemistry Reviews*, *352*, 328-345.
5. Guo, Y. F., Fang, Q. C., Xu, J., Bu, F. X., Zhang, W., Hu, M., & Jiang, J. S. (2018). Synthesis of mesoporous yolk-shell magnetic Prussian blue particles for multi-functional nanomedicine. *Journal of Nanoscience and Nanotechnology*, *18*(5), 3059-3066.
6. Jiang, Y., Yang, Y., Shen, L., Ma, J., Ma, H., & Zhu, N. (2021). Recent advances of prussian blue-based wearable biosensors for healthcare. *Analytical Chemistry*, *94*(1), 297-311.
7. Grandjean, A., Delchet, C., Causse, J., Barré, Y., Guari, Y., & Larionova, J. (2016). Effect of the chemical nature of different transition metal ferrocyanides to entrap Cs. *Journal of Radioanalytical and Nuclear Chemistry*, *307*, 427-436.
8. Hessel, C. M., Pattani, V. P., Rasch, M., Panthani, M. G., Koo, B., Tunnell, J. W., & Korgel, B. A. (2011). Copper selenide nanocrystals for photothermal therapy. *Nano letters*, *11*(6), 2560-2566.
9. Kam, N. W. S., O'Connell, M., Wisdom, J. A., & Dai, H. (2005). Carbon nanotubes as multifunctional biological transporters and near-infrared agents for selective cancer cell destruction. *Proceedings of the National Academy of Sciences*, *102*(33), 11600-11605.
10. Grandjean, F., Samain, L., & Long, G. J. (2016). Characterization and utilization of Prussian blue and its pigments. *Dalton transactions*, *45*(45), 18018-18044.
11. Jia, Z., & Sun, G. (2007). Preparation of prussian blue nanoparticles with single precursor. *Colloids and Surfaces A: Physicochemical and Engineering Aspects*, *302*(1-3), 326-329.
12. Li, D., Liu, M., Li, W., Fu, Q., Wang, L., Lai, E., ... & Zhang, K. (2022). Synthesis of Prussian blue nanoparticles and their antibacterial, antiinflammation and antitumor applications. *Pharmaceuticals*, *15*(7), 769.
13. Uemura, T., & Kitagawa, S. (2003). Prussian blue nanoparticles protected by poly (vinylpyrrolidone). *Journal of the American Chemical Society*, *125*(26), 7814-7815.
14. Zhang, X., Sui, C., Gong, J., Yang, R., Luo, Y., & Qu, L. (2007). Preparation, characterization, and property of polyaniline/Prussian blue micro-composites in a low-temperature hydrothermal process. *Applied surface science*, *253*(22), 9030-9034.
15. Hu, M., Jiang, J.-S., Lin, C.-C., Zeng, Y., 2010. Prussian blue mesocrystals: an example of self-construction. CrystEngComm 12, 2679–2683.
16. Hu, M., Jiang, J. S., Lin, C. C., & Zeng, Y. (2010). Prussian blue mesocrystals: an example of self-construction. *CrystEngComm*, *12*(10), 2679-2683.
17. Qian, J., Xu, J., Kuang, L., & Hua, D. (2017). Cesium Removal from Human Blood by Poly (ethylene glycol)-Decorated Prussian Blue Magnetic Nanoparticles. *ChemPlusChem*, *82*(6), 888-895.
18. Qin, Z., Chen, B., Huang, X., Mao, Y., Li, Y., Yang, F., & Gu, N. (2019). Magnetic internal heating-induced high performance Prussian blue nanoparticle preparation and excellent catalytic activity. *Dalton Transactions*, *48*(46), 17169-17173.
19. Komkova, M. A., Karyakina, E. E., & Karyakin, A. A. (2018). Catalytically synthesized prussian blue nanoparticles defeating natural enzyme peroxidase. *Journal of the American Chemical Society*, *140*(36), 11302-11307.
20. Lee, S. H., & Huh, Y. D. (2012). Preferential evolution of Prussian blue's morphology from cube to hexapod. *Bulletin of the Korean Chemical Society*, *33*(3), 1078-1080.
21. Hu, M., Furukawa, S., Ohtani, R., Sukegawa, H., Nemoto, Y., Reboul, J., ... & Yamauchi, Y. (2012). Synthesis of Prussian blue nanoparticles with a hollow interior by controlled chemical etching. *Angewandte Chemie International Edition*, *51*(4), 984-988.
22. Hu, M., Belik, A. A., Imura, M., & Yamauchi, Y. (2013). Tailored design of multiple nanoarchitectures in metal-cyanide hybrid coordination polymers. *Journal of the American Chemical Society*, *135*(1), 384-391.

23. Shen, Q., Jiang, J., Fan, M., Liu, S., Wang, L., Fan, Q., & Huang, W. (2014). Prussian blue hollow nanostructures: Sacrificial template synthesis and application in hydrogen peroxide sensing. *Journal of Electroanalytical Chemistry*, *712*, 132-138.
24. Cai, X., Zhang, K., Xie, X., Zhu, X., Feng, J., Jin, Z., ... & Chen, H. (2020). Self-assembly hollow manganese Prussian white nanocapsules attenuate Tau-related neuropathology and cognitive decline. *Biomaterials*, *231*, 119678.
25. Zhang, K., Tu, M., Gao, W., Cai, X., Song, F., Chen, Z., ... & Tian, M. (2019). Hollow prussian blue nanozymes drive neuroprotection against ischemic stroke via attenuating oxidative stress, counteracting inflammation, and suppressing cell apoptosis. *Nano letters*, *19*(5), 2812-2823.
26. Ming, H., Torad, N. L., Chiang, Y. D., Wu, K. C. W., & Yamauchi, Y. (2012). Size-and shape-controlled synthesis of Prussian Blue nanoparticles by a polyvinylpyrrolidone-assisted crystallization process. *CrystEngComm*, *14*(10), 3387-3396.
27. Ding, Y., Hu, Y. L., Gu, G., & Xia, X. H. (2009). Controllable synthesis and formation mechanism investigation of Prussian blue nanocrystals by using the polysaccharide hydrolysis method. *The Journal of Physical Chemistry C*, *113*(33), 14838-14843.
28. Qian, L., Zheng, R., & Zheng, L. (2013). Fabrication of Prussian blue nanocubes through reducing a single-source precursor with graphene oxide and their electrocatalytic activity for H 2 O 2. *Journal of nanoparticle research*, *15*, 1-9.
29. de la Escosura, A., Verwegen, M., Sikkema, F. D., Comellas-Aragones, M., Kirilyuk, A., Rasing, T., ... & Cornelissen, J. J. (2008). Viral capsids as templates for the production of monodisperse Prussian blue nanoparticles. *Chemical communications*, (13), 1542-1544.
30. Qiu, J. D., Peng, H. Z., Liang, R. P., & Xiong, M. (2007). Preparation of Three-Dimensional Ordered Macroporous Prussian Blue Film Electrode for Glucose Biosensor Application. *Electroanalysis: An International Journal Devoted to Fundamental and Practical Aspects of Electroanalysis*, *19*(11), 1201-1206.
31. Shen, X., Wu, S., Liu, Y., Wang, K., Xu, Z., & Liu, W. (2009). Morphology syntheses and properties of well-defined Prussian blue nanocrystals by a facile solution approach. *Journal of colloid and interface science*, *329*(1), 188-195.
32. Gao, Y., Yu, G., Xing, K., Gorin, D., Kotelevtsev, Y., Tong, W., & Mao, Z. (2020). Finely tuned Prussian blue-based nanoparticles and their application in disease treatment. *Journal of Materials Chemistry B*, *8*(32), 7121-7134.
33. Wu, X., Cao, M., Hu, C., & He, X. (2006). Sonochemical synthesis of Prussian blue nanocubes from a single-source precursor. *Crystal growth & design*, *6*(1), 26-28.
34. Chen, B., Sun, J., Fan, F., Zhang, X., Qin, Z., Wang, P., ... & Gu, N. (2018). Ferumoxytol of ultrahigh magnetization produced by hydrocooling and magnetically internal heating co-precipitation. *Nanoscale*, *10*(16), 7369-7376.
35. Liang, G., Xu, J., & Wang, X. (2009). Synthesis and characterization of organometallic coordination polymer nanoshells of Prussian blue using miniemulsion periphery polymerization (MEPP). *Journal of the American Chemical Society*, *131*(15), 5378-5379.
36. Vaucher, S., Li, M., & Mann, S. (2000). Synthesis of Prussian blue nanoparticles and nanocrystal superlattices in reverse microemulsions. *Angewandte Chemie*, *112*(10), 1863-1866.
37. Shiba, F., Nito, M., Kawakita, K., & Okawa, Y. (2015). Size control of monodisperse Prussian blue nanoparticles by enforced-nucleation and additional-growth procedures in a citrate reduction system. *Particulate Science and Technology*, *33*(6), 671-676.
38. Shokouhimehr, M., Soehnlen, E. S., Hao, J., Griswold, M., Flask, C., Fan, X., ... & Huang, S. D. (2010). Dual purpose Prussian blue nanoparticles for cellular imaging and drug delivery: a new generation of T 1-weighted MRI contrast and small molecule delivery agents. *Journal of Materials Chemistry*, *20*(25), 5251-5259.
39. Hou, R., Lu, T., Gao, W., Shen, J., Yu, Z., Li, D., ... & Cai, X. (2022). Prussian Blue nanozyme promotes the survival rate of skin flaps by maintaining a normal microenvironment. *ACS nano*, *16*(6), 9559-9571.

40. Pan, Q., Huang, K., Ni, S., Yang, F., & He, D. (2009). Synthesis of two-dimensional micron-size single-crystalline Prussian blue nanosheets by hydrothermal methods assisted by glucose. *Materials Research Bulletin*, *44*(2), 388-392.
41. Zhang, W., Hu, S., Yin, J. J., He, W., Lu, W., Ma, M., ... & Zhang, Y. (2016). Prussian blue nanoparticles as multienzyme mimetics and reactive oxygen species scavengers. *Journal of the American Chemical Society*, *138*(18), 5860-5865.
42. Li, Y., Jin, Z., & Tsubaki, N. (2022). Distinctive synthesis of CdS-based photocatalysts based on a Prussian blue analog induction strategy for efficient solar-driven water splitting applications. *Journal of Materials Chemistry C*, *10*(48), 18213-18225.
43. Hu, M., Jiang, J. S., Ji, R. P., & Zeng, Y. (2009). Prussian Blue mesocrystals prepared by a facile hydrothermal method. *CrystEngComm*, *11*(11), 2257-2259.
44. Zheng, X. J., Kuang, Q., Xu, T., Jiang, Z. Y., Zhang, S. H., Xie, Z. X., ... & Zheng, L. S. (2007). Growth of Prussian blue microcubes under a hydrothermal condition: possible nonclassical crystallization by a mesoscale self-assembly. *The Journal of Physical Chemistry C*, *111*(12), 4499-4502.
45. JWu, L., Pang, T., Wu, L., Guan, Y., Yin, L., & Li, Y. (2020). Preparation and characterization of Prussian blue coated polymeric nanoparticles via dispersion polymerization template. *Journal of Inorganic and Organometallic Polymers and Materials*, *30*, 5074-5084.
46. Liu, L., Hu, Z., Sun, L., Gao, G., & Liu, X. (2015). Controlled synthesis and enhanced electrochemical performance of Prussian blue analogue-derived hollow $FeCo_2O_4$ nanospheres as lithium-ion battery anodes. *RSC Advances*, *5*(46), 36575-36581.
47. Johansson, A., Widenkvist, E., Lu, J., Boman, M., & Jansson, U. (2005). Fabrication of high-aspect-ratio Prussian blue nanotubes using a porous alumina template. *Nano letters*, *5*(8), 1603-1606.
48. Wang, Q., Wu, X., You, H., Min, H., Xu, X., Hao, J., ... & Yang, H. (2022). Template-directed Prussian blue nanocubes supported on Ni foam as the binder-free anode of lithium-ion batteries. *Applied Surface Science*, *571*, 151194.
49. R. McHale, N. Ghasdian, Y. Liu, M. B. Ward, N. S. Hondow, H. Wang, Y. Miao, R. Brydson and X. Wang, Chem. Commun., 2010, 46, 4574–4576.
50. McHale, R., Ghasdian, N., Liu, Y., Wang, H., Miao, Y., & Wang, X. (2010). Synthesis of Prussian blue coordination polymer nanocubes via confinement of the polymerization field using miniemulsion periphery polymerization (MEPP). *Macromolecular rapid communications*, *31*(9-10), 856-860.
51. McHale, R., Liu, Y., Ghasdian, N., Hondow, N. S., Ye, S., Lu, Y., ... & Wang, X. (2011). Dual lanthanide role in the designed synthesis of hollow metal coordination (Prussian Blue analogue) nanocages with large internal cavity and mesoporous cage. *Nanoscale*, *3*(9), 3685-3694.
52. Schauer, C. L., Chen, M. S., Price, R. R., Schoen, P. E., & Ligler, F. S. (2004). Colored thin films for specific metal ion detection. *Environmental science & technology*, *38*(16), 4409-4413.
53. Chen, H., Ma, Y., Wang, X., Wu, X., & Zha, Z. (2017). Facile synthesis of Prussian blue nanoparticles as pH-responsive drug carriers for combined photothermal-chemo treatment of cancer. *RSC advances*, *7*(1), 248-255.
54. Xue, P., Sun, L., Li, Q., Zhang, L., Xu, Z., Li, C. M., & Kang, Y. (2018). PEGylated magnetic Prussian blue nanoparticles as a multifunctional therapeutic agent for combined targeted photothermal ablation and pH-triggered chemotherapy of tumour cells. *Journal of colloid and interface science*, *509*, 384-394.
55. Yang, Y., Jing, L., Li, X., Lin, L., Yue, X., & Dai, Z. (2017). Hyaluronic acid conjugated magnetic prussian blue@ quantum dot nanoparticles for cancer theranostics. *Theranostics*, *7*(2), 466.
56. Zhou, B., Jiang, B. P., Sun, W., Wei, F. M., He, Y., Liang, H., & Shen, X. C. (2018). Water-dispersible prussian blue hyaluronic acid nanocubes with near-infrared photoinduced singlet oxygen production and photothermal activities for cancer theranostics. *ACS applied materials & interfaces*, *10*(21), 18036-18049.
57. Steichen, S. D., Caldorera-Moore, M., & Peppas, N. A. (2013). A review of current nanoparticle and targeting moieties for the delivery of cancer therapeutics. *European journal of pharmaceutical sciences*, *48*(3), 416-427.

58. Chen, W., Zeng, K., Liu, H., Ouyang, J., Wang, L., Liu, Y., ... & Liu, Y. N. (2017). Cell membrane camouflaged hollow prussian blue nanoparticles for synergistic photothermal-/chemotherapy of cancer. *Advanced Functional Materials*, *27*(11), 1605795.
59. Peng, J., Yang, Q., Li, W., Tan, L., Xiao, Y., Chen, L., ... & Qian, Z. (2017). Erythrocyte-membrane-coated prussian blue/manganese dioxide nanoparticles as H_2O_2-responsive oxygen generators to enhance cancer chemotherapy/photothermal therapy. *ACS applied materials & interfaces*, *9*(51), 44410-44422.
60. Bonan, N. F., Ledezma, D. K., Tovar, M. A., Balakrishnan, P. B., & Fernandes, R. (2022). Anti-Fn14-conjugated Prussian blue nanoparticles as a targeted photothermal therapy agent for glioblastoma. *Nanomaterials*, *12*(15), 2645.
61. Ferrara, N., Hillan, K. J., & Novotny, W. (2005). Bevacizumab (Avastin), a humanized anti-VEGF monoclonal antibody for cancer therapy. *Biochemical and biophysical research communications*, *333*(2), 328-335.
62. Xue, P., Bao, J., Zhang, L., Xu, Z., Xu, C., Zhang, Y., & Kang, Y. (2016). Functional magnetic Prussian blue nanoparticles for enhanced gene transfection and photothermal ablation of tumor cells. *Journal of Materials Chemistry B*, *4*(27), 4717-4725.
63. He, X., Yuan, R., Chai, Y., Zhang, Y., & Shi, Y. (2007). A new antibody immobilization strategy based on electro-deposition of gold nanoparticles and Prussian Blue for label-free amperometric immunosensor. *Biotechnology letters*, *29*, 149-155.
64. Chen, S., Yuan, R., Chai, Y., Xu, Y., Min, L., & Li, N. (2008). A new antibody immobilization technique based on organic polymers protected Prussian blue nanoparticles and gold colloidal nanoparticles for amperometric immunosensors. *Sensors and Actuators B: Chemical*, *135*(1), 236-244.
65. Cai, X., Gao, W., Ma, M., Wu, M., Zhang, L., Zheng, Y., ... & Shi, J. (2015). A Prussian Blue-Based Core–Shell Hollow-Structured Mesoporous Nanoparticle as a Smart Theranostic Agent with Ultrahigh pH-Responsive Longitudinal Relaxivity. *Advanced Materials*, *27*(41), 6382-6389.
66. Chang, L., Chang, S., Chen, W., Han, W., Li, Z., Zhang, Z., ... & Chen, D. (2016). Facile one-pot synthesis of magnetic Prussian blue core/shell nanoparticles for radioactive cesium removal. *RSC advances*, *6*(98), 96223-96228.
67. Dumont, M. F., Yadavilli, S., Sze, R. W., Nazarian, J., & Fernandes, R. (2014). Manganese-containing Prussian blue nanoparticles for imaging of pediatric brain tumors. *International Journal of Nanomedicine*, 2581-2595.
68. Bae, H., Ahmad, T., Rhee, I., Chang, Y., Jin, S. U., & Hong, S. (2012). Carbon-coated iron oxide nanoparticles as contrast agents in magnetic resonance imaging. *Nanoscale research letters*, *7*, 1-5.
69. Qiu, W., Zhu, Q., Gao, F., Gao, F., Huang, J., Pan, Y., & Wang, Q. (2017). Graphene oxide directed in-situ synthesis of Prussian blue for non-enzymatic sensing of hydrogen peroxide released from macrophages. *Materials Science and Engineering: C*, *72*, 692-700.
70. Fu, G., Liu, W., Li, Y., Jin, Y., Jiang, L., Liang, X., ... & Dai, Z. (2014). Magnetic Prussian blue nanoparticles for targeted photothermal therapy under magnetic resonance imaging guidance. *Bioconjugate chemistry*, *25*(9), 1655-1663.
71. Dou, Y., Li, X., Yang, W., Guo, Y., Wu, M., Liu, Y., ... & Chang, J. (2017). Pb@ Au core–satellite multifunctional nanotheranostics for magnetic resonance and computed tomography imaging in vivo and synergetic photothermal and radiosensitive therapy. *ACS Applied Materials & Interfaces*, *9*(2), 1263-1272.
72. Gao, K., Sun, Z., Pan, B. G., Qiao, X., & Hong, C. (2018). Electrochemical immunosensor for alpha-fetoprotein based on prussian blue-carbon nanotube@ polydopamine. *Micro & Nano Letters*, *13*(1), 58-62.
73. Coffey, J. C., Wang, J. H., Smith, M. J. F., Bouchier-Hayes, D., Cotter, T. G., & Redmond, H. P. (2003). Excisional surgery for cancer cure: therapy at a cost. *The lancet oncology*, *4*(12), 760-768.
74. Bentzen, S. M. (2006). Preventing or reducing late side effects of radiation therapy: radiobiology meets molecular pathology. *Nature Reviews Cancer*, *6*(9), 702-713.
75. Schwab, M. (Ed.). (2008). *Encyclopedia of cancer*. Springer Science & Business Media.

76. Liu, Z., Zou, H., Zhao, Z., Zhang, P., Shan, G. G., Kwok, R. T., ... & Tang, B. Z. (2019). Tuning organelle specificity and photodynamic therapy efficiency by molecular function design. *ACS nano*, *13*(10), 11283-11293.
77. Ozturk, K., Dow, M., Carlin, D. E., Bejar, R., & Carter, H. (2018). The emerging potential for network analysis to inform precision cancer medicine. *Journal of molecular biology*, *430*(18), 2875-2899.
78. Fu, G., Liu, W., Feng, S., & Yue, X. (2012). Prussian blue nanoparticles operate as a new generation of photothermal ablation agents for cancer therapy. *Chemical communications*, *48*(94), 11567-11569.
79. Hoffman, H. A., Chakrabarti, L., Dumont, M. F., Sandler, A. D., & Fernandes, R. (2014). Prussian blue nanoparticles for laser-induced photothermal therapy of tumors. *RSC advances*, *4*(56), 29729-29734.
80. Cheng, L., Gong, H., Zhu, W., Liu, J., Wang, X., Liu, G., & Liu, Z. (2014). PEGylated Prussian blue nanocubes as a theranostic agent for simultaneous cancer imaging and photothermal therapy. *Biomaterials*, *35*(37), 9844-9852.
81. de Melo-Diogo, D., Pais-Silva, C., Dias, D. R., Moreira, A. F., & Correia, I. J. Adv. Healthcare Mater. 6, 1700073 (2017).
82. Li, Z. H., Chen, Y., Sun, Y., & Zhang, X. Z. (2021). Platinum-doped prussian blue nanozymes for multiwavelength bioimaging guided photothermal therapy of tumor and anti-inflammation. *ACS nano*, *15*(3), 5189-5200.
83. Li, Z., Zeng, Y., Zhang, D., Wu, M., Wu, L., Huang, A., ... & Liu, J. (2014). Glypican-3 antibody functionalized Prussian blue nanoparticles for targeted MR imaging and photothermal therapy of hepatocellular carcinoma. *Journal of Materials Chemistry B*, *2*(23), 3686-3696.
84. Jia, X., Cai, X., Chen, Y., Wang, S., Xu, H., Zhang, K., ... & Chen, H. (2015). Perfluoropentane-encapsulated hollow mesoporous prussian blue nanocubes for activated ultrasound imaging and photothermal therapy of cancer. *ACS applied materials & interfaces*, *7*(8), 4579-4588.
85. Yu, Z., Hu, W., Zhao, H., Miao, X., Guan, Y., Cai, W., ... & Tan, T. T. Y. (2019). Generating New Cross-Relaxation Pathways by Coating Prussian Blue on NaNdF4 To Fabricate Enhanced Photothermal Agents. *Angewandte Chemie International Edition*, *58*(25), 8536-8540.
86. Tian, W., Su, Y., Tian, Y., Wang, S., Su, X., Liu, Y., ... & Lu, G. (2017). Periodic Mesoporous Organosilica Coated Prussian Blue for MR/PA Dual-Modal Imaging-Guided Photothermal-Chemotherapy of Triple Negative Breast Cancer. *Advanced Science*, *4*(3), 1600356.
87. Cui, H., Zhang, X., Zhang, Z., Zhang, M., Zhang, T., Wu, L., ... & Zhang, W. (2023). Killing three birds with one stone: Tumor-membrane-decorated Prussian blue nanovaccines for synergistic management of skin tumors, radiation dermatitis and wounds. *Composites Part B: Engineering*, *264*, 110900.
88. Shang, T., Liu, J., Chen, Y., Hu, Z., Deng, L., Ran, H., ... & Sun, Y. (2018). In Vivo Targeted Cancer Theranostics by Core/Shell-Structured Multifunctional Prussian Blue/PLGA "Nanococktails". *Particle & Particle Systems Characterization*, *35*(2), 1700306.
89. Liu, B., Wang, W., Fan, J., Long, Y., Xiao, F., Daniyal, M., ... & Wang, W. (2019). RBC membrane camouflaged prussian blue nanoparticles for gamabutolin loading and combined chemo/photothermal therapy of breast cancer. *Biomaterials*, *217*, 119301.
90. Lin, X., Cao, Y., Li, J., Zheng, D., Lan, S., Xue, Y., ... & Zhu, X. (2019). Folic acid-modified Prussian blue/polydopamine nanoparticles as an MRI agent for use in targeted chemo/photothermal therapy. *Biomaterials science*, *7*(7), 2996-3006.
91. Liu, Y., Guo, Q., Zhu, X., Feng, W., Wang, L., Ma, L., ... & Li, F. (2016). Optimization of Prussian Blue Coated NaDyF4: x% Lu Nanocomposites for Multifunctional Imaging-Guided Photothermal Therapy. *Advanced Functional Materials*, *26*(28), 5120-5130.
92. Kale, S. S., Burga, R. A., Sweeney, E. E., Zun, Z., Sze, R. W., Tuesca, A., ... & Fernandes, R. (2017). Composite iron oxide–Prussian blue nanoparticles for magnetically guided T1-weighted magnetic resonance imaging and photothermal therapy of tumors. *International Journal of Nanomedicine*, 6413-6424.

93. Yang, Z. L., Tian, W., Wang, Q., Zhao, Y., Zhang, Y. L., Tian, Y., ... & Zhang, L. J. (2018). Oxygen-evolving mesoporous organosilica coated prussian blue nanoplatform for highly efficient photodynamic therapy of tumors. *Advanced Science*, *5*(5), 1700847.
94. Zhu, W., Liu, K., Sun, X., Wang, X., Li, Y., Cheng, L., & Liu, Z. (2015). Mn2+-doped prussian blue nanocubes for bimodal imaging and photothermal therapy with enhanced performance. *ACS Applied Materials & Interfaces*, *7*(21), 11575-11582.
95. Li, J., Liu, X., Tan, L., Cui, Z., Yang, X., Liang, Y., ... & Wu, S. (2019). Zinc-doped Prussian blue enhances photothermal clearance of Staphylococcus aureus and promotes tissue repair in infected wounds. *Nature communications*, *10*(1), 4490.
96. Mrówczyński, R., & Grześkowiak, B. F. (2022). Biomimetic Catechol-Based Nanomaterials for Combined Anticancer Therapies. *Nanoengineering of Biomaterials*, 145-180.
97. Parchur, A. K., Li, Q., & Zhou, A. (2016). Near-infrared photothermal therapy of Prussian-blue-functionalized lanthanide-ion-doped inorganic/plasmonic multifunctional nanostructures for the selective targeting of HER2-expressing breast cancer cells. *Biomaterials science*, *4*(12), 1781-1791.
98. Borgia, F., Giuffrida, R., Caradonna, E., Vaccaro, M., Guarneri, F., & Cannavò, S. P. (2018). Early and late onset side effects of photodynamic therapy. *Biomedicines*, *6*(1), 12.
99. Zheng, X., Jin, Y., Liu, X., Liu, T., Wang, W., & Yu, H. (2021). Photoactivatable nanogenerators of reactive species for cancer therapy. *Bioactive Materials*, *6*(12), 4301-4318.
100. Fan, W., Huang, P., & Chen, X. (2016). Overcoming the Achilles' heel of photodynamic therapy. *Chemical Society Reviews*, *45*(23), 6488-6519.
101. Hamblin, M. R. (2018). Upconversion in photodynamic therapy: plumbing the depths. *Dalton Transactions*, *47*(26), 8571-8580.
102. Li, M., Xia, J., Tian, R., Wang, J., Fan, J., Du, J., ... & Peng, X. (2018). Near-infrared light-initiated molecular superoxide radical generator: rejuvenating photodynamic therapy against hypoxic tumors. *Journal of the American Chemical Society*, *140*(44), 14851-14859.
103. He, Z., Huang, X., Wang, C., Li, X., Liu, Y., Zhou, Z., ... & Chen, X. (2019). A catalase-like metal-organic framework nanohybrid for O2-evolving synergistic chemoradiotherapy. *Angewandte Chemie*, *131*(26), 8844-8848.
104. Wang, D., Shi, R., Zhou, J., Shi, S., Wu, H., Xu, P., ... & Chen, Q. (2018). Photo-enhanced singlet oxygen generation of prussian blue-based nanocatalyst for augmented photodynamic therapy. Iscience, 9, 14-26.
105. JHu, J. J., Chen, Y., Li, Z. H., Peng, S. Y., Sun, Y., & Zhang, X. Z. (2019). Augment of oxidative damage with enhanced photodynamic process and MTH1 inhibition for tumor therapy. *Nano Letters*, *19*(8), 5568-5576.
106. Wang, D., Zhou, J., Chen, R., Shi, R., Zhao, G., Xia, G., ... & Chen, Q. (2016). Controllable synthesis of dual-MOFs nanostructures for pH-responsive artemisinin delivery, magnetic resonance and optical dual-model imaging-guided chemo/photothermal combinational cancer therapy. *Biomaterials*, *100*, 27-40.
107. Chen, H., Ma, Y., Wang, X., & Zha, Z. (2017). Multifunctional phase-change hollow mesoporous Prussian blue nanoparticles as a NIR light responsive drug co-delivery system to overcome cancer therapeutic resistance. *Journal of Materials Chemistry B*, *5*(34), 7051-7058.
108. Zhang, Y., Liu, Y., Gao, X., Li, X., Niu, X., Yuan, Z., & Wang, W. (2019). Near-infrared-light induced nanoparticles with enhanced tumor tissue penetration and intelligent drug release. *Acta Biomaterialia*, *90*, 314-323.
109. Jing, L., Wang, Y., Yang, Y., Yue, X., & Dai, Z. (2016). Hyaluronic acid modified hollow Prussian blue nanoparticles loading 10-hydroxycamptothecin for targeting thermochemotherapy of cancer. *Theranostics*, *6*(1), 40.
110. Chung, E. J., Leon, L., & Rinaldi, C. (Eds.). (2019). *Nanoparticles for biomedical applications: fundamental concepts, biological interactions and clinical applications*. Elsevier.
111. Zhang, P., Sun, F., Liu, S., & Jiang, S. (2016). Anti-PEG antibodies in the clinic: Current issues and beyond PEGylation. *Journal of Controlled Release*, *244*, 184-193.

112. Xue, P., Cheong, K. K., Wu, Y., & Kang, Y. (2015). An in-vitro study of enzyme-responsive Prussian blue nanoparticles for combined tumor chemotherapy and photothermal therapy. *Colloids and Surfaces B: Biointerfaces*, *125*, 277-283.
113. Wang, D., Zhou, J., Shi, R., Wu, H., Chen, R., Duan, B., ... & Chen, Q. (2017). Biodegradable core-shell dual-metal-organic-frameworks nanotheranostic agent for multiple imaging guided combination cancer therapy. *Theranostics*, *7*(18), 4605.
114. B. Liu, W. Wang, J. Fan, Y. Long, F. Xiao, M. Daniyal, C. Tong, Q. Xie, Y. Jian, B. Li, X. Ma and W. Wang, Biomaterials, 2019, 217, 119301.
115. Charo, I. F., & Ransohoff, R. M. (2006). The many roles of chemokines and chemokine receptors in inflammation. *New England Journal of Medicine*, *354*(6), 610-621.
116. Zhang, K., & Kaufman, R. J. (2008). From endoplasmic-reticulum stress to the inflammatory response. *Nature*, *454*(7203), 455-462.
117. Yang, F., Hu, S., Zhang, Y., Cai, X., Huang, Y., Wang, F., ... & Gu, N. (2012). A hydrogen peroxide-responsive O2 nanogenerator for ultrasound and magnetic-resonance dual modality imaging. *Advanced Materials*, *24*(38), 5205-5211.
118. Zhao, J., Cai, X., Gao, W., Zhang, L., Zou, D., Zheng, Y., ... & Chen, H. (2018). Prussian blue nanozyme with multienzyme activity reduces colitis in mice. *ACS applied materials & interfaces*, *10*(31), 26108-26117.
119. Zhao, J., Gao, W., Cai, X., Xu, J., Zou, D., Li, Z., ... & Zheng, Y. (2019). Nanozyme-mediated catalytic nanotherapy for inflammatory bowel disease. *Theranostics*, *9*(10), 2843.
120. Maaoui, H., Jijie, R., Pan, G. H., Drider, D., Caly, D., Bouckaert, J., ... & Boukherroub, R. (2016). A 980 nm driven photothermal ablation of virulent and antibiotic resistant Gram-positive and Gram-negative bacteria strains using Prussian blue nanoparticles. *Journal of colloid and interface science*, *480*, 63-68.
121. Jiang, T., Wang, Y., Li, Z., Aslan, H., Sun, L., Sun, Y., ... & Yu, M. (2019). Prussian blue-encapsulated Fe3O4 nanoparticles for reusable photothermal sterilization of water. *Journal of colloid and interface science*, *540*, 354-361.
122. Hao, Z., Lin, X., Li, J., Yin, Y., Gao, X., Wang, S., & Liu, Y. (2021). Multifunctional nanoplatform for dual-mode sensitive detection of pathogenic bacteria and the real-time bacteria inactivation. *Biosensors and Bioelectronics*, *173*, 112789.
123. Gao, X., Wu, H., Hao, Z., Ji, X., Lin, X., Wang, S., & Liu, Y. (2020). A multifunctional plasmonic chip for bacteria capture, imaging, detection, and in situ elimination for wound therapy. *Nanoscale*, *12*(11), 6489-6497.
124. Luo, Y., Li, J., Liu, X., Tan, L., Cui, Z., Feng, X., ... & Wu, S. (2019). Dual metal–organic framework heterointerface. *ACS Central Science*, *5*(9), 1591-1601.
125. Cai, S., Qian, J., Yang, S., Kuang, L., & Hua, D. (2019). Acetylcysteine-decorated Prussian blue nanoparticles for strong photothermal sterilization and focal infection treatment. *Colloids and Surfaces B: Biointerfaces*, *181*, 31-38.
126. Gu, Z., Zhu, S., Yan, L., Zhao, F., & Zhao, Y. (2019). Graphene-based smart platforms for combined Cancer therapy. *Advanced Materials*, *31*(9), 1800662.
127. Lei, S., Chen, J., Zeng, K., Wang, M., & Ge, X. (2019). Visual dual chemodynamic/photothermal therapeutic nanoplatform based on superoxide dismutase plus Prussian blue. *Nano Research*, *12*, 1071-1082.
128. Tian, B., Wang, C., Du, Y., Dong, S., Feng, L., Liu, B., ... & Yang, P. (2022). Near Infrared-Triggered Theranostic Nanoplatform with Controlled Release of HSP90 Inhibitor for Synergistic Mild Photothermal and Enhanced Nanocatalytic Therapy with Hypoxia Relief. *Small*, *18*(28), 2200786.
129. Zhang, C., Yan, L., Gu, Z., & Zhao, Y. (2019). Strategies based on metal-based nanoparticles for hypoxic-tumor radiotherapy. *Chemical science*, *10*(29), 6932-6943.
130. Ren, C., Cheng, Y., Li, W., Liu, P., Yang, L., Lu, Q., ... & Li, N. (2020). Ultra-small Bi 2 S 3 nanodot-doped reversible Fe (ii/iii)-based hollow mesoporous Prussian blue nanocubes for amplified tumor oxidative stress-augmented photo-/radiotherapy. *Biomaterials science*, *8*(7), 1981-1995.

131. Zhou, J., Li, M., Hou, Y., Luo, Z., Chen, Q., Cao, H., ... & Cai, K. (2018). Engineering of a nanosized biocatalyst for combined tumor starvation and low-temperature photothermal therapy. *ACS nano*, *12*(3), 2858-2872.
132. Liang, J., Sun, Y., Wang, K., Zhang, Y., Guo, L., Bao, Z., ... & Yuan, Y. (2023). Prussian Blue-Derived Nanoplatform for In Situ Amplified Photothermal/Chemodynamic/Starvation Therapy. *ACS Applied Materials & Interfaces*, *15*(14), 18191-18204.
133. Cano-Mejia, J., Burga, R. A., Sweeney, E. E., Fisher, J. P., Bollard, C. M., Sandler, A. D., ... & Fernandes, R. (2017). Prussian blue nanoparticle-based photothermal therapy combined with checkpoint inhibition for photothermal immunotherapy of neuroblastoma. *Nanomedicine: Nanotechnology, Biology and Medicine*, *13*(2), 771-781.
134. Cano-Mejia, J., Bookstaver, M. L., Sweeney, E. E., Jewell, C. M., & Fernandes, R. (2019). Prussian blue nanoparticle-based antigenicity and adjuvanticity trigger robust antitumor immune responses against neuroblastoma. *Biomaterials science*, *7*(5), 1875-1887.
135. Fass, L. (2008). Imaging and cancer: a review. *Molecular oncology*, *2*(2), 115-152.
136. *Griewing, B., Hielscher, H., & Lütcke, A. (1992). The importance of MRI (magnetic resonance imaging) for the diagnosis of brainstem infarction. Bildgebung= Imaging, 59(2), 94-97.*
137. Shokouhimehr, M., Soehnlen, E. S., Khitrin, A., Basu, S., & Huang, S. D. (2010). Biocompatible Prussian blue nanoparticles: Preparation, stability, cytotoxicity, and potential use as an MRI contrast agent. *Inorganic Chemistry Communications*, *13*(1), 58-61.
138. Estelrich, J., Sánchez-Martín, M. J., & Busquets, M. A. (2015). Nanoparticles in magnetic resonance imaging: from simple to dual contrast agents. *International journal of nanomedicine*, 1727-1741.
139. Larionova, J., & Guari, Y. (2019). *Prussian Blue-Type Nanoparticles and Nanocomposites: Synthesis, Devices, and Applications.*
140. Dumont, M. F., Hoffman, H. A., Yoon, P. R., Conklin, L. S., Saha, S. R., Paglione, J., ... & Fernandes, R. (2014). Biofunctionalized gadolinium-containing prussian blue nanoparticles as multimodal molecular imaging agents. *Bioconjugate chemistry*, *25*(1), 129-137.
141. Moore, C., & Jokerst, J. V. (2019). Strategies for image-guided therapy, surgery, and drug delivery using photoacoustic imaging. *Theranostics*, *9*(6), 1550.
142. Liu, Y., Bhattarai, P., Dai, Z., & Chen, X. (2019). Photothermal therapy and photoacoustic imaging via nanotheranostics in fighting cancer. *Chemical Society Reviews*, *48*(7), 2053-2108.
143. Liang, X., Deng, Z., Jing, L., Li, X., Dai, Z., Li, C., & Huang, M. (2013). Prussian blue nanoparticles operate as a contrast agent for enhanced photoacoustic imaging. *Chemical communications*, *49*(94), 11029-11031.
144. Kim, T., Lemaster, J. E., Chen, F., Li, J., & Jokerst, J. V. (2017). Photoacoustic imaging of human mesenchymal stem cells labeled with Prussian blue–poly (l-lysine) nanocomplexes. *ACS nano*, *11*(9), 9022-9032.
145. Moorthy, M. S., Hoang, G., Subramanian, B., Bui, N. Q., Panchanathan, M., Mondal, S., ... & Oh, J. (2018). Prussian blue decorated mesoporous silica hybrid nanocarriers for photoacoustic imaging-guided synergistic chemo-photothermal combination therapy. *Journal of Materials Chemistry B*, *6*(32), 5220-5233.
146. Cai, X., Gao, W., Zhang, L., Ma, M., Liu, T., Du, W., ... & Shi, J. (2016). Enabling Prussian blue with tunable localized surface plasmon resonances: simultaneously enhanced dual-mode imaging and tumor photothermal therapy. *ACS nano*, *10*(12), 11115-11126.
147. Lee, N., Yoo, D., Ling, D., Cho, M. H., Hyeon, T., & Cheon, J. (2015). Iron oxide based nanoparticles for multimodal imaging and magnetoresponsive therapy. *Chemical reviews*, *115*(19), 10637-10689.
148. Fu, Q., Zhu, R., Song, J., Yang, H., & Chen, X. (2019). Photoacoustic imaging: contrast agents and their biomedical applications. *Advanced Materials*, *31*(6), 1805875.
149. Zhang, N., Cai, X., Gao, W., Wang, R., Xu, C., Yao, Y., ... & Zheng, Y. (2016). A multifunctional theranostic nanoagent for dual-mode image-guided HIFU/chemo-synergistic cancer therapy. *Theranostics*, *6*(3), 404.

150. Du, B., Cao, X., Zhao, F., Su, X., Wang, Y., Yan, X., ... & Yao, H. (2016). Multimodal imaging-guided, dual-targeted photothermal therapy for cancer. *Journal of Materials Chemistry B*, *4*(11), 2038-2050.
151. Shi, Y., Shi, Y., Wang, Z., Zhang, J., Hao, R., Zhang, G., ... & Zeng, L. (2023). Glucose-responsive mesoporous prussian blue nanoprobes coated with ultrasmall gold and manganese dioxide for magnetic resonance imaging and enhanced antitumor therapy. *Chemical Engineering Journal*, *453*, 139885.
152. Wang, X., Li, H., Li, F., Han, X., & Chen, G. (2019). Prussian blue-coated lanthanide-doped core/shell/shell nanocrystals for NIR-II image-guided photothermal therapy. *Nanoscale*, *11*(45), 22079-22088.
153. Wang, H., Xu, S., Fan, D., Geng, X., Zhi, G., Wu, D., ... & Wang, X. (2022). Multifunctional microcapsules: a theranostic agent for US/MR/PAT multi-modality imaging and synergistic chemo-photothermal osteosarcoma therapy. *Bioactive materials*, *7*, 453-465.
154. Chen, Y., Wu, L., Wang, Q., Wu, M., Xu, B., Liu, X., & Liu, J. (2016). Toxicological evaluation of Prussian blue nanoparticles after short exposure of mice. *Human & experimental toxicology*, *35*(10), 1123-1132.
155. Sharifi, S., Behzadi, S., Laurent, S., Forrest, M. L., Stroeve, P., & Mahmoudi, M. (2012). Toxicity of nanomaterials. *Chemical Society Reviews*, *41*(6), 2323-2343.

Chapter 3

Fundamental understanding of size and surface modification effects on r_1 relaxivity of Prussian blue nanocube@m-SiO_2: a novel targeted chemo- photodynamic theranostic agent to treat colon cancer

Chapter 3. Fundamental understanding of size and surface modification effects on r_1 relaxivity of Prussian blue nanocube@m-SiO_2: a novel targeted chemo-photodynamic theranostic agent to treat colon cancer

3.1 Introduction

Coordination polymer nanostructures are one of the emerging types of inorganic nanostructures where metal ions are linked together, forming a cyanide bridged infinite network. They have gained increasing interest in recent time due to ability to combine multiple activities within the one multifunctional nano-object which can be ascribed to their molecular characteristics.[1,2] One of the promising candidates in this domain is the Prussian blue (PB), a face-centred cubic (fcc) structure based Metal – Organic Framework (MOF).[3] Its easy tuneable porosity and tailorable structures impart PB into wide range of prospective applications like energy storage, hydrogen storage, electrochromic, photomagnetic devices etc. Apart from pure phase, due to high ligand field stabilization energy (LFSE) in comparison with iron compounds like Fe_3O_4 etc., PB forms thermodynamically stable mixed-valence phase with generic formula $A_{1-x}Fe^{III}[Fe^{II}(CN)_6]_{1-x/4}\Delta_{x/4}$, where A and Δ represent alkali ion and hexacyanoferrate vacancies, that facilitates easy functionalization on PB and widens applicational prospects.[4] Alkali free PB is also known as insoluble PB, containing water molecules with increased amount Fe^{3+} leads to charge balance.[5] PB also exhibits strong potentiality in biomedical applications like drug delivery system, contrast agents (CAs) for different diagnostics purposes including x-ray computed and positron emission tomography, optical biomarkers, ultrasound imaging etc. and NIR assisted therapeutic activity like photothermal ablation, photodynamic therapy etc.[6,7,8] Among various diagnostics modalities, special thrusts is generally given to design PB as CAs for Magnetic Resonance Imaging (MRI), since it has the advantage of non-ionizing type radiation, high sensitivity to afford non-destructive details of soft tissues and functional information on lesions, limitless penetration depth and high spatial resolution (~ 100 μm) in comparison with other imaging modalities.[9,10] Herein, it may be stated that MRI, example of the preferred non-invasive imaging technique, is commonly adopted in modern clinical study to diagnose internal body structure with high spatial resolution and exquisite anatomical contrast efficiency, utilizes the basic principle of Nuclear Magnetic Resonance (NMR) where a magnetic field gradient is applied to encode

signal in all three spatial directions. NMR signals are generally weighted by density of H_2O molecules and the longitudinal (T_1) and / or transverse (T_2) relaxation times of the tissues and the efficiency of CAs depends on two parameters, namely longitudinal (r_1) and transverse (r_2) relaxation of protons. For $\frac{r_2}{r_1} < 2$, CA is positive and it is called T_1-relaxing CA which gives brighter spot of the diagnostic area. Mainly, mononuclear Gd^{3+} complexes with $r_1 \sim 3 – 5$ $mM^{-1}s^{-1}$ at 20 MHz and 298 K are used T_1 CAs. In other case, $\frac{r_2}{r_1} > 2$ gives dark signal, the CA is said to be negative and is defined as T_2-relaxing CA that mostly involves superparamagnetic iron oxide based nanoparticles.[11] In this context, it may be stated that mostly Gd^{3+} based chelating agents, namely DOTAREM® and MAGNEVIST® are used nowadays with dose of ten to twenty mL of 0.5 mM solution depending on body weight besides this they causes a serious side effects like gadolinium toxicity, nephrogenic systemic fibrosis.[12,13] Herein, current research effort focuses on improving the effect of CA in order to be able to reduce the dose of administration of CA with very mild side effect.

Concerning, PB which is being used as sole U.S. Food and Drug Administration approved T_1-weighted CA for MRI has the advantage of high signal-to-noise ratio, fast scanning, bright field image etc. in comparison with T_2-weighted CAs.[6] Despite of several prospects, practical utility of pure PB nanostructures are limited due to instability particularly in acidic pH condition in the neighbourhood of cancer cell or tumor microenvironment, hence they are often stabilized within various matrixes such as polymers, biopolymers, alumina, amorphous and mesoporous silica or by using stabilizing ligands in solution. It is well-reported that these protocols of stabilization of PB nanostructures into different matrixes or in organic phase colloids and only few methods allow the preparation of PB nanostructures in aqueous solutions facilitating the scope of using PB nanostructures in several bioanalytical and biomedical applications.[6,7,14,15] Herein, several reports exist for other materials e.g. Gd_2O_3, Fe_3O_4 etc. to illustrate that various functionalizations alter the contrast efficiency of the agent, as well as size and shape of their nanostructure form play an important role. Though lots of theoretical and experimental efforts were previously given to examine the influence of these parameters in order to increase contrast efficiency, but no such reports, except few, exist to indicate the influence of surface functionalities, shape and size of PB nanostructures on MRI contrast efficiency.[16,17] As an example, PB nanoparticles (~ 13 nm), stabilized with citric acid and conjugated with 5-(amino-acetomido) fluorescein dye, shows modest $r_1 \sim 0.079$ $mM^{-1}s^{-1}$, while Gd^{3+}, Mn^{2+} doping increase r_1 by at least 1 – 2 order of magnitude.[18,19] In this context, Guari *et al.* have demonstrated that Gd^{3+} doped PB nanoparticle, coated with chitosan, exhibits r_1 which is two

times higher than clinically approved paramagnetic Gd^{3+} chelate complexes.[20] Hence, in this paper, our primary objective is to investigate the role of size, surface functional group and defects of PB nanostructures on r_1-relaxation parameter. In this context, it may be mentioned that functionalized nanoparticles are further modified with RGD peptides, Hyaluronic acid etc. for easy localization on over-expressed receptor on cancer cell and chemotherapeutic drugs are loaded to increase therapeutic efficiency.[6,16,21] To best of knowledge, no report exists to indicate the role of target specific agent or drug on efficiency of CAs in MRI, hence in the present chapter we have also given emphasize to understand their influence on r_1- parameter using Hyaluronic acid (HA) and Doxorubicin (DOX) as target specific agent and chemotherapeutic drug respectively. Currently, the experimental parameters influencing r_1-relaxation are expressed in terms of the change of internal time correlation factors like rotational correlation time, residence time, diffusion time, electron correlation time etc., however they are very hard to analyse in case of complicated nanoparticle based CAs containing multiple paramagnetic site, coordinated with water molecules. In this chapter, we have developed an intuitive model according to Solomon – Bloembergen – Morgan theory to explain the variation of r_1-relaxation parameter in each functionalization step.[19] In this chapter, we have developed an intuitive model according to Solomon – Bloembergen – Morgan theory to explain the influence of structural defect, different modification such as m-SiO_2 coating, HA functionalization and DOX loading on r_1 relaxivity values in different sized PBNC nanostructure. Finally, we have evaluated theranostic perfoFrmances of our synthesized PB nanostructures, coated with mesoporous SiO_2 (m-SiO_2) and functionalized with HA, followed by DOX loading on colon carcinoma cell line (HCT 116). Several reports demonstrates that CD44 expression in the colon cancer tissue was substantially higher than that in normal mucosa.[22] On the basis of this background, HA functionalization has been executed which provides target specific cellular uptake to HCT 116 cell line. Moreover, functionalization of HA not only increases CD44 receptor based target specificity but also makes the nanoplatform very much stable for biological environment.[7] Apart from stabilization, herein m-SiO_2 makes HA functionalization easy and its porous structure facilitates DOX loading. In this context, we have compared the localization of our synthesized nanostructures using Human embryonic kidney cell (HEK 293) as reference.

3.2 Experimental section

3.2.1 Chemicals and Cell lines: $K_4[Fe(CN)_6]\cdot 3H_2O$, tetraethyl orthosilicate (TEOS), N-cetyl-N,N,N-trimethyl ammonium bromide (CTAB), citric acid anhydrous, hydrochloric acid

(35 wt%) were brought from Merck. Absolute ethanol, acetone, concentrated ammonia aqueous solution (25 wt %) were purchased from Merck, Amplura. $FeCl_3{\cdot}6H_2O$, doxorubicin hydrochloride, N-(3-Dimethylaminopropyl)-N/-ethylcarbodiimide Hydrochloride (EDC), 1,3-Diphenylisobenzofuran (DPBF) were purchased from Sigma Aldrich. Hyaluronic Acid (HA) was collected from TCI chemicals. Cell culture media components viz. Dulbecco's Modified Eagle Medium (DMEM), Penicillin-Streptomycin-Neomycin (PSN) antibiotic cocktail, Fetal bovine serum (FBS), ethylenediaminetetraacetic acid (EDTA) and trypsin were obtained from Gibco, USA. Other compulsory fine and raw chemicals were obtained from SRL, India, and Sigma-Aldrich, USA. Human colorectal carcinoma (HCT 116) and Human embryonic kidney 293 (HEK 293) cell line were purchased from National Centre for Cell Sciences (NCCS), India. Antibodies were procured from Cell Signalling Technology (CST), and eBioscience, USA. Other reagents were provided from best existing commercial sources and all reactions were performed without further purification.

3.2.2 Synthesis of insoluble Prussian blue Nanocubes: Citric acid capped insoluble Prussian Blue Nanocubes (PBNCs) were synthesized by a little modified reflux technique using single anionic source.[6,23] Briefly, Solution A and Solution B were prepared separately by dissolving 5.40 mg of $FeCl_3.6H_2O$ and 8.45 mg of $K_4Fe(CN)_6.3H_2O$ in 30 mL of DI water, taken into three neck flasks, followed by adding 392.00 mg of citric acid at 60°C. Maintaining the same temperature, Solution A was dropwise added into solution B with vigorous stirring and a bright blue dispersed solution appeared after 1.0 h stirring. After completing the reaction, mixture solution was cooled down at room temperature and dispersed solution was centrifuged at 12,500 rpm for 15 minutes. After washing with acetone for three times, final product in powder form was obtained after drying at 60°C under vacuum condition. In order to get higher sized PBNCs, another experiment was carried out maintain mixing reaction temperature 80°C. Two PBNCs, prepared at two different temperatures, are named as $PBNC_{60}$ and $PBNC_{80}$ respectively.

3.2.3 Synthesis of mesoporous silica coated PBNC: Mesoporous silica (m-SiO_2) coated PBNCs (PBNC@m-SiO_2) was synthesized by CTAB directed sol-gel method.[24] Typically, as-prepared PBNCs (25.00 mg), DI water (1 mL), 25% NH_3 (0.5 mL), and TEOS (13 μL) were mixed with 10 mL ethanol and were stirred continuously for 5 minutes at 30°C. Then CTAB (0.06 g) and DI water (7.5 mL) were added to the above solution. After 12 h of continuous stirring, subsequently 25% NH_3 (140 μL) and TEOS (100 μL) were added with stirring for another 2 h. Then the particles were centrifuged at 12,500 rpm for 15 minutes and were washed

with ethanol for three times. To remove CTAB, the particles were extracted in ethanol solution containing 10 mL water and 1 mL HCl (35%) for 4.5 h. Finally, the mixture was centrifuged again, washed with ethanol thrice and dried at 45°C under vacuum for further use. Two different sized PBNCs, coated with m-SiO_2, were named as $PBNC_{60}$@m-SiO_2 and $PBNC_{80}$@m-SiO_2 respectively.

3.2.4 Functionalization of PBNC@m-SiO_2 with hyaluronic acid: The m-SiO_2 coated PBNC nanostructures were first functionalized with $–NH_2$.[25] Briefly, 20.0 mg as-coated samples were dispersed in 40.0 mL ethanol, subsequently 2.4 mL of APETS was added and was left for 30.0 h with continue stirring at 80 °C under reflux condition. Then the mixture was centrifuged and was washed with ethanol for 3 times for further use (ascertained as Solution C). Secondly, EDC linker was used to link between $–NH_2$ and –COOH of the HA. Briefly 30.0 mg EDC was added with 22.0 mL PBS buffer (pH 7.4) solution containing 12.0 mg HA, followed by continuous stirring for 4.0 h at room temperature. Then, Solution C was added dropwise into the HA containing solution. Furthermore 24.0 h of continuous stirring was conducted after which particles were collected by centrifugation, followed by washing with PBS buffer for 3 times. Finally, the collected particles were designated as $PBNC_{60}$@m-SiO_2@HA and $PBNC_{80}$@m-SiO_2@HA according to $PBNC_{60}$@m-SiO_2 and $PBNC_{80}$@m-SiO_2 as precursors respectively.

3.2.5 Characterization: The crystallography and phase information of synthesized PBNCs were acquired from powder X-ray diffraction pattern, recorded in ULTIMA IV X-Ray Diffractometer (Rigaku) operating at 40kV and 40 mA using CuK_α radiation. Microstructures of the as-prepared samples were investigated by field emission scanning electron microscopy (FESEM, S – 4800, Hitachi, Japan) and high resolution transmission electron microscopy (HRTEM, JEM-2100, JEOL, Japan). Thermal gravimetric analysis (TGA), absorption characteristics (200 – 900 nm), surface charge, and surface functionalizations were determined by DTA-TGA instrument (SHIMADZU, DTG-60H), UV-vis-NIR spectrophotometer (PerkinElmer Instruments, Waltham, MA), Nano-ZetaSizer (Brookhaven Instruments, Holtsville, NY) and Fourier transform infrared spectrometer (FTIR, PerkinElmer, Spectrum-2000) respectively. Quantachrome, NOVA 1000e system was adopted to capture the nitrogen adsorption/desorption isotherms on which Barret-Joyner-Halenda (BHJ) and Brunauer-Emmett-Teller (BET) analyses were carried out in order to determine surface area, pore diameter and pore volume of the as-prepared nanostructure.

3.2.6 NIR triggered extracellular singlet Oxygen ($^1O_2$) generation: To examine $^1O_2$ generation, we chose DPBF probe trapping method by monitoring absorption peak of DPBF at 410 nm through UV-vis spectroscopy. Generation of $^1O_2$ oxidised DPBF leads to decrease in absorption. For this 3 mL of 100 μg/mL $PBNC_{60}$@m-SiO_2@HA alcoholic solution was mixed with 1 mL of 68 μg/mL DPBF alcoholic solution in each vial under irradiation of 808 nm (1.0 Wcm^{-2}) NIR light in time dependant manner. Only DPBF solution or mixed solution of $PBNC_{60}$@m-SiO_2@HA and DPBF under dark was taken as a control.[7]

3.2.7 DOX loading and releasing profile: DOX, an anticancer drug was loaded in the pores of mesoporous silica on $PBNC_{60}$@m-SiO_2@HA to improve anticancer activity. Briefly, 2 mg DOX containing 1.2 mL of PBS solution was dropwise added with 178 μg/mL of 4 mL $PBNC_{60}$@m-SiO_2@HA solution under stirring where concentration of as prepared solution was measured from UV-vis-NIR spectroscopy by monitoring absorption of $PBNC_{60}$. Then the mixed solution was left for overnight with continuous stirring at 300 rpm under dark. After that $PBNC_{60}$@m-SiO_2@HA@DOX nanoplatforms were collected by centrifugation and washing with PBS. Collected $PBNC_{60}$@m-SiO_2@HA@DOX was redispersed in PBS buffer for future use and supernatant was also collected for the measurement of DOX loading efficiency through UV-vis spectroscopy by monitoring absorption at 480 nm. DOX loading efficiency was measured by,

$$\text{DOX loading efficiency (\%)} = \frac{\text{Concentration of the DOX in the nanoplatforms}}{\text{concentration of the given DOX}} * 100\%$$

To investigate release behaviour of DOX from $PBNC_{60}$@m-SiO_2@HA@DOX, we dispersed 1.0 m1 of previous DOX loaded nanoplatform in 4.0 mL PBS buffer (pH 5 & pH 7.4) separately and poured it in dialysis bag (MWCO 12 kDa).[16] After that the dialysis bag was immersed in a beaker containing 50.0 mL of fresh buffer with slow stirring. Then at predetermined time interval 1.0 mL fresh buffer was replaced after collecting 1.0 mL of DOX loaded buffer from beaker to maintain concentration. Finally release profile was measured from UV-vis spectroscopy, monitoring at 480 nm.

3.2.8 Cell culture: Briefly, cells were cultured in DMEM containing 10% fetal bovine serum (FBS) and 1% antibiotic cocktail at 37 °C in a humidified condition under constant 5% CO_2. After 75−80% confluency, cells were harvested with trypsin (0.25%), and EDTA (0.52 mM) in phosphate buffered saline (PBS), plated at a necessary density to allow them to re-equilibrate before the experimentation.[26]

3.2.9 *In-vitro* T_1-weighted cellular MRI contrast measurement: For cellular MR imaging, ~ 6×10^3 numbers of HCT 116 cells were incubated in a 96 well plate. Cells were treated with $PBNC_{60}$@m-SiO_2@HA@DOX under six different concentration of PBNC (0.025, 0.05, 0.1, 0.2, 0.4, 0.6 mM) and incubated for 24 h. Then cells were washed with PBS for three times and fixed using paraformaldehyde. To avoid air susceptibility 100 mL of 2% low melting agarose was added to each well. Then the plate was kept at 4ºC to solidify the cell suspensions. MR contrast measurement of both bare PBNC along with each step of modification were also evaluated at different concentrations (0.025 – 0.6 mM) in 96 well plate under dispersion in PBS. MRI was performed by keeping the samples under a 3T clinical MRI scanner (Siemens MAGNETOM Verio), using a pre-fabricated sample holder. MR phantom images were obtained by applying a spin-echo multi-section pulse sequence. In order to determine the $\boldsymbol{T_1}$ relaxation of the sample, coronal images were acquired under the following constant parameters: magnetic field (B), 3T; inversion time (TI), 1100 ms; echo time (TE), 9.6 ms; repetition time (TR), 2000 ms; matrix size, 256 mm×256 mm; field of view (FOV), 150 mm×150 mm; slice thickness, 3 mm. The MRI signal intensity (SI) and visualization of the phantom images were analysed using the standard software provided by the manufacturer.

The longitudinal relaxivity value (r_1) at a fixed magnetic field (3T) and inversion time (1100 ms) for all sample was extracted from the plot of signal intensity versus concentration of contrast agent (CA) followed by the equation

$$SI = A - Pe^{-(TI*r_1)C}$$

Where SI, TI, C represents signal intensity, inversion of time, concentration of the contrast agent and A, P consider as a constants.[27] Here in whole experiment, the signal intensity from untreated HCT 116 cells and only PBS were taken as a control which contributes as a diamagnetic behaviour.

3.2.10 Cell viability assay: MTT [(4, 5-dimethyl-thiazol-2-yl)-2, 5-diphenyl tetrazolium bromide] assay was carried out to screen the cytotoxic effects of our synthesized nanoplatform in HEK 293 and HCT 116 cell line with concentration and 808 nm NIR laser exposure time dependent manner.[28] Cells at required density (2×10^6 cells/well) were seeded in each well of 96 well plate and treated with different concentrations (0-70 μg/mL) of $PBNC_{60}$@m-SiO_2@HA@DOX and the individuals $PBNC_{60}$, $PBNC_{60}$@m-SiO_2 and $PBNC_{60}$@m-SiO_2@HA. Soon after treatment, plates were kept in an incubator for 24 h at 37 °C in a humidified CO_2-rich condition (5%). After completion of the incubation period, cells were thoroughly washed with PBS followed by the addition of MTT solution (4 mg/mL) and kept it

in an incubator for 4 h. The absorbance of the DMSO-solubilized intracellular formazan salt was recorded at 595 nm using an ELISA reader (Emax, Molecular Device, USA). In all cases, the samples were sonicated before treating in cell line to get homogenized mixtures. The final reported biological data were represented after repeating the experiments in triplicate.

3.2.11 *In-vitro* photodynamic therapy (PDT): On the basis of preliminary screening experimentation, 21 μg/mL concentration of $PBNC_{60}$@m-SiO_2@HA@DOX were chosen for further experimentation, to check whether they exhibit any photosensitizing effect within the cells. Hence, treated HCT 116 and HEK 293 cells were exposed under 808 nm irradiation in a time-dependent manner (0, 10, 20, 30 and 40 min) following the MTT assay to determine the photodynamic and chemo-dynamic efficacy.

3.2.12 Quantification of apoptosis using Annexin V-FITC kit: Apoptosis was examined through the use of an Annexin V-FITC apoptosis detection kit (Calbiochem, CA, USA).[29,30] After treatment of PB_{60}@m-SiO_2@HA@DOX as per IC_{50} value, HCT 116 cells were irradiated for 0, 10 and 20 min, cells were washed and stained with Annexin V-FITC and propidium iodide (PI) in accordance with the manufacturer's instructions. The percentages of apoptotic (early and late), necrotic along with viable cells were evaluated by flow cytometry (BD LSRFortessa, San Jose, CA, USA). 10^6 cells were taken for each sample analysis.

3.2.12 Determination of intracellular ROS (iROS): Mitochondria are the primary source of the amplification of reactive oxygen species (ROS) production in mammalian cells and it plays a significant role in the stimulation of apoptosis in a variety of cells.[31] To determine the iROS, we irradiated the 21 μg/mL of PB_{60}@m-SiO_2@HA@DOX treated HCT 116 cells in time dependent manner, after that the HCT 116 cells were incubated with 10 μM H2DCFH-DA (2′, 7′-dichlorofluorescein diacetate) at 37 °C for 25 min before the analysis by flow cytometer (BD LSRFortessa, San Jose, CA, USA). The increment of DCF fluorescence directly reflects the generated ROS inside cells which were represented as mean fluorescence intensity of DCF where untreated cells considered as a control. 10^6 cells were taken for each sample analysis.

3.2.13 Confocal microscopy: Briefly, after treatment with 21 μg/mL of PB_{60}@m-SiO_2@HA@DOX, HCT 116 cells were irradiated in time dependent manner and incubated for 24h. Then the cover slips containing HCT 116 cells were washed twice for 10 min each in 0.01 M PBS and incubated for 1 h in blocking solution containing 2% normal bovine serum, and 0.3% Triton X-100 in PBS. After blocking, the slides were incubated overnight at 4°C with the proper primary antibody (Gamma H2AX, PARP, Cytochrome c and SOD). Alexa Fluor 555

tagged Gamma H2AX was used as Primary tagged antibody and in case of SOD and Cytochrome c; FITC tagged anti rabbit secondary was used. Secondary antibodies were diluted, 1:100 in blocking solution and incubated for 2h. The slides were then counterstained with 6-diamidino-2-phenylindole (DAPI) for 10 min and mounted with the Prolong Anti-fade Reagent (Molecular Probe, Eugene, OR, USA). The fluorescence intensity of Doxorubicin was also measured by using a confocal laser scanning microscope (FV 10i, Olympus, Japan)**.**[32] Further, the fluorescence intensity of Doxorubicin was also observed in HEK 293 cell line where Phalloidine 488 and DAPI was used as a counter stainer.

3.2.14 Caspase-3 and Caspase-9 activity assays: HCT 116 cells were irradiated under 808 nm NIR light after 21 µg/mL of PB_{60}@m-SiO_2@HA@DOX treatment. Caspase-3 and caspase-9 activities were quantified with the commercially available caspase-3 and caspase-9 colorimetric assay kit (BioVision Research Products, Mountain View, CA), respectively. Caspase activities were detected at 405 nm by a spectrophotometer on an ELISA reader.[33]

3.2.15 Statistical analysis: Data were presented as mean ± SEM. Statistical significance and differences among the groups were assessed via one-way analysis of variance (ANOVA) using OriginPro 8.0 software (San Diego, CA, USA). 'p' value of 0.05 was considered as significant.

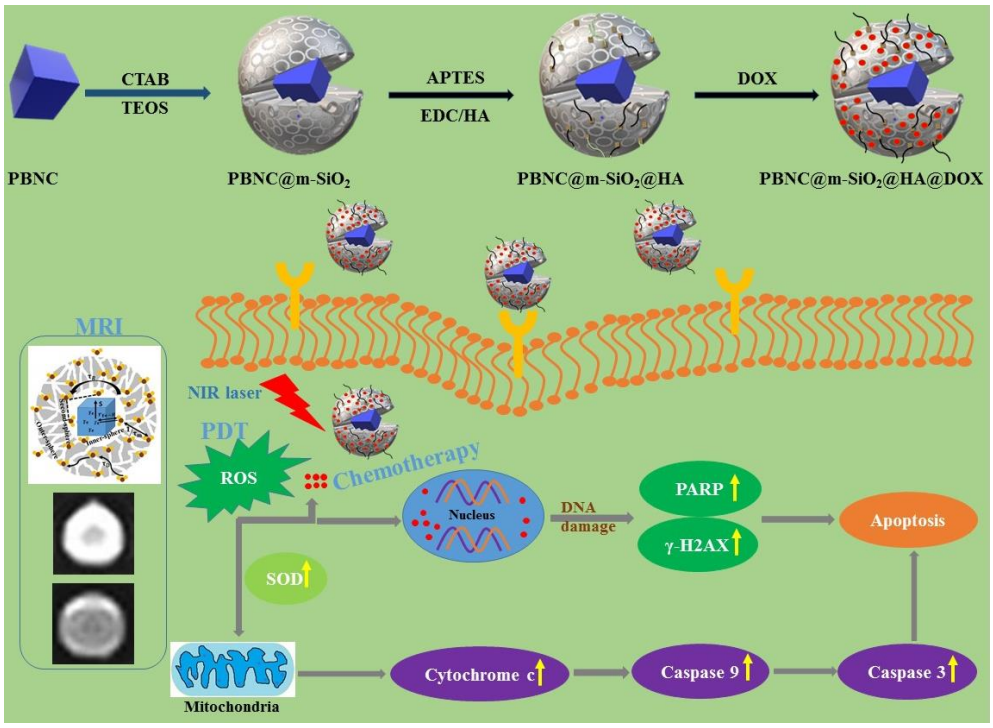

Scheme 1: Demonstration of synthesis of PBNC@m-SiO_2@HA@DOX nanoplatforms, size dependent MRI contrast efficiency and cell death through targeted chemo-photodynamic therapy upon irradiation of 808 NIR laser.

3.3 Result and discussions

3.3.1 Synthesis and Characterization: The preparation, size dependent contrast efficiency in MRI diagnosis and chemo-photodynamic therapeutic activity of PBNC@m-SiO_2@HA@DOX nanoplatform are schematically shown in Scheme 1. Herein, m-SiO_2 has been coated onto PBNC using CTAB-assisted sol-gel technique with subsequent functionalization with HA for stabilization and target specificity against CD44 receptors which is commonly overexpressed within human colorectal carcinoma (HCT 116) cell line. After loading with DOX, PBNC@m-SiO_2@HA@DOX nanoplatforms are examined for combined photodynamic and chemotherapy. Herein, it may be stated that CTAB coating plays the role of secondary surfactant making PBNCs hydrophilic which in consequence acts as seeds for coating of m-SiO_2.

XRD patterns of the samples (shown in Figure 1(a) and (b)) consist of eleven peaks, measured at $2\theta = 17.50, 24.82, 35.42, 39.74, 43.80, 50.96, 54.28, 57.46, 66.37, 69.29, 77.65^0$, can readily be indexed with Bragg's reflection from (200), (220), (400), (420), (422), (440), (600), (620), (640), (642) and (121) planes corresponding to face centred cubic phase of PBNC (JCPDS card no. 73-0687). Absence of any other peak confirms phase purity of the samples. It has been studied previously that bare PBNCs having *Pm3m* space group grows with $[Fe^{2+}(CN)_6]^{4-}$ vacancy sites, replaced by H_2O molecules. They are either bonded directly with Fe^{3+}, known as coordinated H_2O molecule, or bonded with coordinated H_2O molecules, referred as zeolitic-like H_2O molecule. As both of them highly depend on synthesis condition and have significant influence on several physical properties of PBNCs, hence we have qualitatively determined coordinated and zeolitic H_2O molecules from Rietveld analysis using Maud software according to the method as prescribed by Samain *et al.*[34] Herein, it is being considered that ordered vacancies can be described by the parameter κ representing occupancy probability of Fe^{2+} at 1b site corresponding to $[Fe^{2+}(CN)_6]^{4-}$ at the centre of the unit cell, with $\kappa = 1$ illustrates completely ordered structure. Particularly, $\kappa = ¾$ illustrates that 25% of $[Fe^{2+}(CN)_6]^{4-}$ sites remains unoccupied. After rigorous refinements, we have obtained occupancy of atoms at different sites as well as lattice parameters, bond lengths, unit cell volume, crystallite sizes etc. as listed in Table – 1 and 2, while schematic representation of unit cell is presented in Figure 1(c). It is being noted that the particle size and strain increase from $PBNC_{60}$ to $PBNC_{80}$, while lattice parameters, unit cell volume get decreased. In this context, it may be stated that increase in the particle size can be assigned to effect of higher synthesis temperature, while increasing

strain is attributed to decrease in the lattice parameters. A decreasing in Fe^{3+} (3c) – O (6f, 12h) and an increase in the Fe^{3+} (3c) – C (6e) bond length have been noted in $PBNC_{80}$ with respect to $PBNC_{60}$. It is also noticed that occupancy of Fe^{2+} at 1b site remains unchanged; as well occupancy of coordinated H_2O at 6f site changes hardly. In contrast, occupancy of zeolitic H_2O at 8g site is found to be less in $PBNC_{80}$ in comparison with $PBNC_{60}$. Herein, we assign the reduced zeolitic H_2O with lattice parameter.

Table – 1: Variation in occupancy probability of the different atoms of two different sized PBNC as obtained by Rietveld analysis using Maud software.

Atom	site	$PBNC_{60}$		$PBNC_{80}$	
		Position (x)	Occupancy	Position (x)	Occupancy
Fe^{3+}	1a	0.0	1.0	0.0	1.0
	3c	0.0	1.0	0.0	1.0
Fe^{2+}	1b	0.50486345(9)	0.6592583(21)	0.5001262(13)	0.6588522(9)
	3d	0.5002564(13)	0.7803208(17)	0.4998143(19)	0.80423933(18)
N	6e	0.20095892(5)	0.7803186(23)	0.20295562(14)	0.78014165(23)
	6f	0.20777132(6)	0.6590573(8)	0.19910882(12)	0.65888876(12)
	12h	0.3086982(18)	0.7803359(19)	0.3042289(9)	0.7801389(28)
C	6e	0.31160247(2)	0.7803157(12)	0.28431782(17)	0.7801409(11)
	6f	0.2108135(8)	0.6592680(10)	0.4952381(11)	0.6588363(19)
	12h	0.19350913(21)	0.7803082(13)	0.19597772(21)	0.78011984(26)
O	6e	0.20546116(6)	0.2196236(24)	0.20186207(25)	0.21956125(18)
	6f	0.31103197(8)	0.3418713(15)	0.25275186(16)	0.4129339(14)
	12h	0.21343586(11)	0.2196520(17)	0.3001274(8)	0.21956046(13)
O	8g	0.28311816(7)	0.9769835(23)	0.28644013(9)	0.89194755(29)

Table – 2: Unit cell parameters and selective interatomic distances as obtained by Rietveld analysis using Maud software.

Sample		$PBNC_{60}$	$PBNC_{80}$
Lattice parameter (a in Å)		10.16460	10.124104
Unit cell volume ($Å^3$)		1050.192443	1037.684371
Crystallite sizes (nm)		67.9	96.4
Lattice Strain		0.0016	0.0026
Bond length (Å)	Fe^{3+} (3c)-N (12h)	1.9445(16)	1.9799(14)
	Fe^{3+} (3c)-N (6f)	2.1119(17)	2.0153(14)
	Fe^{3+} (1a)-N(6e)	2.0426 (17)	2.0540(15)

	Fe^{2+} (3d)-C(6e)	1.9149(16)	2.1817(16)
	Fe^{2+} (3d)-C(12h)	1.9669(16)	1.9833(14)
	Fe^{3+} (3c)-O(6f)	3.1615(3)	2.5584(18)
	Fe^{3+} (3c)-O(12h)	2.3029(19)	2.0214(14)
	Fe^{3+} (1a)-O(6e)	2.0884(17)	2.0428(15)
	O(6f)-O(8g)	3.2891(4)	3.0721(3)

In order to gain more insight about the variation of coordinated and zeolitic H_2O, we have carried out TG analyses (revealed in figure 1(d)) which corresponds two regions of weight loss, assigned to removal of zeolitic and coordinated H_2O molecules respectively. Careful calculations reveal approximately 25% loss coordinated H_2O molecules from both samples, whereas ~ 22 and 15% zeolitic H_2O molecule losses are noted from samples $PBNC_{60}$ and $PBNC_{80}$ respectively indicating that TG analysis highly corroborates Rietveld refinement. Morphological investigations by FESEM (shown in Figure 2(a) and 2(b)) and subsequent histogram (shown in the inset of Figure 2(a) and 2(b)) illustrate that $PBNC_{60}$ are monodisperse cube with very smooth surface with average size 50 – 70 nm, while $PBNC_{80}$'s size varies widely from 150 to 280 nm retaining cubic shape. TEM image of one representative bare sample (shown in Figure 2(c)) further confirms cubic shape of the as-prepared samples. DLS data ($PBNC_{60}$=192 nm; $PBNC_{60}$@mSiO_2= 522 nm; $PBNC_{60}$@mSiO_2@HA=1045 nm) shows that the diameter of the bare PBNCs is higher than FESEM and TEM results due to hydration layer within the solution and DLS size is calculated based on spherical model considering this layer. More specifically, m-SiO_2 and HA are well-known for its high hydration capacity, thus high rise of size of PBNC after each step i.e. m-SiO_2 coating and HA functionalization corroborate the phenomenon of successful coating and functionalization as well as their stability.[35]

Nitrogen adsorption – desorption isotherms of one typical m-SiO_2 coated PBNCs sample (shown in figure 2(d)) exhibits typical IV curve, illustrating the mesoporous structure, while BET surface area is found to be 938.2 m^2g^{-1} and simultaneous presence of large pore volume ~ 0.29 cm^3g^{-1} and average pore size ~ 3.2 nm. In this context, it may be stated that as pure PBNCs exhibit no N_2 adsorption and we have coated m-SiO_2 maintaining similar experimental condition, thus other m-SiO_2 coated sample is likely to have similar surface area, pore volume and pore diameter.[14] In this context, it may be stated that FTIR and zeta potential analysis have been performed to validate m-SiO_2 coating and functionalization with HA, followed by DOX loading. From Figure 3(a), the zeta potential of bare $PBNC_{60}$ and $PBNC_{60}$@m-SiO_2 are

measured to be –25.7 and –21.7 mV respectively, while modification with APTES and HA reduce zeta potential to –20.1 mV. Such systematic variation of zeta potential indicates successful coating of m-SiO_2 and functionalization of HA onto the surface of PBNC.[36] As zeta potential of PBNC@m-SiO_2@HA is negative, while that of –NH_2 contained DOX is positive, hence it may be stated that DOX will be loaded onto the surface of PBNC@m-SiO_2@HA via forming a bond through electrostatic attraction. Formation of the above mentioned composite has been further conformed by FTIR analysis. As displayed in Figure 3(b), representative FTIR spectra of $PBNC_{60}$, $PBNC_{60}$@m-SiO_2, $PBNC_{60}$@m-SiO_2@HA and $PBNC_{60}$@m-SiO_2@HA@DOX show strong C ≡ N stretching vibration at 2072 cm^{-1} and a broad band in between 3200 and 3675 cm^{-1} due to -OH from surface adsorbed H_2O, which plays active role in adsorption via hydrogen bonding.

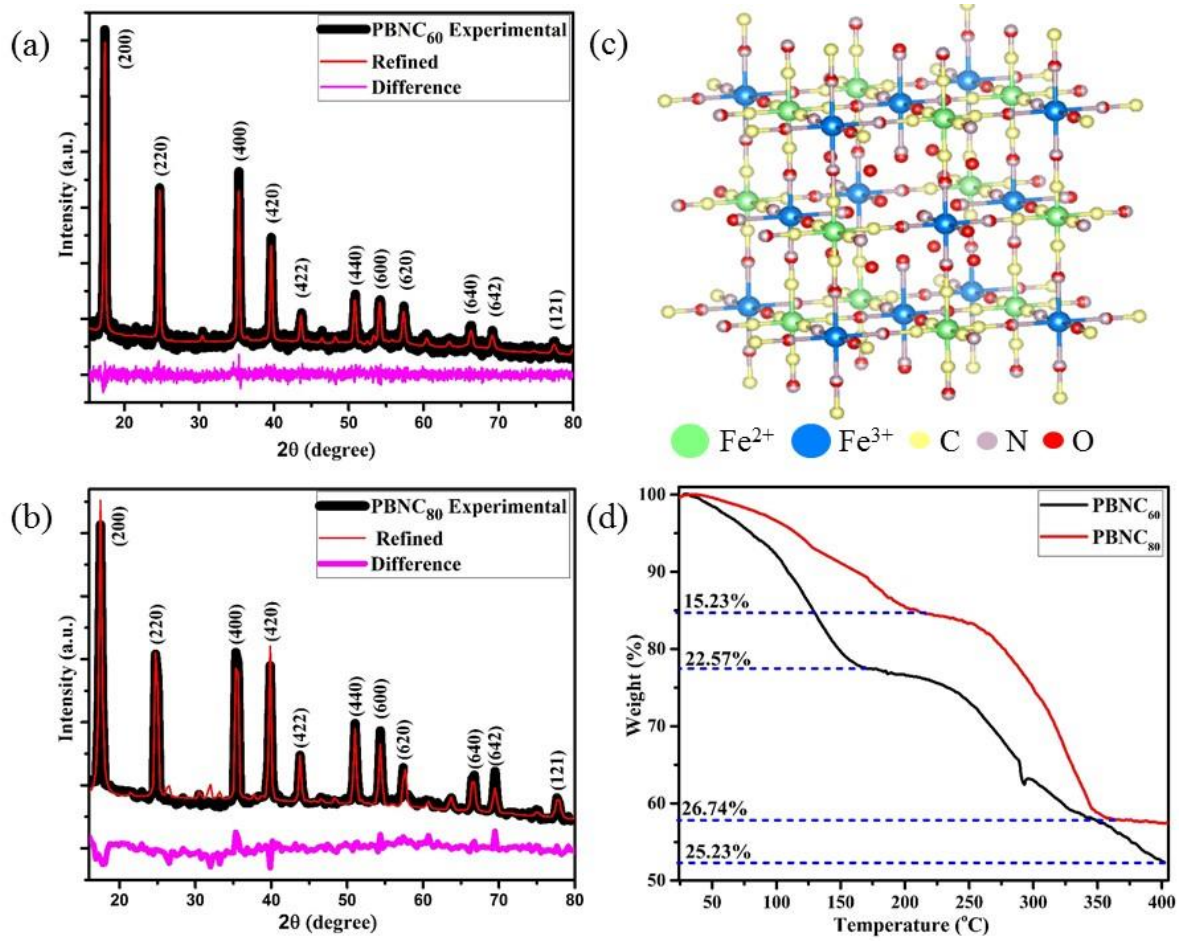

Figure 1: Rietveld refinement of XRD patterns with difference between experimental and refined patterns of (a) $PBNC_{60}$ with R_p=18.68%, R_{wp}=15.71%, χ^2=1.19, (b) $PBNC_{80}$ with R_p=10.42%, R_{wp}=12.34%, χ^2=0.84. (c) Unit cell diagram of $PBNC_{60}$. (d) TGA plot of both $PBNC_{60}$ and $PBNC_{80}$.

In addition, $PBNC_{60}$ exhibits absorption peak at 1721 and 1610 cm^{-1}, assigned to C = O and C = C stretching vibrations of citric acid that acts as an electrostatic stabilizer of $PBNC_{60}$.[37] $PBNC_{60}$@m-SiO_2 illustrates two absorption peaks at 1063 and 798 cm^{-1} corresponding to asymmetric stretching of ν(Si-O-Si), symmetric stretching of ν(Si-O-Si) testifying the formation of Si – O – Si framework, while the peak at 462 cm^{-1} is ascribed to ν(Fe – O – Si) indicating formation of chemical bond between $PBNC_{60}$ and m-SiO_2 and the considerable reduction of the intensity corresponding to C – N stretching with respect to OH indicates the presence of m-SiO_2 (schematically shown in Figure 3(c)) framework around $PBNC_{60}$.[38] Herein, the peak at 1637 cm^{-1} originates from δ(O – H) corresponding to OH present at the surface of m-SiO_2 that facilitates easy functionalization with APTES. $PBNC_{60}$@m-SiO_2@HA shows very strong absorption peaks at 1443 and 1611 cm^{-1} due to ν(COO^-) and δ(N – H) of HA. Briefly, δ(N – H) originates from amidation reaction between COOH bond of HA and -NH_2 group of APTES functionalized m-SiO_2. Furthermore, $PBNC_{60}$@m-SiO_2@HA@DOX displays the absorption peaks at 1572 and 1282 cm^{-1}, assigned to ν(C-H) of aromatic ring and asymmetric ν(C-O-C) of DOX, confirming successful loading of DOX onto $PBNC_{60}$@m-SiO_2@HA through electrostatic attraction.

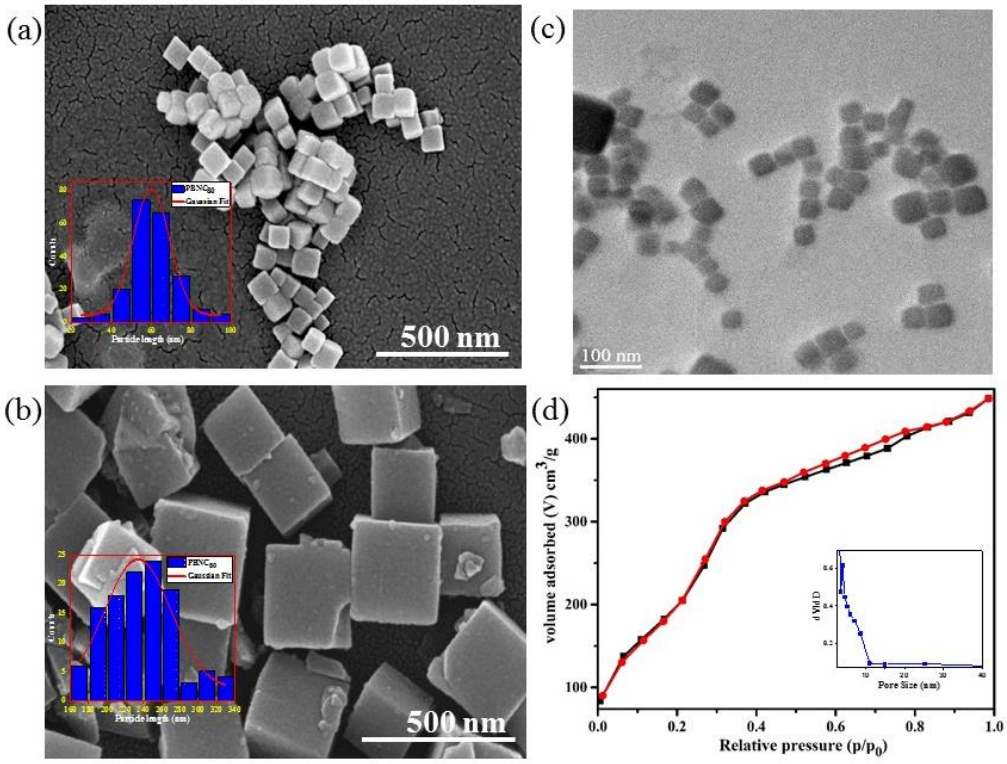

Figure 2: FESEM image with histogram plot in inset of (a) $PBNC_{60}$ and (b) $PBNC_{80}$. (c) TEM image of $PBNC_{60}$. (d) N_2 adsorption – desorption isotherms with pore size distribution in inset of $PBNC_{60}$@m-SiO_2.

Optical absorption spectrum as represented in Figure 3(d) has the absorption maxima at 714 nm for sample $PBNC_{60}$, while that of sample $PBNC_{80}$ gets red-shifted at 852 nm due to higher particle size. In addition, wider full width at half maxima (FWHM) of the absorption spectra indicates non-uniformity in size of $PBNC_{80}$ supporting FESEM studies. Free DOX displays a broad absorption band from 420 nm to 560 nm with centred at 480 nm, hence the absorption band in between 420 and 900 nm with absorption peak at 510 nm is assigned to DOX within PBNC@m-SiO_2@HA@DOX illustrating successful loading of DOX onto PBNC@m-SiO_2@HA, hence the phenomenon well corroborates with FTIR studies.

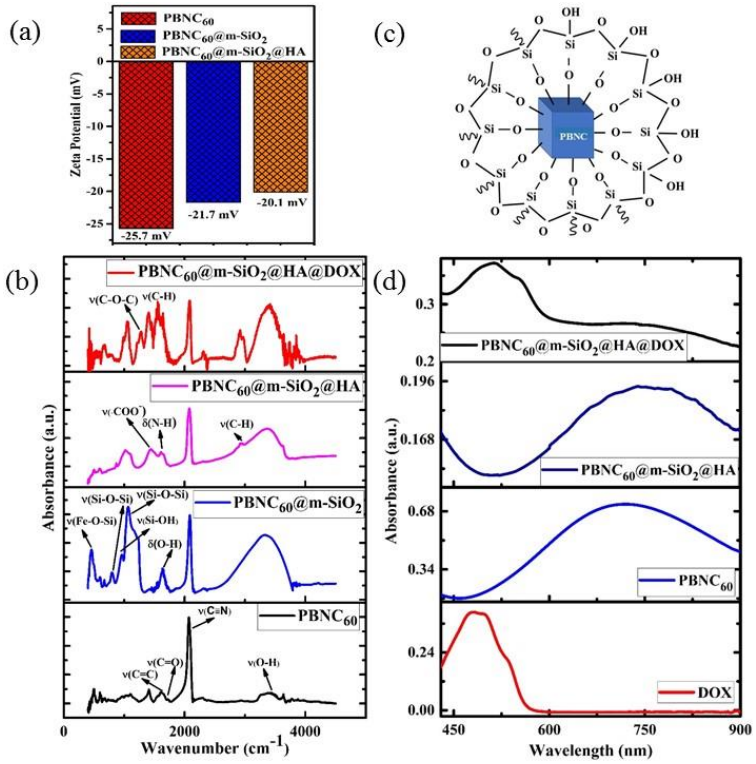

Figure 3: (a) Zeta potential of $PBNC_{60}$, $PBNC_{60}$@m-SiO_2 and $PBNC_{60}$@m-SiO_2@HA. (b) FTIR spectra of $PBNC_{60}$ along with each step of modification. (c) Design of m-SiO_2 coated PBNC. (d) UV-vis-NIR spectroscopy of pure DOX, $PBNC_{60}$, $PBNC_{60}$@m-SiO_2@HA and $PBNC_{60}$@m-SiO_2@HA@DOX.

3.3.2 MRI study and Phantom Images in aqueous medium: size, coating and functionalization dependent of relaxivity: Performance of T_1-weighted contrast agents i.e. shortening of relaxation rate of protons in the presence unit concentration of paramagnetic agents (in $mM^{-1}s^{-1}$), defined by its relaxivity (r_1), of bare as well as functionalized PBNCs are herein explored on 3.0 T analyzer with pure PBS as control. As shown in figure 4(d-e) and Table 3, pristine $PBNC_{60}$ and $PBNC_{80}$ exhibit r_1 relaxivity ~ 5.14 and 3.95 $mM^{-1}s^{-1}$

respectively, whereas r_1 value of $PBNC_{60}$@m-SiO_2 and $PBNC_{80}$@m-SiO_2 raises upto 5.65 and 4.19 $mM^{-1}s^{-1}$. Consecutively, $PBNC_{60}$@m-SiO_2@HA and $PBNC_{80}$@m-SiO_2@HA show r_1 ~ 5.30 and 4.14 $mM^{-1}s^{-1}$ respectively, while $PBNC_{60}$@m-SiO_2@HA@DOX and $PBNC_{80}$@m-SiO_2@HA@DOX exhibit r_1 ~ 3.76 and 2.93 $mM^{-1}s^{-1}$ respectively.

Table – 3: r_1 relaxivity value for both pristine PBNC along with each step of modification.

Sample	$PBNC_{60}$	$PBNC_{80}$
	r_1 ($mM^{-1}s^{-1}$)	r_1 ($mM^{-1}s^{-1}$)
Bare PBNC	5.14	3.95
PBNC@m-SiO_2	5.65	4.19
PBNC@m-SiO_2@HA	5.30	4.14
PBNC@m-SiO_2@HA@DOX	3.76	2.93

Importantly, r_1 of $PBNC_{60}$@m-SiO_2@HA@DOX is found to be larger than that of clinically used Gd-DPTA (~ 3.1 $mM^{-1}s^{-1}$).[39] Possible explanations of higher r_1 of $PBNC_{60}$ relative to $PBNC_{80}$ is as follows: considering PBNC as macromolecules, r_1 consists of contributions from inner-sphere (r_1^{IS}), second sphere (r_1^{SS}) and outer sphere (r_1^{OS}) H_2O molecules and can be written as $r_1 = r_1^{IS} + r_1^{SS} + r_1^{OS}$.[19,24] Briefly, r_1^{IS} depends on interaction between Fe and directly coordinated H_2O molecules, while r_1^{SS} involving the interaction of Fe with nearby zeolitic H_2O molecules. According to Solomon – Bloembergen – Morgan theory r_1^{IS} can be written as given in equation (1):

$$r_1^{IS} \propto \frac{q^{IS}}{55.6} \frac{1}{T_{1M}^{IS} + \tau_m} \qquad (1)$$

where, T_{1M}^{IS}, τ_m and 'q^{IS}' denote relaxation time of coordinated H_2O molecule, inverse of the water-exchange rate (k_{exc}) and number of water molecules respectively.[19,24,40] Previous Rietveld and DTA analysis illustrates similar 'q^{IS}' for both PBNCs indicating that coordinated H_2O molecule doesn't have significant role in the variation of r_1. For coordinated H_2O molecules, τ_m ~ 10^{-9} - 10^{-7}s, while T_{1M}^{IS} varies in between 10^{-4} and 10^{-6} s; thus for all practical purposes $T_{1M}^{IS} >> \tau_m$, hence equation (1) may be simplified into $r_1^{IS} \propto \frac{1}{T_{1M}^{IS}}$. Herein, it is to mention that T_{1M}^{IS} consists of two contributions, namely scalar (T_1^{SC}) and magnetic dipole – dipole (T_1^{DD}) due to electronic and nuclear interactions between water proton and PBNCs respectively and may be written as the following equation (2):

$$\frac{1}{T_{1M}^{IS}} = \frac{1}{T_1^{SC}} + \frac{1}{T_1^{DD}} \qquad (2)$$

At magnetic field ≥ 0.25T, T_1^{SC} appears to be insignificant indicating $r_1^{IS} = \frac{1}{T_1^{DD}}$, whereas at higher field (~ 3.0 T) T_1^{DD} becomes whose expression is given by $\frac{1}{T_1^{DD}} = \frac{1}{r_{Fe-H}^6} \frac{3\tau_{c1}}{1+\omega_L^2\tau_{c1}^2}$, where ω_L and r_{Fe-H} represent the Larmor frequency and Fe – H distance, while τ_{c1}, defined as the time constant of the fluctuating magnetic dipole that consists of two contributions as given below (equation (3)):

$$\frac{1}{\tau_{c1}} = \frac{1}{\tau_m} + \frac{1}{\tau_R} \qquad (3)$$

where, τ_R represents rotational correlation time or inverse of tumbling rate that dominates for smaller molecules. Our Rietveld analysis reveals higher r_{Fe-H} for $PBNC_{60}$ indicating that it should have higher r_1 which is in contrast with our experimental observation, hence it may be concluded that r_{Fe-H} doesn't have significant contribution for PBNCs. Commonly in macromolecules, τ_m (~10^{-9} - 10^{-7} s) is much greater τ_R (~ 10^{-12} s) i.e. $\tau_{c1} \approx \tau_R$, hence we may simplify equation (1) as $r_1^{IS} \propto \frac{3\tau_R}{1+\omega_L^2\tau_R^2}$. Since, our clinical MRI operates at 127.74 MHz frequency; hence neglecting $\omega_L^2\tau_R^2$ in the denominator we have write $r_1^{IS} \propto \tau_R$. Now according to Debye – Stokes relation, $\tau_R = \frac{4\pi\eta r^3}{3k_B T}$, where, η, k_B and T represent viscosity of the medium,[41] Boltzmann constant and absolute temperature indicating that $PBNC_{80}$ should exhibit higher r_1 which is not in consequence with our experimental observation. Thus, it may be conceived that no significant variation in r_1 between $PBNC_{60}$ and $PBNC_{80}$ originates from r_1^{IS}.[42] In this context, we next consider r_1^{SS} contribution to r_1, which is given by equation (4):

$$r_1^{SS} \propto \frac{q^{ss}}{T_{1M}^{ss}} \qquad (4)$$

where q^{ss} and T_{1M}^{ss} represent number and relaxation time of H_2O in the second layer i.e. zeolitic H_2O molecules. As Rietveld and DTA data illustrate more zeolitic H_2O molecules in $PBNC_{60}$ relative to $PNBC_{80}$ and as per previous discussion T_{1M}^{ss} should correspondence higher r_1 for $PBNC_{80}$ that is not supported by experimental observation, hence higher r_1 is assigned to higher r_1^{SS} contribution due to higher to q^{ss} rather than T_{1M}^{ss}.

In comparison with bare nanostructures, PBNC@m-SiO_2 samples show higher r_1 that may be attributed to synergistic effect of enhanced τ_R by virtue of Fe – O – Si bond formation between PBNC and rigid m-SiO_2 and increased proton number of hydroxyl at the surface of m-SiO_2 and H_2O molecules, entrapped at the mesopores of SiO_2.[43] Noticeably, higher fractional change of

relaxivity ($\frac{\Delta r_1}{r_1}$) for sample $PBNC_{60}$ may be explained as follows: considering zero wastage of TEOS, a simple calculation on the basis of conservation of mass illustrate that thickness (l) of m-SiO_2 layer on PBNCs is proportional to size of PBNCs i.e. 'l' is higher for $PBNC_{80}$. As we know, surface to volume ratio (S/V) becomes higher as size of the nanoparticle goes down, thus higher $\frac{\Delta r_1}{r_1}$ ratio may be attributed to S/V ratio. Briefly, entrapped H_2O molecules experience the local field generated by Fe^{2+} and / or Fe^{3+} ions residing at the surface of PBNCs, hence the interaction would be more for H_2O molecules in the vicinity of PBNC's surface and would drastically decrease with increasing distance from surface of PBNCs.[44] Hence the interaction between Fe^{2+} and / or Fe^{3+} at the surface and entrapped H_2O molecules within m-SiO_2 is more in $PBNC_{60}$ giving higher $\frac{\Delta r_1}{r_1}$ in comparison with $PBNC_{80}$ which is schematically represents in Figure 4(a and b).[45] Therefore, we may simply put out that change in longitudinal relaxation of H_2O proton due to functionalization is proportional to S/V ratio of the nanostructure.

HA functionalization further reduces r_1 with reference to PBNC@m-SiO_2 counterpart and it may be explained on the basis of relaxivity contribution from outer sphere according to following expression:

$$r_1^{OS} = \frac{128\pi^2\gamma_I^2 M_n}{405\rho}\left(\frac{1}{1+{}^{L}/_{a}}\right)^3 M_S^2 \tau_D \, J_A(\sqrt{2\omega_I\tau_D}) \qquad (5)$$

where, γ_I, M_n, ρ, M_n and J_A are the gyromagnetic ratio of proton, molarity (mole/liter) and density of PBNCs, saturation magnetization and Ayant's spectral density respectively.[46] Herein, τ_D represents the translational diffusion time ($\tau_D = \frac{r^2}{D}$), where D and 'r' represent is the diffusion coefficient of H_2O molecules and effective radius of the particles which is the sum of the actual radius (r) and thickness (L) of the impermeable surface coating i.e. r = a + L. Herein, we assume that HA functionalization forms an impermeable surface which limits diffusion of H_2O molecules; hence according to equation (5) we attribute reduced r_1 of PBNC@m-SiO_2@HA with respect to PB@m-SiO_2 with impermeable surface due to HA. In this context, we have calculated the ratio $\frac{\Delta r_1}{r_1}$ ~ –0.06 and –0.01 for $PBNC_{60}$@m-SiO_2@HA and $PBNC_{80}$@m-SiO_2@HA respectively and the variation can be understood as follows: from equation (5), we have found $\frac{\Delta r_1^{OS}}{r_1^{OS}} \propto -2\frac{\Delta L}{a}$ indicating that for thick HA, reduction is more. Therefore, it may be concluded that $PBNC_{60}$ containing thicker HA corresponds more

reduction in $\frac{\Delta r_1}{r_1}$ with reference to $PBNC_{80}$ i.e. surface functionalization effect is said to be more prominent for $PBNC_{60}$. Further reduction of r_1 in DOX loaded samples is again assigned to presence of impermeable DOX layer onto the surface of PB@m-SiO_2@HA. In this context, $\frac{\Delta r_1}{r_1}$ ~ –0.29 for both samples indicates identical DOX loading on both samples i.e. DOX loading appears to be independent of size of the nanoparticles. Furthermore, the variation of r_1 relaxivity value due to different functionalization for both PBNC have been pictured (shown in figure 4(c)) through T_1- weighted MRI Phantom images in PBS. The brightening effect with increasing concentration has been observed and the result suggests that $PBNC_{60}$ is more efficient as a MRI CA than $PBNC_{80}$. Besides this, the images reveal that both $PBNC_{60}$@m-SiO_2@HA and $PBNC_{60}$@m-SiO_2@HA@DOX might be used as a MRI CA with minimal concentration for prolonged detection of cancer.

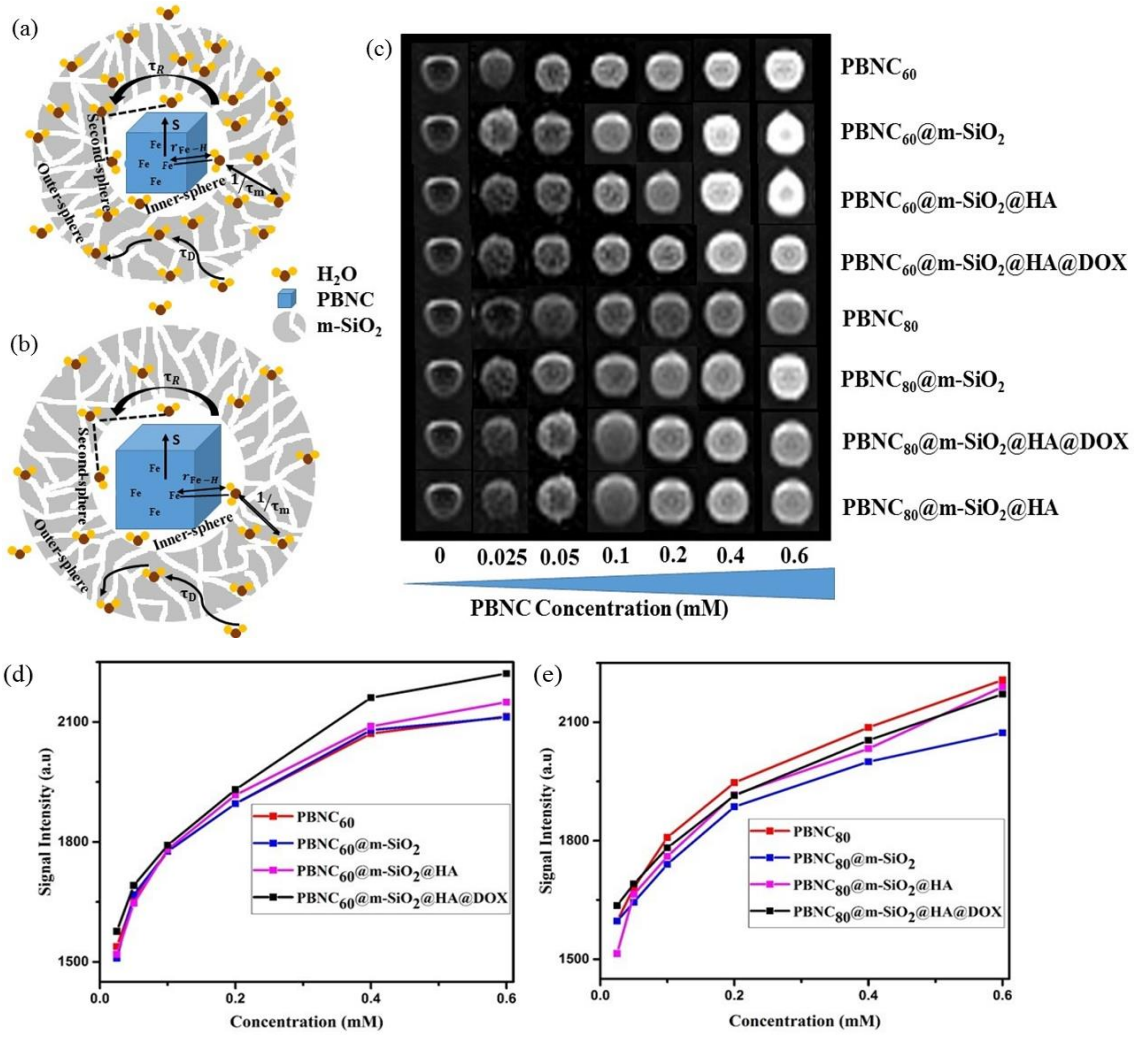

Figure 4: Schematic representation for fractional change in r_1 relaxivity due to m-SiO_2 on (a) $PBNC_{60}$; (b) $PBNC_{80}$. (c) T_1-weighted MR Phantom images of both PBNC along with each

step of modification in PBS at different concentration. Determination of r_1 relaxivity value of (d) $PBNC_{60}$ and (e) $PBNC_{80}$ after each step of modification in PBS.

3.3.3 *In-vitro* cellular theranostic measurement: Motivated by higher r_1 in comparison with commercially available Gd-based CA for MRI, we have employed $PBNC_{60}$@m-SiO_2@HA for *in-vitro* theranostic investigations against HCT 116 cell line. Prior to *in-vitro* studies, we have checked stability, singlet oxygen ($^1O_2$) generation, DOX loading capacity and release kinetics of $PBNC_{60}$@m-SiO_2@HA. Herein, the generation of $^1O_2$, believed to be the major cytotoxic agent giving photodynamic therapy (PDT), has been investigated through DPBF-fading experiment. Figure 5(a) shows the decrease in absorbance intensity at 410 nm as a function of exposure time that illustrates $^1O_2$ generation during irradiation with 808 nm laser light, hence the observation clearly reveals the potentially of $PBNC_{60}$@m-SiO_2@HA for PDT. Very high DOX loading efficiency (~ 94.43%) is attributed to highly porous character of SiO_2 and attractive electrostatic interaction between charged Si – O^- groups of m-SiO_2 and DOX. Drug release profiles, carried out at PBS buffer solutions of different pH, are shown in Figure 5(b). It is noted from figure that only 19% of drug gets released within 22 h at normal PBS buffer solution (pH ~ 7.4), while only 50% drug is released over 22 h and 77% over 70 h at pH ~ 5 which is the pH of most cancerous microenvironment. Herein, the ultraslow release is attributed to hydrophobic-hydrophobic interaction between m-SiO_2 and DOX, while acidic pH leads DOX hydrophilic and facilitates the release process.[47] $PBNC_{60}$@m-SiO_2@HA as checked by monitoring absorbance peak of PBNC is highly stable at normal pH, while 55% gets degraded after 7 days at pH ~ 5 indicating that our synthesized nanoplatform may be a potential candidate for synergistic theranostic application.[48]

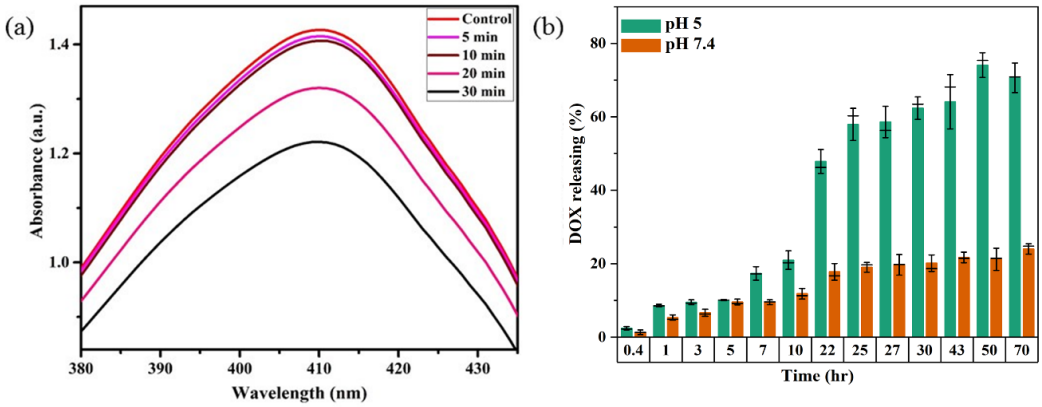

Figure 5: (a) UV-vis spectra for time dependent degradation of DPBF by $PBNC_{60}$@m-SiO_2@HA under NIR laser irradiation. (b) DOX releases plot of $PBNC_{60}$@m-SiO_2@HA@DOX in different pH of PBS buffer without NIR irradiation.

In-vitro cellular toxicity measurement (Shown in Figure 6(a)) has been performed on HCT 116 cells using MTT assay, reveal that $PBNC_{60}$, $PBNC_{60}$@m-SiO_2 and $PBNC_{60}$@m-SiO_2@HA exhibit limited toxicity up to 70 µg/mL concentration, while approximately 91.05% cell death has been observed only in the presence of 40 µg/mL $PBNC_{60}$@m-SiO_2@HA@DOX indicating its cytotoxic efficacy as chemotherapeutic agent. Herein, very low IC_{50} value (~ 21 µg/mL) of $PBNC_{60}$@m-SiO_2@HA@DOX might indicate high uptake due to presence of abundance HA receptor on HCT 116 which has been further confirmed by red fluorescence emission from DOX in the confocal laser scanning microscopic (CLSM) images (shown in Figure 6(b)), taken with light irradiation after 24 h incubation. Thus, HA functionalized nanoplatform has been selectively delivered into cancerous site (HCT 116) via their enhanced permeability and retention (EPR) effect. Additionally, HA has strong affinity towards overexpressed CD44 receptor. So, here receptor based active targeting plays a major role compare to passive targeting.[7,49] In order to eliminate the interference of conjugated DOX during the photodynamic ablation efficiency, we have compared MTT assay results with/without 808 nm laser irradiation for various time (10, 20, 30 and 40 minutes) (shown in Figure 6(c)). The result demonstrates increasing cell death with increase of irradiation time reaching ~ 78% at 20 minutes and the phenomenon suggests high PDT efficiency of the synthesized nanoplatform. Presently, we have observed red fluorescence emission from nuclear region that indicates DOX binding on nucleus and it well corroborates with previous reports.[50] Importantly, we haven't noticed any significant variation in DOX fluorescence with exposure time, however an upregulated expression of SOD at different irradiation indicates more generation of enzymatic antioxidant to neutralize oxidative stress that confirms PDT effect of the nanoplatform. Moreover, DCFH-DA staining method has been employed here to examine iROS production for actual research on the phototoxic efficacy of $PBNC_{60}$@m-SiO_2@HA@DOX. As expected, quantified by DCF fluorescein intensity (shown in Figure 6(d)) on flow cytometry assay (FACS), $PBNC_{60}$@m-SiO_2@HA@DOX leads most remarkable iROS production under laser irradiation compared with that without irradiation. In addition, the figure clearly reveals an increase of DCF fluorescein intensity with increasing light irradiation illustrating prolonged iROS which is advantageous for photodynamic therapy. Hence, the MTT and FACS results indicate that $PBNC_{60}$@m-SiO_2@HA@DOX induced chemo-photodynamic results are more striking than chemo or photodynamic treatment alone.

In general, success of any therapeutic approach significantly depends on early response of the cancer cell to therapeutic process where cell death mechanisms like apoptosis (programmed

cell death), necrosis (accidental cell death) etc. plays a crucial role.[51] Presently, chemo-photodynamic induced cell death mechanism using $PBNC_{60}$@m-SiO_2@HA@DOX has been assessed by FACS measurement using Annexin V-FITC/PI kit. Prior to measurement, as shown in figure 7(a) cell viability has been found to be 99.7% which is used as control. After 24 h incubation with DOX containing nanoplatform (21 µg/mL) under dark, cell viability gets decreased to 83.9% along with 2.5% early/late apoptotic and 11.3% necrotic population. After 10 minutes of light irradiation, cell viability reduces to 22.3% with enhanced early apoptotic (28.9%), late apoptotic (30.4%) and necrotic (18.4%) population. Further increase of irradiation time (20 minutes) reduces cell viability to 0.1% along with increase of necrosis to apoptosis ratio (31.3% late apoptotic and 68.6% necrotic populations). Importantly, very drastic reduction of apoptotic percentage only after at 20 minutes of irradiation indicates high PDT activity of $PBNC_{60}$@m-SiO_2@HA@DOX in comparison with sole chemotherapeutic activity.

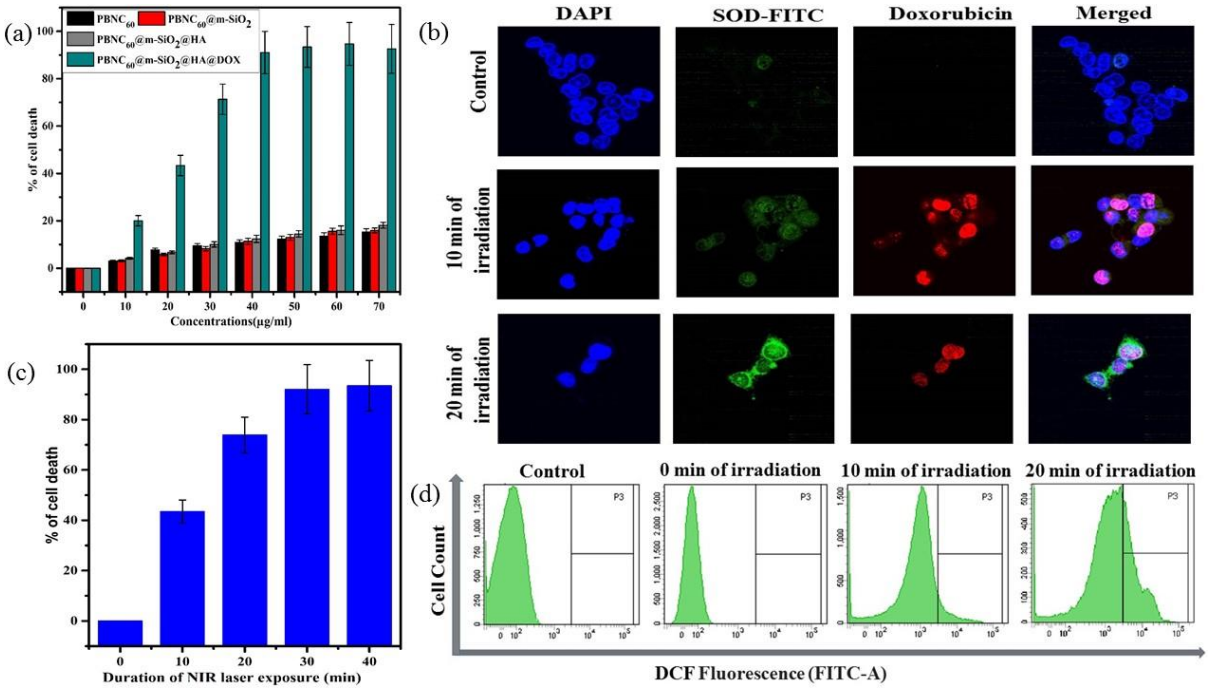

Figure 6: (a) Concentration dependent MTT assay plot after 24 h incubated with $PBNC_{60}$ along with each step of modification in HCT 116 cell line. (b) Expression of SOD and internalization of DOX in $PBNC_{60}$@mSiO_2@HA@DOX (21 µg/mL) treated NIR irradiated (10 and 20 min) HCT 116 cell line; DAPI as a nuclear stainer. (c) Time dependent cell death plot and (d) determination of iROS generation of HCT 116 cells after 24 h incubated with $PBNC_{60}$@mSiO_2@HA@DOX (21 µg/mL) with laser irradiation (808 nm, 1 W cm^{-2}).

Apoptosis is mostly initiated by intracellular (mitochondrial disruption) or extracellular (death receptor activation) stimuli, called intrinsic and extrinsic pathway respectively, whereas extreme physicochemical stress results necrosis.[52] Apoptosis in tissues is asynchronous characteristics that lead signalling pathways from damage site of cell onto central leading to the final execution phase of the apoptosis where different hydrolytic enzymes are activated by a family of caspases based catalyses.[53] Among them, caspase 3 and caspase 9 play most pivotal role in early apoptotic process.[54] In PDT-treated cells, both caspases cause several biochemical changes including phosphatidylserine (PS), phosphatidylethanolamine (PE), plasma membrane depolarization, cell external membrane leaflet, cytoplasm acidification and DNA fragmentation depending on particular cell line, type of PDT agent and its subcellular location, overall dose etc. To determine apoptotic pathways of $PBNC_{60}$@m-SiO_2@HA@DOX mediated chemo-photodynamic therapy, we have carried out a series of CLSM based biochemical assays. It has been noticed from the figure 7(c) that light irradiation enhances expressions for caspase 3 and caspase 9 in comparison with that of without light, taken as control, hence the results demonstrate prominent $^1O_2$ stress induced biochemical changes of PS, PE etc. Herein, it may be stated that altered level of pro/anti-apoptotic proteins triggers the release of cytochrome *c* (cyt-*c*) to the cytosol from outer mitochondrial membrane, hence to confirm whether mitochondria is involved in the apoptosis or not, we have checked *cyt-c* release using confocal microscope. In this context, confocal microscopic data in figure 7(b) shows an increasing expression of *cyt-c* release indicating that the apoptosis initiates from mitochondria. In any cell, mitochondrial superoxide dismutase (SOD) plays an important role to protect from oxidative damage by scavenging $^1O_2$, however excessive $^1O_2$ depletes anti-oxidant defences and disrupts antioxidant/prooxidant balance which leads DNA damage.[55] Presently, we have observed increasing expression of DNA damage (shown in Figure 7(b)) with increasing irradiation time, while $PBNC_{60}$@m-SiO_2@HA@DOX incubated sample without light irradiation has been considered as control. As DNA damage comprises of double-strand breaks (DSB) which may be induced directly or indirectly due to extensive iROS generation. According to literature, limited study exists to illustrate PDT induced DSB, particularly in the presence of 808 nm NIR laser.[56] Presently, we have checked the phenomenon by assessing the expression of phosphorylation of H2AX, which is being well-considered marker of DSBs. Briefly, H2AX, one of the key variant of H2A protein family, consists of the histone octamer of nucleosomes and turns into phosphorylated during DNA damage due to any kind of exogenous and endogenous reasons and forms gamma-H2AX (γ-H2AX). It can be seen from Figure 7(b) that the number of γ-H2AX foci increases with increasing irradiation time, hence the study

demonstrates that the apoptotic is associated with DSBs. Herein, it is worth mentioning that poly(-adenosine diphosphate (ADP)-ribose) polymerase (PARP), an abundant nuclear protein which plays a pivotal role as first responder to maintain genomic integrity and DNA repair, is being considered as an indicator for apoptotic induction, while its inhibition enhances therapeutic efficiency.[57] Presently, we have noticed that PARP cleavage gets enhanced with increasing irradiation time in the presence of 21 µg/mL) of $PBNC_{60}$@m-SiO_2@HA@DOX, while very insignificant PARP expression has been noticed in control. This result confirms that the PDT efficacy of $PBNC_{60}$@m-SiO_2@HA@DOX is due to ROS mediated mitochondria dependent DNA damage pathway. Moreover, our developed targeted naoplatfrom shows enhanced NIR laser induced chemo-photodynamic therapeutic potentiality against HCT 116 cancer compare to other nanoparticles such as Fe_3O_4, Au or various upconversion nanoparticles.[58-60]

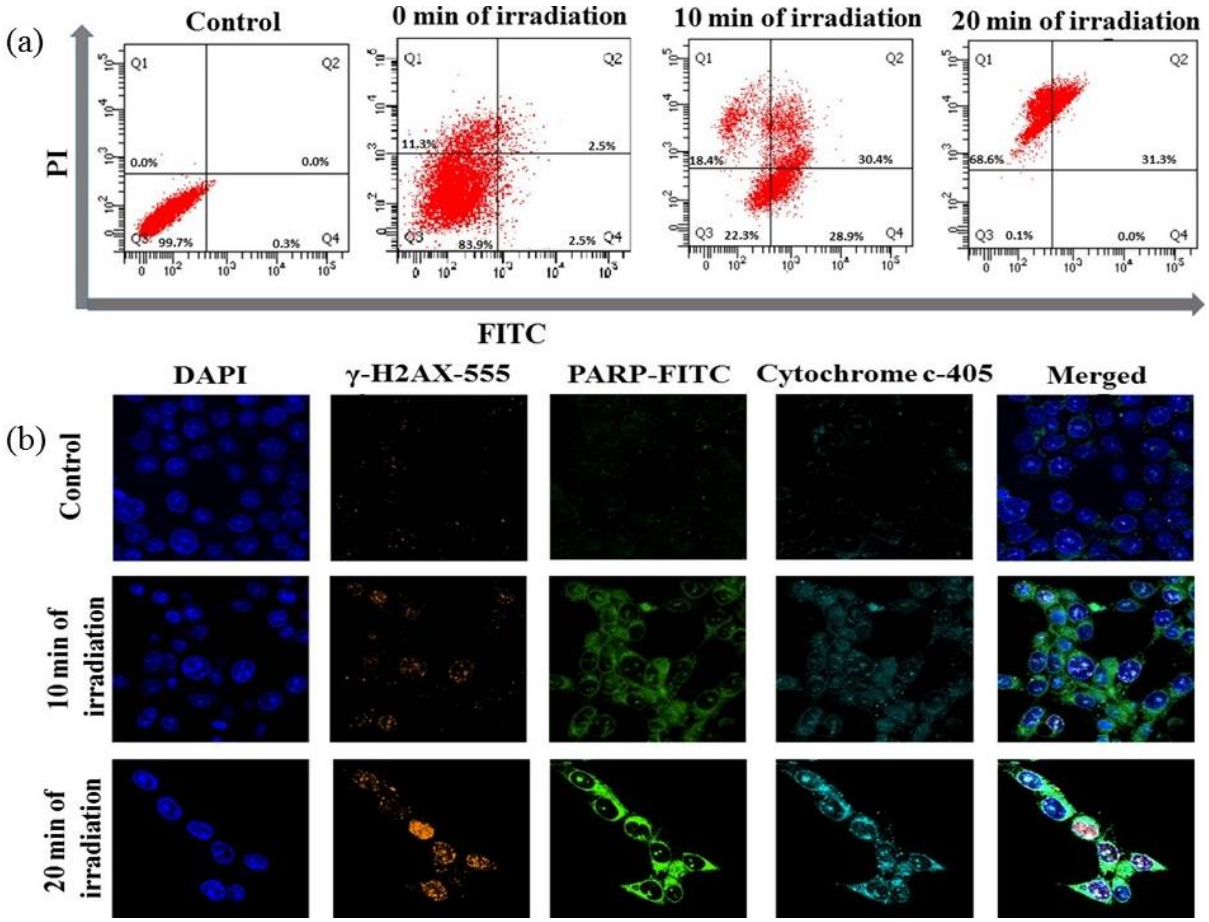

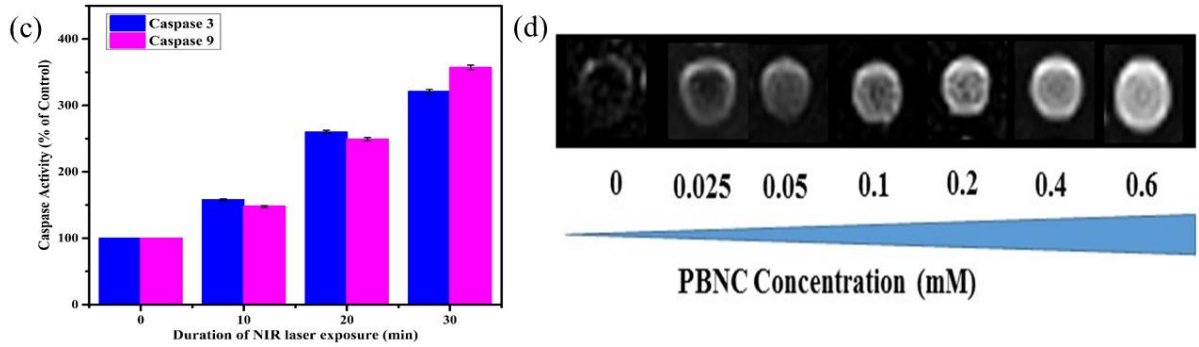

Figure 7: (a) Quantification of apoptosis; (b) Expression of γ-H2AX, PARP and Cytochrome c through CLSM images of HCT 116 cells with $PBNC_{60}$@$mSiO_2$@HA@DOX (21 µg/mL) incubated with 24 h under time dependent laser irradiation; DAPI as a nuclear stainer. (c) Expression of caspase 3 and caspase 9 in $PBNC_{60}$@$mSiO_2$@HA@DOX (21 µg/mL) treated NIR irradiated (10, 20 and 30 min) HCT 116 cell line. (d) *In-vitro* T_1-weighted MR Phantom images of $PBNC_{60}$@$mSiO_2$@HA@DOX incubated with 24 h at different concentration of $PBNC_{60}$.

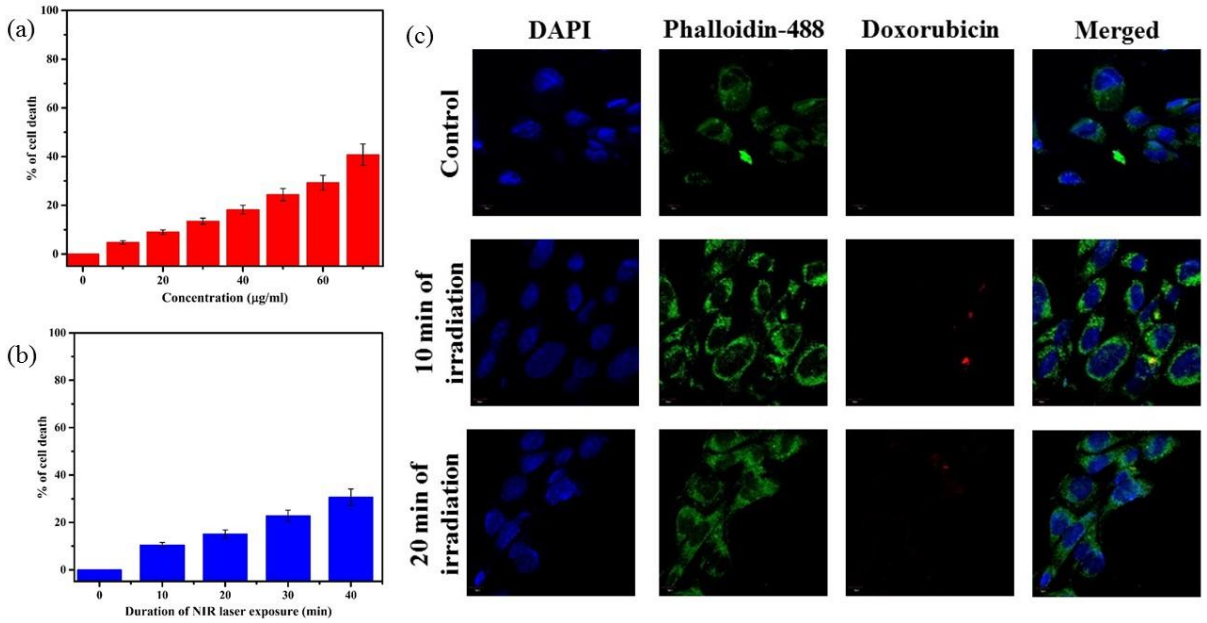

Figure 8: (a) concentration and (b) laser irradiation time dependant MTT assay plot of HEK 293 cells after 24 h incubated with $PBNC_{60}$@m-SiO_2@HA@DOX. (c) Expression of DOX through CLSM images of HEK 293 cells with $PBNC_{60}$@$mSiO_2$@HA@DOX (21 µg/mL) incubated with 24 h under time dependent laser irradiation; DAPI and Phalloidin-448 as a nuclear and cytoskeleton stainer.

Furthermore, *in-vitro* cellular T_1 weighted MRI was also carried out to confirm the efficiency of $PBNC_{60}$@m-SiO_2@HA@DOX as a MRI CA against HCT 116 cells. The concentration dependent brightening effect is visualised through phantom images as shown in figure 7(d) and

r_1 relaxivity is measured to be 3.91 $mM^{-1}s^{-1}$ which is well matched with previously measured in solution. Hence, therapeutics and MR measurements attributed the potential of $PBNC_{60}$@m-SiO_2@HA@DOX as a theranostic CA against HCT 116 cell line with optimal concentration. Herein, MTT assay (shown in Figure 8(a) and (b)) reveals very low death of normal cell (HEK 293), taken as control, which might be attributed to poor uptake of $PBNC_{60}$@m-SiO_2@HA@DOX due to absence of HA receptor and is being further confirmed by confocal microscopic image (shown in Figure 8(c)) from low red fluorescence from DOX. Thus the study reveals very high selectivity of nanoplatform between normal and HCT 116 cells, as well it is expected to be accumulated within HCT 116 cells via enhanced permeability and retention (EPR) effect, and hence the present study illustrates very high HCT 116 cell-killing efficiency of $PBNC_{60}$@m-SiO_2@HA@DOX.

3.4 Conclusions

In summary, we have reported the synthesis of HCT 116 cell specific, NIR (808 nm) triggering, highly dispersed, coordination polymer based nanoplatform $PBNC_{60}$@m-SiO_2@HA by coating $PBNC_{60}$ with m-SiO_2 and the modifying with hyaluronic acid as next generation theranostic nanoplatform for image guided combined photodynamic and chemotherapy. $PBNC_{60}$@m-SiO_2@HA that consists of amphiphilic micelles for conjugating DOX shows good biocompatibility, ultrahigh DOX loading as well as pH responsive DOX release efficiency. Besides this the nanoplatform acts as *in-vitro* T_1-weighted MR agent having r_1 value greater than r_1 of commercially available Gd-based MRI contrast agent. Moreover, a high rate of cell (HCT 116) death is achieved over lower dose of $PBNC_{60}$@m-SiO_2@HA@DOX due to the mutual effect of laser (808 nm) and DOX, followed by iROS mediated mitochondria dependent DNA damage pathway. Therefore, multimodal theranostic nanoplatform demonstrate fascinating approaches and prospects against colon cancer for future perspective.

More interestingly, our details study on higher r_1 value for smaller sized PBNC is assigned to the contribution of second sphere zeolitic water molecules leads to crystal vacancy. Furthermore, variation of r_1 value at each functionalization steps illustrate that m-SiO_2 coating on PBNC increases r_1 due to quantum confinement effect, while HA and DOX addition lowers r_1. Fractional changes in r_1 has been ascribed to size dependent correlation time and diffusion of water molecules where thickness of m-SiO_2 plays a significant role.

References

1. Catala, L., & Mallah, T. (2017). Nanoparticles of Prussian blue analogs and related coordination polymers: From information storage to biomedical applications. Coordination Chemistry Reviews, 346, 32-61.
2. Webb, J. A., Ou, Y. C., Faley, S., Paul, E. P., Hittinger, J. P., Cutright, C. C., ... & Bardhan, R. (2017). Theranostic gold nanoantennas for simultaneous multiplexed Raman imaging of immunomarkers and photothermal therapy. ACS omega, 2(7), 3583-3594.
3. Su, L., Xiong, Y., Yang, H., Zhang, P., & Ye, F. (2016). Prussian blue nanoparticles encapsulated inside a metal–organic framework via in situ growth as promising peroxidase mimetics for enzyme inhibitor screening. Journal of materials chemistry B, 4(1), 128-134.
4. K. R. Dunbar and R. A. Heintz, *Prog. In. Inorg. Chem*, 2007, **45**, 283-391.
5. Shiba, F., Mameuda, U., Tatejima, S., & Okawa, Y. (2019). Synthesis of uniform Prussian blue nanoparticles by a polyol process using a polyethylene glycol aqueous solution. *RSC advances*, *9*(59), 34589-34594.
6. Dou, Y., Li, X., Yang, W., Guo, Y., Wu, M., Liu, Y., ... & Chang, J. (2017). Pb@Au core–satellite multifunctional nanotheranostics for magnetic resonance and computed tomography imaging in vivo and synergetic photothermal and radiosensitive therapy. ACS Applied Materials & Interfaces, 9(2), 1263-1272.
7. Zhou, B., Jiang, B. P., Sun, W., Wei, F. M., He, Y., Liang, H., & Shen, X. C. (2018). Water-dispersible Prussian blue hyaluronic acid nanocubes with near-infrared photoinduced singlet oxygen production and photothermal activities for cancer theranostics. ACS applied materials & interfaces, 10(21), 18036-18049.
8. Long, J., Guari, Y., Guérin, C., & Larionova, J. (2016). Prussian blue type nanoparticles for biomedical applications. Dalton Transactions, 45(44), 17581-17587.
9. Shokouhimehr, M., Soehnlen, E. S., Hao, J., Griswold, M., Flask, C., Fan, X., ... & Huang, S. D. (2010). Dual purpose Prussian blue nanoparticles for cellular imaging and drug delivery: a new generation of T 1-weighted MRI contrast and small molecule delivery agents. Journal of Materials Chemistry, 20(25), 5251-5259.
10. Shokouhimehr, M., Soehnlen, E. S., Khitrin, A., Basu, S., & Huang, S. D. (2010). Biocompatible Prussian blue nanoparticles: Preparation, stability, cytotoxicity, and potential use as an MRI contrast agent. Inorganic Chemistry Communications, 13(1), 58-61.
11. Perrier, M., Kenouche, S., Long, J., Thangavel, K., Larionova, J., Goze-Bac, C., ... & Guari, Y. (2013). Investigation on NMR relaxivity of nano-sized cyano-bridged coordination polymers. Inorganic Chemistry, 52(23), 13402-13414.
12. Mathieu, P., Chalet, M., Clain, M. M., Teulon, L., Benoist, E., Leygue, N., ... & Amiens, C. (2020). Surface engineering of silica nanoparticles with a gadolinium–PCTA complex for efficient T_1-weighted MRI contrast agents. New Journal of Chemistry, 44(41), 18031-18047.
13. López-Pedrouso, M., Lorenzo, J. M., Varela, Z., Fernández, J. Á., & Franco, D. (2022). Finding biomarkers in antioxidant molecular mechanisms for ensuring food safety of bivalves threatened by marine pollution. Antioxidants, 11(2), 369.
14. Su, Y. Y., Teng, Z., Yao, H., Wang, S. J., Tian, Y., Zhang, Y. L., ... & Zhang, L. J. (2016). A multifunctional PB@ $mSiO_2$–PEG/DOX nanoplatform for combined photothermal–chemotherapy of tumor. ACS Applied Materials & Interfaces, 8(27), 17038-17046.
15. Lin, X., Cao, Y., Li, J., Zheng, D., Lan, S., Xue, Y., ... & Zhu, X. (2019). Folic acid-modified Prussian blue/polydopamine nanoparticles as an MRI agent for use in targeted chemo/photothermal therapy. Biomaterials science, 7(7), 2996-3006.
16. Feng, K., Zhang, J., Dong, H., Li, Z., Gu, N., Ma, M., & Zhang, Y. (2021). Prussian blue nanoparticles having various sizes and crystallinities for multienzyme catalysis and magnetic resonance imaging. ACS Applied Nano Materials, 4(5), 5176-5186.
17. Z. Zhou, L. Yang, J. Gao and X. Chen, *Adv. Mater*., 2019, **31**, 1804567-1804598.

18. Zhu, W., Liu, K., Sun, X., Wang, X., Li, Y., Cheng, L., & Liu, Z. (2015). Mn^{2+}-doped prussian blue nanocubes for bimodal imaging and photothermal therapy with enhanced performance. ACS Applied Materials & Interfaces, 7(21), 11575-11582.
19. Dumont, M. F., Hoffman, H. A., Yoon, P. R., Conklin, L. S., Saha, S. R., Paglione, J., ... & Fernandes, R. (2014). Biofunctionalized gadolinium-containing prussian blue nanoparticles as multimodal molecular imaging agents. Bioconjugate chemistry, 25(1), 129-137.
20. Guari, Y., Larionova, J., Corti, M., Lascialfari, A., Marinone, M., Poletti, G., ... & Guérin, C. (2008). Cyano-bridged coordination polymer nanoparticles with high nuclear relaxivity: toward new contrast agents for MRI. Dalton transactions, (28), 3658-3660.
21. M. K. Yu, J. Park and S. Jon, *Theranostics*, 2012, **2**, 3-43.
22. Zhao, L. H., Lin, Q. L., Wei, J., Huai, Y. L., Wang, K. J., & Yan, H. Y. (2015). CD44v6 expression in patients with stage II or stage III sporadic colorectal cancer is superior to CD44 expression for predicting progression. International Journal of Clinical and Experimental Pathology, 8(1), 692.
23. Cheng, L., Gong, H., Zhu, W., Liu, J., Wang, X., Liu, G., & Liu, Z. (2014). PEGylated Prussian blue nanocubes as a theranostic agent for simultaneous cancer imaging and photothermal therapy. *Biomaterials*, *35*(37), 9844-9852.
24. Teng, Z., Su, X., Zheng, Y., Sun, J., Chen, G., Tian, C., ... & Lu, G. (2013). Mesoporous silica hollow spheres with ordered radial mesochannels by a spontaneous self-transformation approach. *Chemistry of Materials*, *25*(1), 98-105.
25. Lim, L. T., Auras, R., & Rubino, M. (2008). Processing technologies for poly (lactic acid). *Progress in polymer science*, *33*(8), 820-852.
26. Mishra, S., Manna, K., Kayal, U., Saha, M., Chatterjee, S., Chandra, D., ... & Saha, K. D. (2020). Folic acid-conjugated magnetic mesoporous silica nanoparticles loaded with quercetin: A theranostic approach for cancer management. *RSC advances*, *10*(39), 23148-23164.
27. Yu, S. M., Choi, S. H., Kim, S. S., Goo, E. H., Ji, Y. S., & Choe, B. Y. (2013). Correlation of the R1 and R2 values of gadolinium-based MRI contrast media with the ΔHounsfield unit of CT contrast media of identical concentration. *Current Applied Physics*, *13*(5), 857-863.
28. Nandi, R., Mishra, S., Maji, T. K., Manna, K., Kar, P., Banerjee, S., ... & Pal, S. K. (2017). A novel nanohybrid for cancer theranostics: folate sensitized Fe 2 O 3 nanoparticles for colorectal cancer diagnosis and photodynamic therapy. *Journal of Materials Chemistry B*, *5*(21), 3927-3939.
29. Bhanja, P., Mishra, S., Manna, K., Mallick, A., Das Saha, K., & Bhaumik, A. (2017). Covalent organic framework material bearing phloroglucinol building units as a potent anticancer agent. *ACS applied materials & interfaces*, *9*(37), 31411-31423.
30. Su, Y., Lu, S., Gao, P., Zheng, M., & Xie, Z. (2019). BODIPY@carbon dot nanocomposites for enhanced photodynamic activity. *Materials Chemistry Frontiers*, *3*(9), 1747-1753.
31. Sai, D. L., Lee, J., Nguyen, D. L., & Kim, Y. P. (2021). Tailoring photosensitive ROS for advanced photodynamic therapy. *Experimental & Molecular Medicine*, *53*(4), 495-504.
32. Alam, A., Mishra, S., Hassan, A., Bera, R., Dutta, S., Das Saha, K., & Das, N. (2020). Triptycene-based and Schiff-Base-linked porous networks: efficient gas uptake, high CO2/N2 selectivity, and excellent antiproliferative activity. *ACS omega*, *5*(8), 4250-4260.
33. Brentnall, M., Rodriguez-Menocal, L., De Guevara, R. L., Cepero, E., & Boise, L. H. (2013). Caspase-9, caspase-3 and caspase-7 have distinct roles during intrinsic apoptosis. *BMC cell biology*, *14*, 1-9.
34. Samain, L., Grandjean, F., Long, G. J., Martinetto, P., Bordet, P., & Strivay, D. (2013). Relationship between the synthesis of Prussian blue pigments, their color, physical properties, and their behavior in paint layers. *The Journal of Physical Chemistry C*, *117*(19), 9693-9712.
35. Amorim, S., Martins, A., Neves, N. M., Reis, R. L., & Pires, R. A. (2014). Hyaluronic acid/poly-L-lysine bilayered silica nanoparticles enhance the osteogenic differentiation of human mesenchymal stem cells. *Journal of materials chemistry B*, *2*(40), 6939-6946.
36. H. Xu, Z. Wang, Y. Li, Y. Gou, H. Zhou, Y. Li, F. Wu, L. Zhang, X. Yang, B. Lu, and Z. Huang, *RSC Adv.*, 2016, **6**, 40427-40435.

37. Hou, X., Xu, H., Pan, L., Tian, Y., Zhang, X., Ma, L., ... & Zhao, J. (2015). Adsorption of bovine serum albumin on superparamagnetic composite microspheres with a Fe 3 O 4/SiO 2 core and mesoporous SiO 2 shell. *RSC Advances*, *5*(126), 103760-103766.
38. Sharma, R. K., Dutta, S., & Sharma, S. (2016). Nickel (ii) complex covalently anchored on core shell structured SiO_2@ Fe_3O_4 nanoparticles: a robust and magnetically retrievable catalyst for direct one-pot reductive amination of ketones. *New Journal of Chemistry*, *40*(3), 2089-2101.
39. Miao, Y., Zhang, H., Cai, J., Chen, Y., Ma, H., Zhang, S., ... & Fan, H. (2021). Structure–relaxivity mechanism of an ultrasmall ferrite nanoparticle T1 MR contrast agent: The impact of dopants controlled crystalline core and surface disordered shell. *Nano Letters*, *21*(2), 1115-1123.
40. Liu, Q., Chen, S., Chen, J., & Du, J. (2015). An asymmetrical polymer vesicle strategy for significantly improving T 1 MRI sensitivity and cancer-targeted drug delivery. *Macromolecules*, *48*(3), 739-749.
41. Chen, Y., Yang, H., Tang, W., Cui, X., Wang, W., Chen, X., ... & Hu, A. (2013). Attaching double chain cationic Gd (III)-containing surfactants on nanosized colloids for highly efficient MRI contrast agents. *Journal of Materials Chemistry B*, *1*(40), 5443-5449.
42. Zhang, H., Li, L., Liu, X. L., Jiao, J., Ng, C. T., Yi, J. B., ... & Fan, H. M. (2017). Ultrasmall ferrite nanoparticles synthesized via dynamic simultaneous thermal decomposition for high-performance and multifunctional T 1 magnetic resonance imaging contrast agent. *ACS nano*, *11*(4), 3614-3631.
43. K. Ni, Z. Zhao, Z. Zhang, L. Yang, L. Wang, H. Ai and J. Gao, *Nanoscale*, 2016, **8**, 3768-3744.
44. Zhang, L., Wang, Y., Tang, Y., Jiao, Z., Xie, C., Zhang, H., ... & Zhang, C. (2013). High MRI performance fluorescent mesoporous silica-coated magnetic nanoparticles for tracking neural progenitor cells in an ischemic mouse model. *Nanoscale*, *5*(10), 4506-4516.
45. L. Zhou, W. Yin, W. Ren, Z. Gu, W. Li, S. Jin, L, Yan, G. Tian, Z. Hu and Y. Zhao, *N. J. Chem*., 2012, **36**, 2599-2606.
46. Zhang, X., Blasiak, B., Marenco, A. J., Trudel, S., Tomanek, B., & van Veggel, F. C. (2016). Design and regulation of NaHoF4 and $NaDyF_4$ nanoparticles for high-field magnetic resonance imaging. *Chemistry of Materials*, *28*(9), 3060-3072.
47. Liu, J., Hu, X., Jin, S., Liang, X. J., & Ma, X. (2022). Enhanced anti-tumor activity of a drug through pH-triggered release and dual targeting by calcium phosphate-covered mesoporous silica vehicles. *Journal of Materials Chemistry B*, *10*(3), 384-395.
48. Zargar, B., & Hatamie, A. (2014). Prussian blue nanoparticles: a simple and fast optical sensor for colorimetric detection of hydralazine in pharmaceutical samples. *Analytical methods*, *6*(15), 5951-5956.
49. Zakaria, M. B., Belik, A. A., Liu, C. H., Hsieh, H. Y., Liao, Y. T., Malgras, V., ... & Wu, K. C. W. (2015). Prussian blue derived nanoporous iron oxides as anticancer drug carriers for magnetic-guided chemotherapy. *Chemistry–An Asian Journal*, *10*(7), 1457-1462.
50. Gao, P., Liu, S., Su, Y., Zheng, M., & Xie, Z. (2019). Fluorine-doped carbon dots with intrinsic nucleus-targeting ability for drug and dye delivery. *Bioconjugate chemistry*, *31*(3), 646-655.
51. Elmore, S. (2007). Apoptosis: a review of programmed cell death. *Toxicologic pathology*, *35*(4), 495-516.
52. Portt, L., Norman, G., Clapp, C., Greenwood, M., & Greenwood, M. T. (2011). Anti-apoptosis and cell survival: a review. *Biochimica et Biophysica Acta (BBA)-Molecular Cell Research*, *1813*(1), 238-259.
53. Oleinick, N. L., Morris, R. L., & Belichenko, I. (2002). The role of apoptosis in response to photodynamic therapy: what, where, why, and how. *Photochemical & Photobiological Sciences*, *1*(1), 1-21.
54. Zhang, D., Jin, Q., Ni, Y., & Zhang, J. (2020). Discovery of necrosis avidity of rhein and its applications in necrosis imaging. *Journal of Drug Targeting*, *28*(9), 904-912.
55. B. L. Tan, M. E. Norhaizan, W. P. P. Liew and H. S. Rahman, *Fron. Pharmacol.*, 2018, **9**, 1162.
56. X. Ji, L. Ge, C. Liu, Z. Tang, Y. Xiao, W. Chen, Z. Lei, W. Gao, S. Blake, D. De, B. Shi, X. Zeng, N. Kong, X. Zhang and W. Tao, *Nat. commun.*, 2021, **12**, 1-17.
57. Rahman, F. U., Ali, A., Guo, R., Zhang, Y. C., Wang, H., Li, Z. T., & Zhang, D. W. (2015). Synthesis and anticancer activities of a novel class of mono-and di-metallic Pt (II)(salicylaldiminato) (DMSO or Picolino) Cl complexes. *Dalton Transactions*, *44*(5), 2166-2175.

58. Maximenko, A., Depciuch, J., Łopuszyńska, N., Stec, M., Światkowska-Warkocka, Ż., Bayev, V., ... & Parlinska-Wojtan, M. (2020). Fe_3O_4@SiO_2@Au nanoparticles for MRI-guided chemo/NIR photothermal therapy of cancer cells. *RSC advances*, *10*(44), 26508-26520.
59. Kim, H. S., & Lee, D. Y. (2018). Near-infrared-responsive cancer photothermal and photodynamic therapy using gold nanoparticles. *Polymers*, *10*(9), 961.
60. Lee, S. Y., Lee, R., Kim, E., Lee, S., & Park, Y. I. (2020). Near-infrared light-triggered photodynamic therapy and apoptosis using upconversion nanoparticles with dual photosensitizers. *Frontiers in bioengineering and biotechnology*, *8*, 275.

Chapter 4

Quercetin@Gd^{3+} doped Prussian blue nanocube induces pyroptotic death of MDA-MB-231 cells: combinational targeted multimodal therapy, dual modal MRI, intuitive modelling of r_1-r_2 relaxivities

Chapter 4. Quercetin@Gd^{3+} doped Prussian blue nanocube induces pyroptotic death of MDA-MB-231 cells: combinational targeted multimodal therapy, dual modal MRI, intuitive modelling of r_1-r_2 relaxivities

4.1 Introduction

Breast cancer is a universal health problem for women leading second most common cause of cancer death.[1] Although, its mortality rate declined a little bit due to advanced theranostic techniques; but the success of mono- and neo-adjuvant chemotherapeutic regimens is very much limited for triple-negative breast cancer (TNBC) due to absence of estrogen receptor (ER), progesterone receptor (PR) and human epidermal growth factor receptor 2 (HER2). In addition, TNBC is the most aggressive invasive having worse prognosis in comparison with other subtypes and comprises 10 – 15% of breast cancer.[2] Although, conventional anthracyclines and taxanes chemotherapeutic agents e.g. doxorubicin (DOX) form the mainstay clinical treatment for TNBC, however they are barely effective for long term treatment due to their inevitable toxicity towards normal cells, cardiotoxicity, bone marrow suppression,[3] acquisition of multidrug resistivity (MDR1) which is caused by ATP-dependent efflux pump *ABCB1* induced up-regulation of p-glycoprotein (P-gp), followed by relapse, rapid cell proliferation, frequent metastasis to visceral and central nervous system etc.[4] In addition, it has also been reported that genetic diversity and mutations ensuing in TNBC affected patients easily creates critical issues in the development of chemotherapeutics.[5] To circumvent above mentioned challenges of therapeutic strategies, new strategy is highly required, wherein researchers are highly active. Many previous studies illustrate that there are few natural phytochemicals such as sulforaphane, quercetin (Qu), curcumin lycopene etc. has anti-TNBC effect, in addition, they are less toxic to normal cells even at high level in comparison with DOX.[6,7] Among them, quercetin (3,3',4',5,7-pentahydroxyflavone), one of the natural flavonoid abundantly found in acai, berries, onions, apples etc., causes cell cycle arrest of gastric cancer cells and human leukemic T cells in late G1 phase,[8] as well limits cell proliferation of MDA-MB-231 cells at G2/M or sub G1 phase,[9,10] while TNBC growth is inhibited through blocking of the cell cycle progression and down-regulation of S-phase kinase associated protein 2 (Skp2). In addition, Qu is found to play a crucial role in the pathway of heat shock proteins, induces apoptosis by down-regulating p53 levels and acts as a potent

inhibitor for tyrosine kinase which regulates cell proliferation for colorectal tumor and HPB-ALL cells etc.[11,12] Hence, the use of Qu for different types of cancers is an active area of research across the globe. It can be stated from previous literature reports that Urokinase-type plasminogen activator (uPA), an extracellular serine proteolytic enzyme, plays a significant role in migration of inflammatory cells, invasion and metastasis of tumor cells and is over expressed on TNBC illustrating that uPA can be an important biomarker for TNBC. Importantly, Qu has special affinity towards uPA with general inhibition (IC_{50} = 7 μM) due to interaction of its catechol group, the primary pharmacophore part of quercetin, with Asp189 of the uPA facilitating cellular uptake.[13] However, poor solubility (2.15 μg mL^{-1} at 25^0C), chemical insatiability in neutral and alkaline environment limit clinical application. In general, oral administration processes unable to lead sustained release, premature excretion from body, hence fluctuation of Qu in plasma levels remains a major drawback for high therapeutic efficacy,[14] hence if the Qu is directly delivered to the diseases sites without premature leakage in the blood stream, then only the therapeutic efficacy would be improved significantly. To attain these, there is an urgent need of nanotechnology based drug delivery system which can lead sustained release, while modern drug delivery systems are designed in such a way that they facilitate multiple therapeutic modalities like photothermal therapy (PTT), photodynamic therapy (PDT) etc. Herein, synergistic effects of the combinational therapies have gained attention due to their inherent non-invasiveness, lower side effects, and high spatiotemporal accuracy.[15] Among different traditional nanomaterials e.g. noble metal, carbon etc., prussian blue nanocube (PBNC), one of the important US Food and Drug Administration (FDA) approved metal organic framework nanostructures, has attracted considerable interest as drug carrier because of their high surface area and intrinsic high optical absorption in NIR region, ascribed to C ≡ N bonds, that leads PDT and PTT activities more efficient. In this context, it may be stated that NIR abetted therapy facilitates treatment of deep lying TNBC making the process more feasible. In addition, it has also been noted from previous literature reports including us that PBNC can be an important contrast agent for magnetic resonance imaging (MRI) which one of the most adopted noninvasive clinical technique to diagnose TNBC anatomically.[16] As MRI signals significantly depend on different specialities or features of the cancer cells, contrast agent is being widely employed to visualize internal structure of TNBC. In general, contrast agents are classified into a positive (T_1) contrast agent that leads the lesion bright and a negative (T_2) contrast agent that makes the lesion dark. It has been observed that signal from single mode of MRI often interferes limiting the diagnosis; wherein, T_1-T_2 dual-

modal contrast agents can generate comparative complementary images with the same in-plane geometries with different contrast, that facilitates great achievement in self-confirmed MRI detection with higher accuracy and precise diagnosis,[17,18] which is an active research area of present time. Previously, we have examined multimodal theranostic efficiencies revealing good potency of PBNC in cancer therapy as well as in diagnosis with r_1 relaxivity ~ 5.14 $mM^{-1}s^{-1}$.[16] As we know that linear (DTPA-type) or macrocyclic (DOTA-type) Gd^{3+} complexes are approved contrast agent for MRI, wherein Gd^{3+} plays significant role.[19]

Herein, we report on the design and synthesis and evaluation of r_1 - r_2 relaxivities, PTT and PDT effects of Gd^{3+} doped PBNC (GPBNC), wherein results yield significant increase of relaxometric parameters benefiting MRI diagnosis and finally theranostic activities of Qu encapsulated optimized GPBNC have been tested against TNBC. Briefly, we have first investigated the effect Gd^{3+} doping on T_1 - T_2 relaxometric parameters, thoroughly discussed the variation according to Solomon-Bloembergen-Morgan (SBM) theory. PTT effect were tested in the presence of 808 nm CW diode laser irradiation and the result shows increase of both PTT due to increase in the extinction absorption coefficient.[20] In contrast, polydopamine (PDA), one kind of mussel-inspired and natural melanin material, has been introduced here to coat GPBNC with theranostic potency in biodegradability, nontoxicity and excellent photothermal conversion efficiency. Besides these advantages, PDA coating also provides abundant surface reactive groups like carboxyl, amino and hydroxyl group that improves stability at acidic environment and helps for further functionalization.[21] Moreover, hydrophilicity of PDA helps netting of H_2O around the nanostructures facilitating relaxometric property which is beneficial for MRI.[22] GPBNC@PDA nanostructures have been further functionalized with di-amine polyethylene glycol (NH_2–PEG–NH_2) to endow a moral physiological stability, more circulation time (GPBNC@PDA@PEG), while their active group makes GPBNC@PDA@PEG easy to functionalized hyaluronic acid (HA) for target specificity and anti-TNBC drug Qu (GPBNC@PDA@PEG@HA@Qu). Herein, GPBNC@PDA@PEG@HA@Qu is expected to exhibit an effectual approach to overcome above limitations. Finally, we have assessed the theranostic efficiency of our developed GPBNC@PDA@PEG@HA@Qu in terms of *in-vitro* therapy and T_1-T_2 weighted MRI diagnosis on TNBC cell line (MDA-MB-231), while our study demonstrates chemo-photo induced cell death followed by both N terminal gardermin D (N-GSDMD) and P2X7 receptor mediated pyroptosis pathways. In this context, we have also compared the toxicity of

GPBNC@PDA@PEG@HA@Qu against Human embryonic kidney cell (HEK 293) as reference.

4.2 Experimental Section

4.2.1 Chemicals and Cell lines: $K_4[Fe(CN)_6]\cdot 3H_2O$, citric acid anhydrous and acetone were purchased from Merck. $FeCl_3\cdot 6H_2O$, $Gd(NO_3)_3\cdot 6H_2O$, Quercetin, N-(3-Dimethylaminopropyl)-N/-ethylcarbodiimide hydrochloride (EDC), Nhydroxysuccinimide (NHS) (98%), 1,3-Diphenylisobenzofuran (DPBF), dopamine hydrochloride and NH_2-PEG-NH_2 were brought from sigma Aldrich. Tris buffer (pH 8.5) and hyaluronic Acid (HA) were collected from Alfa Aesar and TCI chemicals respectively. Cell culture media components viz. Dulbecco's Modified Eagle Medium (DMEM), Fetal bovine serum (FBS), Penicillin-Streptomycin-Neomycin (PSN) antibiotic cocktail, trypsin and ethylenediaminetetraacetic acid (EDTA) were obtained from Gibco, USA. Other essential fine and raw chemicals were provided by SRL, India, and Sigma-Aldrich, USA. MDA-MB-231 carcinoma and Human embryonic kidney 293 (HEK 293) cell lines were bought from National Centre for Cell Sciences (NCCS), India. Antibodies were procured from Cell Signalling Technology (CST), and eBioscience, USA. Other reagents were collected from best existing commercial sources and all chemicals were used without further purification.

4.2.2 Synthesis of pure and Gd^{3+}doped insoluble Prussian Blue Nanocubes: Citric acid capped insoluble pure Prussian Blue Nanocubes (PB), Gd^{3+}doped PB (GPB) and Gd analogous PB (GPBA) were synthesized by reflux process using single anionic source.[16] To synthesize PB, $FeCl_3.6H_2O$ (5.40 mg) and citric acid (98.00 mg) were dissolved in DI water (30 mL) in a three neck flask under magnetic stirring to constitute Solution A. Separately, $K_4Fe(CN)_6.3H_2O$ (8.45 mg) and citric acid (98.00 mg) were added to DI water (30 mL) in another flask using magnetic stirring to constitute Solution B. Then both solutions were heated to 60°C. Maintaining the temperature constant, Solution B was dropwise added into solution A with vigorous stirring and a bright blue dispersed solution appeared after 1.0 h stirring. After completing the reaction, mixture solution was cooled down at room temperature and dispersed solution was centrifuged at 12,500 rpm for 15 minutes. After washing with acetone for three times, final product of pure PB in powder form was obtained after drying at 60°C under vacuum condition. When synthesizing 25, 50 and 75% Gd^{3+}doped PB (GPB) and Gd analogous PB (GPBA) samples, all steps were same except that a mixed solution of $FeCl_3.6H_2O$ and $Gd(NO_3)_3.6H_2O$ at the desired ratio (shown in Table B1, Appendix B) was used as Solution A.

Herein, 25, 50 and 75% Gd^{3+} doped PB were nomenclatured as $GPB_{0.25}$, $GPB_{0.50}$ and $GPB_{0.75}$ respectively.

4.2.3 Surface coating and functionalization of nanocubes: To enhance biocompatibility and stability, as-synthesized sample GPB was coated with PDA (named as GPB@PDA), followed by functionalization with NH_2-PEG-NH_2 and HA for target specificity. Initially, PDA coating was carried out in a protocol where dopamine hydrochloride (10.0 mg) and 10.0 mg of as-synthesized sample was mixed with 10.0 mL of Tris buffer (pH ~ 8.5) separately.[23] After 30 minutes of continuous stirring, they were mixed up and the resultant was stirred continuously for additional 6.0 hr. Finally, the coated nanoparticles were obtained after centrifugation at 12,500 rpm for 15.0 min, followed by washing with DI water for three times. In next step, 5.0 mL of PDA coated nanocube solution was injected with 50.0 mg of PEG, dissolved in 20.0 mL of Tris buffer. After continuous stirring for 10.0 hr, PEG functionalized nanoparticles were obtained after centrifugation, followed by washing with DI. In case of HA functionalization, 5.0 mg of HA was dissolved in 10.0 mL of DI water and was added with 6.0 mg of NHS and 10.0 mg of EDC linker, followed by stirring incessantly for 4.0 hr. Then as-functionalized samples, dispersed in 10.0 ml DI, were added drop-wisely to the linker solution. After continuous stirring for an additional 24.0 hr, followed by centrifugation and washing with DI water, final products, designated GPB@PDA@PEG@HA accordingly, were obtained.

4.2.4 Characterization: The crystallography and phase information of synthesized samples were acquired from powder X-ray diffraction pattern, recorded in ULTIMA IV X-Ray Diffractometer (Rigaku) operating at 40 kV and 40 mA using CuK_{α} radiation. Microstructures of the as-prepared samples were investigated by field emission scanning electron microscopy (FESEM, S – 4800, Hitachi, Japan). Thermal gravimetric analysis (TGA), absorption characteristics (200 – 1200 nm), surface charge, and surface functionalizations were determined by DTA-TGA instrument (SHIMADZU, DTG-60H), UV-vis-NIR spectrophotometer (PerkinElmer Instruments, Waltham, MA), Nano-ZetaSizer (Brookhaven Instruments, Holtsville, NY) and Fourier transform infrared spectrometer (FTIR, PerkinElmer, Spectrum-2000) respectively.

4.2.5 *In-vitro* measurement of T_1 and T_2-weighted MRI contrast efficiency in aqueous media: MR contrast efficiency of all bare samples (PB, GPB and GPBA), dispersed in 0.5% low melting agarose containing PBS solution within 96 well plates, was estimated between the concentration range of 0 to 500.0 μM. MRI was accomplished by keeping the sample containing well plates under a 3T clinically used MRI scanner (Siemens MAGNETOM

Verio), using a pre-fabricated sample holder. In order to determine both r_1 and r_2 relaxivity of the nanocube samples, coronal images were acquired under 3T magnetic field (B) and slice thickness of 3 mm. The inversion recovery (IR) sequence with variable inversion time (TI) was used for T_1 measurement ($^{\text{repetition time (TR)}}/_{\text{echo time (TE)}} = {}^{1900.00}/_{2.71}$, field of view (FOV) = 159×159 mm^2, variable TI = 1100; 1455; 2170 ms, matrix size = 268×268 mm^2). Similarly, T_2 measurements were also determined followed by spin-echo multi-section pulse sequence (TR = 1770 ms and variable TE = 13.3; 26.6; 39.9; 53.2; 66.5; 79.8; 93.1 ms, FOV = 208 mm×230 mm, matrix size, 195 mm×195 mm). In addition, T_1 contrasting effect was further confirmed by visualised flip angle dependant signal intensities followed by 3D gradient spin-echo sequence with short value of TE (=2.71 ms) and TR (=15.00 ms).

4.2.6 MRI data analysis from phantom images: Both T_1-T_2 weighted MR phantom images were acquired from DICOM software and analysed using ImageJ software. For a particular concentration of individual sample, the signal intensity (SI) was averaged within region of interests (ROI) and fitted against TI for T_1 measurements and TE for T_2 measurements which can be ascribed by the following monoexponential decay function:

$$SI_{TI} = S_0(1 - 2e^{(-TI/T_1)}) \quad (1)$$

$$SI_{TE} = S_0 e^{(-TE/T_2)} + S_1 \quad (2)$$

Where SI_{TI} and SI_{TE} are considered as the signal intensity at a particular TI and TE value.[24] Resulted T_1 and T_2 values were altered into relaxation rates $1/T_1$ and $1/T_2$. Finally, the slope was acquired from the linearly fitted plot between relaxation rate ($1/T_1$ or $1/T_2$) and different concentration [C] of the individual sample yields longitudinal (r_1) and transverse (r_2) relaxivities for the respective sample. The linear plot is considered by the following equation[25]:

$$\frac{1}{T_j} = \frac{1}{T_d} + [C]r_j; j = 1,2 \quad (3)$$

Where relaxation rate, $1/T_d$ associated with the contribution of diamagnetic counterpart towards relaxation effect. Herein, PBS has been considered as a control, showing diamagnetic behaviour.

4.2.7 *In-vitro* measurement of photothermal activity in aqueous media: The aqueous solutions (0.2 mg/mL) of bare PB, GPB and GPBA were exposed by NIR laser (808 nm; 5.26 $W{\cdot}cm^{-2}$, total power 1W) separately within 3 ml quartz cuvettes wherein DI water was treated as control. Photothermal images were captured at predetermined time interval (0 – 10 min) by an infrared camera (Magnity Electronics, MAG30, China) and temperature gradient was measured followed by the thermal software, provided by the manufacturer. Moreover,

photothermal stability was also inspected by 10 min of continuous laser exposure followed by another 10 min of laser exposure after tumbling to the previous temperature for a total of three cycles. Additionally, the photothermal conversion efficiency of each bare samples were calculated followed by previous report that described in electronic supporting information.[26]

4.2.8 Calculation of the photothermal conversion efficiency: One of the most extensively used equation to determine photothermal conversion efficiency of PB, GPB and GPBA nanocubes (NC) under 808 nm (5.26 $W{\cdot}cm^{-2}$, total power 1 W) laser irradiation is described as follows:[1,2]

$$\eta = \frac{hA(T_{max}-T_{sur})-Q_w}{I(1-10^{-A_{808}})} \quad (1)$$

Where h and A are the heat transfer coefficient and surface area of the quartz cuvette in which aqueous solution of the NC samples have been exposed under irradiation; T_{max} is steady state temperature of the NC aqueous solution; T_{sur} is the surrounding temperature; Q_w is associated with the converted energy by quartz cuvette contained only aqueous solution from radiant energy which is determined to be 8.4 mW; I is the power of incident NIR laser beam and A_{808} is the absorbance of the particular NC sample at a wavelength of 808 nm.

Herein, to find out hA value, a dimensionless force temperature (θ) has been introduced which is associated with the T_{max}.

$$\theta = \frac{T-T_{sur}}{T_{max}-T_{sur}} \quad (2)$$

And another parameter known as time constant related to the NC sample is defined as

$$\tau_s = \frac{\sum_i m_i c_{pi}}{hA} \quad (3)$$

Where, $\sum_i m_i c_{pi}$ is the product of mass and heat capacity of quartz cuvette, NC sample and solvent in the system. Thus, τ_s can be calculated from the following equation by considering cooling period of the solution:

$$t = -\tau_s ln\theta \quad (4)$$

Then, η can be intended after findings hA value followed by equation S1.

Figure A5(a-e) represents linear plot between cooling period (t) and -lnθ with slope τ_s to be 562.46, 585.47, 557.09, 608.43 and 688.59 s corresponding to PB, $GPB_{0.25}$, $GPB_{0.5}$, $GPB_{0.75}$ and GPBA respectively. Finally, photothermal conversion efficiency is calculated to be 33.85, 51.25, 65.56, 51.45 and 35.49% respectively.

4.2.9 NIR triggered extracellular singlet Oxygen ($^1O_2$) generation: $^1O_2$ generation had been examined through DPBF probe trapping method by monitoring absorbance of DPBF at 410 nm on UV-vis spectrophotometer.[16] $^1O_2$ oxidises DPBF and consequently absorption gets diminished. Herein, 3 mL of 100.0 μg/mL $GPB_{0.50}$@PDA@PEG@HA alcoholic solution was added with 1 mL of 68.0 μg/mL DPBF alcoholic solution in cuvette under time dependant irradiation of NIR laser (808 nm, 1.0 Wcm^{-2}) while mixed solution of $GPB_{0.5}$@PDA@PEG@HA and DPBF under dark was taken as reference.

4.2.10 Quercetin encapsulation efficiency and releasing profile: Qu was loaded on the surface $GPB_{0.50}$@PDA@PEG@HA to incorporate chemotherapeutic strategy. Briefly, 8.1 mg Qu containing 4.0 mL DMSO solution was added dropwise with 1.0 mg/mL of 5.1 mL $GPB_{0.50}$@PDA@PEG@HA Tris solution with continuous stirring for overnight under dark while concentration was determined from calibrated absorption spectra of $GPB_{0.50}$. Then Qu loaded $GPB_{0.50}$@PDA@PEG@HA nanocomposites were collected by centrifugation, followed by washing with PBS. Collected precipitated was redispersed in PBS for future use while supernatant was used for measurement of Qu encapsulation efficiency followed by,

$$\text{Qu loading efficiency (\%)} = \frac{\text{Concentration of the Qu in the nanoparticles}}{\text{concentration of the given Qu}} * 100\%$$

The kinetics of Qu release from the $GPB_{0.50}$@PDA@PEG@HA@Qu was investigated using a dialysis bag (MWCO 12 kDa) from UV-vis spectroscopy by monitoring absorption peak at 382 nm. Briefly, 3.0 mL of previously prepared Qu loaded nanocomposites were dispersed in 5.0 mL of respective PBS solution (pH 5 & pH 7.4) separately and transferred into dialysis bag that was deep into a beaker having 50.0 mL of fresh buffer under slow stirring. Thereafter, 1.0 mL of Qu containing buffer was collected at predetermined time interval by replacing 1.0 ml of fresh buffer into the beaker to ensure concentration consistency.[27] Release kinetics of Qu was then calculated followed by

$$\text{Qu release (\%)} = \frac{\text{Concentration of the Qu released in surrounding medium}}{\text{Total Qu concentration in the nanoparticles}} * 100\%$$

Qu loading was measured from the supernatant through UV-vis spectroscopy by monitoring absorption peak at 382 nm.

4.2.11 Cell Culture: Concisely, cells were cultured in DMEM containing 1% antibiotic cocktail and 10% fetal bovine serum (FBS) at 37 °C in a humidified condition under continuous 5% CO_2. When confluence reached to 75−80%, cells were gathered with 0.25% of trypsin and

0.52 mM of EDTA in PBS. After centrifugation, they were plated at a required density to permit them to re-equilibrate before further investigation.[28]

4.2.12 *In-vitro* T_1 and T_2-weighted cellular MRI contrast measurement: For *in-vitro* cellular MR imaging, ~ 5×10^3 numbers of MDA-MB-231 and HEK 293 cells were incubated in 96 well plate for 24 h. Then Cells were treated with $GPB_{0.50}$@PDA@PEG@HA under six different concentrations of 15.6, 32.1, 62.5, 125.0, 250.0, 500.0 µM with reference to bare $GPB_{0.50}$, determined from calibrated absorption curve and further incubated for another 24 hr. Then they were fixed using paraformaldehyde after washing with PBS for three times. Finally, 100 µL of 2% low melting agarose was added to each well to avoid air susceptibility and store at 4 ºC to solidify the cell suspensions for further capturing MR phantom images as described earlier.[29] Captured images were also analysed in similar pattern.

4.2.13 *In-vitro* Cell Viability Assay: *In-vitro* cell toxicity was evaluated by MTT [(4, 5-dimethyl-thiazol-2-yl)-2, 5-diphenyl tetrazolium bromide] assay against MDA-MB-231 and HEK 293 cell line at different $GPB_{0.50}$@PDA@PEG@HA concentration with and without NIR laser irradiation.[30] Briefly, after cell plating in each well of 96 well plate at 2×10^6 cells/well, they are treated with several concentrations (0 – 37.6 µM) of $GPB_{0.50}$@PDA@PEG@HA@Qu along with the individual $GPB_{0.50}$@PDA@PEG@HA where concentrations were measured from the absorption calibration curve of $GPB_{0.50}$. Thereafter, the plates were incubated for 24 hr in a humidified 5% of CO_2-rich incubator at 37 °C. Then MTT solution (4 mg/mL) was added in each well after proper washing with PBS and further incubated for another 4 hr in dark. After mixing DMSO, absorbance of intracellular formazan salt was measured at 595 nm by ELISA reader (Emax, Molecular Device, USA). Herein, MTT assay had been carried out in triplicate.

4.2.14 *In vitro* photodynamic therapy (PDT): On the basis of initial screening, 13.54 µM of $GPB_{0.50}$@PDA@PEG@HA@Qu were preferred to further check the intracellular photosensitizing effect. Hence, we had irradiated HEK 293 and MDA-MB-231 cells with 808 nm laser in a time-dependent manner (0, 10 and 20 min), followed by the MTT assay to determine the synergistic effect of chemo-dynamic, photothermal, and photodynamic (chemo-photo) efficacy.[31]

4.2.15 Determination of Intracellular ROS: Total intracellular reactive oxygen species (iROS) was evaluated followed by dichlorofluorescin diacetate (DCFH-DA) staining method.[32] MDA-MB-231 Cells were treated with $GPB_{0.50}$@PDA@PEG@HA@Qu (13.54 µM). After 4

hr of treatment the cells were exposed under the irradiation of NIR laser for 0, 5 and 10 min and further incubated for another 24 hr. Then 10 μM DCFH-DA was used to stain the treated and untreated cells. The increment of DCF fluorescence directly reflects the generated ROS inside cells which were represented as mean fluorescence intensity of DCF. Hence the DCF fluorescence was checked by a flow cytometer (BD LSRFortessa, San Jose, CA, USA). In each sample, 1×10^6 cells were analyzed.

4.2.16 Quantification of apoptosis/necrosis using Annexin V-FITC Kit: Apoptotic or nonapoptotic type cell death was inspected through Annexin V-FITC detection kit (Calbiochem, CA, USA).[33] After 4 hr incubation with $GPB_{0.50}$@PDA@PEG@HA@Qu (as per IC_{50} value), MDA-MB-231 cells (10^6 cells/well) were exposed to 808 nm laser light for 0, 5 and 10 min. Subsequently, after 24 hr incubation the cells were washed and stained with Annexin V-FITC and propidium iodide (PI) followed by the manufacturer's instructions. The fractions of necrotic, apoptotic (early and late) and viable cells were estimated by flow cytometric analysis (BD LSRFortessa, San Jose, CA, USA).

4.2.17 Assessment of cellular uptake of nanocomposite by ICP-OES: Cellular uptake of $GPB_{0.50}$@PDA@PEG@HA was performed using ICP-OES (Inductively coupled plasma optical emission spectrometry) technique. Briefly, after plating in 6 well plate MDA-MB-231 and HEK-293 (1×10^6) cells were exposed to synthesized nanocomposite at an initial concentration of 15 and 30 μg/mL for 24 hr. Subsequently, treated cells were washed with PBS for three times and lysed using 200 μL of lysis buffer (9 mM $MgCl_2$, 10 μM 2-ME and 0.1% triton X-100 in DPBS). Following the cell lysis, a mixture of concentrated 69% HNO_3 and 35% HCl (trace metal grade, Merck) at a ratio of 1:3 was added to the cell lysates. Then acid digestion was carried out by heating the mixture to 95°C for a duration of 2 days in a heating block and total amount of iron was measured from ICP-OES instrument (Thermo Fisher Scientific). Untreated digested cell culture media was considered as a control.[34]

4.2.18 Confocal Microscopy: Briefly, after treating with 13.54 μM of $GPB_{0.50}$@PDA@PEG@HA@Qu and NIR exposure for 0, 5 and 10 min, the cover slips containing MDA-MB-231 cells were washed twice for 10 min each in 0.01 M PBS and incubated for 1 hr in blocking solution containing 2% normal bovine serum and 0.3% Triton X-100 in PBS. After blocking, the slides were incubated overnight at 4 °C with the proper primary antibody. Fluorophore-conjugated secondary antibodies were diluted 1:100 in the blocking solution and incubated for another 2 hr. The slides were then counterstained with DAPI for 10 min and mounted with the ProLong Anti-fade Reagent (Molecular Probe, Eugene,

OR, USA).[28] Staining images of the double immunofluorescence were examined using a confocal laser-scanning microscope (FV 10i, Olympus, Japan).

4.2.19 Analysis of protein expressions using Flow Cytometry: Treated MDA-MB-231 cells, were fixed in paraformaldehyde (4%) in PBS (pH 7.4) for 20 min at room temperature, followed by permeabilization (0.1% Triton X-100 in PBS) for 5 min with 0.1% FBS. Then, the permeabilized cells were washed twice using PBS with FBS (3%) and incubated with their respective primary antibodies (cleaved Pannexin-1 and Caspase 1) overnight. After removing the unbound primary antibodies, the cells were further incubated with their particular fluorophore-tagged secondary antibody for 2 h in ice. After that the stained cells were subjected to flow cytometric analysis using a BD LSRFortessa flow cytometer (Becton Dickinson, Franklin Lakes, NJ, USA) equipped with FlowJo software.[29]

4.2.20 Statistical analysis: Data are calculated as mean ± SEM. Statistical significance and differences among the groups were considered *via* two-way statistical analysis (ANOVA) using OriginPro 8.0 software (San Diego, CA, USA). '*p*-value of 0.05 was considered significant.

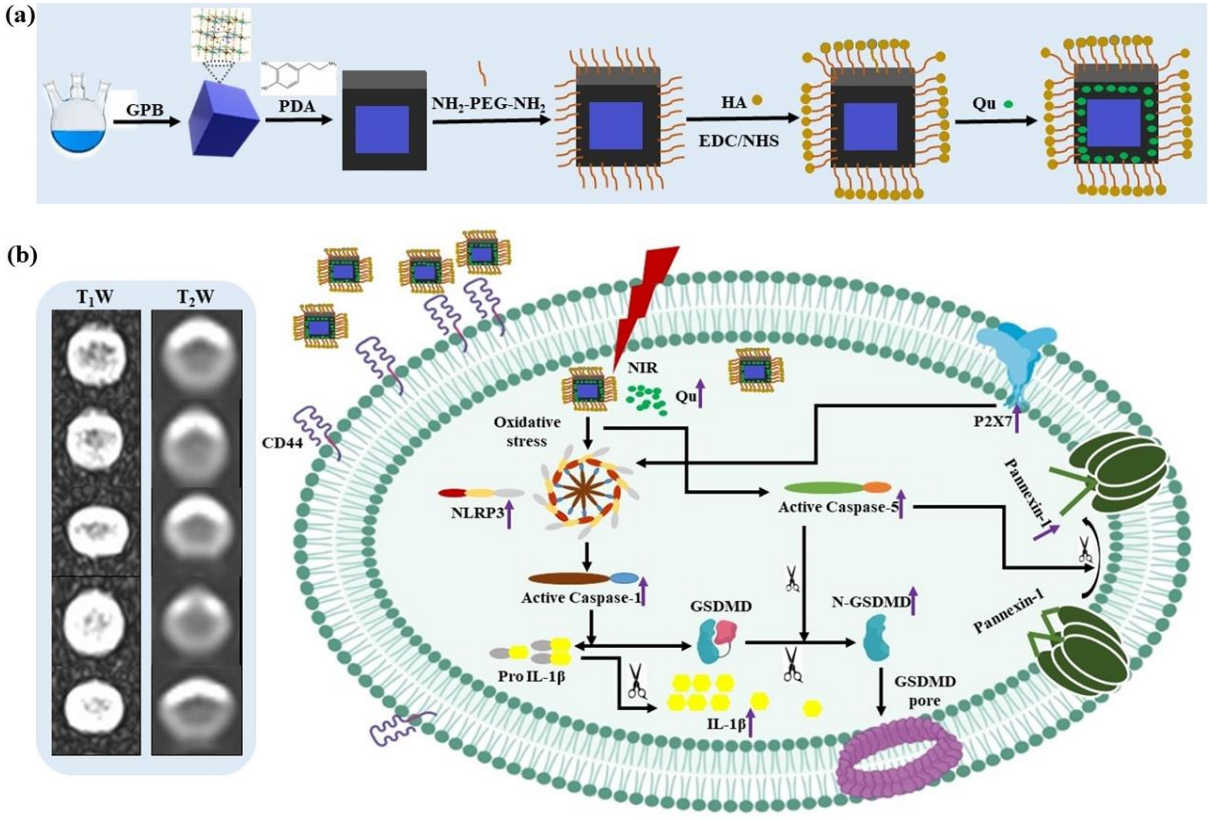

Scheme 1: Schematic representation of (a) functionalization of GPB nanocubes sample, (b)

Gd^{3+} doping dependant MRI diagnostic, chemo-photo induced pyroptotic cell death mechanism.

4.3 Result and Discussion

4.3.1 Synthesis and Characterization: The synthesis, dual mode T_1 – T_2 contrast efficiencies in MRI diagnosis and chemo-photodynamic-photothermal therapeutic activities of $GPB_{0.50}$@PDA@PEG@HA@Qu are schematically shown in Scheme 1((a) and (b)). Herein, a black PDA has been coated onto $GPB_{0.50}$ followed by polymerization of dopamine hydrochloride in Tris buffer (pH~8.5) through subsequent functionalization with $NH_2 - PEG - NH_2$ via a Michael addition and/or Schiff base reactions. HA has been used for improvement of colloidal stability and target specificity towards CD44 receptor which is generally highly abundant in MDA-MB-231 cell. After conjugation with Qu, $GPB_{0.50}$@PDA@PEG@HA@Qu has been studied for synergistic chemo-photodynamic-photothermal therapy and dual modal MRI diagnosis.

XRD patterns of PB (Figure A1(a), Appendix A), GPB (Figure 1(a-c)) and GPBA (Figure 1(d)) match with their cubic phase with *Pm3m* space group (JCPDS card no. 73-0687), whereas an additional peak at 15.05^0 associated with Bragg's reflection from (111) plane that increases with Gd^{3+} doping resembles the covalent bond between Gd^{3+} and cyanide groups.[35] It is well-known that PB grows with inherent $[Fe^{2+}(CN)_6]^{4-}$ vacancies to maintain the electro-neutrality those are being occupied by H_2O. In general, depending on occupancy, H_2O are classified into two categories: (a) coordinated H_2O, coordinated directly with metal ion and (b) uncoordinated H_2O, hydrogen bonded with coordinated H_2O. It has been examined earlier that these vacancies significantly depend on synthesis conditions and plays a crucial role in MR imaging. Presently, we have evaluated them qualitatively from Rietveld analysis using Maud software as suggested by Samain *et al.*[36] Herein, vacancies are orderly present and are represented by the parameter 'κ' which illustrates the occupancy probability of Fe^{2+}(1b) of $[Fe^{2+}(CN)_6]^{4-}$ at the interstitial position of the unit cell. After careful refinement, we have obtained lattice parameters, crystallite sizes, unit cell volume, lattice strain, occupancy of individual atoms etc. as listed in Table – 1 and Table – B2, Appendix B, while the unit cell of representative $GPB_{0.50}$ is shown schematically in Figure A1(b), Appendix A. It is being noted that lattice parameters and unit cell volume increase monotonically with increasing Gd^{3+}doping ratio and is attributable to its higher ionic radius. Most importantly, 'κ' is found to be increasing from PB to $GPB_{0.75}$ suggesting that Gd^{3+} doping reduces $[Fe^{2+}(CN)_6]^{4-}$ vacancy at 1b site which is also supported

by the reduction of H_2O as 6f sites, wherein occupancy of uncoordinated H_2O at 8g site varies hardly. Most importantly, H_2O at 6e and 12h sites are found to be increasing and they may be attributable to hydration effect of Gd^{3+}.[37] in doped samples.

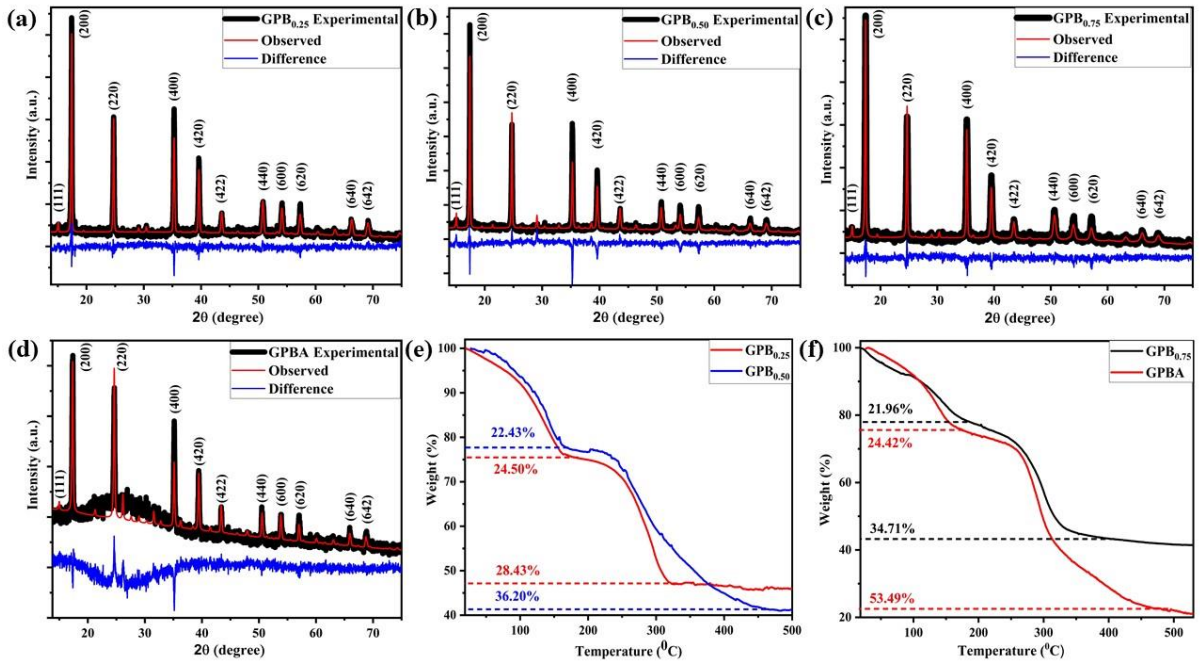

Fig. 1: Reitveld refinement of XRD patterns with difference between experimental and refined patterns of (a) $GPB_{0.25}$, (b) $GPB_{0.50}$, (c) $GPB_{0.75}$, (d) GPBA nanocubes. TGA plot of both (e) $GPB_{0.25}$ and $GPB_{0.50}$, (f) $GPB_{0.75}$ and GPBA.

For better understanding of coordinated and uncoordinated H_2Os, we have further carried out TG measurement on our samples (shown in Figure A1(c), Appendix A and Figure 1(e,f)), wherein results indicate two distinct regions of weight loss, assigned to uncoordinated (~ 160 - 180^0C) and coordinated H_2O (~ 330 – 450^0C) respectively. Herein, careful analyses yield 23% weight loss due to uncoordinated H_2O for all samples whereas ~ 25.23, 28.43, 36.20, 34.71, 53.49% weight losses due to coordinated H_2O are found to be in PB, $GPB_{0.25}$, $GPB_{0.5}$, $GPB_{0.75}$ and GPBA respectively. Hence, Rietveld and TG analyses of GPB samples confirm predominant occupancy of coordinate H_2Os at 6e and 12f sites. Meanwhile, the morphological investigation through FESEM (shown in Figure A2(a), Appendix A and Figure 2(a-d)) and subsequent histogram plots (shown in the inset of Figure A2(a), Appendix A and Figure 2(a-d)) demonstrate that PB, $GPB_{0.25}$, $GPB_{0.5}$, $GPB_{0.75}$ and GPBA are of uniform cubic morphology with average size ~ 60, 72, 145, 367 and 210 nm respectively corroborating Rietveld analyses, while elemental mapping (shown in Figure 2(e-h)) and EDX analysis (shown in Figure A2(b-

d), Appendix A and Figure 2(i))) confirm the uniform distribution of Gd, Fe, C, N and increasing Gd content in well agreement with previous result. Moreover, EDX analysis (shown in Table – B3, Appendix B) also shows that atomic percentage of N element radially increases with Gd^{3+} doping in GPB samples which may be related with $[Fe^{2+}(CN)_6]^{4-}$ vacancy that well corroborates with Rietveld analysis. Additionally, ICP-OES results also support this trend (Shown in Figure A3, Appendix A).

Table 1: Unit cell parameters and selective interatomic distances of PB, GPB, GPBA nanocubes as obtained by Rietveld analysis using Maud software.

Sample		**PB**	**$GPB_{0.25}$**	**$GPB_{0.50}$**	**$GPB_{0.75}$**	**GPBA**
Lattice parameter (a in Å)		10.164	10.175	10.178	10.190	10.207
Unit cell volume ($Å^3$)		1050.19	1051.63	1052.30	1057.87	1064.67
Crystallite sizes (nm)		67.9	82.4	127.2	124.8	108.0
Lattice Strain		0.0016	0.0019	0.00147	0.00179	0.00113
Bond length (Å)	Fe^{3+} (3c)-O(6f)	3.1615(3)	2.56835(18)	2.53648(18)	2.4759(5)	2.5809(11)
	Fe^{3+} (3c)-O(12h)	2.3029(19)	2.03176(14)	2.36411(17)	2.3955(5)	2.04170(9)
	Fe^{3+} (1a)-O(6e)	2.0884(17)	2.05205(15)	2.20499(16)	2.3054(5)	2.06208(9)
	O(6f)-O(8g)	3.2891(4)	3.0784(3)	3.2568(3)	3.1802(7)	3.09349(13)

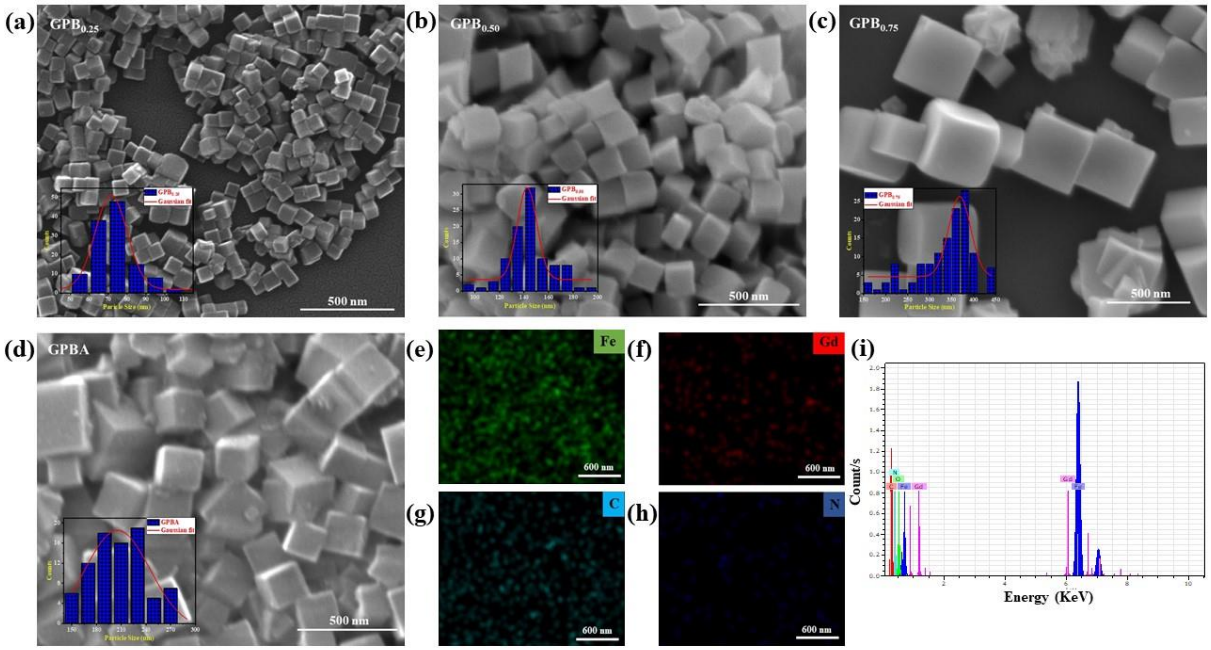

Fig. 2: Characterization of GPB nanocubes. FESEM image and size distribution histogram in

the inset of (a) $GPB_{0.25}$, (b) $GPB_{0.50}$, (c) $GPB_{0.75}$ and (d) GPBA nanocubes. (e-h) Corresponding elemental mapping images of $GPB_{0.50}$. (i) EDX spectrum of $GPB_{0.50}$.

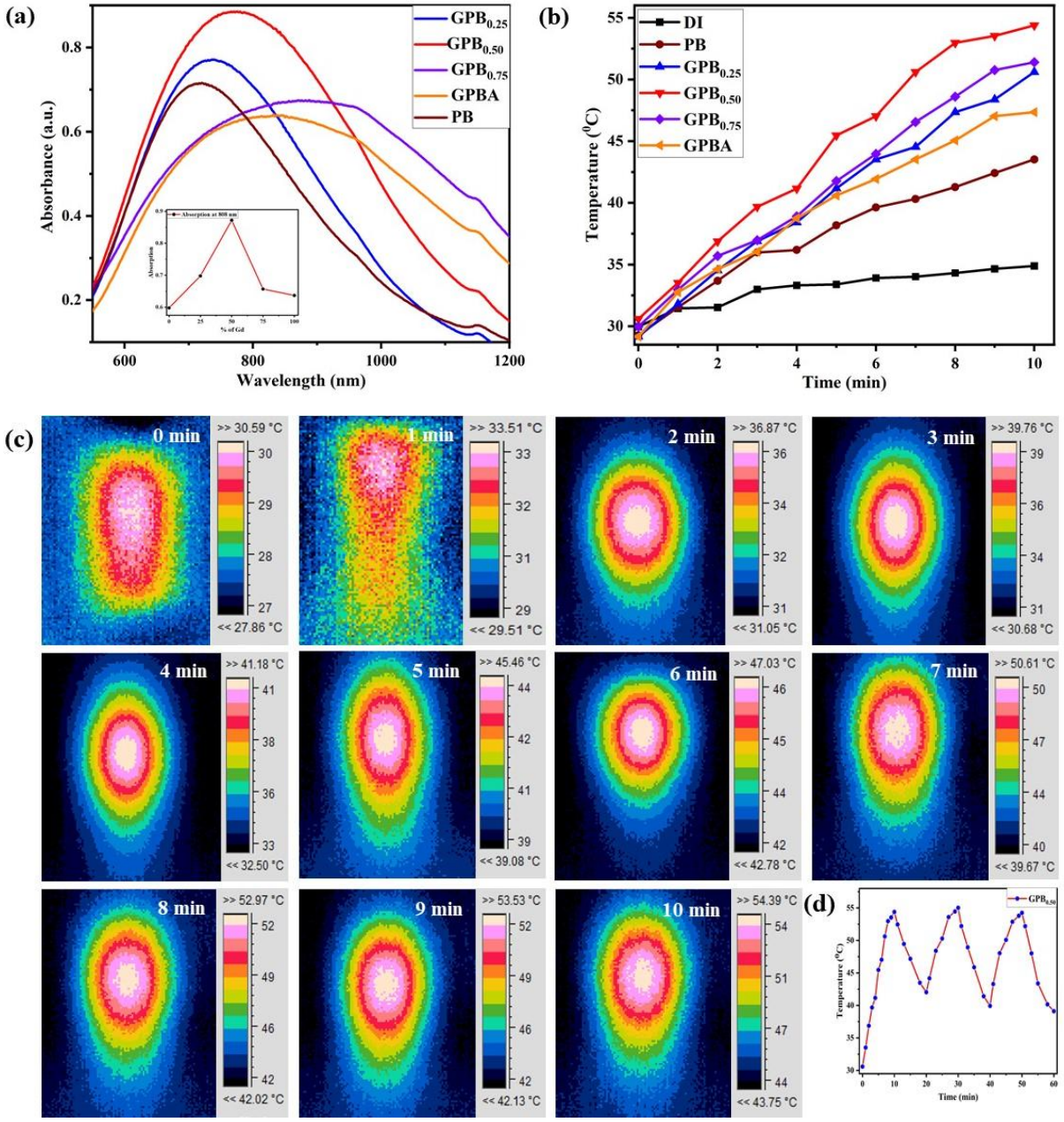

Fig. 3: Photothermal performance of GPB nanocubes. (a) UV-vis absorption spectra and absorption at 808 nm with equivalent concentration in the inset, (b) photothermal heating plot over 10 minutes under 808 nm NIR laser irradiation of $GPB_{0.25}$, $GPB_{0.50}$, $GPB_{0.75}$ and GPBA nanocubes. (c) corresponding photothermal images of $GPB_{0.50}$ nanocube sample. (d) Temperature curves of $GPB_{0.50}$ nanocubes solution under NIR laser exposure for three cycles.

Optical absorption spectra of all bare samples, shown in Figure 3(a), illustrates strong absorption peak at 718 nm from sample PB, assigned to metal to metal charge transfer between

$\{Fe^{III}[(t_{2g})^3(e_g)^2]Fe^{II}[(t_{2g})^6]\}$ and $\{Fe^{II}[(t_{2g})^4(e_g)^2]Fe^{III}[(t_{2g})^5]\}$ through the cyanide bridge, while this peak gets red-shifted to 738, 776, 906 and 844 nm for $GPB_{0.25}$, $GPB_{0.50}$, $GPB_{0.75}$ and GPBA respectively. This red shift may be associated with the localized surface plasmon resonance (LSPR). In general, LSPR originates from the collective and coherent oscillations of the free carriers (namely, electrons or holes) in resonance with the incident light frequency. GPB exhibits tuneable LSPR characteristics through carrier density modulation, dependent on the size, dopant concentration, and dopant distribution inside the structure. That is, Gd^{3+} dopant hybridization with the bands of the host lattice of PB, as well as the interplay of the crystal structure, determines the LSPR characteristics, and a proportional change in the carrier concentration will cause a significant shift in the LSPR optical behaviour. The effect of LSPRs contributes to the NIR absorbance of both PB and GPB, which is mainly ascribed to the collective oscillations of free charge carriers of $[Fe^{2+}(CN)_6]^{4-}$ vacancies. When more Gd^{3+} ions occupy the lattice sites to form Fe−C≡N−Gd, the concentration of the $[Fe^{2+}(CN)_6]^{4-}$ vacancy was decreased (also correlated from Reitveld and TGA), leading to the redshift of the LSPR peak towards lower energies. Therefore, the presence of Gd^{3+} ions in the lattice sites of PB will change the orbital energies and electron density of the cyanide bonds, which also leads to a redshift of the NIR absorbance peak of PB.[38]

4.3.2 Photothermal, MRI investigation of pristine PB, GPB and GPBA: dependence of therapeutic efficiency and r_1/r_2 relaxivity on Gd^{3+} doping:

Photothermal (PTT) activity, studied under 808 nm laser light irradiation, preferred due to low photobleaching and deep tissue penetration, for 10 minutes, reveals temperature rise ~ 43.5, 50.6, 54.4, 51.4 and 47.03^0C for PB, $GPB_{0.25}$, $GPB_{0.50}$, $GPB_{0.75}$ and GPBA respectively (shown in Figure 3(b,c) and Figure A4(a-e), Appendix A). In order to understand the mechanism, we have compared optical absorbance at 808 nm for all samples under identical concentration (shown in the inset of Figure 3(a)) and the measurement illustrates mass extinction coefficient ~ 6.35, 13.97, 18.73, 13.89 and 10.16 $cm^{-1}gm^{-1}L$ of the respective samples indicating that highest PTT activity of $GPB_{0.50}$ can be assigned to its highest extinction coefficient which can be explained as follows: it is well-known that charge transfer between Fe^{3+} and Fe^{2+} facilitates PTT activity,[39] herein the absorption peaks of $GPB_{0.50}$ is measured very close to 808 nm; hence, as expected, higher extinction coefficient offers enhanced PTT effect. In addition, the photothermal conversion efficiency (η) of PB, $GPB_{0.25}$, $GPB_{0.50}$, $GPB_{0.75}$ and GPBA is deliberated to be 33.85, 51.25, 65.56, 51.45 and 35.49% respectively, followed by the equation

1-4 and Figure A5(a-e) at Appendix A, further demonstrates the improved PTT efficiency of $GPB_{0.50}$ sample. We have also checked photostability of this sample and the result (Figure 3(d)) yields that the sample are highly stable under incessant laser irradiation indicating that the samples have potency as PTT agent.

As it is already reported that PB has the capability to shorten longitudinal (T_1) and transverse relaxation times (T_2) of protons from bulk water, attributed to low spin Fe^{2+} – C (S = 0) and high spin Fe^{3+} – N (S = 5/2) respectively,[40] hence PB acts as probe dual mode T_1 and T_2-weighted MRI contrast agent, wherein the contrast efficiencies, indicated by r_1 and r_2 relaxivities respectively. In addition, these five unpaired electrons of Fe^{2+} – C ≡ N – Fe^{3+} unit leads coordination bonds between H_2O and Fe^{3+}, causing relaxation inside PB and consequently r_1 and r_2 relaxivities get enhanced in comparison with other MRI probe.[41] In this study, r_1 and r_2 have been reconnoitred for all synthesized samples on 3.0 T MRI analyser with PBS acts as a control.

Herein, concentration dependent brightening and darkening effect of (shown in Figure 4(a,b) and Figure A6(a-f), Appendix A) PB, $GPB_{0.25}$, $GPB_{0.50}$, $GPB_{0.75}$ and GPBA in T_1-T_2 weighted MR images yield r_1 ~ 5.91, 7.05, 10.06, 11.69 and 11.84 $mM^{-1}s^{-1}$ (Figure A7(a), Appendix A) and r_2 ~ 15.82, 18.07, 24.96, 28.72 and 31.39 $mM^{-1}s^{-1}$ (Figure A7(b), Appendix A) respectively. Additionally, concentration dependant brightening effect in T_1-weighted MRI images (shown in Figure A8(a,b), Appendix A) of PB, $GPB_{0.25}$, $GPB_{0.5}$, $GPB_{0.75}$ and GPBA has also been visualised with two different flip angle (5 and 25^0) followed by 3D gradient spin-echo sequence which further supports our previous result. Of note, both r_1 and r_2 of all samples are higher than that of previously synthesized pure PB nanocubes (r_1 ~ 0.079 and r_2 ~ 0.488 $mM^{-1}s^{-1}$,[42] ultrasmall PB nanoparticles (r_1 ~ 0.13 and r_2 ~ 18.8 $mM^{-1}s^{-1}$),[43] PB / MnO_2 hybrid nanoparticles (r_2 ~ 28.3 $mM^{-1}s^{-1}$),[44] and ProHance, one of the commercially available contrast agents (r_1 ~ 3.00 $mM^{-1}s^{-1}$). Observed monotonic increase of r_1 and r_2 value, ascribed to substitution of Fe^{3+} by Gd^{3+} of high electronic spin (S = 7/2) state with low longitudinal electron – spin relaxation rate, may be understood very briefly as follows: according to Solomon – Bloembergen – Morgan theory, r_i $(i = 1, 2)$ consists of three components: inner sphere (r_i^{IS}), second sphere (r_i^{SS}) and outer sphere (r_i^{OS}) i.e. $r_i = r_i^{IS} + r_i^{SS} + r_i^{OS}$ where r_i^{IS} denotes the contribution from the interaction between Fe^{3+} / Gd^{3+} and coordinated H_2O, r_i^{SS} includes nearby uncoordinated H_2O and r_i^{OS} is associated with rotational motion and translational diffusion of bulk H_2O.[45,46] Of note, r_1 hardly depends on r_1^{OS}, moderately depends on r_1^{SS}, but significantly gets influenced by r_1^{IS}. As per Rietveld and TG analyses,

uncoordinated H_2O is same for all nanocube samples indicating that r_1 gets predominantly varied due to r_1^{IS}. In contrast, it has been studied earlier that r_2^{IS} and r_2^{OS} play crucial role on the variation of r_2 relaxivity. In general, r_1^{IS} and r_2^{IS} are described by the following equations[47]

$$r_1^{IS} \propto \frac{q^{IS}}{55.6} \frac{1}{T_{1M} + \tau_m} \quad (4)$$

$$r_2^{IS} \propto \frac{q^{IS}}{55.6} \left(\frac{1}{\tau_m}\right)\left(\frac{T_{2M}^{-1}\left(T_{2M}^{-1}+\tau_m^{-1}\right)+\Delta\omega_{ex}^2}{\left(T_{2M}^{-1}+\tau_m^{-1}\right)^2+\Delta\omega_{ex}^2}\right) \quad (5)$$

where, T_{iM}, τ_m, $\Delta\omega_{ex}$ and q^{IS} are the relaxation time of coordinated H_2O, inverse of the water-exchange rate (k_{ex}), chemical shift of bound H_2O and hydration state respectively. It has been studied that T_{iM} (~ 10^{-4} - 10^{-6} s) is very high compare to τ_m (~ 10^{-9} - 10^{-7} s), as well as ω_{ex} << T_{2M},[48] hence (4) and (5) can be simplified into the following form: $r_1^{IS} \propto q^{IS} \frac{1}{T_{1M}^{IS}}$ and $r_2^{IS} \propto q^{IS} \frac{1}{T_{2M}^{IS}}$. Herein, it may be stated that T_{1M}^{IS} consists of two different interactions, namely scalar (T_1^{SC}), dipole-dipole (T_1^{DD}), ascribed to electronic and nuclear interactions between H_2O proton and as-synthesized nanocubes, but it has been examined by us that T_{1M} >> T_1^{DD}, whereas Curie spin relaxation mechanism dominates T_{2M}.[16,49] Moreover, it was reported earlier that electronic relaxation time (τ_e) is inconsiderable at high magnetic field (~ 3T) and $\tau_m \gg \tau_R$ which indicates τ_{ci} , $\tau_{cs} \approx \tau_R$, where τ_{ci} (i = 1, 2) and τ_{cs} denote magnetic fluctuation time and curie spin correlation time.[50,16] Herein, τ_R, τ_{ci} (i = 1, 2) and τ_{cs} denote rotational correlation time, magnetic fluctuation time and curie spin correlation time. Based on these approximation, r_1^{IS} and r_2^{IS} are further simplified as follows:

$$r_1^{IS} \propto (q^{IS})\left(\frac{S(S+1)}{r_{M-H}^6}\right)(\tau_R) \quad (6)$$

$$r_2^{IS} \propto (q^{IS})\left(\frac{\{S(S+1)\}^2}{r_{M-H}^6}\right)(\tau_R) \quad (7)$$

Hence, it is to state that r_i^{IS} is directly proportional to q^{IS}, S(S+1), τ_R and inversely proportional to r_{M-H}^6. Herein, our Rietveld, FESEM and TG analyses yield increase of coordinated H_2O and particle size, decrease of r_{M-H}^6 i.e. $Fe^{3+}(3c) - O(6f)$ distance with Gd^{3+} doping. According to Debye – Stoke's relation, $\tau_R = \frac{4\pi\eta r^3}{3k_B T}$, where r, η, T and k_B are size of the nanocube, viscosity of the environment, absolute temperature and Boltzmann constant, i.e. higher particle size facilitates r_i^{IS} contribution. In addition, higher S (= 7/2) of Gd^{3+} than that of Fe^{3+} (= 5/2) also causes enhancement of r_i^{IS}. Hence, increase of r_1^{IS} may be assigned to the synergistic contributions from increasing particle size and coordinated H_2O, decreasing r_{M-H}^6 and higher S. In this context, it can be believed that outer-sphere relaxivity plays a major role compare to

inner-sphere relaxivity in T_2 relaxation that can be expressed as $r_2 = r_2^{IS} + r_2^{OS}$ wherein r_2^{OS} is given by the following expression:

$$\frac{1}{T_2^{OS}} = \frac{(^{256\pi^2\gamma^2}/_{405})V'M_s^2r^2}{D(1+\frac{L}{r})} \qquad (8)$$

where D, V', r, L and M_s are the diffusion coefficient of bulk H_2O, volume fraction, width of the nanocube, thickness of coating layer and saturation magnetization respectively. Very briefly, magnetic moments of paramagnetic nanoparticles produce local magnetic field under an external magnetic field which perturbs the phase coherence of bulk H_2O within its motional average regime and consequently T_2 relaxation time gets shortened. Herein, M-H plot (shown in Figure A9(a-f), Appendix A) at room temperature confirms that the magnetization (M_0) at 3T gradually increases with Gd^{3+} doping leading enhancement of r_2^{OS}, hence faster rise of r_2 in comparison with r_1 is assigned to synergistic contributions from r_2^{IS} and r_2^{OS}. Hence, it may be concluded that contrast efficiency of both T_1, T_2-weighted MR images increase with Gd^{3+} doping.

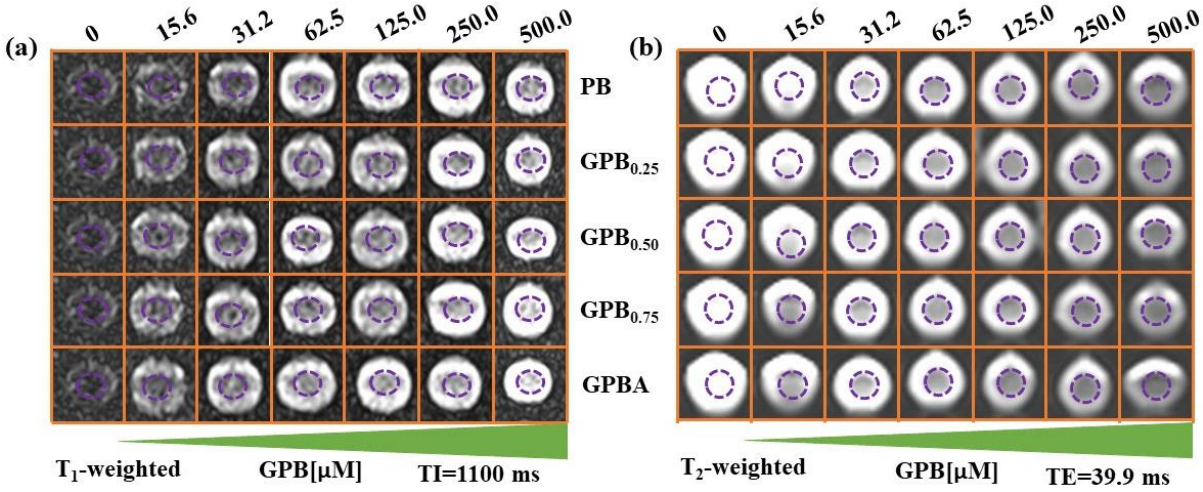

Fig. 4: Concentration dependant (a) T_1 and (b) T_2-weighted MR images at 3 T showing hyper and hypo intensity from PB, $GPB_{0.25}$, $GPB_{0.50}$, $GPB_{0.75}$ and GPBA nanocubes sample. MR images were acquired using inversion recovery sequences for T_1W (TR: 1900 ms, TE: 2.71 ms, TI: 1100 ms) and spin−echo sequences for T_2W (TR: 1770 ms, TE: 39.9).

4.3.3 Functionalization and characterization: Motivated by the fact that $GPB_{0.50}$ exhibits highest molar extinction coefficient, PTT activity upon laser (808nm; 1.0 Wcm^{-2}) irradiation and relatively higher MRI contrast efficiency, we choose $GPB_{0.50}$ for further *in-vitro* theranostic applications. Although, pristine $GPB_{0.50}$ nanocubes are well-dispersed in DI water but in physiological environment they would settle down, therefore ahead of applying them for

in-vitro experiments, we have carried out surface modification through layer-by-layer polymer coating method. Herein, we have coated $GPB_{0.50}$ with PDA (named as $GPB_{0.50}$@PDA), followed by functionalization with PEG and HA ($GPB_{0.50}$@PDA@PEG@HA) to make nanocubes biocompatible, target specific localization and easy internalization.[51] Finally, therapeutic activity has been increased by loading chemotherapeutic drug Qu on $GPB_{0.50}$@PDA@PEG@HA. Herein, Zeta potential and FTIR analyses have validated PDA coating, PEG and HA functionalization and Qu loading. Briefly, zeta potential of bare $GPB_{0.50}$ (shown in Figure 5(a)), measured to be – 38.6 mV, is ascribed to –COOH group of citric acid, while PDA coating increases zeta potential (– 39.9 mV), attributed to the phenolic hydroxyl group of PDA. Due to $–NH_2$ group, PEG functionalization reduces zeta potential (–32.6 mV), but HA causes little bit reduction of the zeta potential –33.8 mV due to –COOH group. In this context, it may be stated that the negatively charged surface of PB has negative effect on the surface modification by HA with same charge as this modification has taken place through complex interaction between iron ion of PB and the carboxyl group of HA, rather than electrostatic interaction.[52] However, such orderly variation in zeta potential confirms the successful coating of PDA and functionalization of PEG and HA on the surface of $GPB_{0.5}$ and high negative value of surface charge indicates excellent water dispersibility. Finally, zeta potential of GdPBA@PDA@PEG@HA@Qu increases to -27.9 mV which indicates successful loading of Qu via interaction between hydroxyl group and amino group of Qu and PDA through covalent bonding.[53,54] Herein, it is to mention that FESEM image (shown in Figure 5(b)) yields that shape of $GPB_{0.50}$ remains same after PDA coating and histogram (shown in the inset of Figure 5(b)) confirms enrichment in size (~10 nm) from bare $GPB_{0.50}$ nanocubes. We have also verified above mentioned functionalization through FTIR measurements, wherein the spectrum (shown in Figure 5(c)), consists of a strong characteristic peak at 2072 cm^{-1} corresponding to $\nu(C \equiv N)$ and a broad band in between 3010 and 3680 cm^{-1}, centred at 3350 cm^{-1} which is attributable to –OH stretching vibration due to H_2O, adsorbed at the surface. Moreover, $GPB_{0.50}$ illustrates additional stretching vibration at 1724 and 1598 cm^{-1}, assigned to C = O and C = C of citric acid that acts as a surface capped stabilizer of bare $GPB_{0.5}$. $GPB_{0.5}$@PDA exhibits peaks at 1296 and 1607 cm^{-1} corresponding to $\nu(C – O)$ and $\delta(N – H)$ in the aromatic ring of PDA testifying the formation of PDA coating around $GPB_{0.50}$, while a considerable enhancement of intensity of the broad absorption peak around 3350 cm^{-1} corresponds to overlapping of aromatic $\nu(N – H)$ and $\nu(O – H)$ of PDA.[55] Herein, it may be stated that the presence of –OH at the surface of PDA facilitates easy functionalization with PEG. $GPB_{0.5}$@PDA@PEG displays two new prominent absorption peaks at 1105 and 2874 cm^{-1} due

to ν(C – O) and ν(C – H) of PEG while a noticeable decrease of the peak at 1607 cm^{-1} from δ(N – H) indicates successful functionalization of PEG on $GPB_{0.50}$@PDA.[56] It has been also noticed that $GPB_{0.50}$@PDA@PEG@HA exhibits a strong absorption peak at 1412 cm^{-1} due to ν(COO^-) while a considerable reduction of intensity of the peak at 1607 cm^{-1} corresponding to δ(N – H) indicates initiation of amidation between -NH_2 group of PEG functionalized PDA and -COOH group of HA. Finally, $GPB_{0.50}$@PDA@PEG@HA@Qu shows a broad absorption band at 3408 cm^{-1} and a sharp peak at 1394 cm^{-1}, assigned to ν(O – H) and δ(O – H) respectively while peaks at 640 and 647 cm^{-1} are ascribed to δ(C – H) of Qu, hence appearance of these peaks indicate presence Qu. Herein, redshift (~ 12 cm^{-1}) of $GPB_{0.5}$'s characteristic peak and improved intensity of the peak at 1612 cm^{-1} due to overlapping δ(N – H) and ν(C = O) confirms successful loading of Qu onto the surface of $GPB_{0.50}$@PDA@PEG@HA.[57] Besides this, optical absorption spectra of bare Qu exhibits a absorption band, centered at 382 nm (Figure 5(d)), while the peak gets shifted at 338 nm for $GPB_{0.50}$@PDA@PEG@HA@Qu corroborating successful loading.

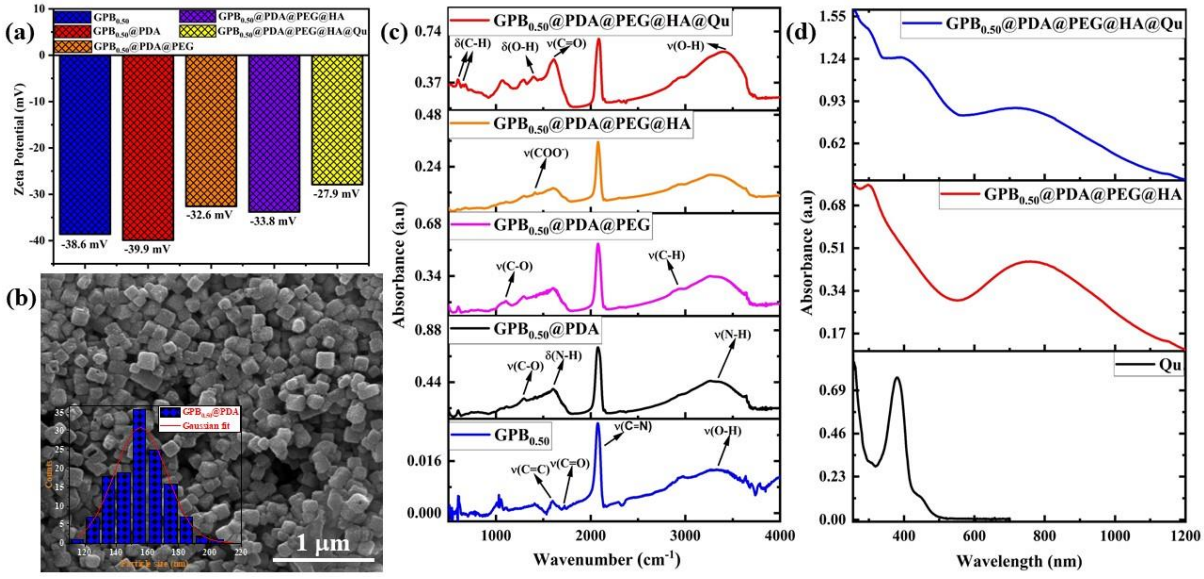

Fig. 5: Characterization after modification of $GPB_{0.50}$. (a) Zeta potential of $GPB_{0.50}$, $GPB_{0.50}$@PDA, $GPB_{0.50}$@PDA@PEG, $GPB_{0.50}$@PDA@PEG@HA and $GPB_{0.50}$@PDA@PEG@HA@Qu. (b) FESEM image and size distribution histogram in the inset of $GPB_{0.50}$@PDA. (c) FTIR spectra of $GPB_{0.50}$ along with each step of modifications. (d) UV-vis absorption spectroscopy of pure Qu, $GPB_{0.50}$@PDA@PEG@HA and $GPB_{0.50}$@PDA@PEG@HA@Qu.

4.3.4 *In-vitro* cellular theranostic measurements: Prior to the *in vitro* investigations of $GPB_{0.50}$@PDA@PEG@HA@Qu against MDA-MB-231 cell line, we have verified Qu loading efficiency and release profile, singlet oxygen ($^1O_2$) generation and stability as they have crucial role in any pharmacological applications. Herein, generation of $^1O_2$, one of the important cytotoxic agent for cancer ablation, has been examined through DPBF-probe fading measurement. Figure 6(a) spectacles the gradual decrease in absorbance peak at 410 nm with different irradiation time yielding generation of extracellular $^1O_2$ under irradiation with 808 nm laser. Thus this study exposes potency of $GPB_{0.50}$@PDA@PEG@HA as PDT agent. $GPB_{0.50}$@PDA@PEG@HA retains its stability in more than one mediums including PBS buffer (pH~7.4) and DMEM (pH~5.0) for at least 7 days (shown in Figure 6(b)) by monitoring absorbance at 776 nm. High loading efficiency (~ 54.6%) of Qu is ascribed to the noncovalent (H-bonding, Vander walls force) or covalent interaction between PDA and Qu as PDA contains abundant amino, hydroxyl and phenyl groups on its surface. Time dependent Qu release profile, (shown in Figure 6(c)) carried out *in vitro* condition, illustrates higher release (58% within 14 hr and 72% over 50 hr) under acidic PBS solution (pH ~ 5.5) compare to normal PBS solution (pH ~ 7.4).

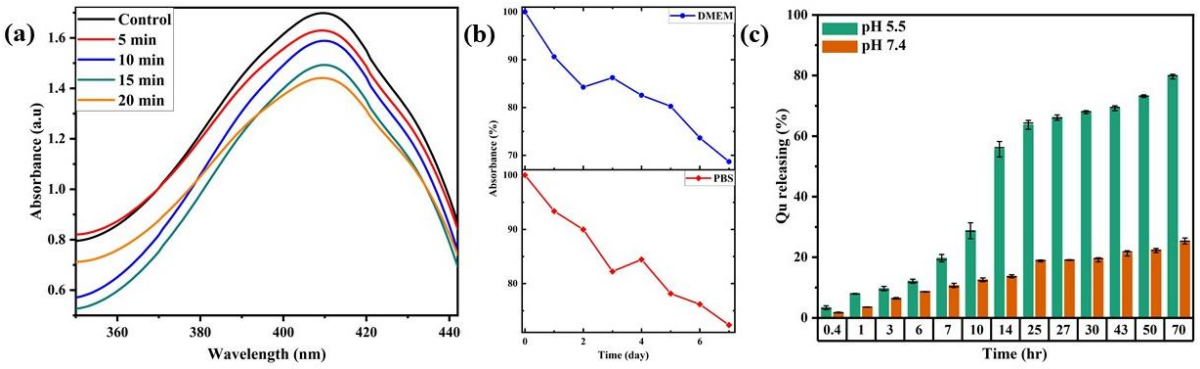

Fig. 6: (a) UV-vis spectra for time-dependent degradation of DPBF by $GPB_{0.50}$@PDA@PEG@HA under NIR laser irradiation. (b) Time dependant absorption intensity at 776 nm of $GPB_{0.50}$@PDA@PEG@HA in PBS buffer (pH~7.4) and DMEM (pH~5.0). (c) Qu-release kinetics of $GPB_{0.50}$@PDA@PEG@HA@Qu in different pH of PBS buffer without NIR exposure.

As depicted in Figure 7(a), dose dependent *in-vitro* toxicity measurements using MTT assay on MDA-MB-231 cells reveals that $GPB_{0.50}$@PDA@PEG@HA doesn't elicit chronic toxic effect beyond 40 µg/mL indicating that the nanoparticles are not toxic at the concentration, while a gradually promoted cell death has been detected with increasing concentration of

$GPB_{0.50}$@PDA@PEG@HA@Qu yielding Qu's potency as a chemotherapeutic agent. Herein, IC_{50} ~ 13.54 µM with concentration of Qu ~ 51.38 µM denotes high uptake by MDA-MB-231 cells that may be attributed to selective binding of HA on glycoprotein codded CD44 overexpression at cell surface.[58] After 24 hr incubation with 13.54 µM of $GPB_{0.5}$@PDA@PEG@HA@Qu in MDA-MB-231 cell line, internalization of the nanoparticles via endocytosis mediated pathway has been further confirmed by green emission from Qu in the confocal laser scanning microscopic (CLSM) images (shown in Figure 8(b)). So, target specific and pH-responsive drug releasing behaviour of our designed nanocomposite resolve the limitation of Qu in clinical usage. Phototoxicity of $GPB_{0.50}$@PDA@PEG@HA@Qu, assessed by MTT assay under various laser (808 nm, 1.0 W/cm^2) irradiation time at a fixed concentration of ~ 13.54 µM (shown in Figure 7(b)), is found to be increasing monotonically with exposure time, realizing ~ 60% cell death within 10 minutes while 44% of cell death occurs with $GPB_{0.50}$@PDA@PEG@HA sample within same irradiation period which indicates high phototherapeutic efficiency of designed samples. Moreover, iROS generation, examined by DCFH-DA staining method through flow cytometry assay, indicates chemo-phototherapeutic activity of $GPB_{0.50}$@PDA@PEG@HA@Qu. Briefly, we have noticed from more DCF fluorescence intensity (shown in Figure 7(c)) upon NIR exposure from $GPB_{0.50}$@PDA@PEG@HA@Qu (~ 13.54 µM) in comparison with that of $GPB_{0.50}$@PDA@PEG@HA indicating chemotherapeutic efficacy of Qu. Herein, we have also observed prolonged iROS production in time dependant manner which is beneficial for phototherapy. Hence, it may be inferred from MTT and DCF fluorescence studies that $GPB_{0.50}$@PDA@PEG@HA@Qu induces synergistic chemo-phototherapeutic activity at minimal dose of IC_{50} ~ 13.54 µM.

In general, early response of a treated cancer cell determines the conquest of an applied therapeutic approach where cell death through apoptosis, necrosis or pyroptosis plays a significant role, hence we have examined the cell death procedure for $GPB_{0.50}$@PDA@PEG@HA@Qu using Annexin V-FITC/PI staining assay. Prior to measurement, figure 7(d) demonstrates that $GPB_{0.50}$@PDA@PEG@HA treated to MDA-MB-231 cells show an enhanced PI staining (27.8%) and a very negligible Annexin V surface staining (6.45%) under 10 min laser exposure where 92.1% cell viability has been found as a control. Moreover, after 24 hr incubation with $GPB_{0.5}$@PDA@PEG@HA@Qu under 5 minute laser irradiation, cell viability decreases to 61.7% with 26.1% PI staining and 10.3% Annexin V surface staining population, while 10 minute irradiation reduces cell viability upto 54.2% with enhanced PI staining (35.5%) and 9.3% Annexin V on the surface. This result appears to

be harmonious with chemo-photo induced non-apoptotic programmed cell death mechanism, while phototherapeutic efficiency predominates over sole chemotherapeutic activity.

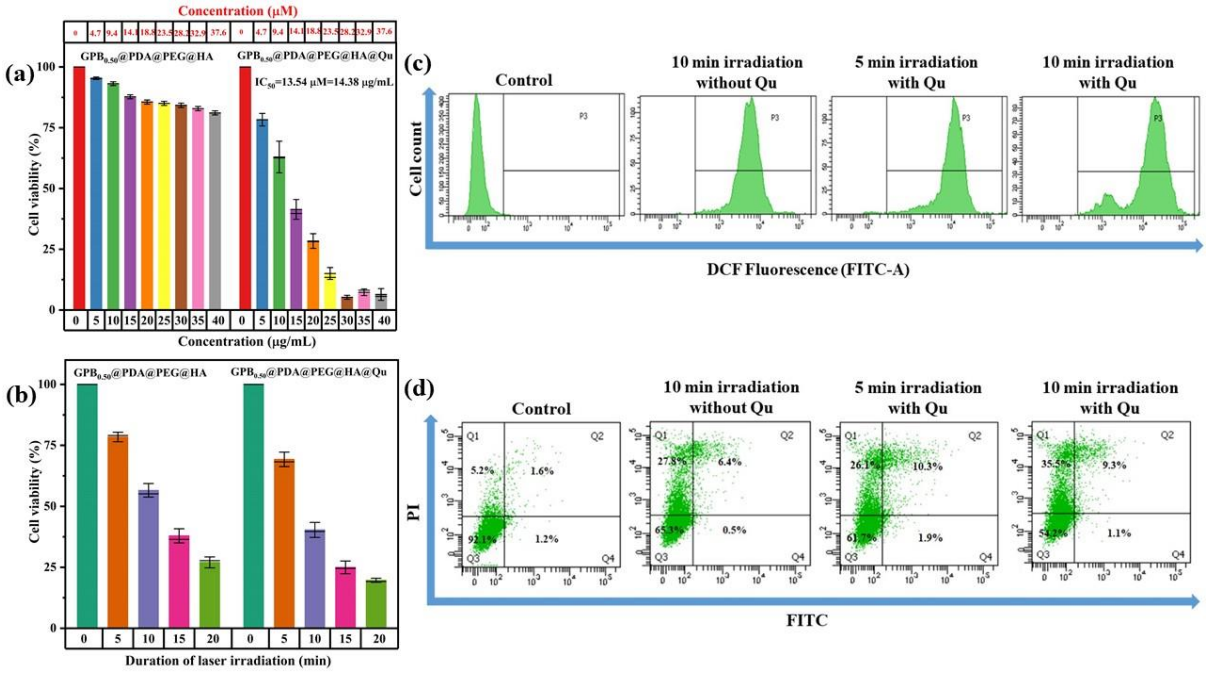

Fig. 7: (a) Concentration dependant and (b) NIR light irradiation time dependant Cell viability plot. (c) Determination of iROS generation. (d) Quantification of apoptosis or nonapoptosis cell death via Flow cytometric dot plot using dual Annexin V-FITC and PI staining. In each experiments MDA-M-231 cells were incubated with both $GPB_{0.50}$@PDA@PEG@HA and $GPB_{0.50}$@PDA@PEG@HA@Qu under time dependant continuous laser irradiation (808 nm, 1 Wcm^{-2}).

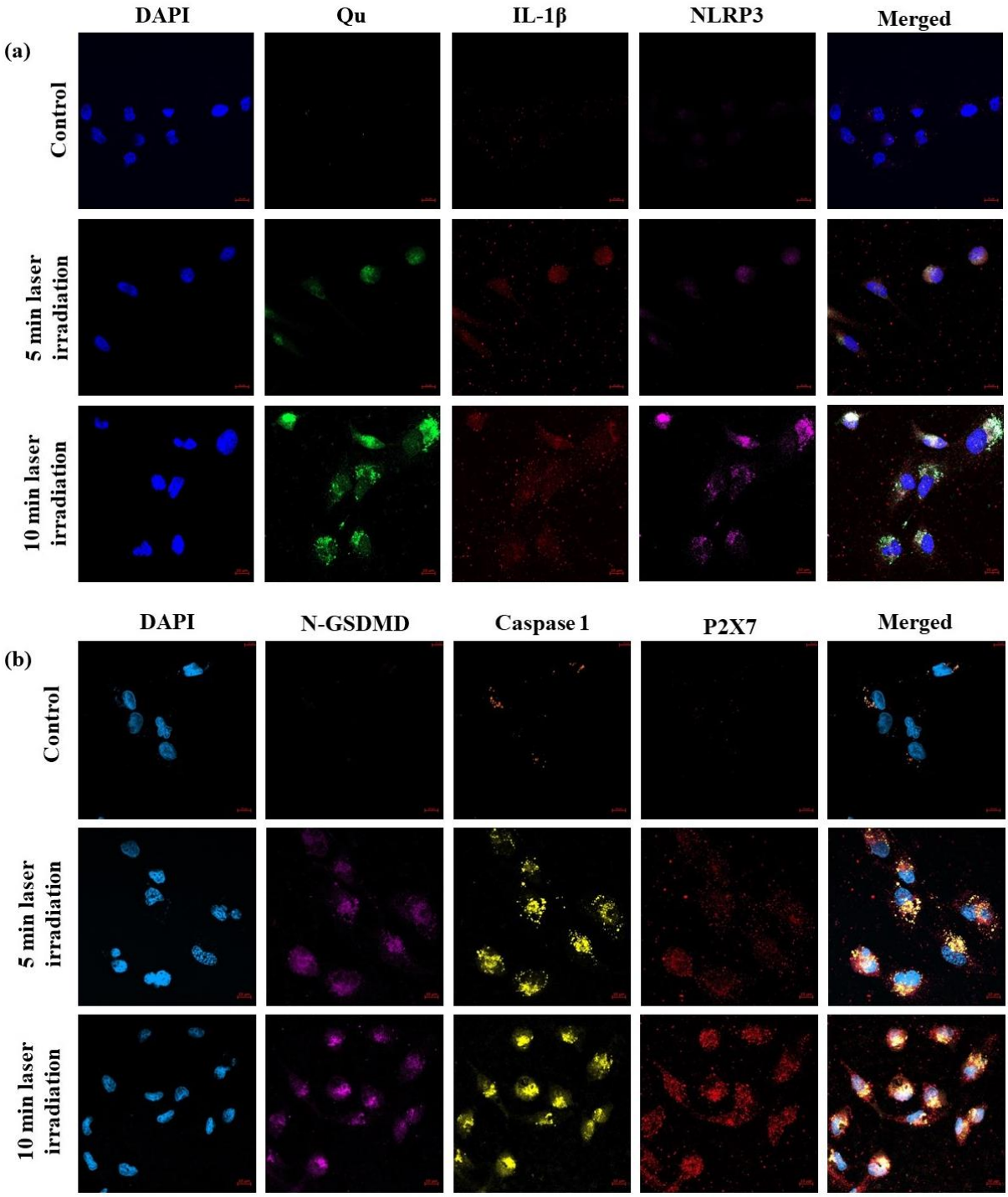

Fig. 8: CLSM images showing expression of (a) Qu, IL-1β and NLRP3 (b) N-GSDMD, caspase 1 and P2X7 in $GPB_{0.50}$@PDA@PEG@HA@Qu nanocomposite-induced MDA-MB-231cells under time dependant laser exposure. DAPI was used as a nuclear stainer.

Encouraged by non-apoptotic cell death mechanism, first we have observed morphological behaviour of MDA-MB-231 cells in response to $GPB_{0.50}$@PDA@PEG@HA@Qu under 10 minute laser exposure from bright field CLSM images. Generally, pyroptosis based cell death

is characterized by the bursting of the cell membrane. In the bright field image as shown in figure A10(a) at Appendix A, the treated cells appear as round or oval-shaped structures that have lost their normal shape and have become distorted, displaying signs of membrane disruption such as small holes or lacerations. Additionally, the nuclei of the treated cells seem to be fragmented or condensed. Overall, bright field image of the treated cells show clear evidence of the hallmark features of pyroptosis based cell death including membrane damage, loss of cytoplasmic content, and nuclear condensation due to chemo-photo therapy induced oxidative stress.[59] Then we have consequently investigated *in-vitro* cell death mechanism of MDA-MB-231 cells which appears to be N-GSDMD mediated pyroptosis pathway (figure A10(b)). As stated, pyroptosis is one kind of inflammasome induced programmed cell death which originates from the formation of porous membrane, followed by membrane rupture, cytoplasmic swelling and secretion of different cytosolic contents like IL-18, IL-1β etc. within extracellular region leading cell death. It was previously identified that pyroptosis follows two different pathways: one is caspase-1 induced canonical inflammasome pathway which gets activated by assembled inflammasome, that is associated with cleavage of GSDMD and secretion of cytokinase such as IL-18, IL-1β and other is non-canonical inflammasome pathway. In addition, it has also been resolved that a variety of inflammasome sensors resembling nucleotide-binding oligomerization domain (NOD) like receptor (NLRs) such as NLRP1, NLRP3, NLRC4 and non-NLRs like pyrin, absent in melanoma 2 (AIM2) are able to amass canonical inflammasomes.[60] The canonical pyroptosis is characterized by overexpression of NLRP3 that is activated with several stimulus like pathogens, toxins, crystalline substances, metabolites, nucleic acids and ATP.[61] In contrast to canonical, non-canonical inflammasome pyroptosis is interceded by human caspase 4/5 those are in general triggered by direct conjugation with intracellular cytosolic lipopolysaccharide (LPS) via N-terminal caspase activation and recruitment domain (CARD).[62] Herein, it is also reported that in spite of inability of activated caspase 4/5 to cleave pro-IL-18/ pro-IL-1β directly, it facilitates secretion and maturation of IL-18, IL-1β through NLRP3 activation via N-GSDMD mediated membrane-pore in some cells.[63] In this context, Yang *et al.* has observed that Pannexin-1 protein is being sheared by activation of caspase 11 resulting cellular ATP release, followed by persuasion of pyroptosis which mostly gets reconciled by P2X7 receptor ion channel.[64] So herein, to examine cell death mechanism by $GPB_{0.50}$@PDA@PEG@HA@Qu initiated synergistic chemo-photo cytocidal action, we have primarily checked appearance level of NLRP3, caspase-1 and N-GSDMD proteins in MDA-MB-231 by CLSM images in a laser irradiation time dependent manner. It is perceived from Figure 8(a) and Figure 8(b) that cells,

incubated with ~ 13.54 µM of $GPB_{0.50}$@PDA@PEG@HA@Qu, exhibit monotonic increase of NLRP3, caspase-1 and N-GSDMD protein appearance under different laser exposure in comparison with untreated cells (control). Prior to discuss protein expressions, this is to mention that the expression of Qu has also been increased at different laser irradiation time, ascribed to laser triggered intracellular Qu release (shown in Figure 8(a)), indicating potency of $GPB_{0.5}$@PDA@PEG@HA@Qu to have synergistic chemo-photo therapeutic activity that induces oxidative stress, in consequently which triggers NLRP3 inflammasome leads to activation of the caspase-1 protein, followed by cleavage of GSDMD into it's mature form. It is also clear from this figure that the expression of pro-inflammatory cytokine IL-1β gets increased under synergistic effect of chemo-photothermal therapy indicating N-GSDMD mediated canonical inflammasome pyroptosis. To check non-canonical inflammasome mediated pyroptosis, we estimate caspase-5, Pannexin-1 expression by FACS and P2X7 appearance by CLSM. Herein, results (Figure 9(a,b) and Figure 8(b)) demonstrate monotonic increase of caspase-5, cleaved Pannexin-1 and P2X7 proteins with increasing laser exposure time, compared to untreated cell (control). Hence, it is inferred that caspase 5 triggers to cleave pannexin-1 which further activates P2X7 receptor channel at membrane indicating non-canonical inflammasome mediated pyroptosis. Therefore, it is concluded that synergistic chemo-photo therapeutic activity of $GPB_{0.5}$@PDA@PEG@HA@Qu at optimal dose induces both N-GSDMD mediated canonical and P2X7 receptor mediated non-canonical pyroptosis death mechanism against MDA-MB-231.

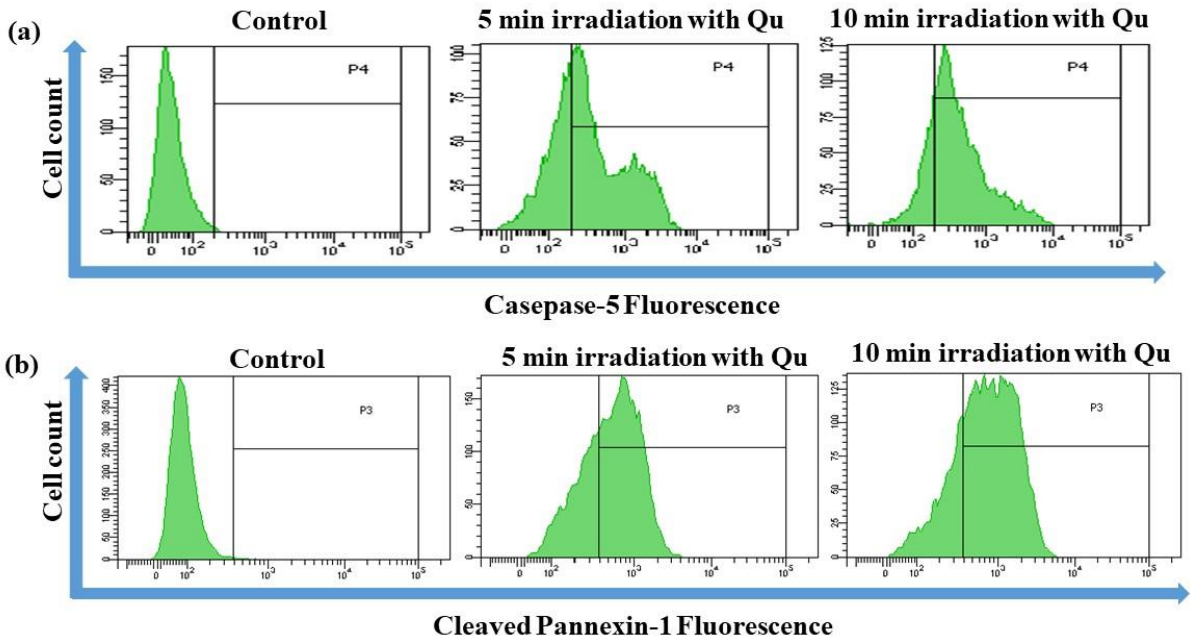

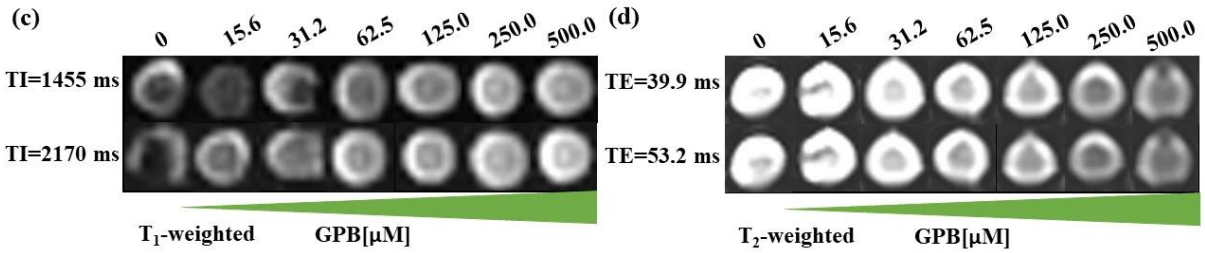

Fig. 9: Representative flow cytometric analysis to quantify the expression level of (a) Caspase 5 and (b) cleaved pannexin-1 by $GPB_{0.50}$@PDA@PEG@HA@Qu under time dependant laser exposure in MDA-MB-231 cells. Concentration dependant *in-vitro* (c) T_1 and (d) T_2-weighted MR images at 3 T showing hyper and hypo intensity from $GPB_{0.50}$@PDA@PEG@HA incubated MDA-MB-231 cells. *In-vitro* MR phantom images were acquired using inversion recovery sequences for T_1W (TE: 2.71 ms, TI: 1455, 2170 ms) and spin−echo sequences for T_2W (TR: 4000 ms, TE: 39.9, 53.2 ms).

Moreover, *in-vitro* T_1-T_2 weighted cellular MRI, carried out to endorse contrast efficiency of $GPB_{0.50}$@PDA@PEG@HA against MDA-MB-231 cells, reveals concentration dependent brightening and darkening effects with r_1, r_2 ~ 9.27 and 24.04 $mM^{-1}s^{-1}$ (shown in figure 9(c and d)). Thus, the result demonstrates that $GPB_{0.50}$@PDA@PEG@HA@Qu can be used as T_1-T_2 weighted MR contrast agent to diagnose MDA-MB-231 cell. Herein, both concentration and laser dependant MTT assay (shown in Figure 10(a) and 10(b)) exposes very squat death of normal HEK 293 cell, considered as control, and it might be ascribed to poor uptake of $GPB_{0.50}$@PDA@PEG@HA@Qu due to limited expression of HA receptor. Moreover, ICP-OES measurement of iron content (shown in Figure A11, Appendix A) in both MDA-MB-231 and HEK 293 cells reveals that uptake of $GPB_{0.50}$@PDA@PEG@HA is very significant in MDA-MB-231 in comparison with HEK 293 which further supports CD44 receptor mediated internalization corroborating well with previous MTT results. In addition, *in-vitro* T_1-T_2 weighted cellular MR images (shown in Figure 10(c) and 10(d)) against HEK 293 cell, treated with $GPB_{0.50}$@PDA@PEG@HA showed insignificant contrasting variation in comparison with control (untreated cells) which supports previous MTT and ICP-OES results. Thus the study reveals very high discrimination of $GPB_{0.50}$@PDA@PEG@HA@Qu between MDA-MB-231 and HEK 293 cells suggesting it can be used as a superior theranostic agent to teat MDA-MB-231 cell.

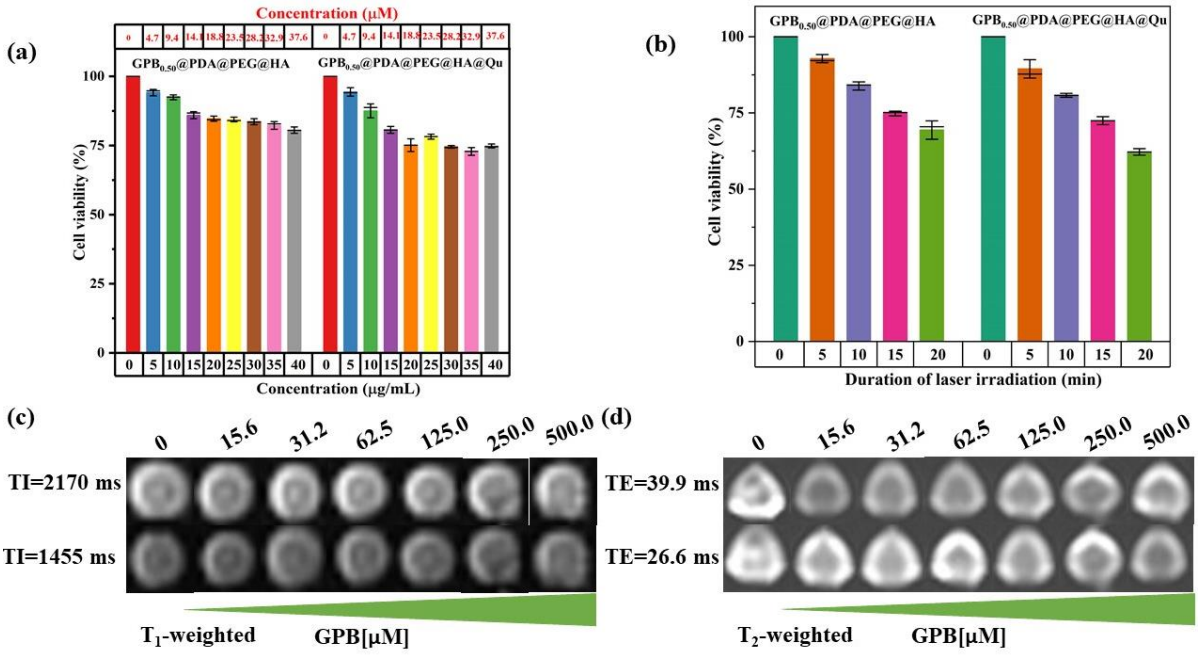

Fig. 10: (a) Concentration dependant and (b) NIR light irradiation time dependant Cell viability plot of HEK 293 cells after 24 hr incubated with $GPB_{0.50}$@PDA@PEG@HA and $GPB_{0.50}$@PDA@PEG@HA@Qu. Concentration dependant *in-vitro* (c) T_1 and (d) T_2-weighted MR images at 3 T showing negligible contrasting variation compare to control from $GPB_{0.50}$@PDA@PEG@HA, incubated HEK 293 cells. MR phantom images were acquired using inversion recovery sequences for T_1W (TE: 2.71 ms, variable TI: 1455, 2170 ms) and spin-echo sequences for T_2W (TR: 4000 ms, variable TE: 39.9, 26.6 ms).

4.4 CONCLUSION

In summary, we have demonstrated the synthesis of MDA-MB-231 cell specific, highly stable, NIR active $GPB_{0.50}$@PDA@PEG@HA@Qu as next generation multimodal theranostic agent in terms of chemo-photo therapy and T_1-T_2 weighted MR imaging with enhanced performance. PDA coating makes easy functionalization with PEG and HA for improving stability and target specificity. Our designed $GPB_{0.50}$@PDA@PEG@HA@Qu nanocomposite exhibits uniform cubic morphology with suitable size and high Qu loading content with pH responsive release behaviour. In particular, the limitations of Qu in clinical usages are adequately overcome by our designed smart targeted drug delivery system. Moreover, a high rate of cell (MDA-MB-231) death is achieved with minimal dose (13.54 μM) due to combined effect of laser exposure and Qu followed by N-GSDMD mediated canonical and P2X7 receptor mediated non-canonical pyroptosis pathway while negligible toxicity to normal cell (HEK 293) demonstrate it's safety. Interestingly, our details analysis on improved trend of r_1 value due to Gd^{3+} tuning

in GPB nanocubes is assigned to inner sphere relaxivity where q^{IS}, S, τ_R and r_{M-H} ($Fe^{3+}(3c) - O(6f)$) plays a significant role. Moreover, a similar pattern has also been observed in r_2 value which consigned to the mutual contribution of inner sphere and outer sphere relaxivity effect where magnetization plays a vital role additionally. Therefore, our findings successfully reveal that synthesized $GPB_{0.50}$@PDA@PEG@HA@Qu nanocomposite shows a fascinating prospects and approaches in terms of multimodal theranostic activity against MDA-MB-231 cell for future perception.

References

1. Peng, X., Wang, R., Wang, T., Yang, W., Wang, H., Gu, W., & Ye, L. (2018). Carbon dots/Prussian blue satellite/core nanocomposites for optical imaging and photothermal therapy. *ACS applied materials & interfaces*, *10*(1), 1084-1092.
2. Yang, V., Gouveia, M. J., Santos, J., Koksch, B., Amorim, I., Gärtner, F., & Vale, N. (2020). Breast cancer: insights in disease and influence of drug methotrexate. *RSC Medicinal Chemistry*, *11*(6), 646-664.
3. Liu, C., Zhao, Z., Gao, R., Zhang, X., Sun, Y., Wu, J., ... & Chen, C. (2022). Matrix metalloproteinase-2-responsive surface-changeable liposomes decorated by multifunctional peptides to overcome the drug resistance of triple-negative breast cancer through enhanced targeting and penetrability. *ACS biomaterials science & engineering*, *8*(7), 2979-2994.
4. Guo, X. M., Yadav, M. B., Khan, M., Hao, C. W., Lin, C. Y., Huang, T., ... & Bian, Z. X. (2021). Bradykinin-Potentiating Peptide-Paclitaxel Conjugate Directed at Ectopically Expressed Angiotensin-Converting Enzyme in Triple-Negative Breast Cancer. *Journal of Medicinal Chemistry*, *64*(23), 17051-17062.
5. Chappell, K., Manna, K., Washam, C. L., Graw, S., Alkam, D., Thompson, M. D., ... & Byrum, S. D. (2021). Multi-omics data integration reveals correlated regulatory features of triple negative breast cancer. *Molecular omics*, *17*(5), 677-691.
6. Nghia, N. N., & Lee, Y. I. (2020). Highly sensitive and selective optosensing of quercetin based on novel complexation with yttrium ions. *Analyst*, *145*(9), 3376-3384.
7. Harwood, M., Danielewska-Nikiel, B., Borzelleca, J. F., Flamm, G. W., Williams, G. M., & Lines, T. C. (2007). A critical review of the data related to the safety of quercetin and lack of evidence of in vivo toxicity, including lack of genotoxic/carcinogenic properties. *Food and chemical toxicology*, *45*(11), 2179-2205.
8. Sahoo, P., Jana, P., Kundu, S., Mishra, S., Chattopadhyay, K., Mukherjee, A., & Ghosh, C. K. (2023). Quercetin@ Gd^{3+} doped Prussian blue nanocubes induce the pyroptotic death of MDA-MB-231 cells: combinational targeted multimodal therapy, dual modal MRI, intuitive modelling of r 1–r 2 relaxivities. *Journal of Materials Chemistry B*, *11*(28), 6646-6663.
9. Huang, H. C., Lin, C. L., & Lin, J. K. (2011). 1, 2, 3, 4, 6-penta-O-galloyl-β-D-glucose, quercetin, curcumin and lycopene induce cell-cycle arrest in MDA-MB-231 and BT474 cells through downregulation of Skp2 protein. *Journal of agricultural and food chemistry*, *59*(12), 6765-6775.
10. Huang, C., Lee, S. Y., Lin, C. L., Tu, T. H., Chen, L. H., Chen, Y. J., & Huang, H. C. (2013). Co-treatment with quercetin and 1, 2, 3, 4, 6-penta-O-galloyl-β-D-glucose causes cell cycle arrest and apoptosis in human breast cancer MDA-MB-231 and AU565 cells. *Journal of agricultural and food chemistry*, *61*(26), 6430-6445.
11. Ferry, D. R., Smith, A., Malkhandi, J., Fyfe, D. W., deTakats, P. G., Anderson, D., ... & Kerr, D. J. (1996). Phase I clinical trial of the flavonoid quercetin: pharmacokinetics and evidence for in vivo tyrosine kinase inhibition. *Clinical cancer research: an official journal of the American Association for Cancer Research*, *2*(4), 659-668.

12. Long, L. H., Clement, M. V., & Halliwell, B. (2000). Artifacts in cell culture: rapid generation of hydrogen peroxide on addition of (−)-epigallocatechin,(−)-epigallocatechin gallate,(+)-catechin, and quercetin to commonly used cell culture media. *Biochemical and Biophysical Research Communications*, *273*(1), 50-53.
13. Gorlatova, N. V., Elokdah, H., Fan, K., Crandall, D. L., & Lawrence, D. A. (2003). Mapping of a conformational epitope on plasminogen activator inhibitor-1 by random mutagenesis: Implications for serpin function. *Journal of Biological Chemistry*, *278*(18), 16329-16335.
14. Parsaei, M., & Akhbari, K. (2022). Smart multifunctional UiO-66 metal–organic framework nanoparticles with outstanding drug-loading/release potential for the targeted delivery of quercetin. *Inorganic Chemistry*, *61*(37), 14528-14543.
15. Macchi, S., Jalihal, A., Hooshmand, N., Zubair, M., Jenkins, S., Alwan, N., ... & Siraj, N. (2022). Enhanced photothermal heating and combination therapy of NIR dye via conversion to self-assembled ionic nanomaterials. *Journal of Materials Chemistry B*, *10*(5), 806-816.
16. Sahoo, P., Kundu, S., Roy, S., Sharma, S. K., Ghosh, J., Mishra, S., ... & Ghosh, C. K. (2022). Fundamental understanding of the size and surface modification effects on r 1, the relaxivity of Prussian blue nanocube@ m-SiO_2: a novel targeted chemo-photodynamic theranostic agent to treat colon cancer. *RSC advances*, *12*(38), 24555-24570.
17. Lu, Y., Zhang, P., Lin, L., Gao, X., Zhou, Y., Feng, J., & Zhang, H. (2022). Ultra-small bimetallic phosphides for dual-modal MRI imaging guided photothermal ablation of tumors. *Dalton Transactions*, *51*(11), 4423-4428.
18. Wang, K., An, L., Tian, Q., Lin, J., & Yang, S. (2018). Gadolinium-labelled iron/iron oxide core/shell nanoparticles as T 1–T 2 contrast agent for magnetic resonance imaging. *RSC advances*, *8*(47), 26764-26770.
19. Davis, J. J., Huang, W. Y., & Davies, G. L. (2012). Location-tuned relaxivity in Gd-doped mesoporous silica nanoparticles. *Journal of Materials Chemistry*, *22*(43), 22848-22850.
20. Bruce, I. J., & Sen, T. (2005). Surface modification of magnetic nanoparticles with alkoxysilanes and their application in magnetic bioseparations. *Langmuir*, *21*(15), 7029-7035.
21. Zhang, Z., Smith, L., Li, W., Jiang, L., Zhou, F., Davies, G. L., & Williams, G. R. (2022). Polydopamine-coated nanocomposite theranostic implants for localized chemotherapy and MRI imaging. *International Journal of Pharmaceutics*, *615*, 121493.
22. Mrówczyński, R. (2017). Polydopamine-based multifunctional (nano) materials for cancer therapy. *ACS applied materials & interfaces*, *10*(9), 7541-7561.
23. Lee, H., Dellatore, S. M., Miller, W. M., & Messersmith, P. B. (2007). Mussel-inspired surface chemistry for multifunctional coatings. *science*, *318*(5849), 426-430.
24. Pintaske, J., Martirosian, P., Graf, H., Erb, G., Lodemann, K. P., Claussen, C. D., & Schick, F. (2006). Relaxivity of gadopentetate dimeglumine (Magnevist), gadobutrol (Gadovist), and gadobenate dimeglumine (MultiHance) in human blood plasma at 0.2, 1.5, and 3 Tesla. *Investigative radiology*, *41*(3), 213-221.
25. Ternent, L., Mayoh, D. A., Lees, M. R., & Davies, G. L. (2016). Heparin-stabilised iron oxide for MR applications: A relaxometric study. *Journal of materials chemistry B*, *4*(18), 3065-3074.
26. Liu, X., Li, B., Fu, F., Xu, K., Zou, R., Wang, Q., ... & Hu, J. (2014). Facile synthesis of biocompatible cysteine-coated CuS nanoparticles with high photothermal conversion efficiency for cancer therapy. *Dalton Transactions*, *43*(30), 11709-11715.
27. Wang, Y., Zhang, Z., Abo-zeid, Y., Bear, J. C., Davies, G. L., Lei, X., & Williams, G. R. (2020). SiO2-coated layered gadolinium hydroxides for simultaneous drug delivery and magnetic resonance imaging. *Journal of Solid State Chemistry*, *286*, 121291.
28. Mishra, S., Das, K., Chatterjee, S., Sahoo, P., Kundu, S., Pal, M., ... & Ghosh, C. K. (2023). Facile and green synthesis of novel fluorescent carbon quantum dots and their silver heterostructure: An in vitro anticancer activity and imaging on colorectal carcinoma. *ACS omega*, *8*(5), 4566-4577.
29. Mishra, S., Manna, K., Kayal, U., Saha, M., Chatterjee, S., Chandra, D., ... & Saha, K. D. (2020). Folic acid-conjugated magnetic mesoporous silica nanoparticles loaded with quercetin: A theranostic approach for cancer management. *RSC advances*, *10*(39), 23148-23164.

30. Nandi, R., Mishra, S., Maji, T. K., Manna, K., Kar, P., Banerjee, S., ... & Pal, S. K. (2017). A novel nanohybrid for cancer theranostics: folate sensitized Fe_2O_3 nanoparticles for colorectal cancer diagnosis and photodynamic therapy. *Journal of Materials Chemistry B*, *5*(21), 3927-3939.
31. Sozmen, F., Kucukoflaz, M., Ergul, M., & Inan, Z. D. S. (2021). Nanoparticles with PDT and PTT synergistic properties working with dual NIR-light source simultaneously. *RSC Advances*, *11*(4), 2383-2389.
32. Sai, D. L., Lee, J., Nguyen, D. L., & Kim, Y. P. (2021). Tailoring photosensitive ROS for advanced photodynamic therapy. *Experimental & Molecular Medicine*, *53*(4), 495-504.
33. Hameed, S., Bhattarai, P., Gong, Z., Liang, X., Yue, X., & Dai, Z. (2023). Ultrasmall porphyrin-silica core–shell dots for enhanced fluorescence imaging-guided cancer photodynamic therapy. *Nanoscale Advances*, *5*(1), 277-289.
34. Mirshafiee, V., Sun, B., Chang, C. H., Liao, Y. P., Jiang, W., Jiang, J., ... & Nel, A. E. (2018). Toxicological profiling of metal oxide nanoparticles in liver context reveals pyroptosis in Kupffer cells and macrophages versus apoptosis in hepatocytes. *ACS nano*, *12*(4), 3836-3852.
35. Tokoro, H., Shiro, M., Hashimoto, K., & Ohkoshi, S. I. (2007). Single crystal of a Prussian blue analog based on rubidium manganese hexacyanoferrate. *Zeitschrift für anorganische und allgemeine Chemie*, *633*(8), 1134-1136.
36. Samain, L., Grandjean, F., Long, G. J., Martinetto, P., Bordet, P., & Strivay, D. (2013). Relationship between the synthesis of Prussian blue pigments, their color, physical properties, and their behavior in paint layers. *The Journal of Physical Chemistry C*, *117*(19), 9693-9712.
37. Lingott, J., Lindner, U., Telgmann, L., Esteban-Fernández, D., Jakubowski, N., & Panne, U. (2016). Gadolinium-uptake by aquatic and terrestrial organisms-distribution determined by laser ablation inductively coupled plasma mass spectrometry. *Environmental Science: Processes & Impacts*, *18*(2), 200-207.
38. Chakraborty, N., Jha, D., Gautam, H. K., & Roy, I. (2020). Peroxidase-like behavior and photothermal effect of chitosan-coated Prussian-blue nanoparticles: dual-modality antibacterial action with enhanced bioaffinity. *Materials Advances*, *1*(4), 774-782.
39. Chen, X., Wang, R., Liu, D., Tian, Y., & Ye, L. (2019). Prussian blue analogue islands on BiOCl-Se nanosheets for MR/CT imaging-guided photothermal/photodynamic cancer therapy. *ACS Applied Bio Materials*, *2*(3), 1213-1224.
40. Chen, F., Teng, L., Lu, C., Zhang, C., Rong, Q., Zhao, Y., ... & Zhang, X. (2020). Activatable magnetic/photoacoustic nanoplatform for redox-unlocked deep-tissue molecular imaging in vivo via prussian blue nanoprobe. *Analytical Chemistry*, *92*(19), 13452-13461.
41. Hao, Y., Mao, L., Zhang, R., Liao, X., Yuan, M., & Liao, W. (2021). Multifunctional biodegradable Prussian blue analogue for synergetic photothermal/photodynamic/chemodynamic therapy and intrinsic tumor metastasis inhibition. *ACS Applied Bio Materials*, *4*(9), 7081-7093.
42. Shokouhimehr, M., Soehnlen, E. S., Hao, J., Griswold, M., Flask, C., Fan, X., ... & Huang, S. D. (2010). Dual purpose Prussian blue nanoparticles for cellular imaging and drug delivery: a new generation of T 1-weighted MRI contrast and small molecule delivery agents. *Journal of Materials Chemistry*, *20*(25), 5251-5259.
43. Qin, Z., Chen, B., Mao, Y., Shi, C., Li, Y., Huang, X., ... & Gu, N. (2020). Achieving ultrasmall Prussian blue nanoparticles as high-performance biomedical agents with multifunctions. *ACS applied materials & interfaces*, *12*(51), 57382-57390.
44. Peng, J., Dong, M., Ran, B., Li, W., Hao, Y., Yang, Q., ... & Qian, Z. (2017). "One-for-all"-type, biodegradable prussian blue/manganese dioxide hybrid nanocrystal for trimodal imaging-guided photothermal therapy and oxygen regulation of breast cancer. *ACS applied materials & interfaces*, *9*(16), 13875-13886.
45. Perrier, M., Kenouche, S., Long, J., Thangavel, K., Larionova, J., Goze-Bac, C., ... & Guari, Y. (2013). Investigation on NMR relaxivity of nano-sized cyano-bridged coordination polymers. *Inorganic Chemistry*, *52*(23), 13402-13414.

46. Tear, L. R., Maguire, M. L., Tropiano, M., Yao, K., Farrer, N. J., Faulkner, S., & Schneider, J. E. (2020). Enhancing 31 P NMR relaxation rates with a kinetically inert gadolinium complex. *Dalton Transactions*, *49*(9), 2989-2993.
47. Baranyai, Z., Carniato, F., Nucera, A., Horváth, D., Tei, L., Platas-Iglesias, C., & Botta, M. (2021). Defining the conditions for the development of the emerging class of Fe III-based MRI contrast agents. *Chemical Science*, *12*(33), 11138-11145.
48. Caravan, P., Farrar, C. T., Frullano, L., & Uppal, R. (2009). Influence of molecular parameters and increasing magnetic field strength on relaxivity of gadolinium-and manganese-based T_1 contrast agents. *Contrast media & molecular imaging*, *4*(2), 89-100.
49. Ravera, E., Gigli, L., Fiorucci, L., Luchinat, C., & Parigi, G. (2022). The evolution of paramagnetic NMR as a tool in structural biology. *Physical Chemistry Chemical Physics*, *24*(29), 17397-17416.
50. Wahsner, J., Gale, E. M., Rodríguez-Rodríguez, A., & Caravan, P. (2018). Chemistry of MRI contrast agents: current challenges and new frontiers. *Chemical reviews*, *119*(2), 957-1057.
51. Mou, C., Yang, Y., Bai, Y., Yuan, P., Wang, Y., & Zhang, L. (2019). Hyaluronic acid and polydopamine functionalized phase change nanoparticles for ultrasound imaging-guided photothermal-chemotherapy. *Journal of materials chemistry B*, *7*(8), 1246-1257.
52. Zhou, B., Jiang, B. P., Sun, W., Wei, F. M., He, Y., Liang, H., & Shen, X. C. (2018). Water-dispersible Prussian blue hyaluronic acid nanocubes with near-infrared photoinduced singlet oxygen production and photothermal activities for cancer theranostics. *ACS applied materials & interfaces*, *10*(21), 18036-18049.
53. Chen, S., Zhu, L., Wen, W., Lu, L., Zhou, C., & Luo, B. (2019). Fabrication and evaluation of 3D printed poly (L-lactide) scaffold functionalized with quercetin-polydopamine for bone tissue engineering. *ACS Biomaterials Science & Engineering*, *5*(5), 2506-2518.
54. Selvaraj, S., Shanmugasundaram, S., Maruthamuthu, M., Venkidasamy, B., & Shanmugasundaram, S. (2021). Facile synthesis and characterization of quercetin-loaded alginate nanoparticles for enhanced in vitro anticancer effect against human leukemic cancer U937 cells. *Journal of Cluster Science*, *32*, 1507-1518.
55. Luo, R., Tang, L., Zhong, S., Yang, Z., Wang, J., Weng, Y., ... & Huang, N. (2013). In vitro investigation of enhanced hemocompatibility and endothelial cell proliferation associated with quinone-rich polydopamine coating. *ACS applied materials & interfaces*, *5*(5), 1704-1714.
56. Lin, X., Cao, Y., Li, J., Zheng, D., Lan, S., Xue, Y., ... & Zhu, X. (2019). Folic acid-modified Prussian blue/polydopamine nanoparticles as an MRI agent for use in targeted chemo/photothermal therapy. *Biomaterials science*, *7*(7), 2996-3006.
57. Kaviarasi, S., Shalini Devi, K. S., Vinoth, P., Sridharan, V., Yuba, E., Harada, A., & Krishnan, U. M. (2019). Synthesis, Characterization, and Biomedical Applications of an Alkylated Quercetin–Gadolinium Complex. *ACS Biomaterials Science & Engineering*, *5*(3), 1215-1227.
58. Yeh, C. J., Zulueta, M. M. L., Li, Y. K., & Hung, S. C. (2020). Synthesis of hyaluronic acid oligosaccharides with a GlcNAc–GlcA repeating pattern and their binding affinity with CD44. *Organic & Biomolecular Chemistry*, *18*(28), 5370-5387.
59. Wu, M., Liu, X., Chen, H., Duan, Y., Liu, J., Pan, Y., & Liu, B. (2021). Activation of pyroptosis by membrane-anchoring AIE photosensitizer design: new prospect for photodynamic cancer cell ablation. *Angewandte Chemie*, *133*(16), 9175-9180.
60. Yu, P., Zhang, X., Liu, N., Tang, L., Peng, C., & Chen, X. (2021). Pyroptosis: mechanisms and diseases. *Signal transduction and targeted therapy*, *6*(1), 128.
61. Swanson, K. V., Deng, M., & Ting, J. P. Y. (2019). The NLRP3 inflammasome: molecular activation and regulation to therapeutics. *Nature Reviews Immunology*, *19*(8), 477-489.
62. J. Shi, Y. Zhao, Y. Wang, W. Gao, J. Ding, P. Li, L. Hu and F. Shao, *Nature*, 2019, **514**, 187-192.
63. Shi, J., Gao, W., & Shao, F. (2017). Pyroptosis: gasdermin-mediated programmed necrotic cell death. *Trends in biochemical sciences*, *42*(4), 245-254.
64. Yang, D., He, Y., Muñoz-Planillo, R., Liu, Q., & Núñez, G. (2015). Caspase-11 requires the pannexin-1 channel and the purinergic P2X7 pore to mediate pyroptosis and endotoxic shock. *Immunity*, *43*(5), 923-932.

Chapter 5

Lanthanide doped Prussian blue nanocube for dual-responsive DOX delivery to treat MDA-MB-231 cells: multimodal targeted therapeutic approach, understanding of doping effects on r_1-r_2 relaxivities

Chapter 5. Lanthanide doped Prussian blue nanocube for dual-responsive DOX delivery to treat MDA-MB-231 cells: multimodal targeted therapeutic approach, understanding of doping effects on r_1-r_2 relaxivities

5.1 Introduction

Triple negative breast cancer (TNBC) is a subtype of breast cancer that lakes the receptors for estrogen, progesterone and human epidermal growth factor 2 proteins, which are commonly targets for hormone therapies. This makes TNBC more aggressive and difficult to treat compared to other breast cancer types. TNBC has a higher risk of recurrence and metastasis, and its prognosis can be less favourable compared to other type of breast cancer. The conventional treatment for TNBC primarily involves chemotherapy, often combined with surgery and radiation therapy. Chemotherapy can be used before surgery (neoadjuvant therapy) to shrink the tumor, or after surgery (adjuvant therapy) to eliminate any remaining cancer cells. However, traditional chemotherapy drugs often distribute partially in healthy tissue, reaching tumor tissues with low effective concentrations due to their lack of specificity, thus potentially causing long-term complications in healthy organs, such as heart and lung damage.[1] Additionally, TNBC can sometimes be resistant to chemotherapy, resulting in limited effectiveness and potential recurrence. Moreover, the genetic variability and mutations found in TNBC patients pose significant challenges in creating effective chemotherapeutic treatments.[2] To address these challenges, there is an immediate demand for a nanotechnology based drug delivery platform to achieve sustained release. Contemporary drug delivery platforms are tailored to accommodate multimodal therapeutic strategies like photothermal therapy (PTT) and photodynamic therapy (PDT). Consequently, the synergistic effects of combined therapies are garnering interest due to their inherent non-invasiveness, reduced side effects and precise spatiotemporal control.[3] Among various nanoparticles such as Fe_3O_4, carbon Au and noble metals, prussian blue nanocubes (PBNCs), an FDA-approved metal-organic framework (MOF) nanostructure, have garnered significant interest as a multimodal theranostic agent. These NCs boast inherent strong optical absorption in the near-infrared (NIR) spectrum, attributed to the Fe^{2+}-C ≡ N-Fe^{3+} bonds which enhances the photo therapeutic (PTT+PDT) efficiency.[4] NIR assisted therapeutic strategy enable feasible care to deeply situated TNBC, providing a potential path to more effective management. In addition, previous research, including our own, has indicated that PBNCs may serve as important contrast agent

(CA) for T_1-T_2 weighted dual modal magnetic resonance imaging (MRI), a widely used noninvasive technique for anatomically diagnosing TNBC.[4,5] It has been noted that signals from single-mode MRI can sometimes interfere with the diagnostic process, making it challenging to obtain clear results whereas dual modal CA can produce complementary images with the same in-plane geometries but different contrasts, enabling self-confirmed MRI detection with greater accuracy and precise diagnosis.[6,7] This area is currently a significant focus of research. Previously, we have explored the potential of Gd^{3+}-doped PBNC for multimodal theranostics in TNBC which showed improved phototherapeutic performance and enhanced T_1-T_2W MR contrast efficiency, with r_1, r_2 relaxivity ~ 10.06, 24.96 $mM^{-1}s^{-1}$ respectively.[5] Although the r_1 value as well as the brightening effect of this nanoparticles were superior, there is still a need for modification to boost its T_2 efficiency. Generally, lanthanide elements such as Dy^{3+}, Yb^{3+}, Er^{3+} plays crucial role in this context.[8,9]

Importantly, uncoated prussian blue based nanocubes exhibit a restricted drug loading capacity and are sensitive to biological environmental factors like pH and ionic strength, resulting in potential instability and degradation.[10] So modification is imperative. To address this issue, diverse drug carriers have been explored, including polymers, inorganic nanoparticles, micelles etc. Among them, mesoporous silica ($mSiO_2$) coating emerges as a promising options for drug delivery, mainly due to their mesopores structures, large surface area, minimal toxicity, remarkable stability, and easy functionalization capabilities.[11] However, concerning drug delivery systems, the limited intracellular drug release poses a challenge, restricting the effective delivery of antitumor drugs to cancer cells and causing unwanted side effects. To address this issue, there is growing interest in developing stimuli-responsive nanoplatform for tumor specific drug delivery. External stimuli like temperature, light, magnetic fields have been previously used to release drugs from drug carrier.[12,13] Moreover, internal stimuli in the tumor microenvironment like redox state, pH, enzymes, differ significantly from healthy tissue and can be used as stimuli for delivering drugs at specific tumor site.[14] Among them, redox stimuli are effective for developing redox-responsive drug carrier for cancer treatment due to the presence of reducing agents like glutathione (GSH) in the tumor microenvironment. In general, a drug carrier responsive to a single stimulus has limited efficiency in delivering drugs to tumor cells. Single stimuli, such as pH or redox, may not be adequate to trigger rapid drug release into cytoplasm, especially when cells endocytose a large number of drug carriers simultaneously, leading to partial carrier excretion. Therefore, a dual-responsive drug delivery

system offers advantages in enhancing delivery and optimizing drug utilization for tumor therapy.[15]

In order to mitigate the side effects associated with drug delivery systems, two primary approaches are typically employed: enhancing the biocompatibility of the system and conferring it with targeting capabilities for intracellular drug delivery. While $mSiO_2$ coating exhibits reasonably good biocompatibility, there remains considerable potential for further enhancement. A practical approach involves using an end-capping agent to seal the mesopores of $mSiO_2$, preventing drug leakage en route to the tumor site. This, consequently, mitigates the adverse effects of toxicity. Previously, various extracellular matrix components like bovine serum albumin (BSA), collagen, lysozyme, gelatin etc. have been utilized as sealing agents for $mSiO_2$-coated drug delivery carriers, enhancing their biocompatibility.[16] In this context, Cytochrome C (CytC), an electron transporter oxidative metabolism, has been demonstrated to possess biocompatibility with dimensions ~ 2.5*2.5*3.7 nm, rendering it a suitable candidate as a sealing agent for $mSiO_2$-coated drug delivery carriers.[17] Furthermore, CytC serves as a significant mediator of apoptosis, facilitating the recruitment and activation of caspase upon its release from cell mitochondria into the cytoplasm.[18] As for targeted intracellular drug delivery, numerous motifs serve as active targeting agents, including peptides, antibody, DNA aptamer, folic acid, lactobionic acid, hyaluronic acid (HA) etc.[10] Previously, it has been revealed that HA effectively targets MDA-MB-231 cells due to its ability to bind specifically to the CD44 recptor, which is overexpressed on the surface of these cells.

Herein, we report our findings concerning design, development and assessment of r_1 - r_2 relaxivities, PDT and PTT effects of a novel $mSiO_2$ coated lanthanide ions (Ln^{3+}/Gd^{3+}) doped prussian blue (LnGPB) nanoplatform, designed to respond to dual stimuli for targeted drug delivery *in-vivo* against TNBC. Briefly, we initially explore the impact of lanthanide ion (Ln: Dy/Er/Yb) doping on T_1 - T_2 relaxometric parameters, extensively analysing the changes in accordance with Solomon-Bloembergen-Morgan (SBM) theory. Subsequently, we assess the PTT effects of these samples under 808 nm laser exposure. Conversely, $mSiO_2$ has been utilized here to coat LnGPBNC for drug encapsulation, aiming to bolster the overall theranostic potency. Following this, LnGPB@$mSiO_2$ nanocubes undergo additional modification with Cys·HCL and CPA respectively, to integrate redox-responsive disulfide bonds and pH-responsive boronate ester bonds, serving as intermediate linkages. Next, HA conjugated CytC has been further immobilized after DOX loading for controlled drug release which seal the pores of $mSiO_2$. Upon arrival at the tumor site through targeted delivery, the DOX loading

nanoplatform undergoes degradation of the intermediary linkers due to the elevated levels of glutathione (GSH) and acidic pH within the tumor microenvironment. This breakdown triggered swift drug release, effectively induced apoptosis due to synergistic treatment. Thus we hypothesize that the combination of Cys, CPA functionalization, CytC end capping and HA immobilization on LnGPB@$mSiO_2$ nanoplatform would yield a highly effective multifunctional theranostic agent which would minimize off-target drug delivery by responding to dual stimuli, facilitating drug release exclusively at the specific tumor site.

5.2 Experimental Section

5.2.1 Chemicals and cell line: Citric acid anhydrous, $K_4[Fe(CN)_6]\cdot 3H_2O$, N-cetyl-N,N,N-trimethyl ammonium bromide (CTAB), tetraethyl orthosilicate (TEOS), HCl (35 wt%), isopropanol and acetone were bought from Merck, India. $FeCl_3\cdot 6H_2O$, $Gd(NO_3)_3\cdot 6H_2O$, $Dy(NO_3)_3\cdot H_2O$, $Er(NO_3)_3\cdot 5H_2O$, Doxorubicin hydrochloride, Nhydroxysuccinimide (NHS) (98%), 4-carboxyphenylboronic acid (CPA), GSH, N-(3-Dimethylaminopropyl)-N′-ethylcarbodiimide hydrochloride (EDC), cytochrome-C and 1,3-Diphenylisobenzofuran (DPBF) were purchased from sigma Aldrich. [(3-Triethoxysilyl)propyl] succinic anhydride (TESPA), Hyaluronic Acid (HA) and $Yb(NO_3)_3\cdot H_2O$, cystamine dihydrochloride (Cys·HCl) were obtained from TCI chemicals and alfa aesar respectively. Cell culture media components viz. Fetal bovine serum (FBS), Dulbecco's Modified Eagle Medium F-12 (DMEM), Penicillin-Streptomycin-Neomycin (PSN) antibiotic cocktail, related growth factors (i.e insulin, hydrocortisone, Epidermal Growth Factor (EGF), Fibroblast Growth Factor (FGF) etc.) were purchased from Gibco, USA. Other essential fine and raw chemicals were delivered by Sigma-Aldrich, USA, and SRL, India. Triple negative breast cancer (MDA-MB-231) carcinoma and Human embryonic kidney 293 (HEK 293) cell lines were bought from National Centre for Cell Sciences (NCCS), India. Antibodies were procured from Cell Signalling Technology (CST), Invitogen and Abcam. Other reagents were obtained from best existing commercial sources and all chemicals were used without further purification.

5.2.2 Synthesis Method

Synthesis of Ln^{3+}/Gd^{3+}-PB (Ln: Dy, Er, Yb): Citric acid encapsulated insoluble lanthanide ions (Ln^{3+}/Gd^{3+}) doped prussian blue nanocubes (LnGPBNC) were developed via reflux method, employing a singular anionic precursor. To synthesize DyGPB, a combination of $K_4(CN)_6\cdot 3H_2O$ (8.54 mg) and citric acid (98.00 mg) were dissolved in deionized (DI) water (30 mL) within a three-necked flask to form solution A. Simultaneously, in a separate flask, a

mixture of $FeCl_3 \cdot 6H_2O$ (1.35 mg), $Gd(NO_3)_3 \cdot 6H_2O$ (2.26 mg), $Dy(NO_3)_3 \cdot H_2O$ (3.48 mg) and citric acid (98.00 mg) were introduced into DI water (30 mL) employing magnetic stirring to constitute solution B. Subsequently, both solutions were subjected to heating at 60 ^oC. While diligently preserving the temperature, solution A was meticulously mixed in a dropwise manner into solution B and continuously stirring for 1.0 hr. Upon the culmination of reaction, the resulted dispersed solution was cooled down at room temperature and subjected to centrifugation at 12500 rpm for 15 minutes. Following a thorough washing with acetone for three times, the final product was collected subsequent to drying at 60 ^oC under vacuum condition. Be similar to this preparation process, ErGPB/YbGPB were also synthesized at a desired ratio (shown in Table B4, Appendix B) of $FeCl_3 \cdot 6H_2O$, $Gd(NO_3)_3 \cdot 6H_2O$ and $Er(NO_3)_3 \cdot 5H_2O$/ $Yb(NO_3)_3 \cdot H_2O$ as solution A.[5]

Surface coating with mesoporous silica (LnGPB@mSiO$_2$): Mesoporous silica coated LnGPB (LnGPB@mSiO$_2$) were synthesized using CTAB-guided sol-gel process.[19] Typically, a mixture of LnGPB (40.0 mg), CTAB (350.0 mg) and anhydrous ethanol (30.0 mL) were subjected to ultrasonication for 30 minutes. Subsequently, 180.0 mL of DI water was introduced into the resulted blue solution that was further stirred at 35 ^oC for 1 hr. Following this, TEOS (220.0 µL) and a concentrated ammonia aqueous solution (250.0 µL, pH ~ 9) were rapidly added and the reaction mixture was continuously stirred for another 48 hr at 35 ^oC. Afterward, the resulting products were separated by centrifugation and washed with ethanol thrice. Then the collected product was agitated in a 30.0 mL of scrubbing solution (pH ~ 1) containing ethanol and 35% of HCL (volume ratio = 250:1) for 6 hr to remove excess CTAB. Finally, the sample was dried after centrifugation at 50 ^oC in vacuum to yield the as-synthesized LnGPB@mSiO$_2$ nanocubes.

Carboxylation of LnGPB@mSiO$_2$ (LnGPB@mSiO$_2$@COOH): Carboxylation of LnGPB@mSiO$_2$ was executed in accordance with the earlier report.[20] Briefly, LnGPB@mSiO$_2$ (35.0 mg) was evenly dispersed in 35.0 mL of isopropanol with continuous stirring for 30 min and then TESPA anhydrous solution (320.0 µL) was gradually introduced into the aforementioned solution. The resulting solution was then refluxed at 75 ^oC for 42 hr. Afterward, the nanocubes were isolated through centrifugation at 12,500 rpm for 12 minutes, followed by several washing with methanol. The resulting product was then subjected to high vacuum at a temperature of 50 ^oC, yielding LnGPB@mSiO$_2$@COOH.

Synthesis of disulfide linking LnGPB@mSiO$_2$ (LnGPB@mSiO$_2$@S-S-NH$_2$): The disulfide bond linking LnGPB@mSiO$_2$ were performed as follows.[21] Briefly, the LnGPB@mSiO$_2$@COOH (40.0 mg) were dispersed into a mixture solution consisting of EDC (23.0 mg) and NHS (17.0 mg) in PBS (30.0 mL, pH 5.5) under rigorous stirring for 4 hr, followed by the addition of Cys·HCL (500.0 mg) to the aforementioned mixture. The resultant solution was then stirred at ambient temperature for another 24 hr. LnGPB@mSiO$_2$@S-S-NH$_2$ were acquired through centrifugation (12500 rpm, 10 min) and subsequently washed with ethanol and DI water. The final product was desiccated at a temperature of 50 ^{o}C under high vacuum for further utilization.

CPA-modification of LnGPB@mSiO$_2$@S-S-NH$_2$ (LnGPB@mSiO$_2$@S-S@CPA): Typically, a dispersion of as-synthesized LnGPB@mSiO$_2$@S-S-NH$_2$ nanocubes was prepared in 15.0 mL of DMSO. Subsequently, a solution containing CPA (75.0 mg), dissolved in 5.0 mL of DMSO along with NHS (50.0 mg) and EDC (100.0 mg) was prepared. Following 4 hr of stirring at room temperature, the solution was introduced into the LnGPB@mSiO$_2$@S-S-NH$_2$ dispersion. The resulting mixture solution was then stirred at room temperature for an additional 24 hr. Afterward, the nanocubes were collected through centrifugation at 12,500 rpm for 10 minutes, followed by several washing with DMSO, water and methanol respectively. The resulting product was then desiccated at a temperature of 50 ^{o}C under high vacuum, yielding LnGPB@mSiO$_2$@S-S@CPA.

Synthesis of HA grafted CytC (CytC-HA): The synthesis of hyaluronic acid (HA) grafted Cytochrome C (CytC) was followed a previously documented method utilizing EDC/NHS as crosslinking agents.[22] Briefly, HA (100 mg) were dissolved in a PBS solution (20 mL, pH 5.0), comprising NHS (30 mg) and EDC (60 mg) and agitated at room temperature for 4 hr. Subsequently, CytC (100 mg) was introduced into the solution and stirred for an additional 36 hr. The resulting product was purified using a dialysis bag (12,000 MWCO) against DI water for 3 days. Finally, the as-synthesized CytC-HA was dried through lyophilization for future applications.

DOX loading and functionalization with CytC-HA (LnGPB@mSiO$_2$@S-S@CPA@DOX @CyH): In this study, Doxorubicin hydrochloride (DOX) was served as a model drug. To encapsulate this drug, 6.0 mL of DOX (9.03 mg) containing PBS solution was dropwisely added to the 9.66 mL of LnGPB@mSiO$_2$@S-S@CPA solution (12.7 mg) with gently stirring for 24 hr under dark. Subsequently, the solutions were adjusted to a mildly

alkaline pH of 8 using a buffer solution, and CytC-HA (70.0 mg) were introduced, followed by an additional 36 hr of stirring. Following centrifugation and thorough PBS wash, the resultant LnGPB@mSiO$_2$@S-S@CPA@DOX @CyH nanoplatform was dried under vacuum.

To measure the DOX loading efficiency (DLE) of the nanoplatform, concentration of the non-encapsulated DOX was measured from the absorption calibration curve of DOX at a wavelength of 480 nm. DLE was measured using following equation:[5]

$$\text{DLE}\ (\%) = \frac{(\text{Total DOX concentration} - \text{DOX concentration in the supernatant})}{\text{Total DOX concentration}} \times 100\% \qquad (1)$$

5.2.3 Characterization: The crystallographic structure, phase information, atomic positions and bond distances of our synthesized samples were obtained from powder X-ray diffraction patterns captured using the ULTIMA IV X-Ray Diffractometer (Rigaku), operating at 40 kV and 40 mA with CuK_α radiation. Additionally, atomic pair distribution data were recorded in the Bruker D8 Advance Davinci diffractometer using Ag radiation (**λ**=0.5608Å) with maximum achievable Q-value of 22 Å^{-1} in rotating capillary configuration using Lynxeye detector. The microstructure along with elemental analysis of the prepared samples were examined using field emission scanning electron microscopy (FESEM) (S – 4800, Hitachi, Japan) and energy dispersive X-ray spectroscopy (EDX) (Bruker XFlash). Absorption properties (200 – 1200 nm), Thermal gravimetric analysis (TGA), surface functional group, surface charge analysis were measured using the UV-vis-NIR spectrophotometer (PerkinElmer Instruments, Waltham, MA), DTA-TGA instrument (SHIMADZU, DTG-60H), Fourier transform infrared spectrometer (FTIR, PerkinElmer, Spectrum-2000), and Nano-ZetaSizer (Brookhaven Instruments, Holtsville, NY) respectively. Nitrogen adsorption/desorption isotherms were recorded using the Quantachrome NOVA 1000e system for performing Barrett–Joyner–Halenda (BHJ) and Brunauer–Emmett–Teller (BET) analyses, allowing the evaluation of surface area, pore size, and pore volume of the prepared samples.

5.2.4 *Ex vitro* measurement of T_1-T_2W MRI contrast efficiency in aqueous suspension: The MR contrasting efficiency of all bare LnGPB samples, distributed within 96- well plates filled with a solution comprising 0.5% low melting agarose and PBS, was evaluated across concentration range from 0 to 182 µM. MR imaging was conducted using a clinical MRI scanner (Siemens MAGNETOM Verio), with the samples placed in pre-fabricated sample holder. To determine both the r_1 and r_2 relaxivity of the samples, coronal images were obtained under a 3T magnetic field (B) with a slice thickness of 4 mm. For T_1

measurements, an inversion recovery (IR) sequence with variable inversion times (TI) was employed $\left(\text{repetition time (TR)}\right)/\text{echo time (TE)} = 6000.0/8.6$, variable TI = 1100; 1455; 2170 ms, matrix size = 256×256 mm^2, field of view (FOV) = 220×220 mm^2). Similarly, T_2 measurements were obtained using a spin-echo multi-section pulse sequence (TR = 4000 ms, variable TE = 13.3; 26.6; 39.9; 53.2; 66.5; 79.8; 93.1; 106.4; 119.7; 133.0; 146.3; 159.6; 172.9; 186.2; 199.5; and 212.8 ms, matrix size = 195×195 mm^2, FOV = 208×230 mm^2).

5.2.5 MRI data analysis from phantom images: Dual modal MR phantom images were captured using DICOM software and then analysed utilizing ImageJ software. For each specific concentration of the individual sample, the signal intensity (SI) was averaged within designated regions of interest (ROI) and plotted against the inversion time (TI) for T_1 measurements and the echo time (TE) for T_2 measurements, employing a monoexponential decay model:[23]

$$SI_{TI} = S_0(1 - 2e^{(-TI/T_1)}) \quad (2)$$

$$SI_{TE} = S_0 e^{(-TE/T_2)} + S_1 \quad (3)$$

Here, SI_{TI} and SI_{TE} represented the signal intensity at particular TI and TE values respectively. Subsequently, the slope was determined from the linearly fitted plot between the resulting relaxation rates ($1/T_1$ or $1/T_2$) and varying concentration [C] of the individual sample, yielding longitudinal (r_1) and transverse (r_2) relaxivities for the respective sample. The linear plot followed the equation:

$$\frac{1}{T_j} = \frac{1}{T_d} + [C]r_j; j = 1,2 \quad (4)$$

Where the relaxation rate, $1/T_d$ signified the impact of diamagnetic components on relaxation. In this context, PBS containing low melting agarose served as a control, exhibiting diamagnetic characteristics.

5.2.6 Measurement of photothermal activity in aqueous media: The aqueous suspensions containing pristine LnGPB samples at a concentration of 0.1 mg/mL were subjected to NIR laser irradiation (808 nm; 4.32 $W.cm^{-2}$, total power 1.2W) individually within 3 mL quartz cuvettes, with DI water serving as a control. Infrared thermal camera (Magnity Electronics, MAG30, China) was used to capture photothermal images at specified time intervals (0-11 min), and temperature changes were measured using the manufacturer provided 'Raycam' thermal software. Furthermore, photothermal stability was evaluated by subjecting the samples to 11 min of continuous laser exposure, followed by another 11 min of laser exposure after the temperature had returned to its initial level within 11 min, repeated for a

total of three cycles. Additionally, the photothermal conversion efficiency (η) of these samples were determined according to a previously reported method detailed in the previous chapter.[24]

5.2.7 NIR-triggered extracellular singlet oxygen ($^1O_2$) generation: Singlet oxygen ($^1O_2$) generation was investigated using DPBF probe trapping method, where the absorbance of DPBF was monitored at 410 nm using UV-vis spectrophotometer. $^1O_2$ oxidized DPBF, resulting in a decrease in absorption. In this study, 3 mL alcoholic solution of DyGPB@mSiO$_2$@S-S@CPA@CyH (100 μg/mL) was mixed with 1 mL of BPBF alcoholic solution (25.0 μg/mL) in a cuvette. The mixture was then subjected to time-dependant NIR laser (808 nm, 1.0 Wcm^{-2}) irradiation. A mixed solution of DyGPB@mSiO$_2$@S-S@CPA@CyH and DPBF under dark was used as a reference.

5.2.8 pH and redox triggered DOX release profile: The pH and redox triggered release profiles of DOX from DyGPB@mSiO$_2$@S-S@CPA@DOX@CyH were assessed using UV-vis spectrophotometer. Briefly, 0.8 mL of DyGPB@mSiO$_2$@S-S@CPA@DOX @CyH (2 mg/mL) was suspended into separate centrifuge tubes containing PBS (4.2 mL) across various experimental conditions (pH 5.0, pH 7.4, pH 5.0 + GSH 8 mM and pH 7.4 + GSH 8 mM) and incubated at room temperature with continuous shaking. Subsequently, these solutions were centrifuged at 12,000 rpm for 12 min at a predetermined time interval, and 1.0 mL of soup was collected to assess the concentration of released DOX. Following this, an equivalent volume of fresh respective PBS was added to ensure uniform concentrations. The experiment was carried out in triplicate. Concentration of released DOX was calculated from concentration calibrated curve using UV-vis spectroscopy.[25]

5.2.9 Cell culture: The cells were cultivated in Dulbecco's Modified Eagle Medium (DMEM) supplemented with 10% (v/v) heat-inactivated fetal bovine serum (FBS), 2 mM L-glutamine, 100 units/mL of penicillin, and 100 μg/mL of streptomycin. Cell cultures were maintained in 75 cm^2 culture flasks at a temperature of 37°C under a humidified atmosphere with 5% CO2 in an incubator.[26]

5.2.10 *In vitro* cell viability assay: The cell viability was assessed through the MTT assay, following the protocol outlined by Mosmann et al.[27] In brief, cells were seeded at a density of 1×10^5 cells/ml in a 96-well microtiter plate (100 μL/well), with multiple replications. Treatments were administered for 24 hrs using various concentrations (0, 1.7,9.38, 17.9, 27.28, 35.8, and 71.61 μM). Following the respective incubation period, 10 μL of 5 mg/mL MTT stock solution was added to each well and allowed to incubate for 4 hr at 37°C. The resultant

formazan crystals were dissolved in dimethyl sulfoxide (DMSO), and the absorbance was quantified at 570 nm using a microplate reader (Thermofisher).

5.2.11 *In vitro* photodynamic therapy (PDT): Following initial screening, 35.8 µM of DyGPB@mSiO$_2$@S-S@CPA@DOX@CyH was taken for further investigation of its intracellular photosensitizing effect. Subsequently, both MDA-MB-231 and HEK 293 cells were exposed to an 808 nm laser in a time dependant manner (0, 10, 20 min). Finally, MTT assay was executed to assess the combined chemo-photothermal-photodynamic (chemo-photo) therapeutic efficacy.[28]

5.2.12 Determination of intracellular ROS: Intracellular reactive oxygen species (iROS) level was determined using dichlorofluorescin diacetate (DCFH-DA) staining technique (Thermofisher Scientific, USA), as described by manufacturer. Briefly, MDA-MB-231 cells (1×10^6 cells/mL) were treated with DyGPB@mSiO$_2$@S-S@CPA@DOX@CyH (as per IC_{50} value) and exposed to 808 nm laser irradiation for 15 min following a hr incubation period. After a 24 hr total incubation, the cells were washed with PBS, centrifused, and resuspended in culture media under gentle pipetting to achieve single-cell suspension. Next the cells were stained with 20 µM DCFH-DA and incubated for 30 min at room temperature. Following the incubation, the cells were washed again and resuspended in 400 µL of PBS. Fluorescence emission was measured at 535 nm (excitation at 488 nm) using flow cytometry (BD LSRFortessa, San Jose, CA, USA). Herein, the increase in DCF fluorescence indicates the level of ROS produced within the cells.[29]

5.2.13 Labelling of apoptotic cells for flow cytometry using an Annexin V/PI kit: Cell apoptosis was evaluated using Annexin V-PI staining kit (Thermofisher Scientific, USA). Briefly, MDA-MB-231 cells (1×10^6 cells/mL) were treated with DyGPB@mSiO$_2$@S-S@CPA@DOX@CyH (as per IC_{50} value) and then exposed to 808 nm laser light for 15 and 20 min after a 6 hr incubation period. Following a 24 hr incubation, the cells were rinsed with cold PBS, centrifused, and then resuspended in 100 µL of binding buffer. Subsequently, the cells were stained with 5 µL of FITC conjugated Annexine V and 1 µL of propidium iodide (PI) (100 µg/mL) and allowed to incubate for 15 min at room temperature. After incubation, 400 µL binding buffer was further added and fluorescence emission was measured at 530 and 575 nm respectively using flow cytometry. The percentages of early apoptosis (Annexine V^+/PI^-), late apoptosis (Annexine V^+/PI^+), necrosis (Annexine V^-/PI^+) and viable cells (Annexine V^-/PI^-) were assessed based on staining patterns.

5.2.14 Immunocytochemistry: MDA-MB-231 carcinoma cells (5×10^4 cells/well) seeded on 4-well chamber slides were subjected to treatment with IC_{50} concentration of our synthesized nanocomposite along with exposure of light and incubated for 24 hr. Subsequently, the cells were fixed in 4% formaldehyde solution in phosphate-buffered saline (PBS) for 15 minutes, permeabilized with 0.3% Triton-X 100 in PBS for 1 hr, and blocked for nonspecific binding sites using 2% bovine serum albumin (BSA). Immunostaining was performed by incubating the slides overnight with primary anti-human antibodies (dilution as per manufacturer). Following primary antibody incubation, the slides were exposed to the secondary antibody (Abchem). Photomicrographs were acquired using a Leica Microscope.

5.2.15 Statistical analysis: The data were presented as the means of three replicates along with the standard deviation (± SD). Analysis of variance (ANOVA) calculations were performed using OriginPro 8.0 software (San Diego, CA, USA). A p-value of less than 0.05 was regarded as statistically significant.

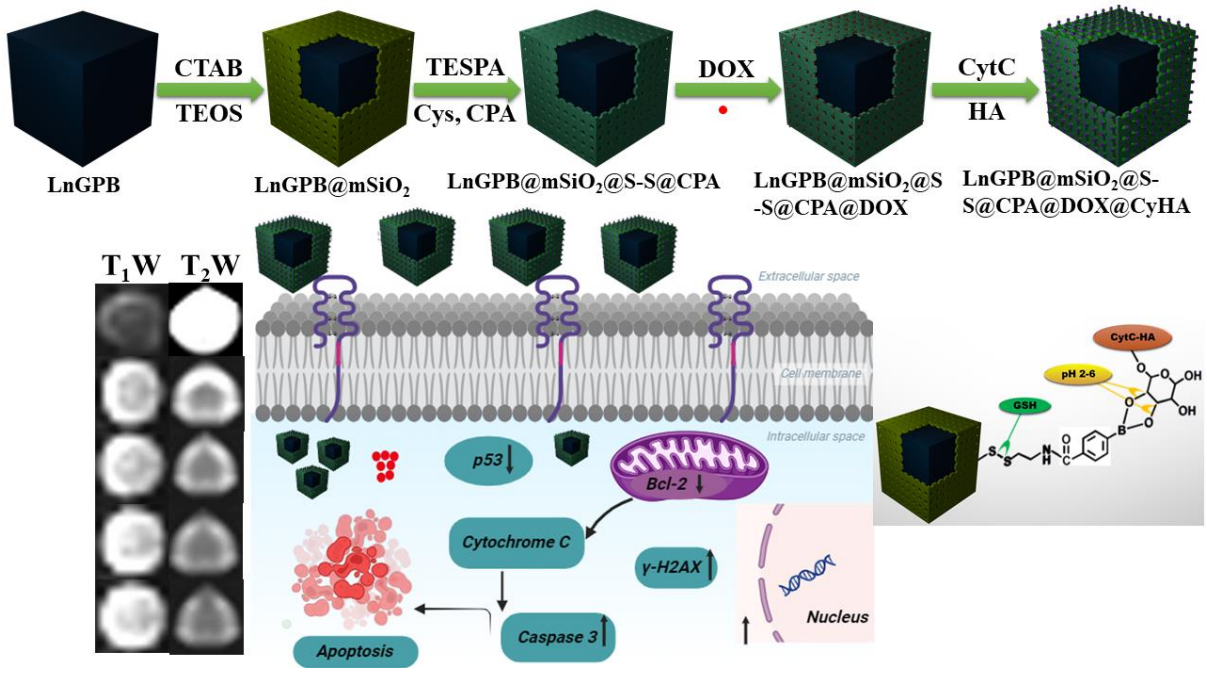

Scheme 1: Schematic representation of functionalization of LnGPB nanocubes sample and Ln^{3+} doping dependant MRI diagnostic, chemo-photo induced apoptotic cell death pathway.

5.3 RESULT AND DISCUSSION

5.3.1 Synthesis and Characterization: In this study, we investigated the synthesis process and doping dependant multifunctional theranostic potential including chemo-photothermal-photodynamic therapy and T_1-T_2 weighted MRI diagnosis of

DyGPB@mSiO_2@S-S@CPA@CytC-HA@DOX nanoplatform, schematically represented in Scheme 1). Three distinct lanthanide-doped GPBNC (Ln: Dy, Er, Yb) were synthesized and characterized thoroughly. Then, mSiO_2 was coated on the surface of DyGPB using CTAB directed sol-gel technique with subsequent functionalization with TESPA via covalent bonding between silane group and hydroxyl group to further improve biocompatibility and biodispersibility. Then S-S bond and CPA were subsequently conjugated via amidation reaction. Finally, after DOX loading CytC-HA was immobilized via boronate ester bonding that was acting as a gatekeeper. It is important to note that the disulfide and boronate ester bonds are sensitive to high GSH and acidic stimulus respectively.

XRD patterns of LnGPBNCs (shown in Figure 1(a-c)) showed a significant alignment with the face centred cubic phase characterized by the Pm3m space group (JCPDS card number: 73-0687), while absence of any extra peaks other than PB reaffirmed phase purity of the samples. Numerous researchers, ourselves among them, investigated that PBNCs developed with inherent defects, particularly, vacancies of $[Fe^{2+}(CN)_6]^{4-}$, which were balanced by H_2O molecules to maintain electro-neutrality. Based on their occupancy, H_2O molecules were categorized as coordinated or zeolitic, depending on whether they directly coordinated with metal ions surrounding vacancy sites or hydrogen bonded with coordinated H_2Os. Previously, it was established that the existence of these vacancies heavily relies on the synthesis condition and plays a pivotal role in MR imaging. Presently, we qualitatively assessed these vacancies through Reitveld analysis using the Maud software, following the methodology proposed by Samain et al.[30] These vacancies were systematically arranged and quantified using the parameter 'κ', showcasing the probability of occupancy of $Fe^{2+}(1b)$ within $[Fe^{2+}(CN)_6]^{4-}$ at the interstitial sites of the unit cell. Through meticulous refinement, we derived lattice parameters, crystallite sizes, unit cell volume, lattice strain and occupancy of the individual atoms, documented in Table 1 while unit cell structure of the representative DyGPB was schematically represented in Figure 1(d). Lattice parameter and unit cell volume observed to be elevated in ErGPB compared to DyGPB and YbGPB. Most importantly, 'κ' were found to be 0.764, 0.591 and 0.569 for DyGPB, ErGPB and YbGPB nanocubes respectively, indicating that doping of Dy^{3+} had the most pronounced effect in reducing $[Fe^{2+}(CN)_6]^{4-}$ vacancy which was also further supported by the reduction of total coordinated H_2O content at 6e, 6f and 12h sites (shown in Table B5, Appendix B).

Table 1: Unit cell parameters of LnGPB nanocubes as obtained by Rietveld analysis using Maud software.

Sample	**DyGPB**	**ErGPB**	**YbGPB**
Lattice parameter (a in Å)	10.18800	10.20100	10.19609
Unit cell volume (Å^3)	1057.38907	1061.55296	1059.97867
Crystallite sizes (nm)	33.83	59.59	90.91
Lattice Strain	$1.17*10^{-3}$	$1.57*10^{-3}$	$2.61*10^{-3}$

Pair distribution function analysis: To obtain more precise information regarding the vacancy of $[Fe^{2+}(CN)_6]^{4-}$within a unit cell of LnGPB, Atomic Pair Distribution Function (APDF) analysis was performed on the respective samples to analyze structural information from atomic point of view based on the local atomic distributions from total scattering experiment. APDF yields the probability of finding [G(r)] a pair of atoms and/or ions at a distance r from one another. While coherent Bragg X-ray scattering furnishes average information about the overall long-range structure, the diffuse X-ray scattering is associated with localized structural disorder and distortions within a compound. The broadening of the reflections within this function is influenced by the distribution of distances around the average value, arising from thermal vibrations or positional disorder. Meanwhile, the intensity and position of the reflections provide insight into the coordination number of the parent atom and the distances between atom pairs respectively. In this context, it is noteworthy to highlight that Reitveld refinement is considered effective in characterizing long-range ordering, but it falls to depicting local order at a length scale shorter than or similar to the lattice parameter. The PDF function G (r) gives the probability of finding any two atoms separated by a distance r, which is to be obtained by Fourier transformation of the total scattering function from Braggs peaks as well as from diffuse peaks by

$$G(r) = 4\pi r\,[\rho(r) - \rho_o] \qquad (5)$$

Where, ρ (r) = local atom number density and ρ_0 = average atom number density. Since, the PDF technique takes both Bragg and diffuse scattering into account; it provides information, not only about the long range atomic ordering but also about the short-range ordering in materials. PDF data were recorded in the Bruker D8 Advance Davinci diffractometer using Ag radiation (**λ**=0.5608Å) with maximum achievable Q-value of 22 Å^{-1} in rotating capillary configuration **using Lynxeye detector.** The experimental Atomic Pair distribution curve of

LnGPB samples were shown in the Figure 1(e,f). More specifically, the comparisons revealed a striking similarity between the functions of ErGPB and YbGPB samples, whereas the DyGPB sample exhibited a significant divergence in peak broadening, position and G (r). However, we encountered challenges in fitting the observed PDF data because of their inherent structural defect caused by the existence of vacancies, a characteristic defect found in most cubic polynuclear transition metal-cyanide complexes. Therefore, we compared the bond distances of our bare LnGPB samples with those from a previously published article (listed in Table 2). The observed results distinctly indicated a rise in the bond distances for all C-N, Fe^{2+}-C, Ln/Gd/Fe^{3+}-N (M^{3+}-N) and Ln/Gd/Fe^{3+}-O (M^{3+}-O) peaks as we progressed from DyGPB to YbGPB samples (Table 3). Meanwhile, the G (r) of the Peak-1, Peak-2 and Peak-4 were significantly lower in DyGPB sample in compared to other two ErGPB and YbGPB samples. Hence, variation in the values of G (r) and broadening of PDF curve for all three samples clearly indicates the variation of structural vacancies due to formation of $[Fe^{2+}(CN)_6]^{4-}$ sites vacancies. These variations may also be due to the inherent structural disorder arising from the presence of vacancies.[31] Additionally, the decrease in bond distances in DyGPB is due to more ordering with respect to bare PB. However, the position and broadening of the peaks in the LnGPB samples were well corroborated with the previously refined average 'κ' value.

Table 2: Interatomic bond distances of LnGPB nanocubes as obtained from PDF measurement

Sample	**Peak-1 C-N distance (Å)**	**Peak-2 Fe^{2+}-C distance (Å)**	**Peak-3 M^{3+}-N distance (Å)**	**Peak-4 M^{3+}-O distance (Å)**
$Fe_4^{3+}[Fe^{2+}(CN)_6]_3.xH_2O^a$	1.13(6)	1.92(5)	2.04(4)	2.5(1)
$Dy_2^{3+}Gd_1^{3+}Fe_1^{3+}[Fe^{2+}(CN)_6]_3.xH_2O$	1.05	1.51	1.97	2.45
$Er_2^{3+}Gd_1^{3+}Fe_1^{3+}[Fe^{2+}(CN)_6]_3.xH_2O$	1.17	1.65	2.08	2.55
$Yb_2^{3+}Gd_1^{3+}Fe_1^{3+}[Fe^{2+}(CN)_6]_3.xH_2O$	1.24	1.69	2.13	2.57

[a] average bond distances as reported in ref 32

Table 3: Comparison of G(r) and FWHM value of the selective peaks as obtained from PDF measurement

Sample	Peak-1		Peak-2		Peak-3	
	Value of G (r)	FWHM (Å)	Value of G (r)	FWHM (Å)	Value of G (r)	FWHM (Å)
DyGPB	0.049	0.2404	0.023	0.2479	0.083	0.3069
ErGPB	0.094	0.2496	0.088	0.2566	0.097	0.2906
YbGPB	0.147	0.2518	0.124	0.2756	0.072	0.3764

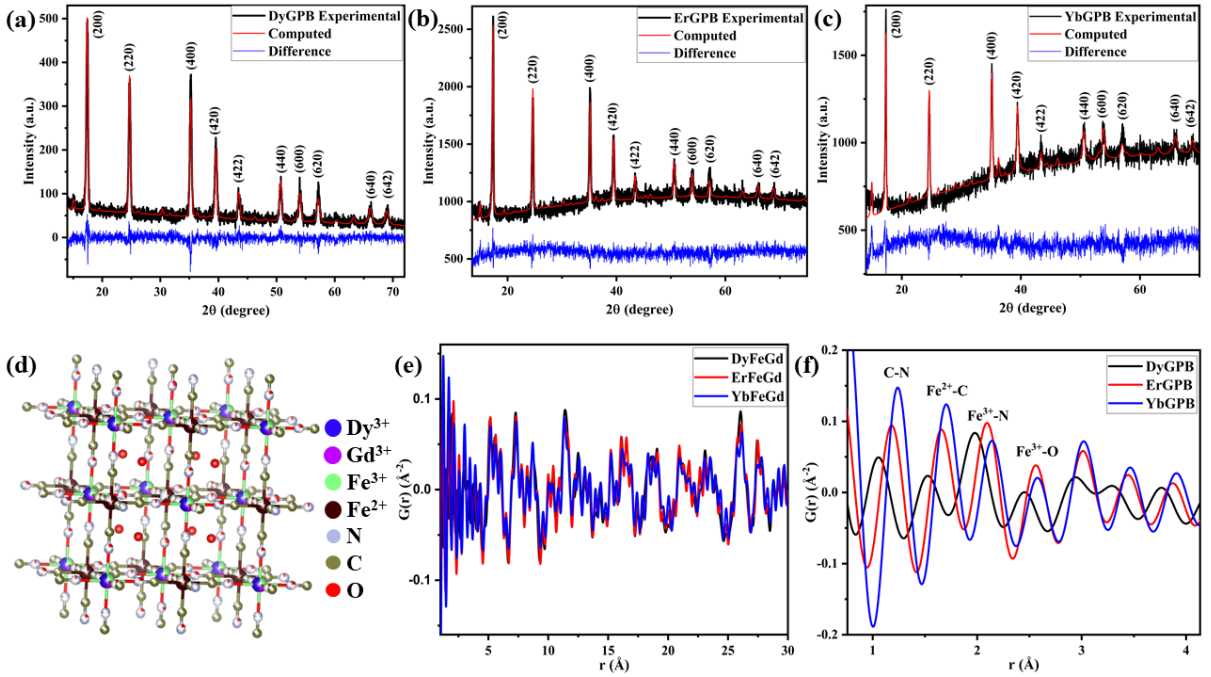

Figure 1: Reitveld refinement of XRD patterns with difference between experimental and refined patterns of (a) DyGPB, (b) ErGPB, (c) YbGPB nanocubes. (d) Unit cell structure of representative DyGPB nanocube. Pair distribution functions of LnGPB nanocubes (e) long range order and (f) short range order.

For better understanding of zeolitic and coordinated H_2Os, we conducted additional TG measurement of our LnGPB samples (shown in Figure A12(a-c) at Appendix A). The result revealed two distinct weight loss regions, attributed to zeolitic (~ 180-220 ^oC) and coordinated H_2Os (~ 300-370 ^oC) respectively. Through meticulous analyses, we determined ~ 18.96, 17.68, 21.87% weight losses due to zeolitic H_2Os while ~ 28.77, 30.15, 30.46% weight losses were associated with coordinated H_2Os in DyGPB, ErGPB and YbGPB respectively.

Consequently, the Reitveld, PDF and TG analyses on LnGPB samples validated the predominant presence of coordinated H_2Os at 6f and 12h sites. Simultaneously, the morphological investigation conducted via FESEM (shown in Figure 2(a-c)), along with subsequent histogram plots (shown in inset of Figure 2(a-c)), illustrated the consistent cubic morphology of DyGPB, YbGPB and ErGPB with average particle sizes ~ 230, 310 and 330 nm respectively. Furthermore, the elemental mapping of DyGPB (shown in Figure 2(d)) and the EDX analysis (shown in Figure A13(a-c) at Appendix A and Table B6, Appendix B) of LnGPB samples affirmed the uniform distribution of Ln, Gd, Fe, N and C atoms in the respective samples.

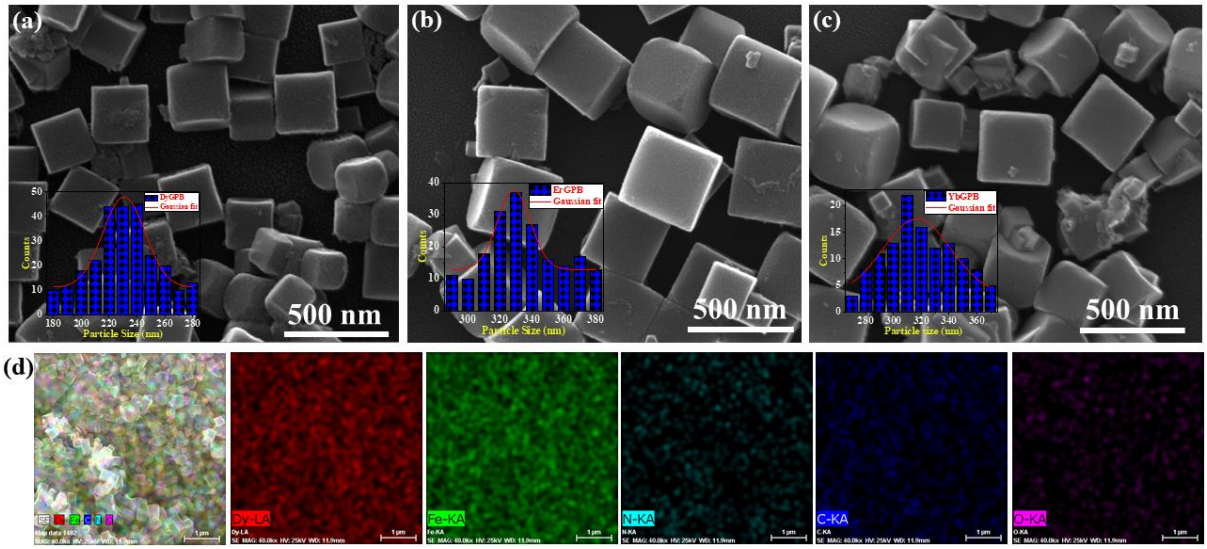

Figure 2: Characterization of LnGPB nanocubes. FESEM image and size distribution histogram in the inset of (a) DyGPB, (b) ErGPB and (c) YbGPB nanocubes. (d) Corresponding elemental mapping images of representative DyGPB.

Our prior investigation demonstrated that PBNC exhibited strong absorption peak at 718 nm, attributed to the metal-metal charge transfer between $\{Fe^{III}[(t_{2g})^3(e_g)^2]Fe^{II}[(t_{2g})^6]\}$ and $\{Fe^{II}[(t_{2g})^4(e_g)^2]Fe^{III}[(t_{2g})^5]\}$ through the cyanide bridge.[33] Upon incorporation of Ln^{3+}/Gd^{3+}, the absorption peak of LnGPB samples (shown in Figure 3(a)) underwent a redshifted to 784, 844 and 936 nm for ErGPB, DyGPB and YbGPB respectively which may be associated with LSPR. Presently, reduced carrier concentration, linked with increasing $[Fe^{2+}(CN)_6]^{4-}$ vacancies, causes redshift of LSPR from DyGPB to ErGPB and YbGPB. So, presence of Ln^{3+}/Gd^{3+} at the lattice site of PB results alterations in electron density and orbital energy within the cyanide bonds which also leads to a redshift of NIR absorbance peak.

5.3.2 Photothermal, MRI investigation of bare LnGPB nanocubes in aqueous suspension:

Photothermal activity (PTT), investigated under 808 nm laser exposure, is favoured for it's minimal photobleaching and effective penetration into deep tissue. The temperature elevation observed over an 11-minute period was ~ 53.07, 51.85 and 51.40 ^{0}C for ErGPB, DyGPB and YbGPB respectively (shown in figure 3(b,d) and figure A14(a,b,c) at Appendix A). To comprehend the underlying mechanism, we conducted a comparative analysis of optical absorbance at 808 nm across all the samples with identical concentration (shown in Figure 3(a)) which revealed the mass extinction coefficients ~ 19.32, 18.32 and 14.24 $cm^{-1}gm^{-1}L$ for ErGPB, DyGPB and YbGPB respectively (figure A15(a,b,c) at Appendix A). The explanation lay in the well-established understanding that the charge transfers between $Fe^{3+}/Gd^{3+}/Ln^{3+}$ and Fe^{2+} facilitated PTT activity. In this context, the absorption peak of ErGPB were found to be very close to 808 nm, and consequently, a higher extinction coefficient resulted in an enhanced PTT effect, as anticipated. Additionally, the photothermal conversion efficiency (η) of ErGPB, DyGPB and YbGPB was considered to be 64.25, 63.55 and 56.03% respectively, which further illustrated the enhanced PTT efficiency of ErGPBNC. Furthermore, we conducted an assessment of the photostability of this sample, and the result indicated that the sample remained highly stable under continuous laser irradiation, affirming their potential as PTT agent (shown in Figure 3(c)).

Previously, it was documented that PBNC possessed the ability to abbreviate the both transverse relaxation times (T_2) and longitudinal (T_1) relaxation times of protons in bulk water, which was ascribed to the presence of high spin Fe^{3+} – N (S = 5/2) moieties, leading PBNC to function dual-mode for T_1W and T_2W MRI probe.[34] Herein, the dual modal contrasting efficiency of our as synthesized pristine samples were examined using 3.0 T MRI analyser, with PBS serving as a control. In this context, the concentration dependent darkening and brightening effect in MRI phantom images (shown in Figure 4(a,b)) were observed for aqueous suspension of DyGPB, YbGPB and ErGPB samples, resulting in r_1 ~ 7.84, 6.51, 5.47 $mM^{-1}s^{-1}$ (shown in Figure A17(a-c), Appendix A) and r_2 ~ 29.3, 25.60, 26.34 $mM^{-1}s^{-1}$ (shown in Figure A17(d-f), Appendix A) respectively. Herein, both relaxation rates of different concentration of an individual sample was found by fitting the plot of signal intensity against varying TI for T_1 or TE for T_2 (shown in Figure A16 for a representative sample DyGPB with varying TE value).

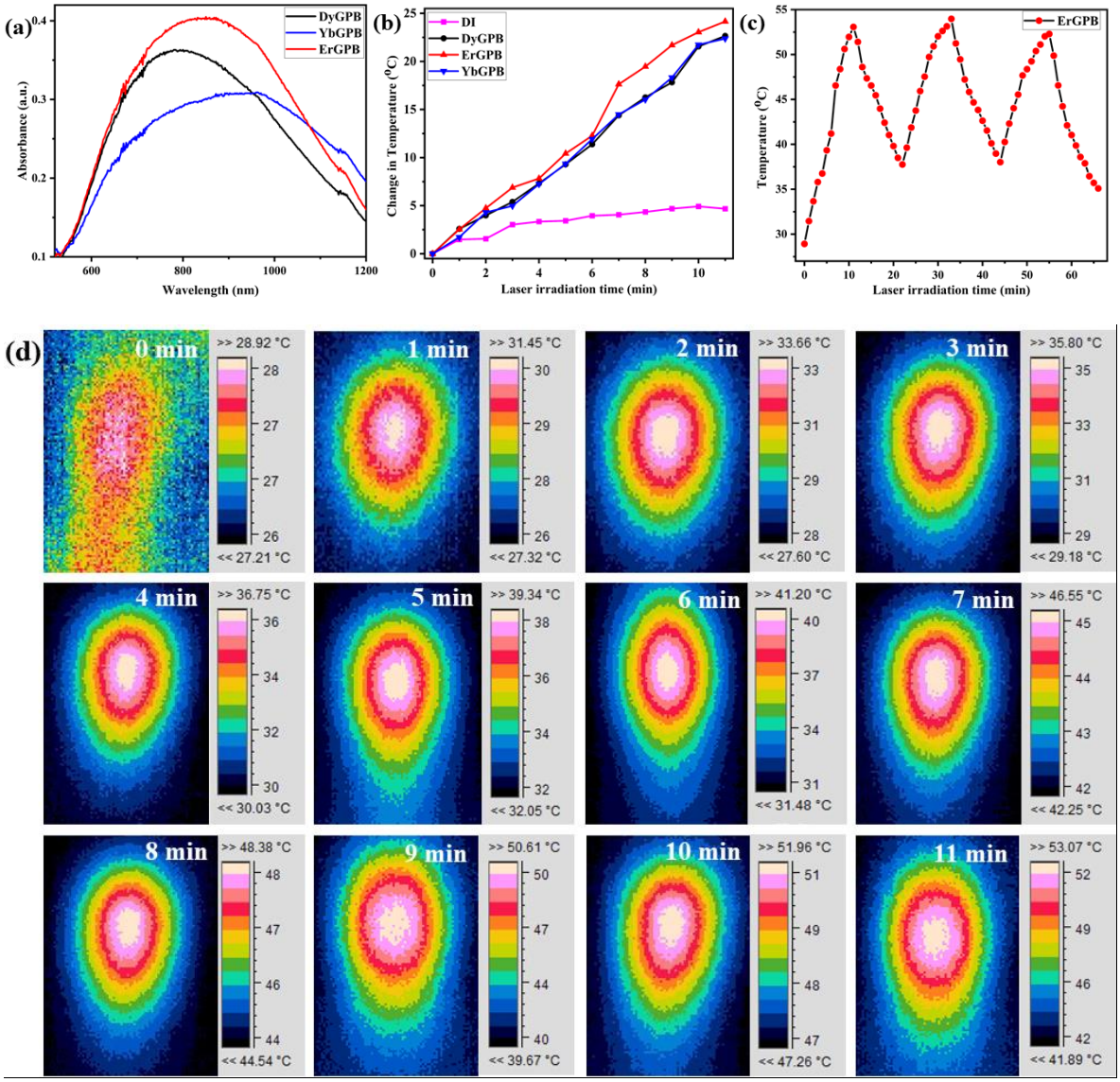

Figure 3: (a) Photothermal performance of LnGPB nanocubes. (a) UV-vis absorption spectra and absorption at 808 nm with equivalent concentration in the inset, (b) photothermal heating plot over 10 minutes under 808 nm NIR laser irradiation of DyGPB, ErGPB and YbGPB nanocubes. (c) Temperature curves of ErGPB nanocubes solution under NIR laser exposure for three cycles. (d) corresponding photothermal images of ErGPB nanocube sample.

Of note, both r_1 and r_2 of all samples are higher than that of previously synthesized pure PB nanocubes (r_1 ~ 0.079 and r_2 ~ 0.488 $mM^{-1}s^{-1}$,[35] ultrasmall PB nanoparticles (r_1 ~ 0.13 and r_2 ~ 18.8 $mM^{-1}s^{-1}$),[36] PB / MnO_2 hybrid nanoparticles (r_2 ~ 28.3 $mM^{-1}s^{-1}$),[37] and ProHance, one of the commercially available contrast agents (r_1 ~ 3.00 $mM^{-1}s^{-1}$). The findings clearly indicated that DyGPB sample exhibited highest r_1 and r_2 value, compared to other LnGPB samples which might be understood very briefly as follows: according to the Solomon – Bloembergen – Morgan theory, relaxivity (r_j, where $j = 1, 2$) is comprised of three

contributions: inner sphere (r_j^{IS}), second sphere (r_j^{SS}) and outer sphere (r_j^{OS}) i.e. $r_j = r_j^{IS} + r_j^{SS} + r_j^{OS}$. Specifically, r_j^{IS} signifies the contribution arising from the interaction between metal ions (Fe^{3+} / Gd^{3+}/Ln^{3+}) and coordinated H_2Os, r_j^{SS} involves nearby zeolitic H_2Os and r_j^{OS} is linked to the translational and rotational diffusion of bulk H_2Os. It is noteworthy that the r_1 is minimally impacted by r_1^{OS}, moderately influenced by r_1^{SS} but significantly influenced by r_1^{IS}. In contrast, r_2 is predominantly varied by r_2^{OS}. Typically, r_1^{IS} are expressed as follows-[38]

$$r_1^{IS} \propto \frac{q^{IS}}{T_{1M} + \tau_m} \qquad (6)$$

Where q^{IS}, T_{1M} and τ_m and are the inner sphere hydration state, relaxation time of coordinated H_2O and inverse of the water-exchange rate (k_{ex}) respectively. Recent research indicated that T_{1M} (~ 10^{-4} - 10^{-6} s) exhibited significantly higher values when compared to τ_m (~ 10^{-9} - 10^{-7} s).[39] Consequently, equation (6) can be simplified as $r_1^{IS} \propto \frac{q^{IS}}{T_{1M}^{IS}}$. It is noteworthy that T_{1M}^{IS} comprises two distinct interactions, specifically dipole-dipole (T_1^{DD}) and scalar (T_1^{SC}), attributed to nuclear and electronic interactions between H_2O protons and as-synthesized samples. However, recent studies revealed that T_{1M} significantly surpassed T_1^{DD}, enabling it's expression as-

$$\frac{1}{T_{1M}} = \frac{1}{T_1^{DD}} = \left(\frac{2}{15}\right) * \left({}^{\mu_0}/_{4\pi}\right) * \left(\frac{\gamma^2 g^2 \mu_B^2 S(S+1)}{r_{M-H}^6}\right) * \left[\frac{7\tau_c}{(1+\omega_e^2\tau_c^2)} + \frac{3\tau_c}{(1+\omega_p^2\tau_c^2)}\right] \qquad (7)$$

Where, ω_p, ω_e denote the Larmor frequencies of the proton and electron respectively and τ_c represent the magnetic fluctuation time, defined by below equation (8).

$$\frac{1}{\tau_c} = \frac{1}{\tau_m} + \frac{1}{\tau_R} + \frac{1}{\tau_e} \qquad (8)$$

Here, τ_e and τ_R denote electronic and rotational correlation time respectively. Previous reports indicate that τ_e is insignificant at high magnetic field (~ 3T), while τ_R ~ 10^{-12} s and τ_m ~ 10^{-9} - 10^{-7}s suggest $\tau_m \gg \tau_R$ i.e. $\tau_c \approx \tau_R$.[40] Since, $\omega_e \gg \omega_p$, the contribution from the latter can be disregarded at the operational frequency of MRI (~ 27.74 MHz). Consequently, r_1^{IS} can be further simplified as follows:

$$r_1^{IS} \propto (q^{IS})\left(\frac{S(S+1)}{r_{M-H}^6}\right)(\tau_R) \qquad (9)$$

Therefore, it can be asserted that r_i^{IS} is directly correlated with q^{IS}, S(S+1), τ_R and inversely correlated with r_{M-H}^6. Furthermore, according to Debye – Stoke's relation, $\tau_R = \frac{4\pi\eta r^3}{3k_B T}$, where η, r, k_B and T represent viscosity of the environment, size of the nanocube, Boltzmann constant and absolute temperature respectively, which elucidates that a larger particle size facilitates r_1^{IS} contribution. Herein, our Rietveld analysis, TG analysis and FESEM images yielded that smaller sized pristine DyGPB sample contained the least amount of coordinated H_2Os. Surprisingly, this sample exhibited the highest r_1 value in contrast to both the YbGPB and ErGPB samples which contradict with our earlier findings. Furthermore, PDF analysis (shown in Table 2) clearly indicated that DyGPB sample exhibited the smallest Ln/Gd/Fe^{3+}-O distance, signifying a reduction in r_{M-H}^6. Concurrently, EDX analysis (shown in Table B6, Appendix B) illustrated a higher concentration of Gd^{3+} (S = 7/2) and Dy^{3+} (S = 5/2) in DyGPB sample compared to YbGPB (Yb: S = 1/2) and ErGPB (Er: S = 3/2), leading to an increase in S(S+1). Consequently, the observed decrease in r_{M-H}^6 and concurrent increase in S(S+1) contribute to the enhancement of the r_1 value for DyGPB sample.

In this scenario, it is hypothesized that the outer sphere relaxivity plays a more significant role than that of the inner sphere in T_2 relaxation, which can be represented as $r_2 = r_2^{OS}$. In general, r_2 relaxivity is influenced by two correlation times: the static correlation time $1/\Delta\omega$ (where $\Delta\omega$ is the difference in larmor frequency between the particle and infinity) and diffusion correlation time, τ_D which can be expressed as follows:[41]

$$\Delta\omega = \gamma \frac{M_s}{3}$$

$$\tau_D = \frac{r^2}{D}$$

Where, D, r and M_s are the diffusion coefficient of surrounding H_2O, radius and saturation magnetization of particles respectively. Our experimental findings (shown in Table 3) affirmed that all pristine LnGPB samples met the criteria for the motional averaging regime (MAR), which implied that the time (τ_D) taken by H_2O molecule to diffuse a distance of $\sqrt{2}r$ in any direction is shorter than $1/\Delta\omega$, denoted as $\tau_D\,\Delta\omega < 1$. In contrast, in paramagnetic molecular systems, both magnetic center and surrounding H_2O molecules move too swiftly to undergo an efficient dephasing process. Consequently, r_2^{OS} in MAR shows a positive correlation with size

(i.e τ_D) and magnetic moment of particles in a specific surrounding medium, which can be expressed as follows:[42]

$$\frac{1}{T_2^{OS}} = \frac{\left(256\pi^2\gamma^2/405\right)V'M_s^2}{\left(1+\frac{L}{r}\right)}(\tau_D)$$

Where, V', L and r represent the volume fraction, coating layer thickness and width of a sample, respectively. The T_2 relaxation curve (shown in Figure A17(d-f), Appendix A) for aqueous suspensions of LnGPB samples demonstrated that DyGPB nanocubes displayed the highest r_2 compared to other LnGPB variants. Herein, the M-H profile at room temperature (shown in Figure A18(a-c), Appendix A) validated that the magnetization (M_0) at 3T progressively raised from YbGPB to DyGPB, resulting in an enhancement of r_2. Conversely, the τ_D values for the corresponding samples, as indicated in Table 3, exhibited variations based on their size, in contradiction to the observed trend in r_2. Importantly, the variation in the product of M_0^2 and τ_D for the LnGPB samples exhibited a consistent trend with their r_2 value. Hence, it can be inferred that the magnetic moment of these samples significantly contributed to the enhancement of r_2 contrasting efficiency.

Table 3: Comparison of particle size, magnetization, $\Delta\omega$ and τ_D of different LnGPB samples.

Sample Name	Size (nm)	Magnetization (emu/gm)	$1/\Delta\omega$ (s)	τ_D (µs)
DyGPB	230	5.802	0.0130	21.16
ErGPB	330	1.706	0.0094	43.56
YbGPB	310	0.600	0.0167	38.44

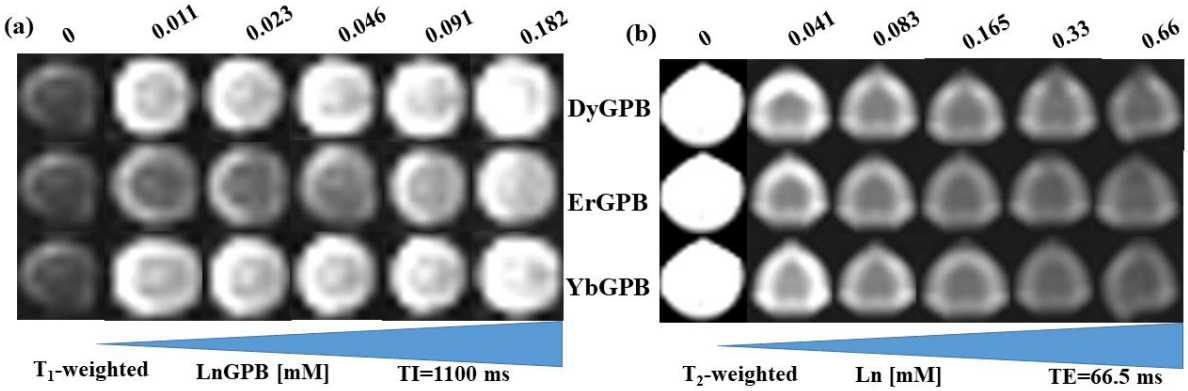

Figure 4: Concentration dependant (a) T_1 and (b) T_2-weighted MR images at 3 T showing hyper and hypo intensity from DyGPB, ErGPB and YbGPB nanocubes sample. MR images

were acquired using inversion recovery sequences for T_1W (TR: 6000 ms, TE: 8.6 ms, TI: 1100 ms) and spin−echo sequences for T_2W (TR: 4000 ms, TE: 66.5).

5.3.3 Functionalization and characterization: Driven by the superior T_2 contrasting efficiency and comparatively elevated PTT performance under laser irradiation observed in DyGPB nanocubes, we selected DyGPB for further *in-vitro* theranostic applications. To further validate the affective immobilization of the mentioned molecules onto DyGPB nanocubes and monitor their surface changes, FTIR analysis and Zeta potential measurements were performed in a systematic manner. The obtained FTIR spectrums (shown in Figure A19(a-f,i), Appendix A) displayed a distinct prominent absorption signal at 2090 cm^{-1} representing the vibration of $\nu(C \equiv N)$, along with a wide band between 3000 and 3580 cm^{-1}, centred at 3182 cm^{-1}, associated with the ν(-OH) due to surface-adsorbed H_2O. Furthermore, DyGPB displayed additional intense absorption signals at 1102, 1415 and 1604 cm^{-1}, attributed to the vibration of ν(C-OH), ν(C-C) and ν(C=O) of citric acid which served as a surface-capped stabilizer.[5] DyGPB@$mSiO_2$ illustrated the absorption signals at 1085, 798 and 984 cm^{-1}, assigned to asymmetric, symmetric stretching vibration of Si-O-Si bridges and ν(Si-OH) which testified the creation of the Si-O-Si framework.[43] Additionally, a notable reduction in the intensity of $\nu(C \equiv N)$ compared to ν(-OH) suggested the existence of $mSiO_2$ framework around DyGPB. Moreover, following HCL-ethanol wash, the absence of the ν(-CH) vibration signal between 2820 and 2970 cm^{-1} from CTAB signified the effective elimination of the pore template. Herein, it can be affirmed that the existence of -OH functional group on the surface of $mSiO_2$ enabled further functionalization with TESPA. In contrast to DyGPB@$mSiO_2$, DyGPB@$mSiO_2$@COOH exhibited additional absorption signals at 2953, 2888 and 1680 cm^{-1}, attributed to the vibration of ν_s(-CH_2), ν_{as}(-CH_2) and ν_s(C=O) respectively, which suggested the successful carboxylation of DyGPB@$mSiO_2$. After immobilization with Cys·HCL, two new absorption signals emerged at 1605, 1528 cm^{-1}, assigned to the stretching vibration of amide I and amide II groups. This finding demonstrated the covalent attachment of S-S with DyGPB@$mSiO_2$@COOH. Additionally, the intensity of the vibrational signal at 1680 cm^{-1} (ν_s(C=O)) considerable reduced, owing to the introduction of Cys·HCL molecules. DyGPB@$mSiO_2$@S-S@CPA displayed a new absorption signal at 1323 cm^{-1} due to the ν(B-O) vibration of CPA molecules, while a noticeable increase in the signal intensity at 1605 cm^{-1} from ν_I(N-H) indicated initiation of amidation reaction between the -COOH group in CPA and -NH_2 group on the surface of DyGPB@$mSiO_2$@S-S-NH_2.[44] Following the loading of DOX, DyGPB@$mSiO_2$@S-S@CPA@DOX exhibited distinct absorption signal at 1210 cm^{-1}, associated with the

asymmetric stretching vibration of ν_{as}(C-O-C) while the signals at 1583 and 1726 cm^{-1} were ascribed to ν(C=C) and ν(C=O) of DOX. Consequently, the presence of these absorption signals confirmed the existence of DOX in the nanoplatform. Finally, upon further interaction with CytC-HA, DyGPB@$mSiO_2$@S-S@CPA@DOX@CyH displayed a novel signal at 996 cm^{-1} corresponding to CytC-HA, specifically assigned to ν(C-O). Concurrently, there was an increase in intensity and a shift to 1607 and 1652 cm^{-1} respectively for the amide II and amide amide I signals respectively, compared to the absorption signal of CytC-HA, while the confirmation of CytC conjugation with HA was established through FTIR analysis, as described broadly in ESI (shown in Figure A19(g,h), Appendix A).[45] The results strongly indicated the successful immobilization of CytC-HA with DyGPB@$mSiO_2$@S-S@CPA@DOX and sealed it's mesopores after DOX loading. Besides, the effective functionalization of various functional groups was validated through zeta potential measurement (shown in Figure 5(a)). Specifically, zeta potential of bare DyGPB was recorded at -19.4 mV, primarily ascribed to the –COOH group of citric acid. In contrast, zeta potential decreased to -26.6 mV, linked to the phenolic hydroxyl group of $mSiO_2$. Following carboxylation, the zeta potential of DyGPB@$mSiO_2$@COOH dropped to -29.0 mV, attributed to the negatively charged –COOH of TESPA. For DyGPB@$mSiO_2$@S-S-NH_2, zeta potential increased to -21.7 mV, indicating the conjugation of positively charged Cys·HCL molecules. Subsequent CPA modification resulted in a zeta potential shift to -28.6 mV, and further loading with DOX increased it to -5.94 mV. Finally, after immobilization with CytC-HA the zeta potential decreased to -13.9 mV. These findings suggest the successful fabrication of DyGPB@$mSiO_2$@S-S@CPA@DOX@CyH. Furthermore, the optical absorption spectra of DOX (shown in Figure 5(b)) revealed an absorption band centered at 491 nm. In contrast, the peak shifted to 505 nm for DyGPB@$mSiO_2$@S-S@CPA@DOX nanoplatform, providing supportive evidence for successful loading and well corroborated with previous FTIR result. In this context it is noteworthy to highlight that the FESEM image (shown in Figure A20(a), Appendix A) indicated that the morphology of DyGPB remained unchanged following the coating with $mSiO_2$ and histogram (shown in the inset of Figure A20(a)) validated an increase in size (~ 50 nm) in the coated DyGPB compaired to their bare counterpart. In addition, the nitrogen adsorption–desorption isotherms for DyGPB@$mSiO_2$ sample (shown in Figure A20(b), Appendix A) demonstrated a characteristic IV curve, indicative of a mesoporous structure. The BET surface area was determined to be 145.5 $m^2 g^{-1}$, affirming the successful coating of DyGPB with $mSiO_2$. Simultaneously, the sample exhibited a substantial pore

volume (shown in the inset of Figure A20(b)) of ~ 0.13 cm^3 g^{-1} and an average pore size of ~ 1.28 nm, further confirmed that DOX can easily loaded into the pores.

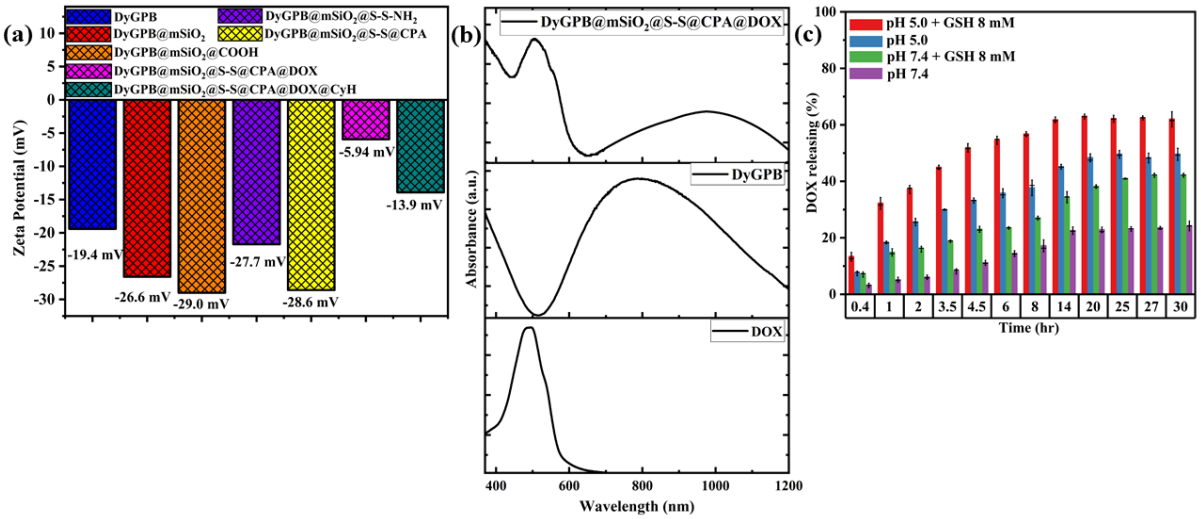

Figure 5: Characterization after modification of DyGPB. (a) Zeta potential of DyGPB nanocubes along with each step of modifications. (b) UV-vis absorption spectroscopy of pure DOX, bare DyGPB and DyGPB@$mSiO_2$@S-S@CPA@DOX nanoplatform. (c) DOX release profile in different medium.

5.3.4 pH and redox responsive DOX release profile and loading efficiency, stability and extracellular $^1O_2$ generation:

Prior to the *in vitro* investigations of DyGPB@$mSiO_2$@S-S@CPA@DOX@CyH against MDA-MB-231 cell line, we verified DOX loading efficiency and dual stimuli responsive release profile, singlet oxygen ($^1O_2$) generation and stability as they have crucial role in any pharmacological applications. High loading efficiency (~ 95.05%) of DOX is ascribed to the highly porous character of SiO_2 and attractive electrostatic interaction between the charged $Si–O^-$ groups of *m*-SiO_2 and DOX. To explore the real-time pH and redox responsive DOX release profile of DyGPB@$mSiO_2$@S-S@CPA@DOX@CyH nanoplatform, GSH was employed in this study as a stimulus in both normal (pH~7.4) and acidic (pH~5.0) PBS as it was well known that the cytoplasm of tumor cell and tumor microenvironment contained a rich abundance of GSH (shown in Figure 5(c)). In the physiological environment (only normal PBS) DyGPB@$mSiO_2$@S-S@CPA@DOX@CyH exhibited excellent sealing efficiency as only a negligible amount of DOX (~23% over 25 hr) was released. Conversely, in the acidic environment (only acidic PBS) the nanoplatform demonstrated pH sensitivity, releasing a high amount of DOX (~49% over 25 hr), ascribed to the disassociation of boronate ester linkage in

the acidic environment. Additionally, ~41% of DOX was released upon exposure to the GSH (8 mM) in normal PBS environment, credited to the cleavage of disulfide linkage within the nanoplatform by GSH. To mimic the intracellular milieu of tumor cell more comprehensively, the nanoplatforms were dispersed in acidic PBS combined with GSH (8 mM), leading to a rapid DOX release of ~62% within 25 hr which could be attributed to the concurrent dissociation of boronate ester linkage and cleavage of S-S bonds within the nanoplatform. Hence, the findings indicated that our developed DyGPB@mSiO$_2$@S-S@CPA@DOX@CyH nanoplatform could be activated by both GSH and pH, leading to rapid DOX release (~62%) as compared to single-stimulus activation.[46,47,48] Herein, generation of $^1O_2$, one of the important cytotoxic agent for cancer ablation, was examined through DPBF-probe fading measurement. Figure A21(a) at Appendix A showed the gradual decrease in absorbance peak at 410 nm with different irradiation time yielding generation of extracellular $^1O_2$ under irradiation with 808 nm laser. Thus this study exposed potency of DyGPB@mSiO$_2$@S-S@CPA@CyH as PDT agent. DyGPB@mSiO$_2$@S-S@CPA@CyH retained its stability in more than one mediums including PBS buffer (pH~7.4 and pH~5.5) and DMEM (pH~5.0) for at least 3 days (shown in Figure A21(b) at Appendix A) by monitoring absorbance at 844 nm.

5.3.5 *In-vitro* cellular theranostic evaluations:

To evaluate the dose-dependent potential cytotoxicity effect of DyGPB@mSiO$_2$@S-S@CPA and DyGPB@mSiO$_2$@S-S@CPA@DOX @CyH nanoplatform, MTT assay was performed on MDA-MB-231 cells. The results (shown in Figure 6(a)) revealed that DyGPB@mSiO$_2$@S-S@CPA demonstrated no chronic toxic effect beyond a concentration of 71.6 µM, indicating the good cytocompatibility at this concentration while a gradual decrease in cell viability was observed with increasing concentration of DyGPB@mSiO$_2$@S-S@CPA@DOX@CyH. Herein, the DyGPB@mSiO$_2$@S-S@CPA@DOX exhibited an IC_{50} = 35.8 µM concerning DyGPB, indicating its internalization into MDA-MB-231 cells through the EPR effect and active targeting endocytosis. Subsequently, the nanoplatform triggered the DOX release in response to intracellular acidic environment and overexpression of GSH. Then, the phototoxicity of DyGPB@mSiO$_2$@S-S@CPA@DOX@CyH was evaluated through the MTT assay at a consistent concentration of 35.8 µM under various laser (808 nm; 1.0 Wcm^{-2}) irradiation times (shown in Figure A22(a), Appendix A). The results demonstrated a continuous rise in cell death proportionally with exposure time, achieving ~63% of cell death within 10 min. In comparison, the nanocomposite alone induced only ~43% of cell death, indicating the notable phototherapeutic efficiency of the developed nanocomposite. Moreover,

Fluorescence microscopic (FLM) was utilized to examine the distributions and quantitatively analyse the uptake of both DyGPB@mSiO$_2$@S-S@CPA@FITC and DyGPB@mSiO$_2$@S-S@CPA@FITC@CyH nanoplatform by MDA-MB-231 cells (shown in Figure A22(b), Appendix A). The observations indicated that majority of the nanocomposites were distributed within the nucleus compare to cytoplasm after incubation for 24 hr, as confirmed by the green emission of FITC. Additionally, the fluorescence intensity quantification analysis showed that MDA-MB-231 cells endocytosed a greater quantity of the DyGPB@mSiO$_2$@S-S@CPA@FITC@CyH nanocomposite compared to DyGPB@mSiO$_2$@S-S@CPA@FITC which might be attributed to the presence of conjugated HA, enhancing cellular uptake. Prior research has established the well documented connection between oxidative stress in cell, characterized by generation of iROS, and the accelerated cell death.[49] Herein, we further examined iROS generation by assessing the fluorescence intensity of DCF using a flow cytometer. Notably, we observed a heightened DCF fluorescence intensity (shown in Figure 6(b)) upon exposure to NIR laser from DyGPB@mSiO$_2$@S-S@CPA@DOX@CyH (~35.8 µM), in contrast to the nanocomposite alone. Consequently, the MTT and DCF fluorescence analyses collectively suggested that DyGPB@mSiO$_2$@S-S@CPA@DOX@CyH elicited a synergistic chemo-photherapeutic effect at a minimal dosage of ~35.8 µM.

In general, early response of cancer cell under treatment influences the success of the therapeutic strategy employed, with cell death via apoptosis, necrosis or pyroptosis being pivotal. Therefore, we investigated the cell death process associated with DyGPB@mSiO$_2$@S-S@CPA@DOX@CyH (~35.8 µM) in the presence and absence of NIR laser using an Annexin V-FITC/PI staining assay. Prior to assessment, Figure 6(c) illustrated that the treatment of MDA-MB-231 cells with DyGPB@mSiO$_2$@S-S@CPA@DOX@CyH resulted in enhanced PI staining (52.5%) and Annexin V surface staining (42.4%), while the control group exhibited 99.9% cell viability. Additionally, the cells treated with nanocomposite followed by 15 min of laser irradiation displayed minimal PI staining (5.6%) and an increased population of Annexin V surface staining (89.5%), and with 20 min of laser irradiation, Annexin V surface staining further rose to 95.4%. This outcome appeared consistent with programmed apoptotic cell death. The findings were attributed to the photo-induced therapeutic effect along with the sustained release of DOX into the cell cytoplasm triggered by both pH and GSH, ultimately inducing apoptosis and cell death.

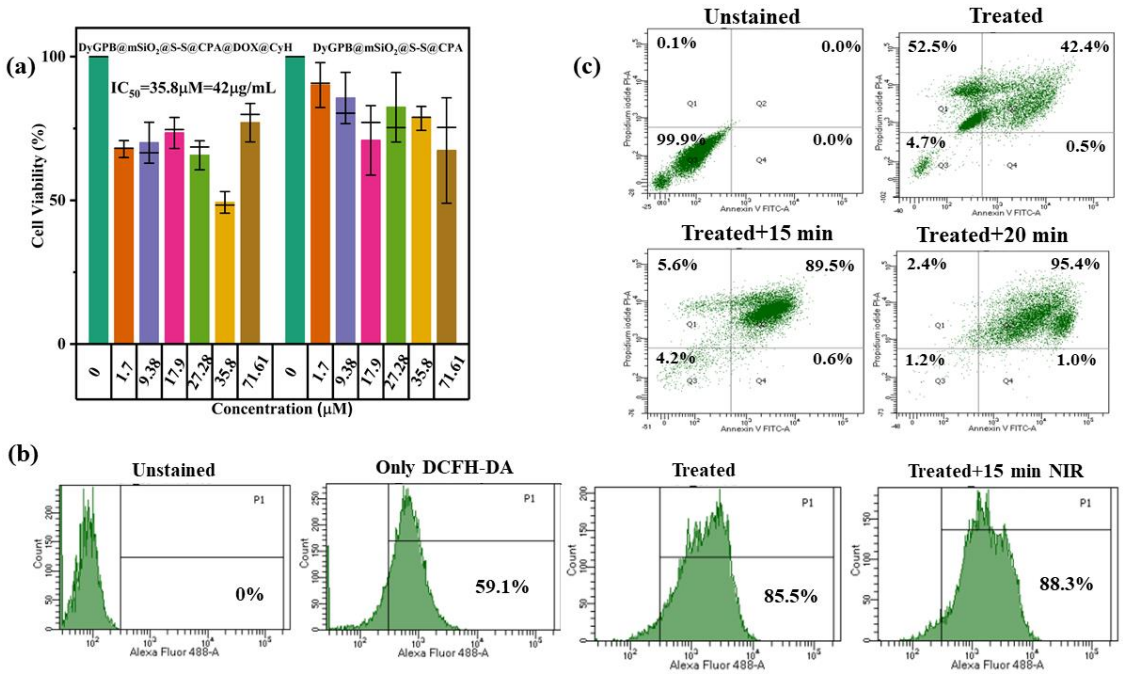

Figure 6: (a) Concentration dependant Cell viability plot. (b) Determination of iROS generation. (c) Quantification of apoptosis or nonapoptosis cell death via Flow cytometric dot plot using dual Annexin V-FITC and PI staining. In each experiments MDA-M-231 cells were incubated with DyGPB@mSiO$_2$@S-S@CPA@DOX@CyH under continuous laser irradiation (808 nm, 1 Wcm^{-2}).

Finally, we checked various proteins expression to reveal the apoptosis mechanism of MDA-MB-21 cells caused by DyGPB@mSiO$_2$@S-S@CPA@DOX@CyH nanocomposite (as per IC_{50} value) under 15 min of laser irradiation. It is reported that the tumor suppressor protein, p53 plays a pivotal role in the apoptotic response to genotoxic stressors. Consequently, we aimed to investigate the impact of our designed nanocomposite on the p53-dependent pathway for apoptosis induction. As prior DOX release profile clearly demonstrated an accelerating release pattern under the combined influence of acidic pH and high GSH levels, characteristics of the tumor microenvironment. Hence our initial investigation focused on determining whether DOX triggers apoptosis via p53-dependent pathway using drug ligand interaction. The outcomes (shown in Figure A22(a), Appendix A)) unequivocally indicated that DOX activates the p53 protein with a binding energy of -7.9 kcal which was well supported by previous literature consequently inducing p53-mediated apoptosis which served as a fundamental cellular mechanism to thwart neoplastic progression by eliminating genetically damaged or improperly stimulated proliferating cells.[50] As stated, the activation of p53 promotes the members of the Bcl-2 protein family that act as pivotal regulators of apoptosis, with both proapoptotic and antiapoptotic functions. Bcl-2 proteins form heterodimers by binding to

proapoptotic partners like Bax, and the balance of Bax to Bcl-2 ratios dictates whether apoptosis is promoted or inhibited within targeted site. Bax, a primary target of p53, modulates cell demise by participating in the disruption of mitochondrial integrity, leading to the release of cytochrome c into the cytosol. Subsequently, cytochrome c engages apoptotic protease-activating factor-1 (Apaf-1), culminating in the activation of caspase-3, another pivotal mediators of apoptosis. Importantly, early stages of apoptosis are marked by mitochondrial dysfunction mediated by members of the Bcl-2 family, encompassing the anti-apoptotic Bcl-2 and the pro-apoptotic Bax. Additionally, p53 may impede Bcl-2 expression and incite mitochondrial apoptotic signalling by elevating levels of reactive oxygen species (ROS).[51] Importantly, γ-H2AX, a variant of histone H2A, plays a pivotal role as a molecular marker for DNA double-strand breaks (DSBs), a type of DNA damage that can trigger apoptosis when repair mechanisms are overwhelmed or ineffective. Upon encountering genotoxic insults, such as those induced by the synthesized nanocomposite in our study, MDA-MB-231 cells undergo DNA damage, including the formation of DSBs. In response to these breaks, histone H2AX is rapidly phosphorylated at serine 139 to form gamma H2AX foci at the sites of DNA damage. This phosphorylation event serves as a recruitment signal for DNA repair factors, facilitating the assembly of repair complexes at the damaged DNA loci. However, when the extent of DNA damage surpasses the capacity of the cellular repair machinery, as may occur under conditions of severe or persistent genotoxic stress, the activation of apoptosis becomes a critical safeguard mechanism to eliminate irreparably damaged cells and prevent the propagation of genetic abnormalities.[52] Herein, the STRING database also indicated the strong correlation between p53 (TP53), BAX, BCL2, Cytochrome C (CYTS), Caspase 3 (CASP3) and γ-H2AX (H2AX) (shown in Figure A23, Appendix A).

So, in order to validate the predicted mechanism, we primarily checked the expression of p53 and its signaling pathway associated proteins such as Bcl2, Cytochrome C, Caspase 3 and γ-H2AX through FLM images after treating the cells by DyGPB@mSiO_2@S-S@CPA@DOX@CyH nanocomposite (as per IC_{50} value) under 15 min of laser irradiation *in vitro* (shown in Figure 7 and 8). The DyGPB@mSiO_2@S-S@CPA@DOX@CyH nanocomposite treatment of MDA-MB-231 cells resulted in a significant increase of fluorescence intensity in cytochrome C and Caspase 3 accompanied by a decrease of p53 and Bcl-2 in comparison with untreated cells. Meanwhile, cells treated with nanocomposite along with 15 min of NIR laser (808 nm; 1 Wcm^{-2}) exposure showed a similar trend, enabled TNBC cell death via apoptosis. Furthermore, the fluorescence intensity of γ-H2AX expression (shown

in Figure 8) in cells treated with the nanocomposite exhibited only a very slight enhancement, whereas cells treated with the nanocomposite combined with NIR laser irradiation displayed a substantial increase in fluorescence intensity compared to untreated cells. This difference in fluorescence intensity after 24 hr of incubation may be attributed to the distinct mechanisms underlying DNA damage induction and repair dynamics. In absence of NIR exposure, our developed NC showed its potential cytotoxicity due to dual-responsive DOX release which induced DNA damage through intercalation into DNA and inhibition of topoisomerase II activity, leading to the formation of DNA lesions, including SSBs and DSBs. However, the repair of these DNA lesions by the cellular machinery, particularly the efficient repair of DSBs, may attenuate the accumulation of γ-H2AX foci, resulting in minimal γ-H2AX fluorescence expression in DOX-treated cells. On the other hand, when NC treatment was combined with NIR laser irradiation, it can potentiate the DNA damage response due to the generated $^1O_2$, which can exacerbate DNA damage by oxidizing DNA bases and further inducing DNA strand breaks. Therefore, it was concluded that synergistic chemo-photo therapeutic activity of DyGPB@mSiO$_2$@S-S@CPA@DOX@CyH at optimal dose induced apoptosis death mechanism against MDA-MB-231.

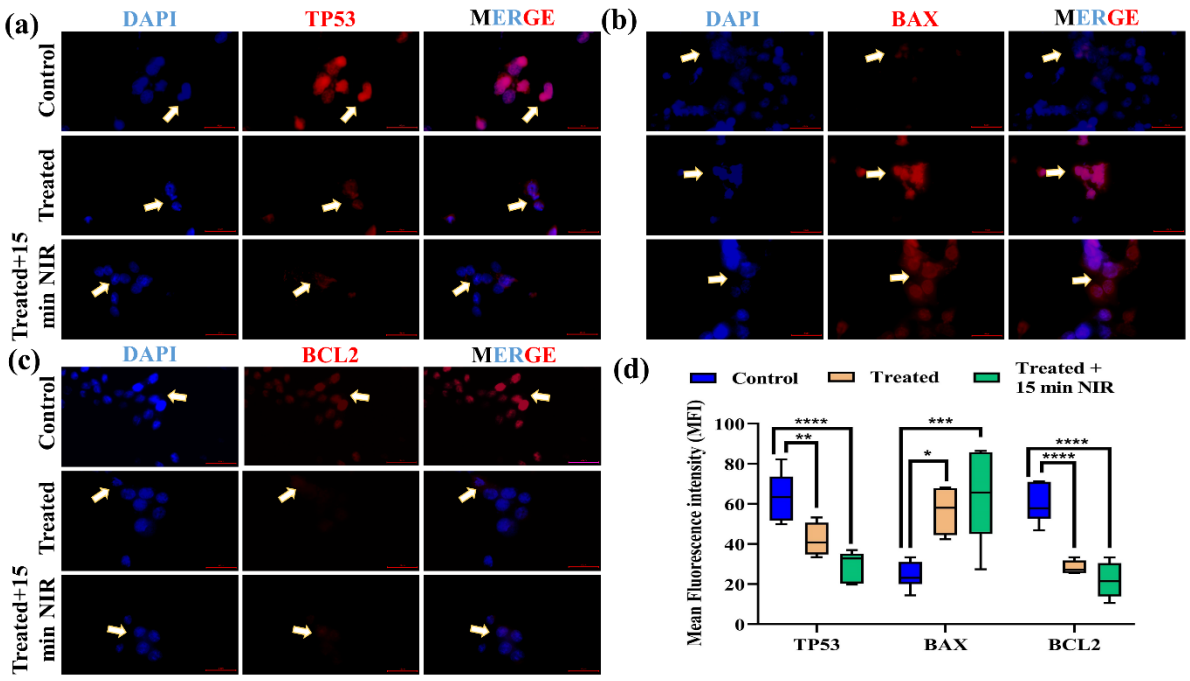

Figure 7: Fluorescence based immunocytochemical localization of (a) TP53, (b) BAX and (c) BCL2. (d) MFI analysis of respective treatment panel of proteins. Student t test was utilized to correlate the significance *p < 0.0332, **p < 0.0021, ***p < 0.0002, ****p < 0.0001.

Herein, both concentration and laser dependant MTT assay (shown in Figure A24, Appendix A) exposed very squat death of normal HEK 293 cell, considered as control, and it might be ascribed to poor uptake of DyGPB@mSiO$_2$@S-S@CPA@DOX@CyH due to limited expression of HA receptor. Thus the study reveals very high discrimination of this nanocomposites between MDA-MB-231 and HEK 293 cells suggesting it can be used as a superior theranostic agent to teat MDA-MB-231 cell.

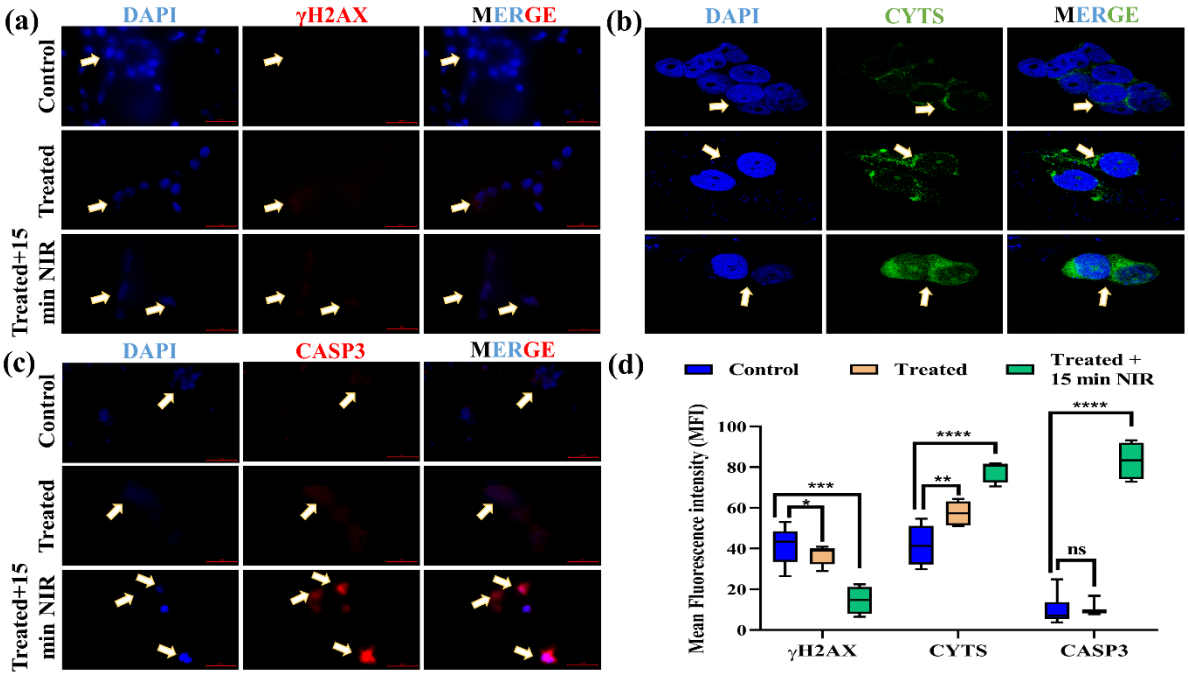

Figure 8: Fluorescence based immunocytochemical localization of (a) γH2AX, (b) CYTS and (c) CASP3. (d) MFI analysis of respective treatment panel of proteins. Student t test was utilized to correlate the significance *p < 0.0332, **p < 0.0021, ***p < 0.0002, ****p < 0.0001.

5.4 CONCLUSION

In summary, in this chapter we developed MDA-MB-231 cell specific, stable, biocompatible, NIR active, pH and redox dual responsive drug delivery nanocomposite, based on DyGPB nanocubes as next generation multimodal cancer theranostic agent, showcasing enhanced performance in chemo-photo therapy and T_1-T_2 weighted MR imaging where CytC has been used as an end-capping agent, boronate ester and disulfide bonds as an intermediate linker and HA as a targeting ligand. The nanocomposite exhibited uniform cubic morphology with suitable size and high DOX loading efficiency with acidic pH and GSH sensitivity for controlled DOX release behaviour. Moreover, a high rate of cell (MDA-MB-231) death was achieved with minimal dose (35.8 µM) due to combined effect of laser exposure and DOX, leading to *in-vitro* cell apoptosis while minimal cell death to normal cell (HER 293)

demonstrated its biocompatibility. More interestingly, doping of Gd^{3+} and Dy^{3+} in PBNC improved $T_1 - T_2$ relaxation efficiency compared to bare PBNC. Overall, our synthesized nanocomposite showed a fascinating prospects and approaches in terms of multimodal theranostic activity against MDA-MB-231 cell for future perception.

References

1. Obidiro, O., Battogtokh, G., & Akala, E. O. (2023). Triple negative breast cancer treatment options and limitations: future outlook. *Pharmaceutics*, *15*(7), 1796.
2. Chappell, K., Manna, K., Washam, C. L., Graw, S., Alkam, D., Thompson, M. D., ... & Byrum, S. D. (2021). Multi-omics data integration reveals correlated regulatory features of triple negative breast cancer. *Molecular omics*, *17*(5), 677-691.
3. Macchi, S., Jalihal, A., Hooshmand, N., Zubair, M., Jenkins, S., Alwan, N., ... & Siraj, N. (2022). Enhanced photothermal heating and combination therapy of NIR dye via conversion to self-assembled ionic nanomaterials. *Journal of Materials Chemistry B*, *10*(5), 806-816.
4. Qin, Z., Li, Y., & Gu, N. (2018). Progress in applications of Prussian blue nanoparticles in biomedicine. *Advanced healthcare materials*, *7*(20), 1800347.
5. Sahoo, P., Jana, P., Kundu, S., Mishra, S., Chattopadhyay, K., Mukherjee, A., & Ghosh, C. K. (2023). Quercetin@ Gd 3+ doped Prussian blue nanocubes induce the pyroptotic death of MDA-MB-231 cells: combinational targeted multimodal therapy, dual modal MRI, intuitive modelling of r 1–r 2 relaxivities. *Journal of Materials Chemistry B*, *11*(28), 6646-6663.
6. Lu, Y., Zhang, P., Lin, L., Gao, X., Zhou, Y., Feng, J., & Zhang, H. (2022). Ultra-small bimetallic phosphides for dual-modal MRI imaging guided photothermal ablation of tumors. *Dalton Transactions*, *51*(11), 4423-4428.
7. Wang, K., An, L., Tian, Q., Lin, J., & Yang, S. (2018). Gadolinium-labelled iron/iron oxide core/shell nanoparticles as T 1–T 2 contrast agent for magnetic resonance imaging. *RSC advances*, *8*(47), 26764-26770.
8. Bottrill, M., Kwok, L., & Long, N. J. (2006). Lanthanides in magnetic resonance imaging. *Chemical Society Reviews*, *35*(6), 557-571.
9. Zheng, B., Fan, J., Chen, B., Qin, X., Wang, J., Wang, F., ... & Liu, X. (2022). Rare-earth doping in nanostructured inorganic materials. *Chemical reviews*, *122*(6), 5519-5603.
10. Gautam, M., Poudel, K., Yong, C. S., & Kim, J. O. (2018). Prussian blue nanoparticles: Synthesis, surface modification, and application in cancer treatment. *International journal of pharmaceutics*, *549*(1-2), 31-49.
11. Luo, Z., Ding, X., Hu, Y., Wu, S., Xiang, Y., Zeng, Y., ... & Zhao, Y. (2013). Engineering a hollow nanocontainer platform with multifunctional molecular machines for tumor-targeted therapy in vitro and in vivo. *ACS nano*, *7*(11), 10271-10284.
12. Han, K., Lei, Q., Wang, S. B., Hu, J. J., Qiu, W. X., Zhu, J. Y., ... & Zhang, X. Z. (2015). Dual-stage-light-guided tumor inhibition by mitochondria-targeted photodynamic therapy. *Advanced Functional Materials*, *25*(20), 2961-2971.
13. Hayashi, K., Nakamura, M., Miki, H., Ozaki, S., Abe, M., Matsumoto, T., ... & Ishimura, K. (2014). Magnetically responsive smart nanoparticles for cancer treatment with a combination of magnetic hyperthermia and remote-control drug release. *Theranostics*, *4*(8), 834.
14. Fukumura, D., & Jain, R. K. (2007). Tumor microenvironment abnormalities: causes, consequences, and strategies to normalize. *Journal of cellular biochemistry*, *101*(4), 937-949.
15. Xiao, D., Jia, H. Z., Zhang, J., Liu, C. W., Zhuo, R. X., & Zhang, X. Z. (2014). A dual-responsive mesoporous silica nanoparticle for tumor-triggered targeting drug delivery. *Small*, *10*(3), 591-598.

16. Luo, Z., Cai, K., Hu, Y., Zhao, L., Liu, P., Duan, L., & Yang, W. (2011). Mesoporous silica nanoparticles end-capped with collagen: redox-responsive nanoreservoirs for targeted drug delivery. *Angewandte Chemie International Edition*, *3*(50), 640-643.
17. Kao, K. C., Lee, C. H., Lin, T. S., & Mou, C. Y. (2010). Cytochrome c covalently immobilized on mesoporous silicas as a peroxidase: Orientation effect. *Journal of Materials Chemistry*, *20*(22), 4653-4662.
18. Lee, J. Y., Park, Y., Pun, S., Lee, S. S., Lo, J. F., & Lee, L. P. (2015). Real-time investigation of cytochrome c release profiles in living neuronal cells undergoing amyloid beta oligomer-induced apoptosis. *Nanoscale*, *7*(23), 10340-10343.
19. Mei, X., Han, Y., Xi, J., Liu, J., Xu, L., Yuan, J., ... & Li, J. (2022). Preparation of hollow mesoporous prussian blue coated with mesoporous silica shell nanocubes for photothermal therapy and drug carrier. *Materials Letters*, *312*, 131697.
20. Demin, A. M., Vakhrushev, A. V., Pershina, A. G., Valova, M. S., Efimova, L. V., Syomchina, A. A., ... & Charushin, V. N. (2022). Magnetic-responsive doxorubicin-containing materials based on Fe3O4 nanoparticles with a SiO2/PEG shell and study of their effects on cancer cell lines. *International journal of molecular sciences*, *23*(16), 9093.
21. Liu, R., Zhao, X., Wu, T., & Feng, P. (2008). Tunable redox-responsive hybrid nanogated ensembles. *Journal of the American Chemical Society*, *130*(44), 14418-14419.
22. Luo, Z., Cai, K., Hu, Y., Zhang, B., & Xu, D. (2012). Cell-specific intracellular anticancer drug delivery from mesoporous silica nanoparticles with pH sensitivity. *Advanced healthcare materials*, *1*(3), 321-325.
23. Pintaske, J., Martirosian, P., Graf, H., Erb, G., Lodemann, K. P., Claussen, C. D., & Schick, F. (2006). Relaxivity of gadopentetate dimeglumine (Magnevist), gadobutrol (Gadovist), and gadobenate dimeglumine (MultiHance) in human blood plasma at 0.2, 1.5, and 3 Tesla. *Investigative radiology*, *41*(3), 213-221.
24. Liu, X., Li, B., Fu, F., Xu, K., Zou, R., Wang, Q., ... & Hu, J. (2014). Facile synthesis of biocompatible cysteine-coated CuS nanoparticles with high photothermal conversion efficiency for cancer therapy. *Dalton Transactions*, *43*(30), 11709-11715.
25. Zheng, X., Zhang, J., Wang, J., Qi, X., Rosenholm, J. M., & Cai, K. (2015). Polydopamine coatings in confined nanopore space: toward improved retention and release of hydrophilic cargo. *The Journal of Physical Chemistry C*, *119*(43), 24512-24521.
26. Jeyarani, S., Vinita, N. M., Puja, P., Senthamilselvi, S., Devan, U., Velangani, A. J., ... & Kumar, P. (2020). Biomimetic gold nanoparticles for its cytotoxicity and biocompatibility evidenced by fluorescence-based assays in cancer (MDA-MB-231) and non-cancerous (HEK-293) cells. *Journal of Photochemistry and Photobiology B: Biology*, *202*, 111715.
27. Mosmann, T. (1983). Rapid colorimetric assay for cellular growth and survival: application to proliferation and cytotoxicity assays. *Journal of immunological methods*, *65*(1-2), 55-63.
28. Eduardo, F. D. P., Bueno, D. F., de Freitas, P. M., Marques, M. M., Passos-Bueno, M. R., Eduardo, C. D. P., & Zatz, M. (2008). Stem cell proliferation under low intensity laser irradiation: a preliminary study. *Lasers in Surgery and Medicine: The Official Journal of the American Society for Laser Medicine and Surgery*, *40*(6), 433-438.
29. Patra, R., Halder, S., Saha, R., Jana, K., & Sarkar, K. (2024). Highly Efficient Photoswitchable Smart Polymeric Nanovehicle for Gene and Anticancer Drug Delivery in Triple-Negative Breast Cancer. *ACS Biomaterials Science & Engineering*.
30. Samain, L., Grandjean, F., Long, G. J., Martinetto, P., Bordet, P., & Strivay, D. (2013). Relationship between the synthesis of Prussian blue pigments, their color, physical properties, and their behavior in paint layers. *The Journal of Physical Chemistry C*, *117*(19), 9693-9712.
31. Brown, D. B. (Ed.). (2012). *Mixed-valence compounds: theory and applications in chemistry, physics, geology, and biology* (Vol. 58). Springer Science & Business Media.

32. Samain, L., Grandjean, F., Long, G. J., Martinetto, P., Bordet, P., & Strivay, D. (2013). Relationship between the synthesis of Prussian blue pigments, their color, physical properties, and their behavior in paint layers. *The Journal of Physical Chemistry C*, *117*(19), 9693-9712.
33. Chakraborty, N., Jha, D., Gautam, H. K., & Roy, I. (2020). Peroxidase-like behavior and photothermal effect of chitosan-coated Prussian-blue nanoparticles: dual-modality antibacterial action with enhanced bioaffinity. *Materials Advances*, *1*(4), 774-782.
34. Chen, F., Teng, L., Lu, C., Zhang, C., Rong, Q., Zhao, Y., ... & Zhang, X. (2020). Activatable magnetic/photoacoustic nanoplatform for redox-unlocked deep-tissue molecular imaging in vivo via prussian blue nanoprobe. *Analytical Chemistry*, *92*(19), 13452-13461.
35. Shokouhimehr, M., Soehnlen, E. S., Hao, J., Griswold, M., Flask, C., Fan, X., ... & Huang, S. D. (2010). Dual purpose Prussian blue nanoparticles for cellular imaging and drug delivery: a new generation of T 1-weighted MRI contrast and small molecule delivery agents. *Journal of Materials Chemistry*, *20*(25), 5251-5259.
36. Qin, Z., Chen, B., Mao, Y., Shi, C., Li, Y., Huang, X., ... & Gu, N. (2020). Achieving ultrasmall Prussian blue nanoparticles as high-performance biomedical agents with multifunctions. *ACS applied materials & interfaces*, *12*(51), 57382-57390.
37. Peng, J., Dong, M., Ran, B., Li, W., Hao, Y., Yang, Q., ... & Qian, Z. (2017). "One-for-all"-type, biodegradable prussian blue/manganese dioxide hybrid nanocrystal for trimodal imaging-guided photothermal therapy and oxygen regulation of breast cancer. *ACS applied materials & interfaces*, *9*(16), 13875-13886.
38. Baranyai, Z., Carniato, F., Nucera, A., Horváth, D., Tei, L., Platas-Iglesias, C., & Botta, M. (2021). Defining the conditions for the development of the emerging class of Fe III-based MRI contrast agents. *Chemical Science*, *12*(33), 11138-11145.
39. Caravan, P., Farrar, C. T., Frullano, L., & Uppal, R. (2009). Influence of molecular parameters and increasing magnetic field strength on relaxivity of gadolinium-and manganese-based T1 contrast agents. *Contrast media & molecular imaging*, *4*(2), 89-100.
40. Wahsner, J., Gale, E. M., Rodríguez-Rodríguez, A., & Caravan, P. (2018). Chemistry of MRI contrast agents: current challenges and new frontiers. *Chemical reviews*, *119*(2), 957-1057.
41. Norek, M., Kampert, E., Zeitler, U., & Peters, J. A. (2008). Tuning of the size of Dy_2O_3 nanoparticles for optimal performance as an MRI contrast agent. *Journal of the American Chemical Society*, *130*(15), 5335-5340.
42. Ravera, E., Gigli, L., Fiorucci, L., Luchinat, C., & Parigi, G. (2022). The evolution of paramagnetic NMR as a tool in structural biology. *Physical Chemistry Chemical Physics*, *24*(29), 17397-17416.
43. R. K. Sharma , S. Dutta and S. Sharma , *New J. Chem.*, 2015, **40** , 2089-2101.
44. Rodríguez-Cuamatzi, P., Arillo-Flores, O. I., Bernal-Uruchurtu, M. I., & Höpfl, H. (2005). Theoretical and experimental evaluation of homo-and heterodimeric hydrogen-bonded motifs containing boronic acids, carboxylic acids, and carboxylate anions: Application for the generation of highly stable hydrogen-bonded supramolecular systems. *Crystal growth & design*, *5*(1), 167-175.
45. Luo Z, Cai KY, Hu Y, Zhang BL, Xu DW. Cell-Specific Intracellular Anticancer Drug Delivery from Mesoporous Silica Nanoparticles with pH Sensitivity. Adv Healthc Mater. 2012;1:321-5.
46. Wang B, Chen LM, Sun YJ et al. Development of phenylboronic acid functionalized nanoparticles for emodin delivery. J Mater Chem B 2015;3:3840–7.
47. Fahmi MZ, Chen JK, Huang CC et al. Phenylboronic acid-modified magnetic nanoparticles as a platform for carbon dot conjugation and doxorubicin delivery. J Mater Chem B 2015;3:5532–43.
48. Pan YJ, Chen YY, Wang DR et al. Redox/pH dual stimuli-responsive biodegradable nanohydrogels with varying responses to dithiothreitol and glutathione for controlled drug release. Biomaterials 2012; 33:6570–579.
49. Noh, J., Kwon, B., Han, E., Park, M., Yang, W., Cho, W., ... & Lee, D. (2015). Amplification of oxidative stress by a dual stimuli-responsive hybrid drug enhances cancer cell death. *Nature communications*, *6*(1), 6907.

50. Nurhayati, A. P. D., Rihandoko, A., Fadlan, A., Ghaissani, S. S., Jadid, N., & Setiawan, E. (2022). Anti-cancer potency by induced apoptosis by molecular docking P53, caspase, cyclin D1, cytotoxicity analysis and phagocytosis activity of trisindoline 1, 3 and 4. *Saudi Pharmaceutical Journal*, *30*(9), 1345-1359.
51. Shen, Y., & White, E. (2001). p53-dependent apoptosis pathways.
52. Varvara, P. V., Karaolanis, G., Valavanis, C., Stanc, G., Tzaida, O., Trihia, H., ... & Perrea, D. (2019). gamma-H2AX: A potential biomarker in breast cancer. *Tumor Biology*, *41*(9), 1010428319878536.

Chapter 6

Grand Conclusions

Chapter 6. Summary of the Findings and Conclusion of the Present Work.

In the pursuit of advancing cancer treatment modalities, the present work embarks on a development of a Prussian blue based multimodal novel theranostic nanocomposite in a single nanoplatform. The journey begins with a critical examination of the limitations inherent in conventional cancer chemotherapeutic approaches and the indispensable role played by MRI contrast agents in diagnosis and monitoring.

Drawing from the transformative potential of nanotechnology, the research endeavor delves into the realm of targeted theranostics, aiming to revolutionize cancer treatment paradigms. Through a meticulous literature survey, the groundwork is laid for the utilization of prussian blue-based nanoparticles as a core NP in cancer theranostics, showcasing their promising potential in augmenting efficacy while mitigating adverse effects. Each chapter contributes a distinct facet to the overarching narrative. Chapter 3 elucidates that the synthesized $PBNC_{60}$@m-SiO_2@HA consisting amphiphilic micelles for conjugation of DOX shows good biocompatibility, ultrahigh DOX loading as well as pH responsive DOX release efficiency. Besides this the nanoplatform acts as *in vitro* T_1-weighted MR agent having r_1 value greater than r_1 of commercially available Gd-based MRI contrast agent. Moreover, a high rate of cell (HCT 116) death is achieved over lower dose of $PBNC_{60}$@m-SiO_2@HA@DOX due to the mutual effect of laser (808 nm) and DOX, followed by iROS mediated mitochondria dependent DNA damage pathway. More interestingly, details study on higher r_1 value for smaller sized PBNC is assigned to the contribution of second sphere zeolitic water molecules leads to crystal vacancy. Furthermore, variation of r_1 value at each functionalization steps illustrate that m-SiO_2 coating on PBNC increases r_1 due to quantum confinement effect, while HA and DOX addition lowers r_1. Fractional changes in r_1 has been ascribed to size dependent correlation time and diffusion of water molecules where thickness of m-SiO_2 plays a significant role. Chapter 4 explores the synthesis of MDA-MB-231 cell specific, highly stable, NIR active $GPB_{0.50}$@PDA@PEG@HA@Qu as next generation multimodal theranostic agent in terms of chemo-photo therapy and T_1-T_2 weighted MR imaging with enhanced performance. In particular, the limitations of Qu in clinical usages are adequately overcome by our designed smart targeted drug delivery system. Moreover, a high rate of cell (MDA-MB-231) death is achieved with minimal dose (13.54 μM) due to combined effect of laser exposure and Qu followed by N-GSDMD mediated canonical and P2X7 receptor mediated non-canonical

pyroptosis pathway while negligible toxicity to normal cell (HEK 293) demonstrate it's safety. Interestingly, details analysis on improved trend of r_1 value due to Gd^{3+} tuning in GPB nanocubes is assigned to inner sphere relaxivity where q^{IS}, S, τ_R and r_{M-H} ($Fe^{3+}(3c) - O(6f)$) plays a significant role. Moreover, a similar pattern has also been observed in r_2 value which consigned to the mutual contribution of inner sphere and outer sphere relaxivity effect where magnetization plays a vital role additionally. Chapter 5 delves into the development of MDA-MB-231 cell specific, stable, biocompatible, NIR active, pH and redox dual responsive drug delivery nanocomposite, based on DyGPB nanocubes as next generation multimodal cancer theranostic agent, showcasing enhanced performance in chemo-photo therapy and T_1-T_2 weighted MR imaging where CytC has been used as an end-capping agent, boronate ester and disulfide bonds as an intermediate linker and HA as a targeting ligand. The nanocomposite exhibits uniform cubic morphology with suitable size and high DOX loading efficiency with acidic pH and GSH sensitivity for controlled DOX release behaviour. Moreover, a high rate of cell (MDA-MB-231) death has been achieved with minimal dose (35.8 µM) due to combined effect of laser exposure and DOX, leading to *in-vitro* cell apoptosis while minimal cell death to normal cell (HER 293) demonstrated its biocompatibility. More interestingly, doping of Gd^{3+} and Dy^{3+} in PBNC improved $T_1 - T_2$ relaxation efficiency compared to bare PBNC.

Overall, these chapters underscore the advancement of prussian blue-based nanocomposites for bolstered *in-vitro* cancer theranostics (including chemo, PTT, PDT, and dual-modal MRI) through various doping in core NP and surface alterations tailored for targeting, biocompatibility, drug loading and stimuli responsive drug releasing. By this approach, hydrophobic natural flavonoid drug was also successfully delivered at targeted cancer site. Additionally, the chapters intricately detail the fundamental insights into the variation of r_1 and r_2 relaxivity, influenced by diverse sizes, distinct functionalization and doping in core prussian blue nanoparticles, elucidated through SBM theory.

In essence, the culmination of this research represents a significant step forward in the quest to combat cancer, offering a glimpse into a future where targeted, multimodal theranostic approaches redefine the treatment landscape, ushering in an era of precision medicine.

Chapter 7

Scope of the Future Work

Chapter 4. Scope of The Future Work- Some Possible Avenues for Futuristics Exploration.

In this present work we have focused on the development of prussian blue-based nanocomposites for bolstered *in-vitro* cancer theranostics (including chemo, PTT, PDT, and dual-modal MRI) through various doping in core NP and surface alterations tailored for targeting, biocompatibility, drug loading and stimuli responsive drug releasing. By this approach, we successfully delivered hydrophobic natural flavonoid into the targeted cancer site. In addition, we have also provide the fundamental insights into the variation of r_1 and r_2 relaxivity, influenced by diverse sizes, distinct functionalization and doping in core prussian blue nanoparticles, elucidated through SBM theory. In this scenario, here are some future aspects that can be considered for further exploration.

1. ***In-vivo* studies:** Conducting *in-vivo* studies to evaluate the biocompatibility, targeting efficacy, and therapeutic response of the synthesized nanocomposites in animal models. This will provide valuable insights into their potential clinical translation and efficacy in a more physiological environment.
2. **Biodegradability, stability and long-term safety assessment:** Further investigation required to ensure their safety and biocompatibility and more importantly stability in biological environment for prolonged therapeutic applications.
3. **Advanced targeting strategies**: Exploring advanced targeting strategies beyond receptor based targeting such as peptide or antibody based targeting to further improve the specificity and selectivity of the nanocomposites towards cells.
4. **Enhanced imaging modalities**: Exploring additional imaging modalities beyond dual-modal MRI, such as fluorescence imaging, upconversion fluorescence imaging, or photoacoustic imaging (PAI), to further enhance the theranostic capabilities and improve imaging sensitivity and specificity. In this context, it is important to note that we already observed photoluminescence and upconversion luminescence property in lanthanide doped prussian blue nanoparticles.

5. **Theranostic nanocomposite libraries**: Expanding the scope of the research to explore the synthesis and characterization of a library of theranostic nanocomposites with

diverse compositions, structures, and properties to identify lead candidates with optimized therapeutic and diagnostic capabilities.

6. **Integration with emerging technologies**: Integrating the theranostic nanocomposites with emerging technologies such as artificial intelligence (AI), machine learning (ML), or 3D printing for personalized medicine approaches, real-time monitoring, and adaptive treatment strategies.
7. **Clinical translation and translational research**: Conducting translational research to bridge the gap between preclinical findings and clinical applications, including scalability of synthesis methods, regulatory considerations, and clinical trial design for future clinical testing.

Appendix A

Chapter 4

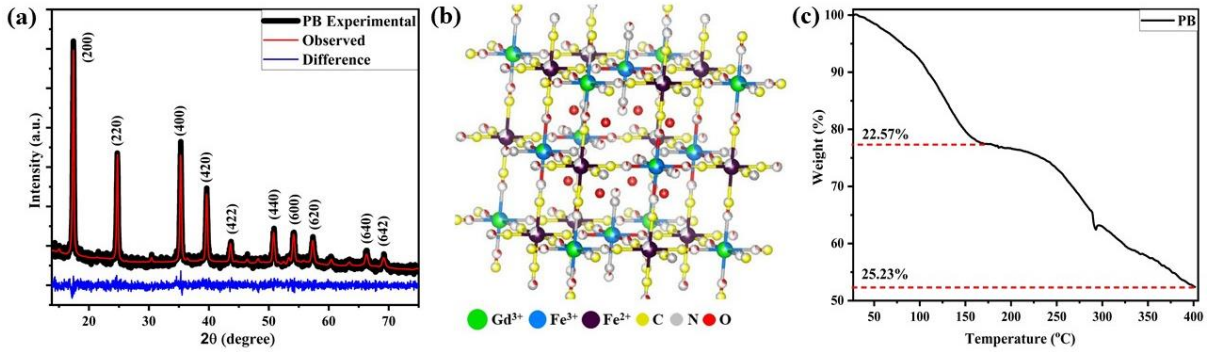

Fig. A1: (a)Reitveld refinement of PB XRD pattern with difference between experimental and refined patterns. (b) Unit cell structure of representative $GPB_{0.50}$ nanocube. (c) TGA plot of PB.

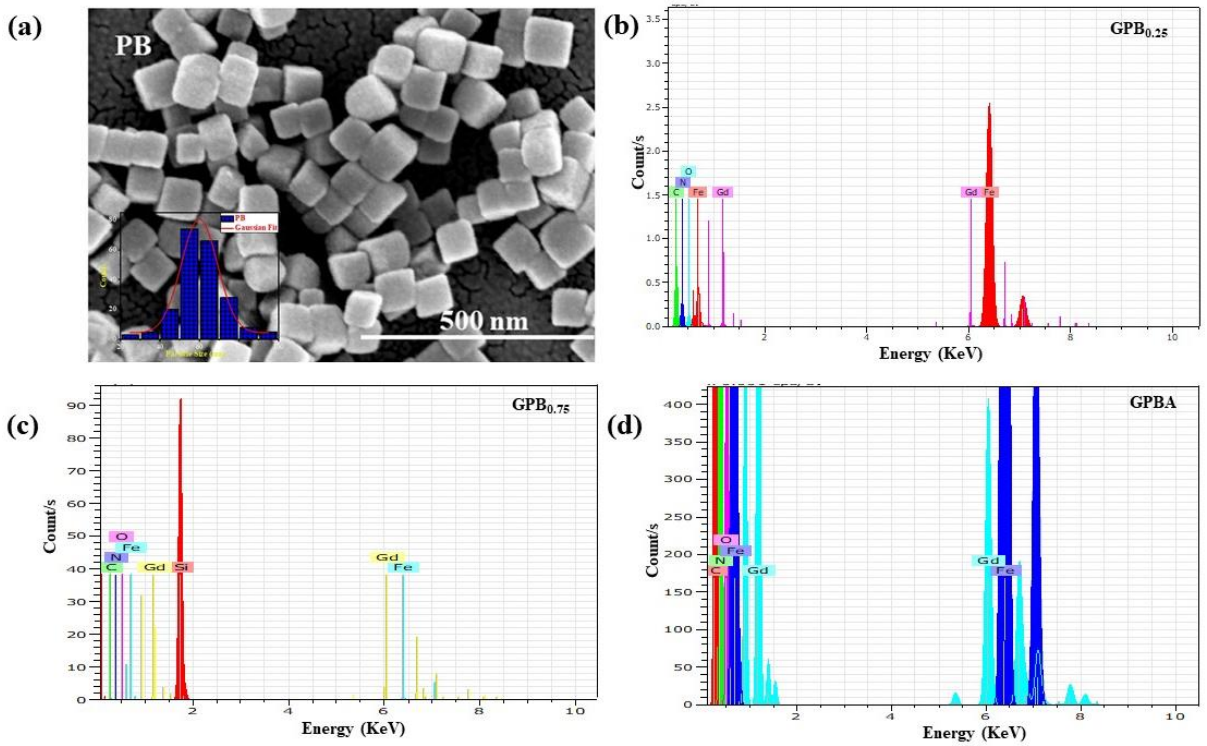

Fig. A2: (a) FESEM image and size distribution histogram in the inset of PB nanocubes. EDX spectrum of (b) $GPB_{0.25}$, (c) $GPB_{0.50}$ and (d) GPBA nanocubes.

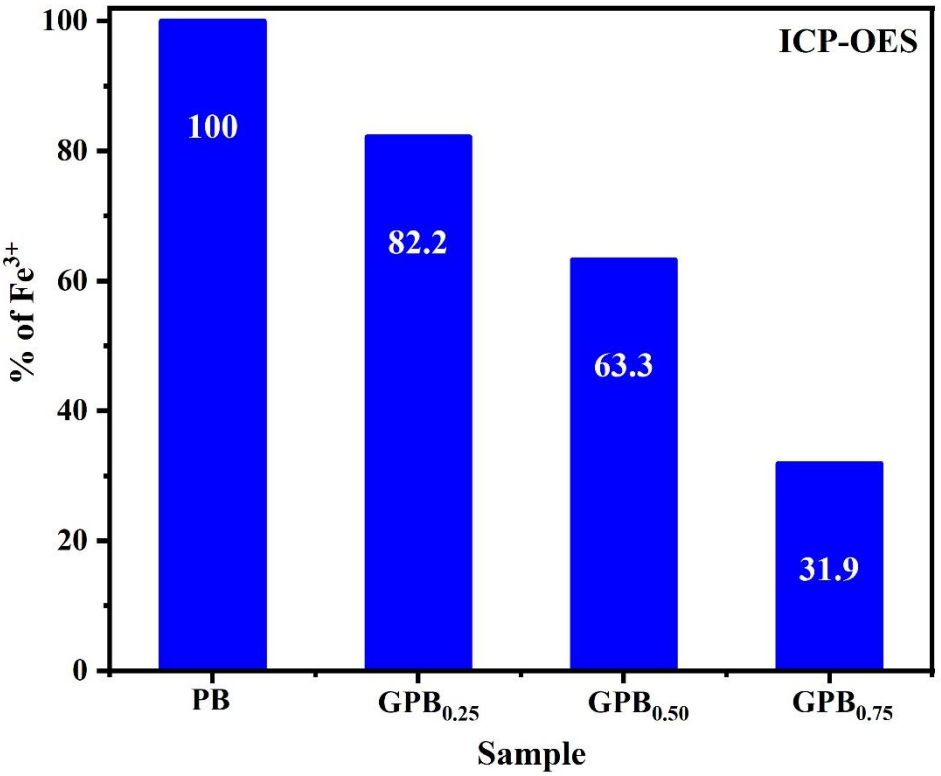

Fig. A3: ICP-OES measurement to find percentage Fe^{3+} content in bare PB and GPB samples (initial concentration of exposed samples was 40 µg/mL).

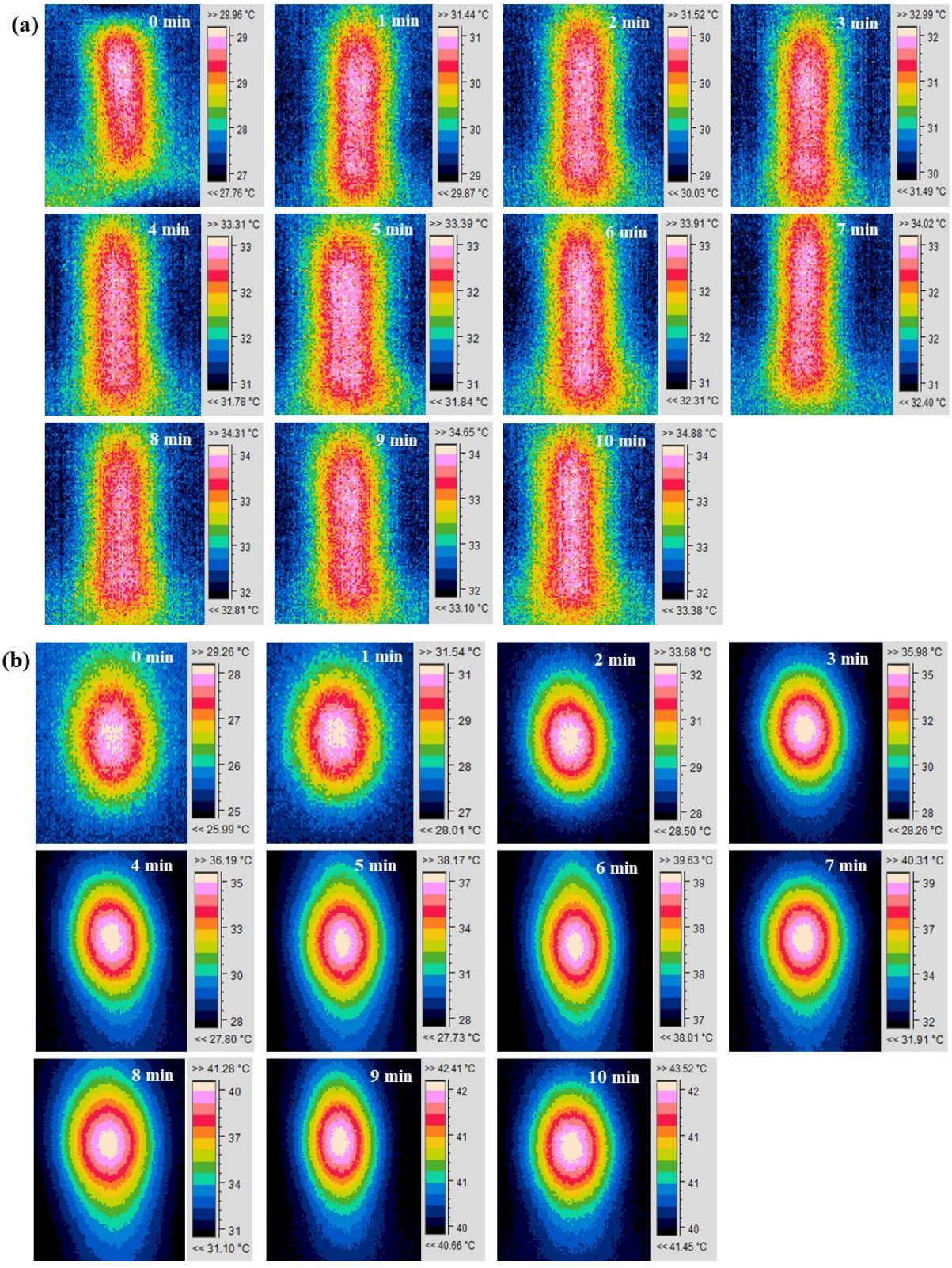
(a)
0 min
>> 29.96 °C
<< 27.76 °C
1 min
>> 31.44 °C
<< 29.87 °C
2 min
>> 31.52 °C
<< 30.03 °C
3 min
>> 32.99 °C
<< 31.49 °C
4 min
>> 33.31 °C
<< 31.78 °C
5 min
>> 33.39 °C
<< 31.84 °C
6 min
>> 33.91 °C
<< 32.31 °C
7 min
>> 34.02 °C
<< 32.40 °C
8 min
>> 34.31 °C
<< 32.81 °C
9 min
>> 34.65 °C
<< 33.10 °C
10 min
>> 34.88 °C
<< 33.38 °C
(b)
0 min
>> 29.26 °C
<< 25.99 °C
1 min
>> 31.54 °C
<< 28.01 °C
2 min
>> 33.68 °C
<< 28.50 °C
3 min
>> 35.98 °C
<< 28.26 °C
4 min
>> 36.19 °C
<< 27.80 °C
5 min
>> 38.17 °C
<< 27.73 °C
6 min
>> 39.63 °C
<< 38.01 °C
7 min
>> 40.31 °C
<< 31.91 °C
8 min
>> 41.28 °C
<< 31.10 °C
9 min
>> 42.41 °C
<< 40.66 °C
10 min
>> 43.52 °C
<< 41.45 °C

(c)

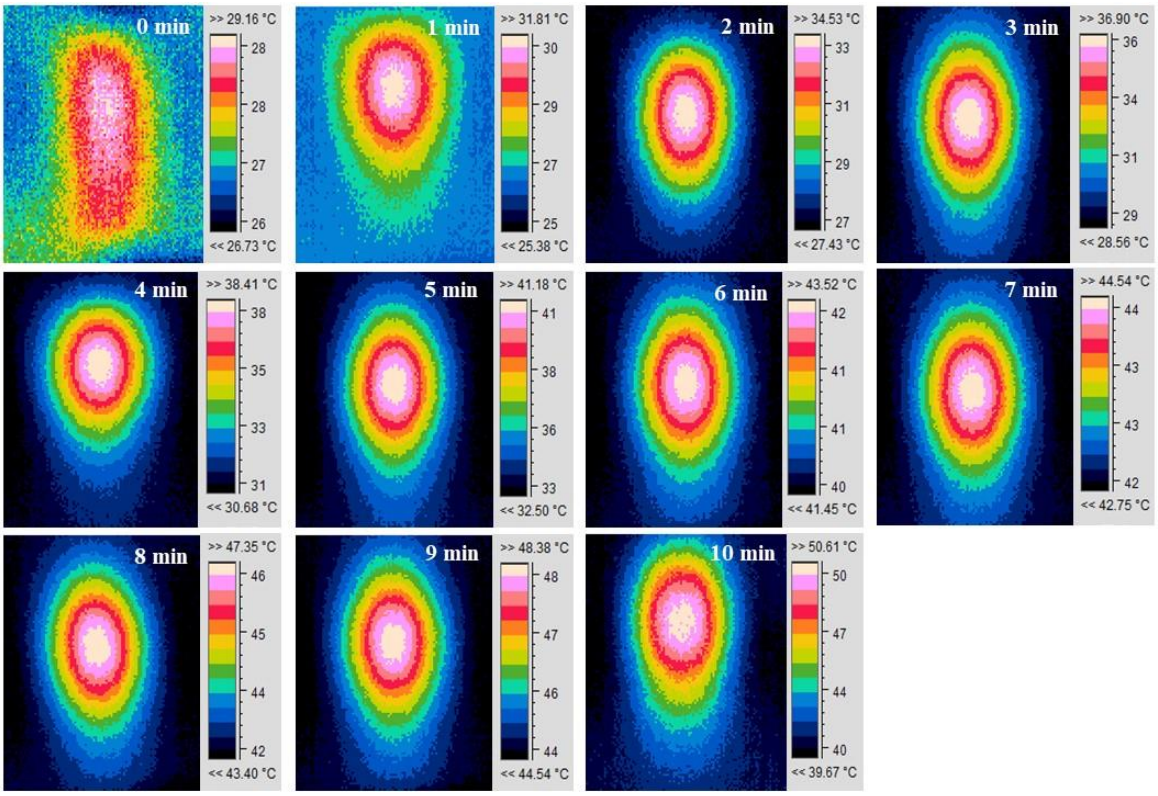
0 min
>> 29.16 °C
28
28
27
26
<< 26.73 °C
1 min
>> 31.81 °C
30
29
27
25
<< 25.38 °C
2 min
>> 34.53 °C
33
31
29
27
<< 27.43 °C
3 min
>> 36.90 °C
36
34
31
29
<< 28.56 °C
4 min
>> 38.41 °C
38
35
33
31
<< 30.68 °C
5 min
>> 41.18 °C
41
38
36
33
<< 32.50 °C
6 min
>> 43.52 °C
42
41
41
40
<< 41.45 °C
7 min
>> 44.54 °C
44
43
43
42
<< 42.75 °C
8 min
>> 47.35 °C
46
45
44
42
<< 43.40 °C
9 min
>> 48.38 °C
48
47
46
44
<< 44.54 °C
10 min
>> 50.61 °C
50
47
44
40
<< 39.67 °C

(d)

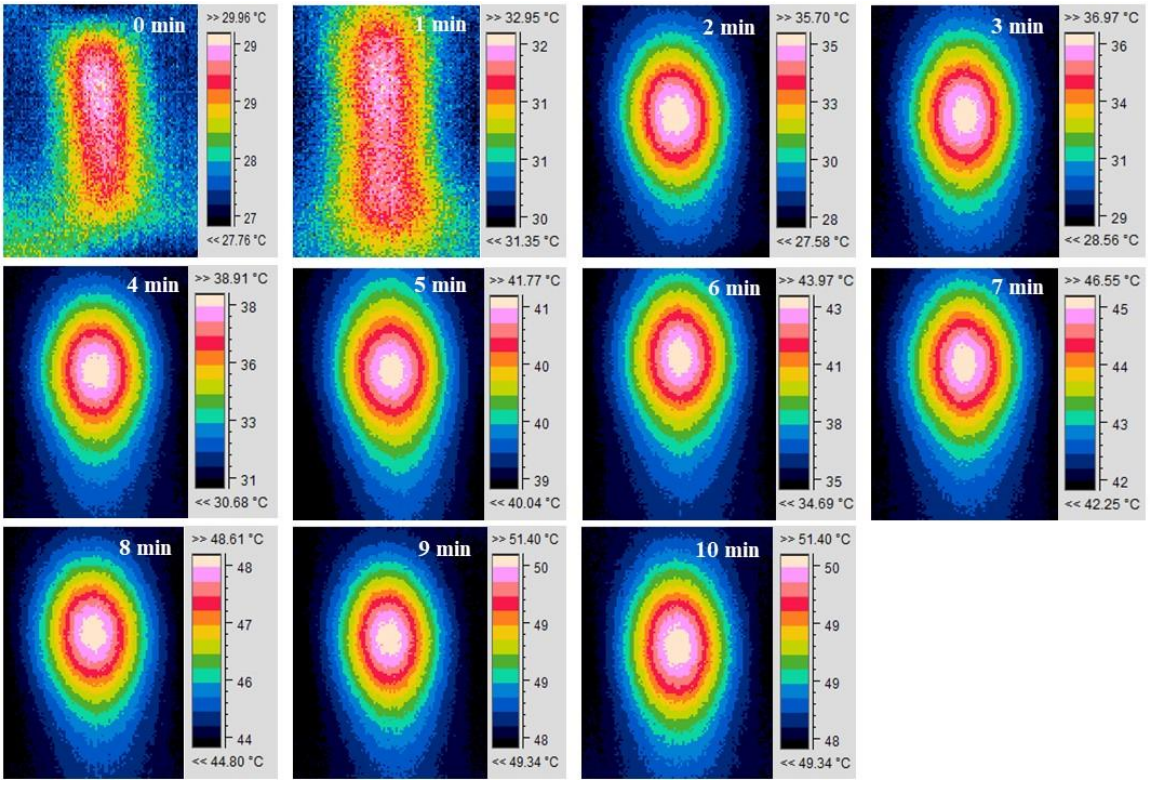
0 min
>> 29.96 °C
29
29
28
27
<< 27.76 °C
1 min
>> 32.95 °C
32
31
31
30
<< 31.35 °C
2 min
>> 35.70 °C
35
33
30
28
<< 27.58 °C
3 min
>> 36.97 °C
36
34
31
29
<< 28.56 °C
4 min
>> 38.91 °C
38
36
33
31
<< 30.68 °C
5 min
>> 41.77 °C
41
40
40
39
<< 40.04 °C
6 min
>> 43.97 °C
43
41
38
35
<< 34.69 °C
7 min
>> 46.55 °C
45
44
43
42
<< 42.25 °C
8 min
>> 48.61 °C
48
47
46
44
<< 44.80 °C
9 min
>> 51.40 °C
50
49
49
48
<< 49.34 °C
10 min
>> 51.40 °C
50
49
49
48
<< 49.34 °C

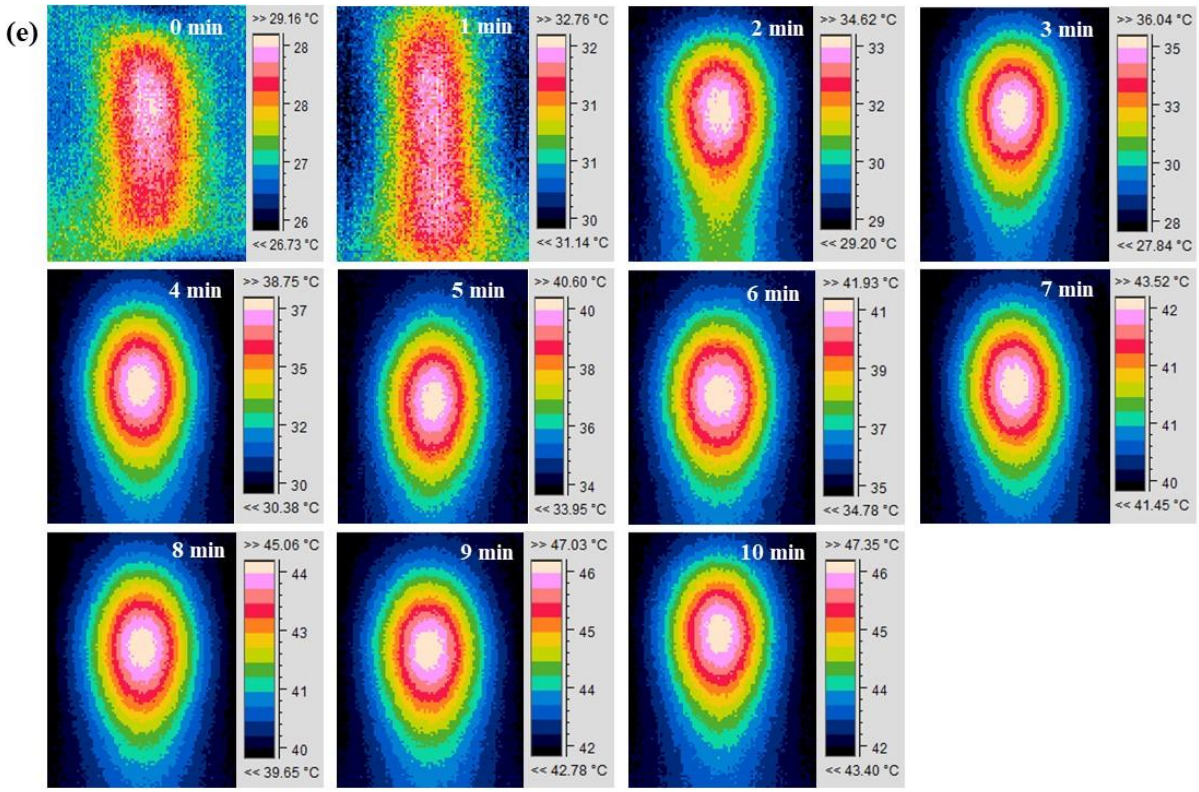

Fig. A4: Thermographs of (a) DI, (b) PB, (c) $GPB_{0.25}$, (d) $GPB_{0.75}$, (e) GPBA nanocubes sample under 808 nm NIR laser irradiation over 10 minutes.

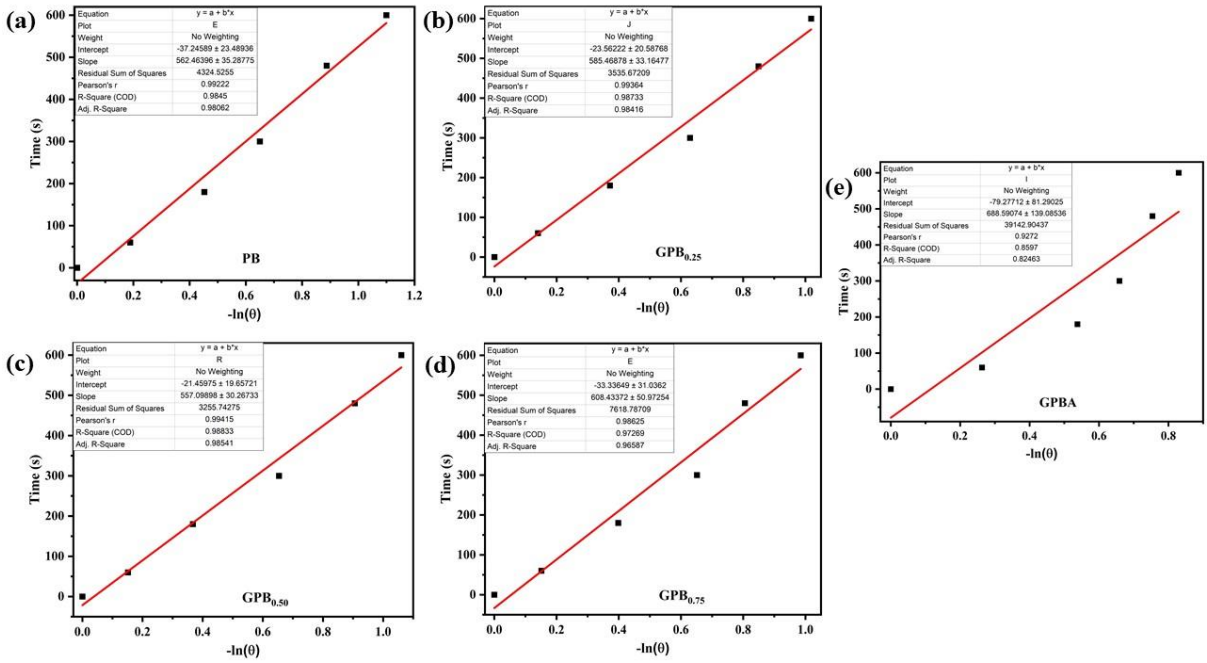

Fig. A5: Plot and linear fit of time versus negative natural logarithm of the temperature

increment for the cooling rate of (a) PB, (b) $GPB_{0.25}$, (c)$GPB_{0.50}$, (d) $GPB_{0.75}$ and (e) GPBA under 808 nm laser.

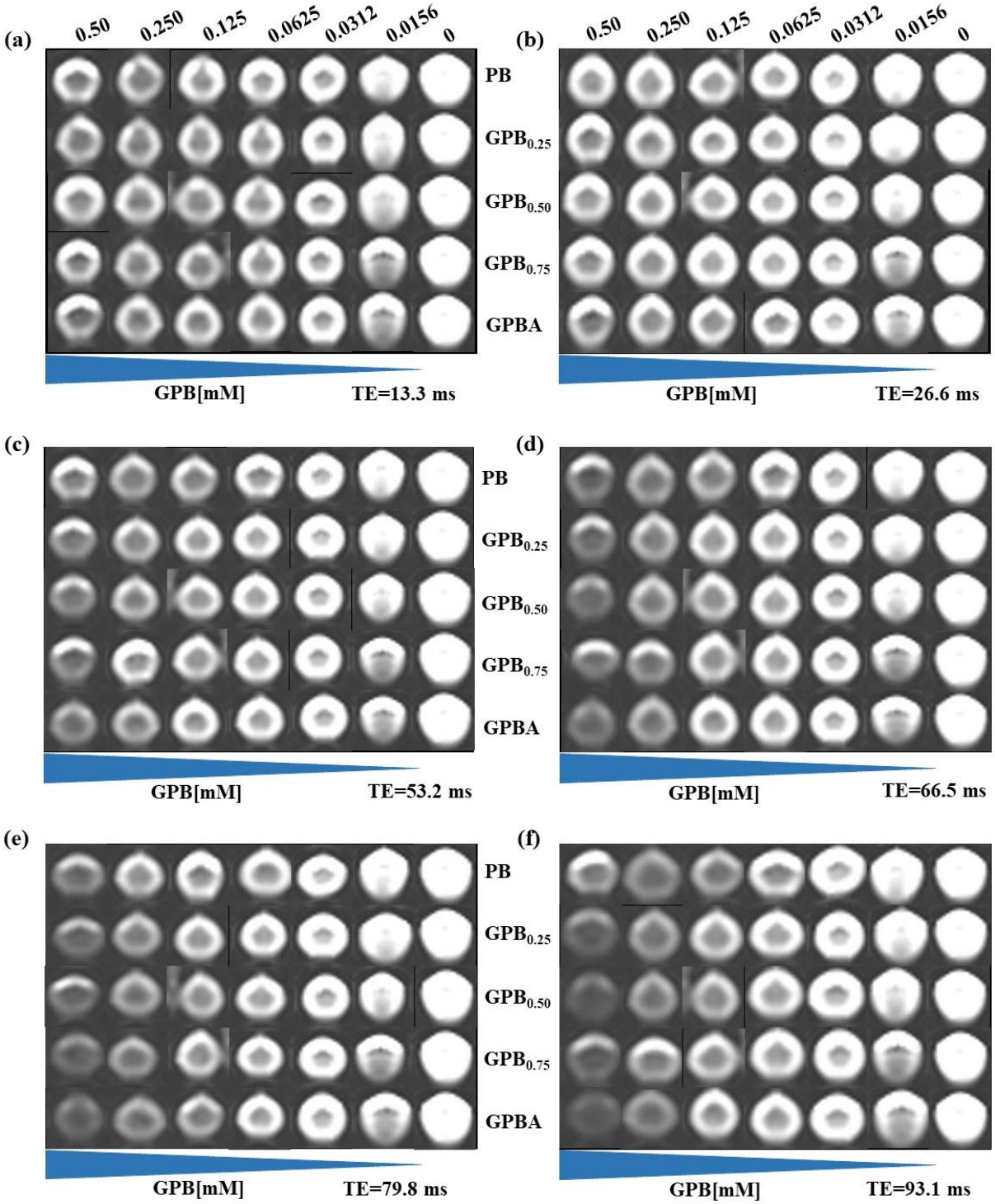

Fig. A6: Concentration dependant T_2 weighted MR images at 3 T showing hypo intensity from PB, $GPB_{0.25}$, $GPB_{0.50}$, $GPB_{0.75}$ and GPBA using spin-echo sequences with TR: 1770 ms and variable TE of (a) 13.3 ms, (b) 26.6 ms, (c) 53.2 ms, (d) 66.5 ms, (e) 79.8 ms and (f) 93.1 ms.

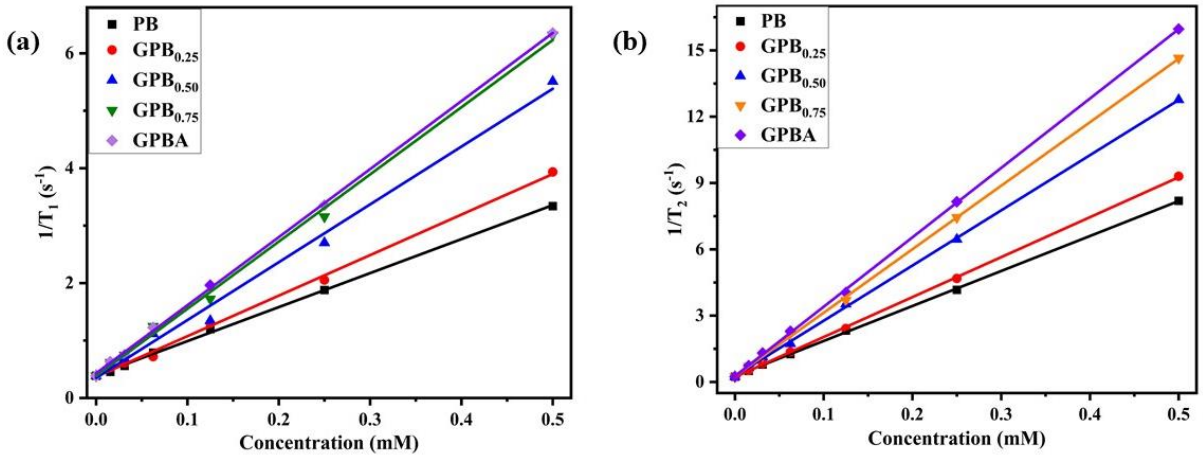

Fig. A7: Concentration dependent (a) T_1 and (b) T_2 relaxation rates. The relaxivities values were determined to be r_1 ~ 5.91, 7.05, 10.06, 11.69 11.84 $mM^{-1}s^{-1}$ and r_2 ~ 15.82, 18.07, 24.96, 28.72 31.39 $mM^{-1}s^{-1}$.

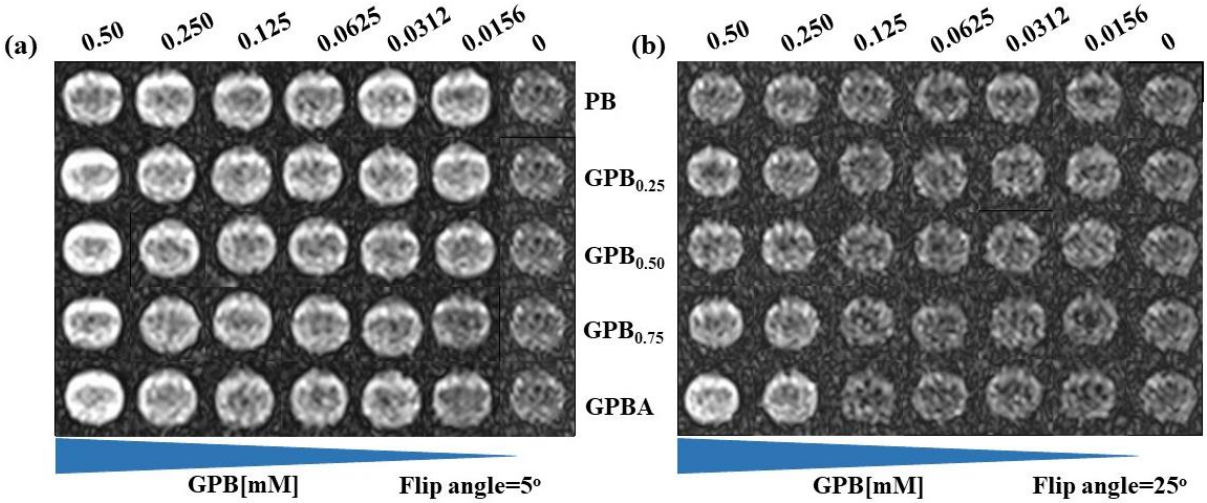

Fig. A8: Concentration dependant T_1 weighted MR images at 3 T showing brightening effect from PB, $GPB_{0.25}$, $GPB_{0.50}$, $GPB_{0.75}$ and GPBA using 3D gradient spin-echo sequences with TR: 15 ms, TE: 2.71 ms and variable flip angle of (a) 5^0 and (b) 25^0.

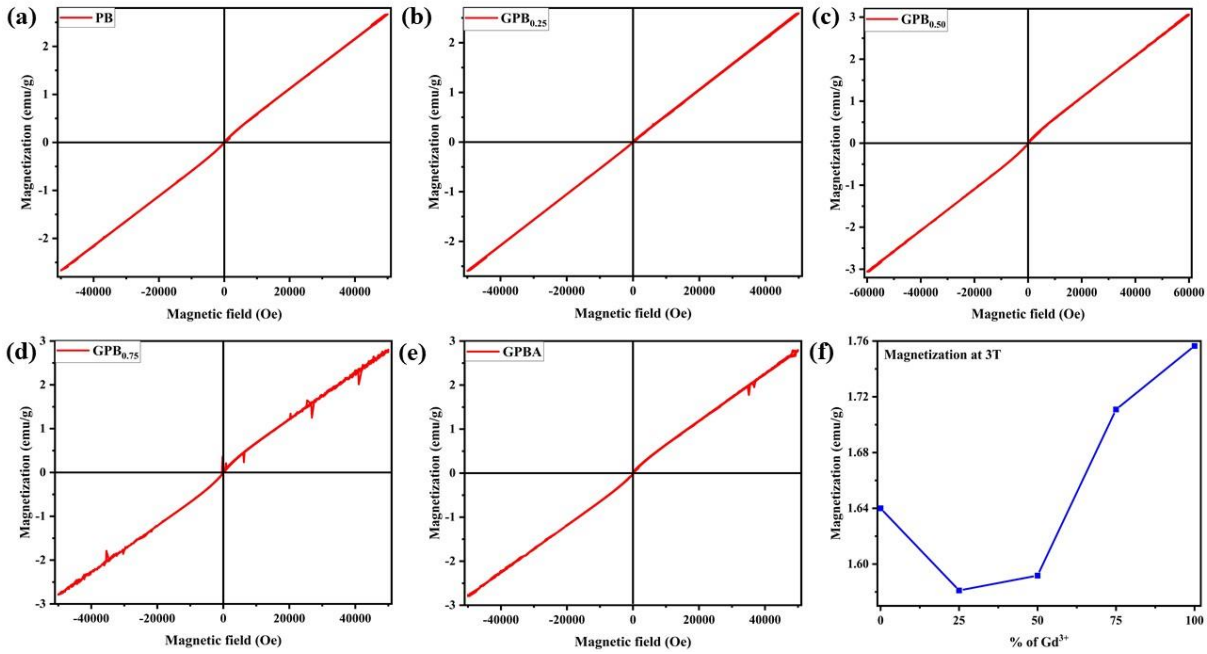

Fig. A9: SQUID magnetometry. Isothermal magnetization as a function of field at 300 K for (a) PB, (b) $GPB_{0.25}$, (c) $GPB_{0.50}$, (d) $GPB_{0.75}$ and (e) GPBA nanocubes sample. (f) Magnetization at 3T as a function of different Gd^{3+} doping in PB nanocubes at 300 K.

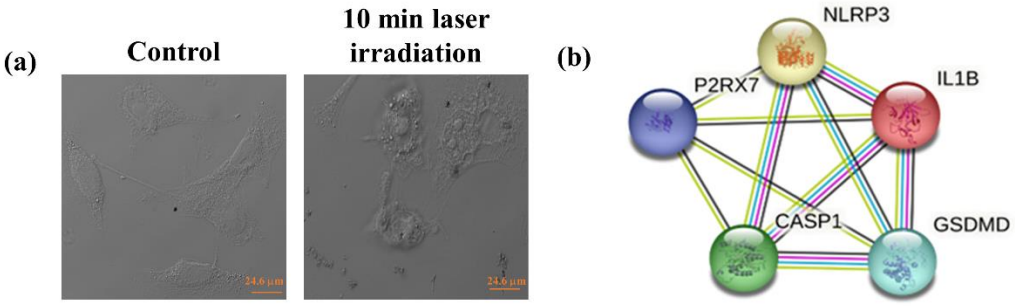

Fig. A10: (a) CLSM bright field image showing the induction of cell membrane disruption and nuclear condensation by $GPB_{0.50}$@PDA@PEG@HA@Qu under 10 minutes laser exposure in MDA-MB-231 cells. (b) STRING database for predicted cell death pathway.

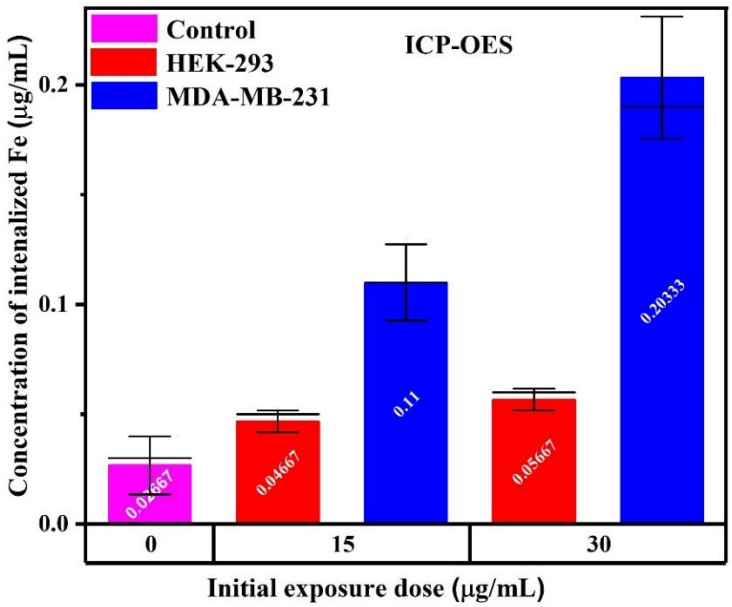

Fig. A11: ICP-OES analysis to quantify Fe uptake in HEK 293 and MDA-MB-231 cell. After 24 hr of incubation with 15 and 30 µg/mL of the $GPB_{0.50}$@PDA@PEG@HA nanocomposite, HEK 293 and MDA-MB-231 cell pellets were collected and acid digested for measurement.

Chapter 5

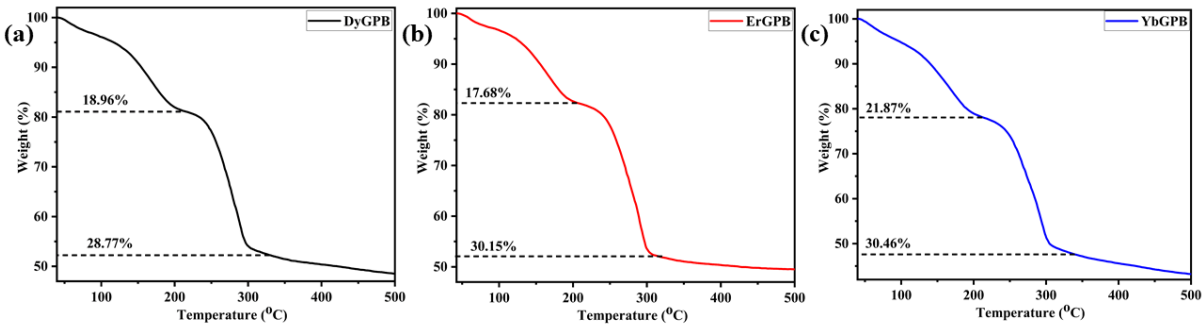

Figure A12: TGA plot of (a) DyGPB, (b) ErGPB and (c) YbGPB nanocubes.

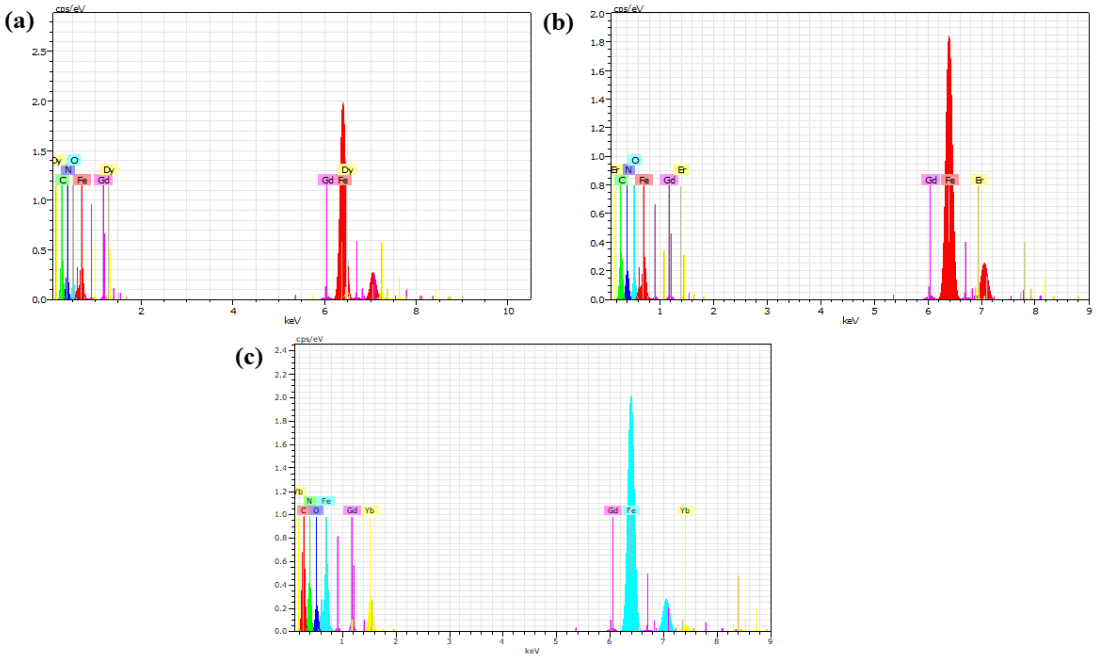

Figure A13: EDX spectrum of (a) DyGPB, (b) ErGPB and (c) YbGPB nanocubes.

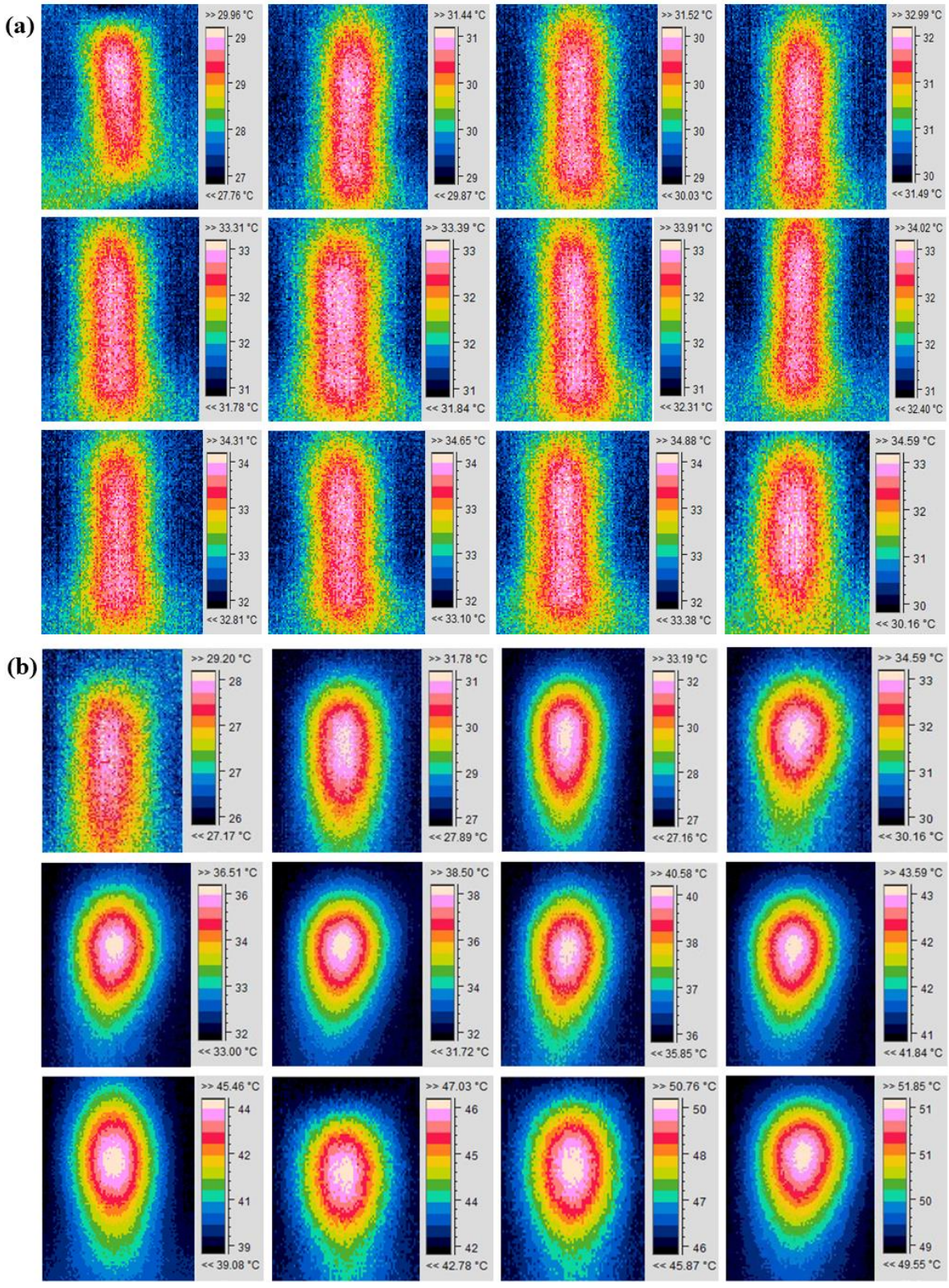
(a)
>> 29.96 °C
<< 27.76 °C
>> 31.44 °C
<< 29.87 °C
>> 31.52 °C
<< 30.03 °C
>> 32.99 °C
<< 31.49 °C
>> 33.31 °C
<< 31.78 °C
>> 33.39 °C
<< 31.84 °C
>> 33.91 °C
<< 32.31 °C
>> 34.02 °C
<< 32.40 °C
>> 34.31 °C
<< 32.81 °C
>> 34.65 °C
<< 33.10 °C
>> 34.88 °C
<< 33.38 °C
>> 34.59 °C
<< 30.16 °C
(b)
>> 29.20 °C
<< 27.17 °C
>> 31.78 °C
<< 27.89 °C
>> 33.19 °C
<< 27.16 °C
>> 34.59 °C
<< 30.16 °C
>> 36.51 °C
<< 33.00 °C
>> 38.50 °C
<< 31.72 °C
>> 40.58 °C
<< 35.85 °C
>> 43.59 °C
<< 41.84 °C
>> 45.46 °C
<< 39.08 °C
>> 47.03 °C
<< 42.78 °C
>> 50.76 °C
<< 45.87 °C
>> 51.85 °C
<< 49.55 °C

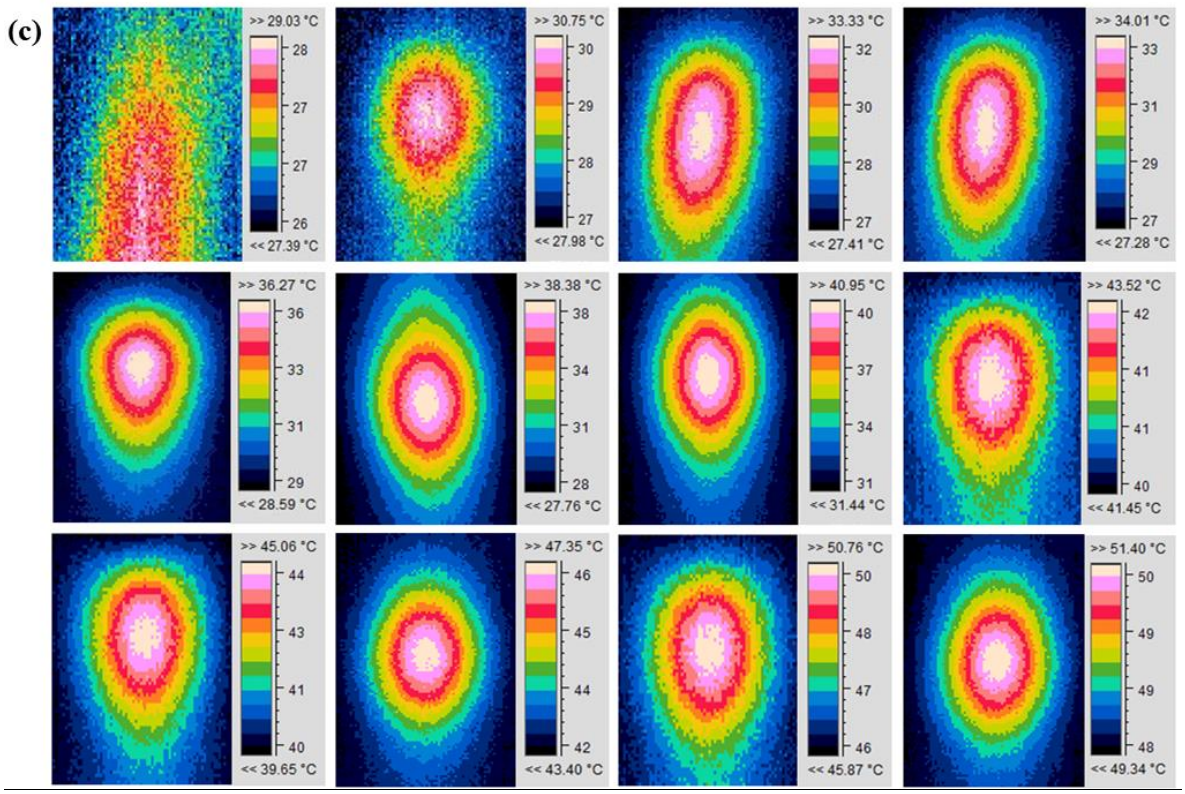

Figure A14: Thermograph of (a) DI, (b) DyGPB and (c) YbGPB nanocubes sample under 808 nm NIR laser irradiation over 11 minutes.

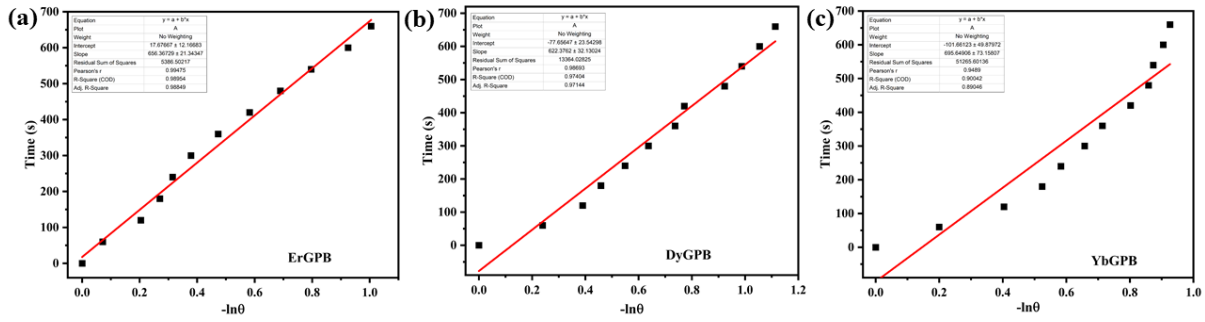

Figure A15: Plot and linear fit of time versus negative natural logarithm of the temperature increment for the cooling rate of (a) ErGPB, (b) DyGPB and (c)YbGPB under 808 nm laser.

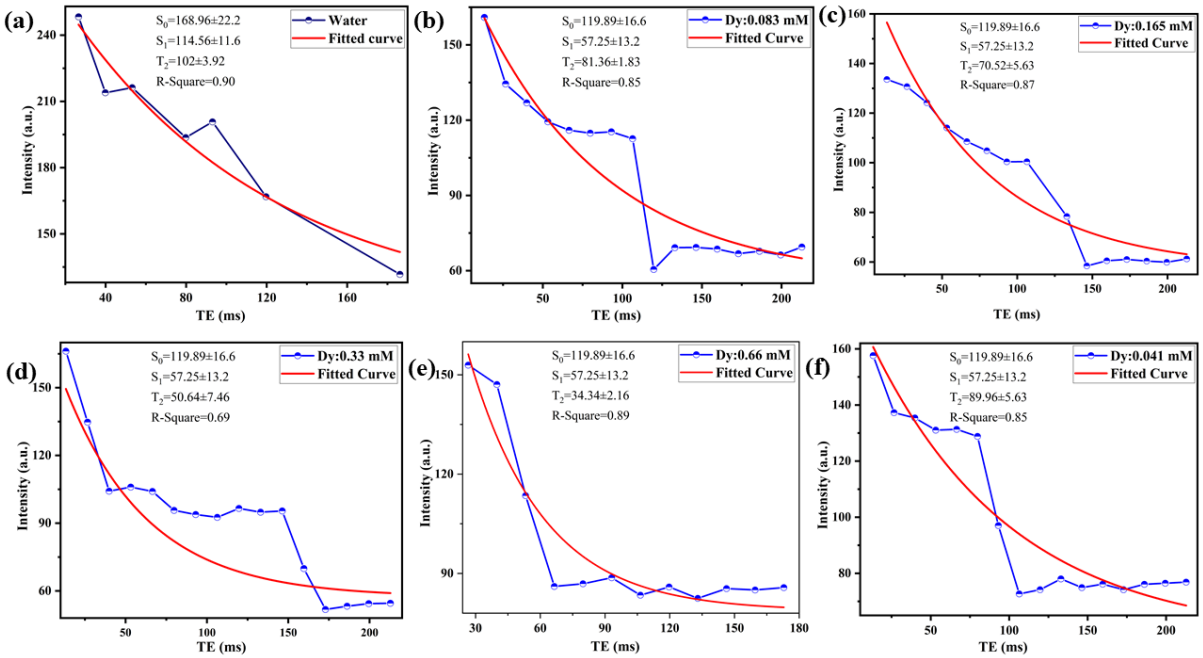

Figure A16: TE Vs signal intensity plot for different concentration of representative DyGPB nanocubes for determination of T_2 relaxation time.

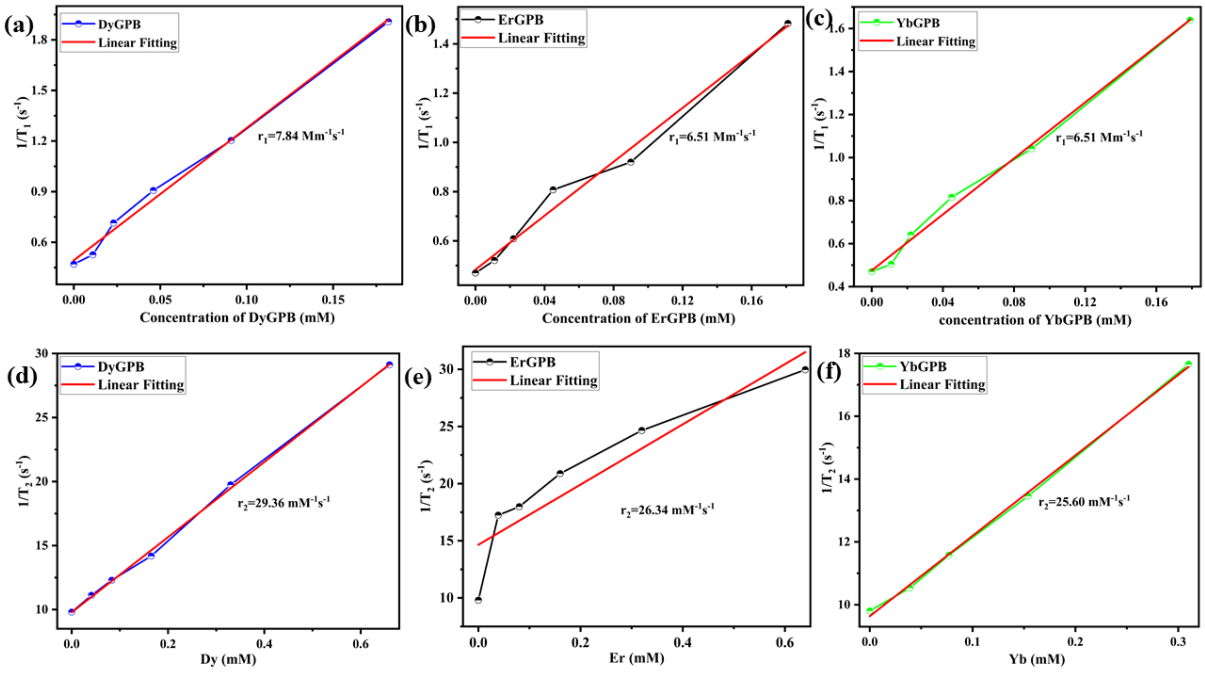

Figure A17: Concentration dependent (a-c) T_1 and (d-f) T_2 relaxation rates.

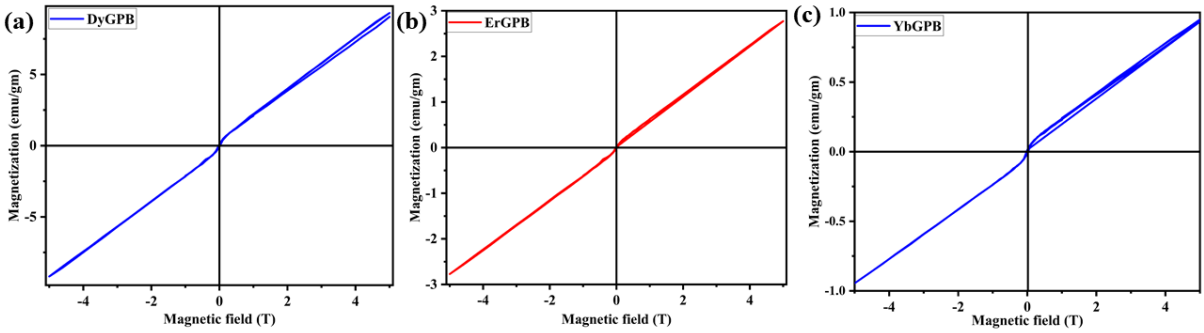

Figure A18: SQUID magnetometry. Isothermal magnetization as a function of field at 300 K for (a) PB, (b) $GPB_{0.25}$, (c) $GPB_{0.50}$, (d) $GPB_{0.75}$ and (e) GPBA nanocubes sample.

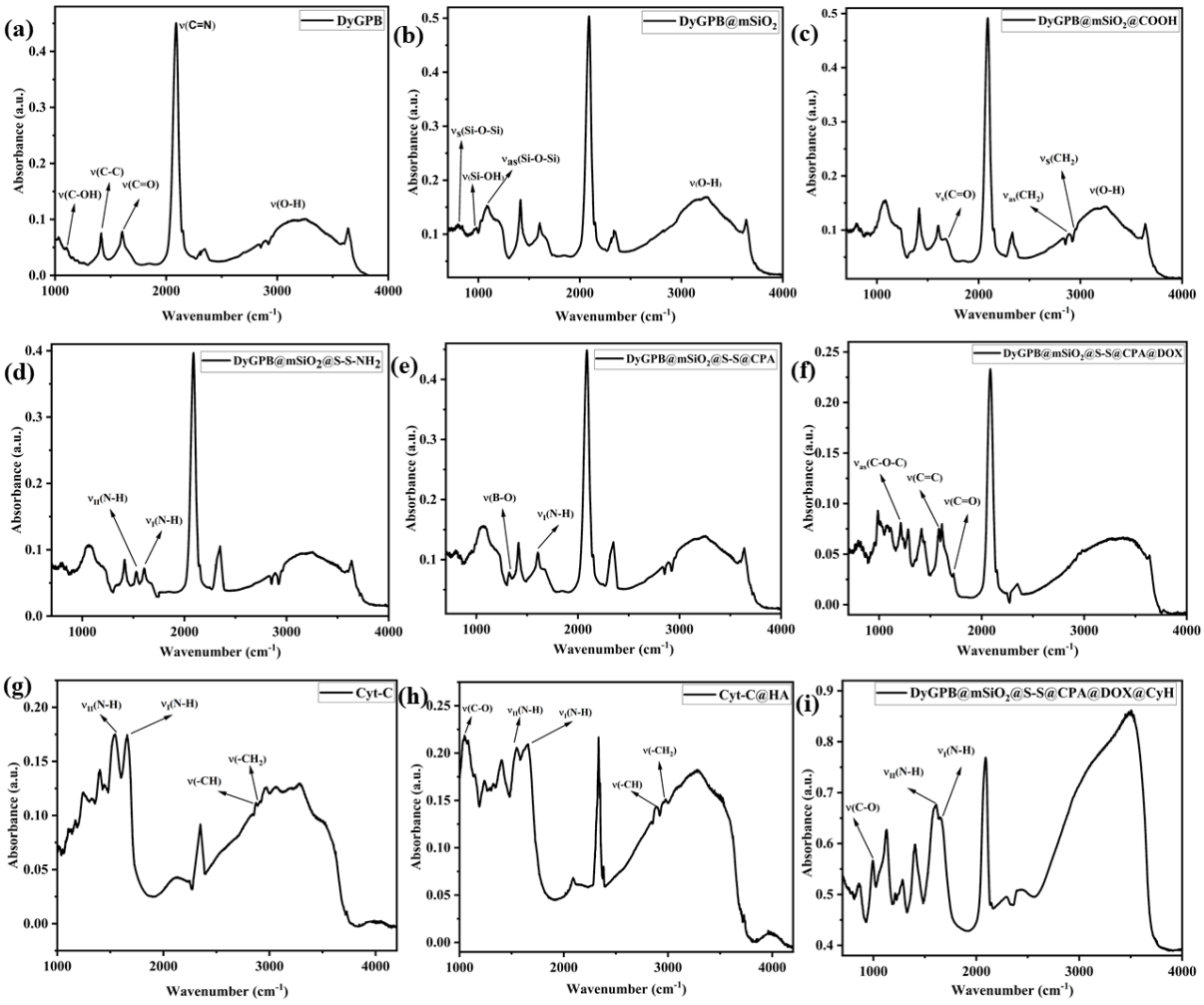

Figure A19: (a-i) FTIR spectra of DyGPB along with each step of modifications.

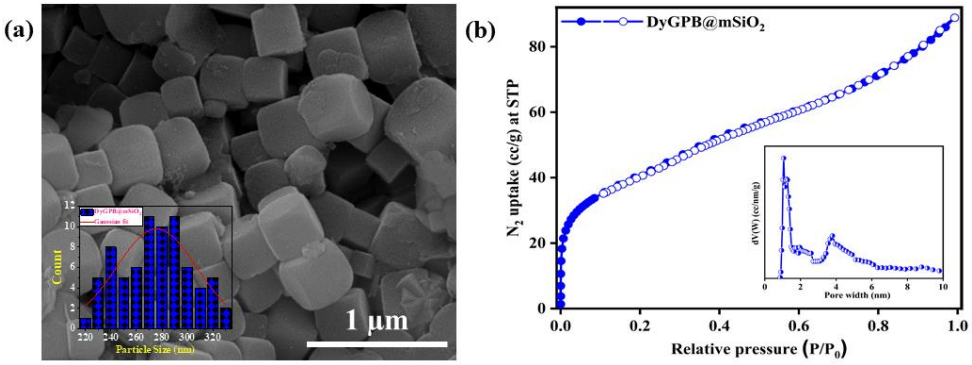

Figure A20: (a) FESEM image and size distribution histogram in the inset of DyGPB@mSiO$_2$. (b) N_2 adsorption–desorption isotherms with pore size distribution in the inset of DyGPB@mSiO$_2$.

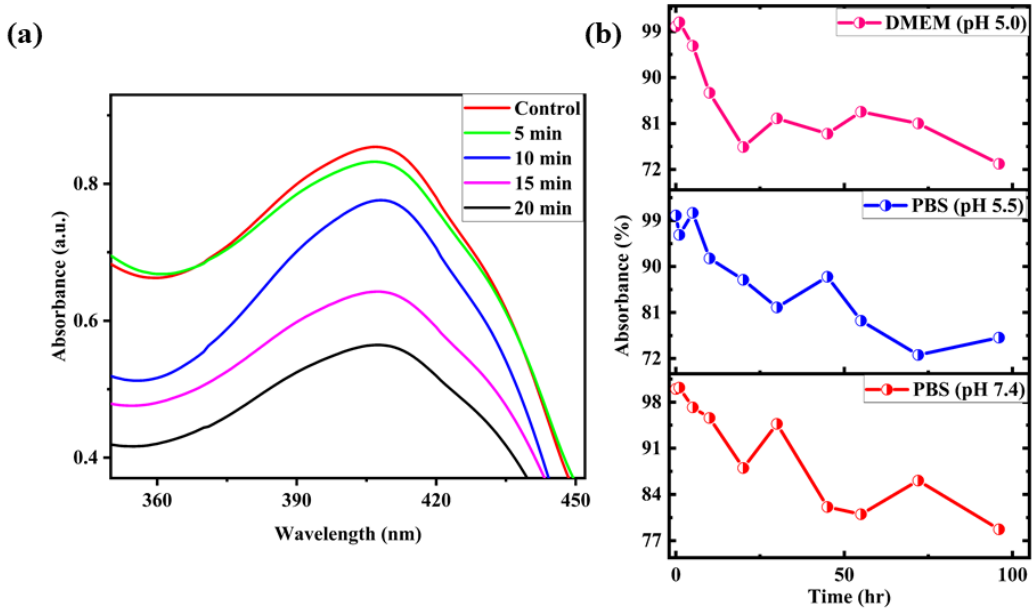

Figure A21: (a) extracellular singlet generation and (b) stability at different biological environments of DyGPB@mSiO$_2$@S-S@CPA@CyH nanoplatform.

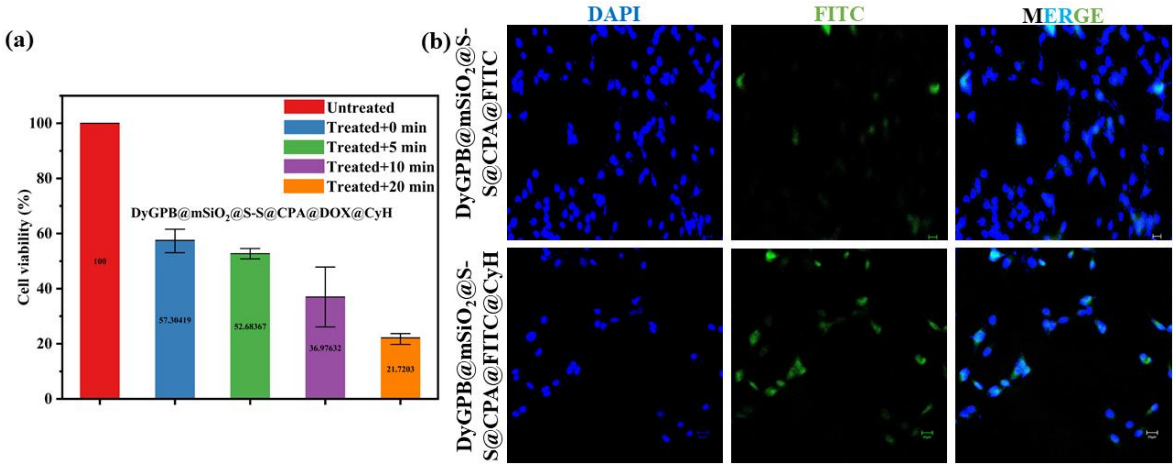

Figure A22: (a) NIR light irradiation time dependant Cell viability plot in MDA-MB-231 cells. (b) Fluorescence microscopic images of MDA-MB-231 cells incubated with DyGPB@mSiO$_2$@S-S@CPA@FITC and DyGPB@mSiO$_2$@S-S@CPA@FITC@CyH respectively. The cell nuclei were labeled with DAPI (blue), released FITC nanoparticles within cell shows green. Scar bar: 25 µm.

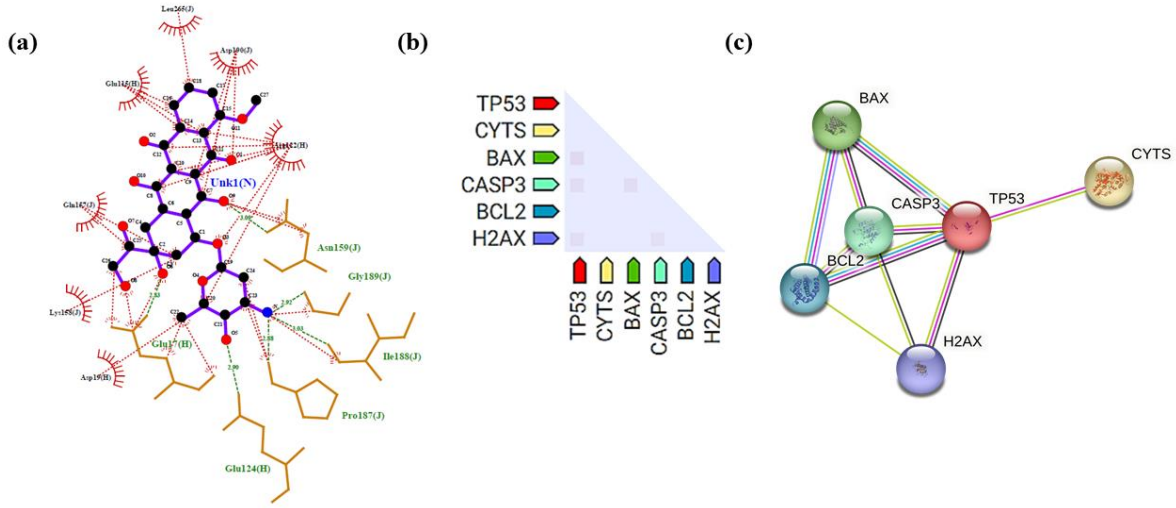

Figure A23: (a) p53 and DOX interaction. (b) Coexpression scores based on RNA expression patterns, and on protein co-regulation provided by ProteomeHD. (c) Protein protein interaction network and predictable pathway through STRING database

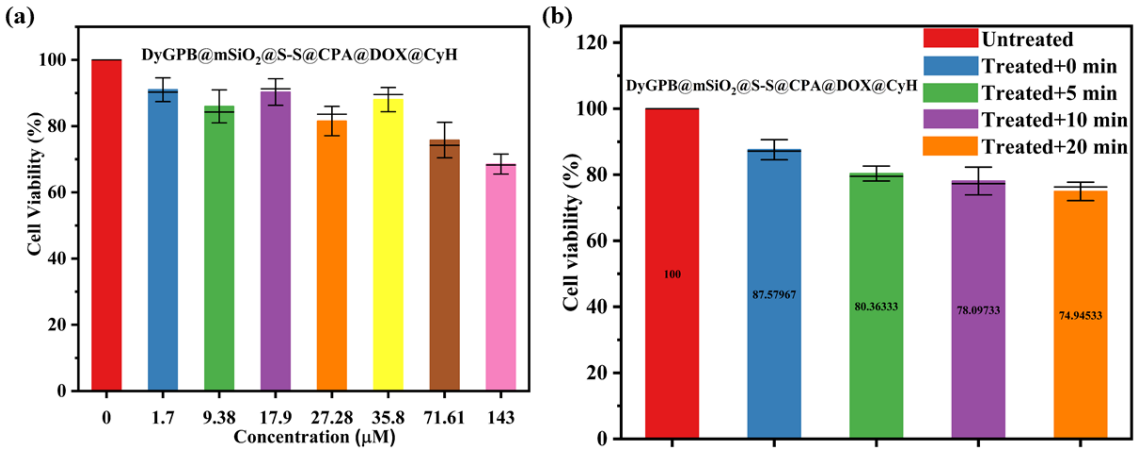

Figure A24: (a) Concentration dependant and (b) NIR light irradiation time dependant cell viability assay in HEK-293 cells.

Appendix B

Chapter 4

Table B1: Feeding amounts of reactants during synthesis in Solution A

Sample Name	$FeCl_3.6H_2O$ (mmol)	$Gd(NO_3)_3.6H_2O$ (mmol)
PB	0.0198	0.00
$GPB_{0.25}$	0.0148	0.0049
$GPB_{0.50}$	0.0099	0.0099
$GPB_{0.75}$	0.0049	0.0148
GPBA	0.00	0.0198

Table B2: Variation in the occupancy probability of the different atoms in the unit cell structure of PB, GPB and GPBA as obtained by Rietveld analysis using the Maud software

Atom	**site**	**PB**, R_p=18.68, R_{wp}=15.71		**$GPB_{0.25}$**, R_p=16.55, R_{wp}=13.42	
		Position (x)	**Occupancy**	**Position (x)**	**Occupancy**
Fe^{3+}	1a	0.0	1.0	0.0	0.7732842(20)
	3c	0.0	1.0	0.0	0.9133229(8)
Fe^{2+}	1b	0.50486345(9)	**0.6592583(21)**	0.5	**0.75717217(23)**
	3d	0.5002564(13)	0.7803208(17)	0.5	0.8512476(11)
N	6e	0.20095892(5)	0.7803186(23)	0.21973883(21)	0.6524139(17)
	6f	0.20777132(6)	0.6590573(8)	0.19607785(19)	0.68172204(26)
	12h	0.3086982(18)	0.7803359(19)	0.29398748(9)	0.7618029(9)
C	6e	0.31160247(2)	0.7803157(12)	0.2527187(13)	0.7553462(21)
	6f	0.2108135(8)	0.6592680(10)	0.3369625(17)	0.5803227(25)
	12h	0.19350913(21)	0.7803082(13)	0.24345358(7)	0.8885231(11)
O	6e	0.20546116(6)	0.2196236(24)	0.28894728(15)	0.20116886(13)
	6f	0.31103197(8)	0.3418713(15)	0.19607785(8)	0.3532405(20)
	12h	0.21343586(11)	0.2196520(17)	0.2519634(13)	0.19178203(6)
O	8g	0.28311816(7)	0.9769835(23)	0.24846497(4)	1.0557612(3)
Gd^{3+}	1a	0.0		0.0	0.2878626(8)
	3c	0.0		0.0	0.024392676(3)

Atom	**site**	**$GPB_{0.50}$**, R_p=18.01, R_{wp}=16.70		**$GPB_{0.75}$**, R_p=15.01, R_{wp}=12.36	
		Position (x)	**Occupancy**	**Position (x)**	**Occupancy**
Fe^{3+}	1a	0.0	0.19958599(6)	0.0	0.04379456(3)

	3c	0.0	0.6955486(7)	0.0	0.22820742(4)
Fe^{2+}	1b	0.5	**0.8748906(7)**	0.5	**0.8925268(5)**
	3d	0.5	0.72967404(6)	0.5	0.6744579(10)
N	6e	0.24126482(11)	0.29024577(8)	0.22482389(5)	0.34185156(28)
	6f	0.22089453(8)	0.87297755(11)	0.20800404(2)	0.935618(11)
	12h	0.2812284(9)	0.7125842(7)	0.29865497(1)	0.83086663(13)
C	6e	0.28790888(17)	0.711003(9)	0.23690972(1)	0.96722984(22)
	6f	0.3432895(12)	0.8710056(7)	0.3080017(2)	0.96336(15)
	12h	0.17622626(8)	0.7115617(6)	0.19111414(1)	0.93343514(14)
O	6e	0.26116607(16)	0.29032323(6)	0.22464009(3)	0.36714977(9)
	6f	0.21971194(21)	0.13004822(4)	0.2045692(3)	0.083756045(7)
	12h	0.2779372(7)	0.2905587(4)	0.2578505(1)	0.36965746(6)
O	8g	0.27506152(13)	0.98139584(8)	0.27008986(1)	0.9853173(17)
Gd^{3+}	1a	0.0	0.7909804(8)	0.0	0.8079837(13)
	3c	0.0	0.29800105(2)	0.0	0.60148686(9)
	3c	0.0	0.29800105(2)	0.0	0.60148686(9)

Atom	**site**	**GPBA**, R_p=11.75, R_{wp}=14.95	
		Position (x)	**Occupancy**
Gd^{3+}	1a	0.0	1
	3c	0.0	1
Fe^{2+}	1b	0.5	**0.40191638(8)**
	3d	0.5	0.8972872(5)
N	6e	0.28806(14)	0.8323061(12)
	6f	0.43577(17)	0.31923234(17)
	12h	0.3258(7)	0.9944583(14)
C	6e	0.27169(21)	0.9518085(8)
	6f	0.43577(4)	0.37184647(2)
	12h	0.19898(6)	0.878701(3)
O	6e	0.57235(11)	0.1460648(6)
	6f	0.43577(14)	0.6850089(12)
	12h	0.86476(9)	0.17641485(15)
O	8g	0.28206(3)	0.97429556(4)

Table B3: Elemental analysis as obtained from FESEM-EDX measurement

Sample	at% of Fe	at% of Gd	at% of N
$GPB_{0.25}$	28.60	0.05	42.67
$GPB_{0.50}$	23.47	0.35	52.19
$GPB_{0.75}$	12.81	0.43	73.31
GPBA	10.81	1.21	66.37

Chapter 5

Table B4: Feeding amounts of reactants during synthesis in Solution B

Sample Name	$FeCl_3.6H_2O$ (mmol)	$Gd(NO_3)_3.6H_2O$ (mmol)	$Ln(NO_3)_3{\cdot}H_2O$ (mmol)
DyGPB	0.0049	0.0049	0.0099
ErGPB	0.0049	0.0049	0.0099
YbGPB	0.0049	0.0049	0.0099

Table B5: Variation in the occupancy probability of the different atoms in the unit cell structure of PB, GPB and GPBA as obtained by Rietveld analysis using the Maud software

Atom	**site**	**DyGPB**, R_b=16.12, R_{wp}=14.31		**ErGPB**, R_b=16.55, R_{wp}=13.42	
		Position (x)	**Occupancy**	**Position (x)**	**Occupancy**
Fe^{3+}	1a	0.0	0.165	0.0	0.175
	3c	0.0	0.297	0.0	0.138
Fe^{2+}	1b	0.50000	**0.764**	0.50000	**0.591**
	3d	0.50000	0.755	0.50000	0.898
N	6e	0.21918	0.894	0.30057	0.938
	6f	0.29215	0.702	0.28896	0.567
	12h	0.30253	0.828	0.21862	0.383
C	6e	0.47523	0.145	0.81184	0.852
	6f	0.19546	0.563	0.19615	0.372
	12h	0.19599	0.627	0.22216	0.656
O	6e	0.66997	0.204	0.01581	0.103
	6f	0.20364	0.478	0.28896	0.190
	12h	0.29175	0.152	0.22850	0.606
O	8g	0.28032	0.780	0.23671	0.777
Gd^{3+}	1a	0.0	0.166	0.0	0.159

	3c	0.0	0.123	0.0	0.195
Ln^{3+}	1a	0.0	0.530	0.0	0.409
	3c	0.0	0.454	0.0	0.478

Atom	**site**	**YbGPB**, R_b=14.63, R_{wp}=4.71	
		Position (x)	**Occupancy**
Fe^{2+}	1b	0.5	**0.5690012**
	3d	0.5	0.8794047
Fe^{3+}	1a	0.0	0.27332488
	3c	0.0	0.22522584
Gd^{3+}	1a	0.0	0.19224042
	3c	0.0	0.1483181
Ln^{3+}	1a	0.0	0.31081828
	3c	0.0	0.20412911
N	6e	0.26837584	0.9385618
	6f	0.2984405	0.3853153
	12h	0.23231922	1.013478
C	6e	0.26837584	0.9545968
	6f	0.19365923	0.39602667
	12h	0.2153907	0.81666696
O	6e	0.26837584	0.18375193
	6f	0.17019	0.709
	12h	0.23231922	0.19078782
O	8g	0.19679	0.983

Table B6: Elemental analysis as obtained from FESEM-EDX measurement

Sample	**at% of Fe**	**at% of Gd**	**at% of Ln**	**at% of O**	**at% of N**
DyGPB	30.19	0.36	0.85	32.01	36.59
ErGPB	24.06	0.25	0.75	24.42	50.52
YbGPB	26.02	0.29	0.93	26.46	46.30

Thesis_panchanan

ORIGINALITY REPORT

10%
SIMILARITY INDEX

PRIMARY SOURCES

1	Sudip Kundu, Pulak Jana, Panchanan Sahoo, Sourav Kumar Nandi et al. "Curcumin-based Nanoformulation for the Pyroptotic Death of MDA-MB-231 Cells", ACS Applied Nano Materials, 2024 Crossref	967 words — 2%
2	pubmed.ncbi.nlm.nih.gov Internet	535 words — 1%
3	www.ncbi.nlm.nih.gov Internet	426 words — 1%
4	iimshillong-sb.webdesigner.wizdes.com Internet	300 words — < 1%
5	Aparna Datta, Snehasis Mishra, Krishnendu Manna, Krishna Das Saha, Siddhartha Mukherjee, Somenath Roy. "Pro-Oxidant Therapeutic Activities of Cerium Oxide Nanoparticles in Colorectal Carcinoma Cells", ACS Omega, 2020 Crossref	221 words — < 1%
6	repository.bose.res.in:8080 Internet	201 words — < 1%
7	link.springer.com Internet	191 words — < 1%

8	www.mdpi.com Internet	182 words — < 1%
9	repository.kaust.edu.sa Internet	162 words — < 1%
10	Piyali Bhanja, Snehasis Mishra, Krishnendu Manna, Arijit Mallick, Krishna Das Saha, Asim Bhaumik. "Covalent Organic Framework Material Bearing Phloroglucinol Building Units as a Potent Anticancer Agent", ACS Applied Materials & Interfaces, 2017 Crossref	146 words — < 1%
11	www.researchgate.net Internet	130 words — < 1%
12	onlinelibrary.wiley.com Internet	127 words — < 1%
13	www.rsc.org Internet	120 words — < 1%
14	pubs.rsc.org Internet	113 words — < 1%
15	Milan Gautam, Kishwor Poudel, Chul Soon Yong, Jong Oh Kim. "Prussian blue nanoparticles: Synthesis, surface modification, and application in cancer treatment", International Journal of Pharmaceutics, 2018 Crossref	99 words — < 1%
16	Xianwen Wang, Liang Cheng. "Multifunctional Prussian blue-based nanomaterials: Preparation, modification, and theranostic applications", Coordination Chemistry Reviews, 2020 Crossref	96 words — < 1%

17	www.jaduniv.edu.in Internet	94 words — < 1%
18	Bo Zhou, Bang-Ping Jiang, Wanying Sun, Fang-Mian Wei, Yun He, Hong Liang, Xing-Can Shen. "Water-Dispersible Prussian Blue Hyaluronic Acid Nanocubes with Near-Infrared Photoinduced Singlet Oxygen Production and Photothermal Activities for Cancer Theranostics", ACS Applied Materials & Interfaces, 2018 Crossref	88 words — < 1%
19	Ripan K. Biswas, Prosenjit Khan, Smita Mukherjee, Anoop K. Mukhopadhyay, Jiten Ghosh, K. Muraleedharan. "Study of short range structure of amorphous Silica from PDF using Ag radiation in laboratory XRD system, RAMAN and NEXAFS", Journal of Non-Crystalline Solids, 2018 Crossref	88 words — < 1%
20	docecity.com Internet	82 words — < 1%
21	fatcat.wiki Internet	71 words — < 1%
22	Maria Antònia Busquets, Joan Estelrich. "Prussian blue nanoparticles: synthesis, surface modification, and biomedical applications", Drug Discovery Today, 2020 Crossref	63 words — < 1%
23	www.geocities.ws Internet	62 words — < 1%
24	Xiaojun Cai, Wei Gao, Linlin Zhang, Ming Ma, Tianzhi Liu, Wenxian Du, Yuanyi Zheng, Hangrong	52 words — < 1%

Chen, Jianlin Shi. "Enabling Prussian Blue with Tunable Localized Surface Plasmon Resonances: Simultaneously Enhanced Dual-Mode Imaging and Tumor Photothermal Therapy", ACS Nano, 2016
Crossref

25 Snehasis Mishra, Kaustav das, Sujan Chatterjee, Panchanan Sahoo, Sudip Kundu, Mrinal Pal, Asim Bhaumik, Chandan Kumar Ghosh. " Facile and Green Synthesis of Novel Fluorescent Carbon Quantum Dots and Their Silver Heterostructure: An Anticancer Activity and Imaging on Colorectal Carcinoma ", ACS Omega, 2023 — 49 words — < 1%
Crossref

26 Liangliang Dai, Jinghua Li, Beilu Zhang, Junjie Liu, Zhong Luo, Kaiyong Cai. " Redox-Responsive Nanocarrier Based on Heparin End-Capped Mesoporous Silica Nanoparticles for Targeted Tumor Therapy and ", Langmuir, 2014 — 48 words — < 1%
Crossref

27 Marine Perrier, Samir Kenouche, Jêrôme Long, Kalaivani Thangavel et al. "Investigation on NMR Relaxivity of Nano-Sized Cyano-Bridged Coordination Polymers", Inorganic Chemistry, 2013 — 48 words — < 1%
Crossref

28 Boshi Tian, Chen Wang, Yaqian Du, Shuming Dong, Lili Feng, Bin Liu, Shikai Liu, He Ding, Shili Gai, Fei He, Piaoping Yang. "Near Infrared-Triggered Theranostic Nanoplatform with Controlled Release of HSP90 Inhibitor for Synergistic Mild Photothermal and Enhanced Nanocatalytic Therapy with Hypoxia Relief", Small, 2022 — 39 words — < 1%
Crossref

29 Kaiyuan Tang, Xiao Li, Yanling Hu, Xiaonan Zhang et al. "Recent advances in Prussian blue-based — 38 words — < 1%

photothermal therapy in cancer treatment", Biomaterials Science, 2023
Crossref

30 www.oncotarget.com
Internet
37 words — < 1%

31 Minhuan Lan, Shaojing Zhao, Weimin Liu, Chun-Sing Lee, Wenjun Zhang, Pengfei Wang. "Photosensitizers for Photodynamic Therapy", Advanced Healthcare Materials, 2019
Crossref
35 words — < 1%

32 Yong Gao, Guocan Yu, Kuoran Xing, Dmitry Gorin, Yuri Kotelevtsev, Weijun Tong, Zhengwei Mao. "Finely tuned Prussian blue-based nanoparticles and their application in disease treatment", Journal of Materials Chemistry B, 2020
Crossref
35 words — < 1%

33 Zhang, Juchen, Zengying Qiao, Peipei Yang, Jie Pan, Lei Wang, and Hao Wang. "Recent Advances in Near-Infrared Absorption Nanomaterials as Photoacoustic Contrast Agents for Biomedical Imaging", Chinese Journal of Chemistry, 2014.
Crossref
34 words — < 1%

34 jbiomedsci.biomedcentral.com
Internet
34 words — < 1%

35 www.eprints.iicb.res.in
Internet
34 words — < 1%

36 drum.lib.umd.edu
Internet
33 words — < 1%

37 Banalata Sahoo, K. Sanjana P. Devi, Sujan Dutta, Tapas K. Maiti, Panchanan Pramanik, Dibakar Dhara. "Biocompatible mesoporous silica-coated superparamagnetic manganese ferrite nanoparticles for targeted drug delivery and MR imaging applications", Journal of Colloid and Interface Science, 2014
Crossref
32 words — < 1%

38 Dongjian Zhang, Qiaomei Jin, Cuihua Jiang, Meng Gao, Yicheng Ni, Jian Zhang. "Imaging Cell Death: Focus on Early Evaluation of Tumor Response to Therapy", Bioconjugate Chemistry, 2020
Crossref
32 words — < 1%

39 www.nature.com
Internet
30 words — < 1%

40 Andreas Helck, Wieland H. Sommer, Ernst Klotz, Matthias Wessely et al. "Determination of Glomerular Filtration Rate Using Dynamic CT-Angiography", Investigative Radiology, 2010
Crossref
29 words — < 1%

41 rcastoragev2.blob.core.windows.net
Internet
29 words — < 1%

42 tr.overleaf.com
Internet
28 words — < 1%

43 Zijian Zhou, Ruiliang Bai, Zhantong Wang, Henry Bryant et al. " An Albumin-Binding – Dual-Modal MRI Contrast Agents for Improved Sensitivity and Accuracy in Tumor Imaging ", Bioconjugate Chemistry, 2019
Crossref
27 words — < 1%

44 file.scirp.org
Internet
27 words — < 1%

45	jnanobiotechnology.biomedcentral.com Internet	27 words — < 1%
46	universe.bits-pilani.ac.in Internet	27 words — < 1%
47	www.frontiersin.org Internet	26 words — < 1%
48	Louise Samain, Fernande Grandjean, Gary J. Long, Pauline Martinetto, Pierre Bordet, David Strivay. "Relationship between the Synthesis of Prussian Blue Pigments, Their Color, Physical Properties, and Their Behavior in Paint Layers", The Journal of Physical Chemistry C, 2013 Crossref	25 words — < 1%
49	Shan Lei, Jinxing Chen, Kun Zeng, Mozhen Wang, Xuewu Ge. "Visual dual chemodynamic/photothermal therapeutic nanoplatform based on superoxide dismutase plus Prussian blue", Nano Research, 2019 Crossref	25 words — < 1%
50	Xiaoqing Jia, Xiaojun Cai, Yu Chen, Shige Wang, Huixiong Xu, Kun Zhang, Ming Ma, Huixia Wu, Jianlin Shi, Hangrong Chen. "Perfluoropentane-Encapsulated Hollow Mesoporous Prussian Blue Nanocubes for Activated Ultrasound Imaging and Photothermal Therapy of Cancer", ACS Applied Materials & Interfaces, 2015 Crossref	25 words — < 1%
51	www.allresearchjournal.com Internet	23 words — < 1%
52	Shihong Chen, Ruo Yuan, Yaqin Chai, Yang Xu, Ligen Min, Na Li. "A new antibody immobilization	21 words — < 1%

technique based on organic polymers protected Prussian blue nanoparticles and gold colloidal nanoparticles for amperometric immunosensors", Sensors and Actuators B: Chemical, 2008
Crossref

53 www.tandfonline.com
Internet
20 words — < 1%

54 Fernande Grandjean, Louise Samain, Gary J. Long. "Characterization and utilization of Prussian blue and its pigments", Dalton Transactions, 2016
Crossref
19 words — < 1%

55 Mukul Bikash Maity, Suprava Bhunia, Arka Patra, Panchanan Sahoo, Snehasis Mishra, Chittaranjan Sinha. " Use of diformyl-triazolo Schiff base for Zn sensing and intracellular live cell imaging ", Applied Organometallic Chemistry, 2023
Crossref
19 words — < 1%

56 Yu Lu, Peng Zhang, Lihao Lin, Xuan Gao, Yifei Zhou, Jing Feng, Hongjie Zhang. "Ultra-small bimetallic phosphides for dual-modal MRI imaging guided photothermal ablation of tumors", Dalton Transactions, 2022
Crossref
19 words — < 1%

57 Małgorzata Norek, Erik Kampert, Uli Zeitler, Joop A. Peters. " Tuning of the Size of Dy O Nanoparticles for Optimal Performance as an MRI Contrast Agent ", Journal of the American Chemical Society, 2008
Crossref
18 words — < 1%

58 www.coursehero.com
Internet
18 words — < 1%

59	Bo Zhou, Bang-Ping Jiang, Wanying Sun, Fang-Mian Wei, Yun He, Hong Liang, Xing-Can Shen. "Water-Dispersible Prussian Blue-Hyaluronic Acid Nanocubes with Near-Infrared Photoinduced Singlet Oxygen Production and Photothermal Activities for Cancer Theranostics", ACS Applied Materials & Interfaces, 2018 Crossref	17 words — < 1%
60	Fangfang Chen, Lili Teng, Chang Lu, Cheng Zhang, Qiming Rong, Yan Zhao, Yue Yang, Youjuan Wang, Guosheng Song, Xiaobing Zhang. " Activatable Magnetic/Photoacoustic Nanoplatform for Redox-Unlocked Deep-Tissue Molecular Imaging via Prussian Blue Nanoprobe ", Analytical Chemistry, 2020 Crossref	17 words — < 1%
61	oaji.net Internet	17 words — < 1%
62	soar-ir.repo.nii.ac.jp Internet	17 words — < 1%
63	www.cancercenter.com Internet	17 words — < 1%
64	Jun Zhou, Menghuan Li, Yanhua Hou, Zhong Luo et al. "Engineering of a Nanosized Biocatalyst for Combined Tumor Starvation and Low-Temperature Photothermal Therapy", ACS Nano, 2018 Crossref	16 words — < 1%
65	Nipun Babu Varukattu, Wan Lin, Raju Vivek, Chandrababu Rejeeth, Shanmugam Sabarathinam, Zhimeng Yao, Hao Zhang. "Targeted and Intrinsic Activity of HA-Functionalized PEI-Nanoceria as a Nano	16 words — < 1%

Reactor in Potential Triple-Negative Breast Cancer Treatment", ACS Applied Bio Materials, 2019
Crossref

66 Wenwen Zhu, Kai Liu, Xiaoqi Sun, Xin Wang, Yonggang Li, Liang Cheng, Zhuang Liu. " Mn - Doped Prussian Blue Nanocubes for Bimodal Imaging and Photothermal Therapy with Enhanced Performance ", ACS Applied Materials & Interfaces, 2015 — 16 words — < 1%
Crossref

67 Yun Yan Su, Zhaogang Teng, Hui Yao, Shou Ju Wang et al. " A Multifunctional PB@mSiO – PEG/DOX Nanoplatform for Combined Photothermal–Chemotherapy of Tumor ", ACS Applied Materials & Interfaces, 2016 — 16 words — < 1%
Crossref

68 acris.aalto.fi — 16 words — < 1%
Internet

69 www.karger.com — 16 words — < 1%
Internet

70 Dey, Sayan, Swarupananda Bhattacharjee, Mahua Ghosh Chaudhuri, Raj Shekhar Bose, Suman Halder, and Chandan Kr. Ghosh. "Synthesis of pure nickel(iii) oxide nanoparticles at room temperature for Cr(vi) ion removal", RSC Advances, 2015. — 15 words — < 1%
Crossref

71 Matthieu F. Dumont, Hilary A. Hoffman, Pryscilla R. S. Yoon, Laurie S. Conklin et al. "Biofunctionalized Gadolinium-Containing Prussian Blue Nanoparticles as Multimodal Molecular Imaging Agents", Bioconjugate Chemistry, 2013 — 15 words — < 1%
Crossref

72	ndl.ethernet.edu.et Internet	15 words — < 1%
73	worldwidescience.org Internet	15 words — < 1%
74	www2.mdpi.com Internet	15 words — < 1%
75	Yan Dou, Xue Li, Weitao Yang, Yanyan Guo, Menglin Wu, Yajuan Liu, Xiaodong Li, Xuening Zhang, Jin Chang. "PB@Au Core–Satellite Multifunctional Nanotheranostics for Magnetic Resonance and Computed Tomography Imaging in Vivo and Synergetic Photothermal and Radiosensitive Therapy", ACS Applied Materials & Interfaces, 2017 Crossref	14 words — < 1%
76	d.docksci.com Internet	14 words — < 1%
77	lirias.kuleuven.be Internet	14 words — < 1%
78	mdpi-res.com Internet	14 words — < 1%
79	publicatt.unicatt.it Internet	14 words — < 1%

EXCLUDE QUOTES	ON	EXCLUDE SOURCES	OFF
EXCLUDE BIBLIOGRAPHY	ON	EXCLUDE MATCHES	< 14 WORDS